Coupled Models of Glacial Isostasy and Ice Sheet Dynamics

by

Christopher Zweck, BSc(Hons)

Submitted in fulfilment of
the requirements for the degree of
Doctor of Philosophy
University of Tasmania, September 1997

I hereby declare that this thesis does not incorporate without acknowledgement any material previously submitted for a degree of diploma at any university. To the best of my knowledge and belief this thesis contains no material previously published or written by another person except where due acknowledgement is made.

Christopher Zweck

This thesis may be made available for loan and limited copying in accordance with the Copyright Act 1968.

Christopher Zweck

Acknowledgements

I would like to thank Garth Paltridge for excellent supervision during the course of this work. Thanks also go to Roland Warner and Bill Budd for their encouragement and support. Many thanks also to Richard Coleman for the OSU91A satellite data and extraction code.

Abstract

This thesis deals with the incorporation of isostatic processes into realistic models of ice sheet dynamics. A viscoelastic half-space model of isostatic adjustment is developed, and as an initial exercise is coupled to a model of the Antarctic ice sheet simulating the last glacial cycle. The ice sheet model is a three-dimensional, time-dependent model originally formulated by Jenssen (1977) where the driving input data are net accumulation of snow and eustatic sea level change. This allows examination of the sensitivity of the ice sheet simulation to changes in the parameters of the isostatic model. In general, the maximum ice volume generated over a glacial cycle decreases with increasing mantle viscosity and increasing lithospheric rigidity.

To obtain realistic values for the isostatic parameters of mantle viscosity and lithospheric rigidity the retreat of the Northern Hemisphere ice sheets and the subsequent isostatic adjustment since the last ice age is simulated. The isostatic parameters are adjusted until the overall model provides the best match to relative sea level data, with the eustatic component of the relative sea level change prescribed. (The maximum value of the amplitude of the prescribed sea level change is 130 m as determined from the Huon Peninsula in Papua New Guinea). Initially the simulation and matching procedure is performed using a simple ice sheet model whose time dependent extent is set by the ICE4G dataset (Peltier, 1994) and whose thickness and volume is set on the assumption of a parabolic profile of thickness. From these trials the model parameters that most realistically reproduce the observed isostatic adjustment associated with the retreat of the Laurentide ice sheet are 3×10^{21} Pa s for lower mantle viscosity, 2×10^{21} Pa s for upper mantle viscosity and 1×10^{25} N m for lithospheric rigidity. For the Fennoscandian ice sheet the corresponding parameter values are 6×10^{21} Pa s, 4×10^{21} Pa s and 6×10^{24} N m. The trials are then repeated with the parabolic profile ice sheet assumption replaced by generation of ice sheet thickness using the Jenssen ice sheet model. For the Laurentide ice sheet the same earth model parameters are recovered. For the Fennoscandian ice sheet the use of the Jenssen model to simulate ice thickness produces earth model parameters of 1.3×10^{21} Pa s for both the lower and upper mantle viscosity and

2×10^{25} N m for the lithospheric rigidity. A problem with the analysis is that the maximum volume of the combined ice sheets corresponds only to 50 m of eustatic sea level change in the case of the parabolic profile simulation and to 40 m when using the Jenssen model.

The sensitivity of the Antarctic ice sheet to regional variations in lithospheric rigidity is examined. Using a range of simple relations between crustal thickness (for which there exists data on geographic distribution) and lithospheric thickness, it is determined that the main effect of non-uniform lithospheric thickness is on the extent of the Ronne and Amery ice shelves.

The constraint of prescribed eustatic sea level change since the last ice age is removed by linking the Laurentide, Fennoscandian and Antarctic ice sheet models via the common sea level change determined by the deglaciation of the combined ice sheets. The constraint on Northern Hemisphere ice sheet extent is also removed by allowing the ice sheet model (the Jenssen model) to determine its own extent when driven by climatology and the Milankovitch cycles of solar input. This overall model produces a realistic eustatic sea level change since the last ice age (130 m), but unrealistic changes in relative sea level. In some locations the calculated relative sea level changes are too large by 200 m.

The problem of obtaining a consistent simulation of both eustatic and relative sea level change is not resolved. There are three possible explanations. First there may have been an extensive ice sheet over Siberia, which has not been accounted for in this or any other analysis. Second the calculations here assume linearity between isostatic disequilibrium and rate of adjustment. This may not be the case. Third, significant changes in ice volume may have occurred before the relative sea level record was laid down in the geological record.

CONTENTS

LIST OF TABLES

LIST OF FIGURES

1. INTRODUCTION

The retreat of the ice sheets at the end of the last ice age is arguably the most profound change to the surface of the earth in recent geological time. This transformation is a key focus of inquiry for two distinct fields of research. On the one hand the isostatic adjustment following the ice retreat is one of a limited set of phenomena that allow investigation of the properties of the deeper earth. On the other hand the behaviour of the ice in response to the climate change which drove the retreat allows the development of an understanding of the behaviour of present day ice sheets.

Naturally the choice of which ice sheet to study in these fields is determined by the availability of data. The glacio-geomorphology and isostatic adjustment of former ice sheets such as the Laurentide and Fennoscandian are well understood, but their thickness and elevation at the last glacial maximum are debatable. For these reasons they are examined more in isostatic modelling than in ice sheet modelling. For ice sheets such as Antarctica and Greenland the present day ice sheet thickness and elevation are well constrained, but the extent and isostatic adjustment of these ice sheets at the last glacial maximum are not. For these reasons they are examined more closely in ice sheet modelling than in isostatic modelling.

The study of ice sheets and the study of glacial isostasy have emerged from separate disciplines. As a result of this separation it is not surprising that in each discipline assumptions regarding the other are invoked. Peltier (1996b) states:

> Errors in our knowledge of either mantle viscosity or deglaciation history could, in principle, propagate into our inference of the other. The widely varying inferences of mantle viscosity that have appeared in recent literature could thus be a simple consequence of errors in the deglaciation

history. Similarly, recently proposed models of the deglaciation history may be sensitive to errors in the model of the radial variation of viscosity.

Several authors have examined this sensitivity and suggested that the conclusions generated from isostatic models are sensitive to the form of the ice sheet assumed in the calculation (Han & Wahr, 1995; Fang & Hager, 1996). Ice sheet modelling results show a sensitivity to assumptions about how isostasy is implemented (Le Meur & Huybrechts, 1996; Lingle & Clark, 1985).

The present thesis concerns the results from the coupling of a reasonably detailed 'limited area' ice sheet model to a reasonably detailed 'limited area' earth model. In Chapter 4 a glacial cycle simulation of the behaviour of the Antarctic ice sheet is conducted to determine its sensitivity to different isostatic models and parameters. In Chapters 5 and 6 a model is used to simulate the glacio-isostatic adjustment observed around North America and Northern Europe in order to determine the magnitudes of earth model parameters that realistically reproduce the isostatic adjustment in these regions. These chapters also examine the sensitivity of the calculations to assumptions relating to the representation of the ice sheets. Chapter 7 discusses the implications of non-uniform lithospheric thickness in glacio-isostatic models of Antarctica. Chapter 8 discusses the coupling of the Laurentide, Fennoscandian and Antarctic ice sheets through a common first-order representation of eustatic sea level change in an effort to reproduce the observed sea level changes over the last glacial cycle.

2. LITERATURE REVIEW

This section reviews the physical interactions between isostasy and ice sheets. It is divided into three sections. The first reviews the treatment of isostasy in ice sheet models. The second reviews the treatment of ice sheets in models of isostasy. The last section reviews the results of coupled earth/ice-sheet models.

In much of this thesis there is reference to eustatic and relative sea level change. It should be explained that in the present study eustatic sea level change is the change in sea level elevation which results from changes in ocean volume with time. In the present study the change in ocean volume is assumed to reflect changes resulting from the growth and retreat of ice sheets. Relative sea level indicates changes in ocean surface area with respect to the present day surface profile of the earth. Thus relative sea level changes account for both the isostatic adjustment of the earth and the eustatic sea level change of the ocean.

2.1 The Treatment of Glacial Isostasy in Ice Sheet Models

The most common approach to incorporating glacial isostasy in ice sheet models is to use the 'thin channel flow' assumption. This assumption represents the earth's mantle as a viscous 'asthenosphere' where flow is confined to a channel of finite thickness overlying a rigid substratum. The channel thickness is assumed to be small compared to the spatial scale of the ice sheet. The thin channel flow concept was introduced by Van Bremmelen and Berlage in 1935 (Walcott, 1973) at the same time that Haskell (1935) introduced a 'half-space' isostatic model in which isostatic adjustment was not confined to a thin channel but occurred at depth in the earth's mantle. Haskell's model was used more or less universally until 1963 because Daly (1934) suggested that the thin channel model predicted a peripheral bulge at the edge of the ice sheet during its advance much

larger than the geological evidence suggested. Takeuchi (1963) reintroduced the thin channel model with the justification that it predicted more realistic isostatic adjustment rates than the half-space model (Peltier, 1980). Coupled with a model of lithospheric adjustment introduced by McConnell (1965) the thin channel model has been adopted as an adequate representation of glacial isostasy for ice sheet modelling by authors such as Huybrechts (1992) and Letreguilly and Ritz (1993).

The thin channel model predicts submergence peripheral to the Northern Hemisphere ice sheets during their retreat (Officer et al., 1988). Peripheral submergence following ice sheet retreat has been documented in the geological record (Livermann, 1994), but McConnell (1965) realised that this behaviour is also produced by a half-space earth model with viscosity that increases radially towards the earth's core. Investigations subsequent to those of McConnell have incorporated viscosity stratifications as a function of depth to explain the peripheral submergence, with authors such as Fjeldskar and Cathles (1991) invoking the notion of a 'low viscosity channel' beneath the lithosphere which produces similar behaviour to the thin channel flow model. Sigmundsson (1991) suggested that the existence of a low viscosity channel with viscosity 1×10^{19} Pa s can explain the relative sea level data for Iceland. Sigmundsson noted however that this result could reflect a lateral variation in viscosity, as Iceland is located directly over a mid-oceanic ridge. Breuer and Wolf (1995) suggest that a channel with viscosity in the range 3×10^{18} Pa s to 2×10^{19} Pa s can explain the adjustment in the Svalbard Archipelago. However Mitrovica (1996) notes that varied estimates of mantle viscosity have been made for the Svalbard Archipelago, and attributes this variation to the limited knowledge of the ice sheet history over the region. Lambeck et al (1996) suggest that for the British Isles it is necessary to invoke a low viscosity channel if the thickness of the lithosphere is assumed to be less than 50 km. A lithospheric thickness of less than 50 km was also found to be consistent with the low viscosity channel concept of Fjeldskar and Cathles.

There is then some debate about the existence of a thin channel beneath the lithosphere. However Peltier (1980) rejects the thin channel flow model by

denying the existence of a rigid substratum beneath a low viscosity channel on the basis of seismic evidence. Certainly the use of the thin channel assumption can greatly influence the modelled behaviour of the ice sheet itself. Letreguilly and Ritz (1993) concluded that, when using the thin channel adjustment model in an ice sheet model, an advancing ice sheet produces an isostatic forebulge a few hundred metres high so that the shallow sea floor to the front of the sheet is raised above sea level and is subsequently covered by the ice. The forebulge results from an excess of mantle material at the edge of the ice sheet that has been 'squeezed out' from beneath the ice to accommodate the isostatic adjustment. For a half-space model the induced flow in the earth's mantle is predominantly vertical and a forebulge of a few hundred metres is not possible. This would in turn suggest that the shallow sea floor to the periphery of the ice sheet is not raised above sea level and is not covered by ice. The advance of the ice sheet is therefore overestimated by the use of the thin channel flow model.

The bias of the thin channel flow model towards a greater ice advance during a period of growth has also been reported by Marsiat (1994). In her study a larger magnitude of advance and retreat for the ice sheet occurs when using a thin channel earth model than when using a simple physically-parametrised isostatic adjustment model. For reasons similar to those suggested by Letreguilly and Ritz, Marsiat concluded that the forebulge created around the ice sheet by the thin channel flow model allows the ice to advance further over the surface of the continent. Her results showed that 38% more ice is generated over a glacial cycle when using the thin channel flow model than when using the parametrised adjustment model, corresponding to a maximum difference in the generated eustatic sea level change of 36 m.

Using arguments similar to the above, Oerlemans and Van der Veen (1984) suggested that isostasy accelerates both the growth and retreat of ice sheets. The thin channel flow model exaggerates ice sheet advance because the peripheral bulge enhances the ice sheet grounding. During retreat the peripheral bulge collapses and accelerates the ungrounding of the ice sheet. However Payne et al (1989) reported that the retreat of the marine based ice sheet of the

West Antarctic Peninsula is accelerated by an increase in the viscosity of the thin channel model. This result is not consistent with the suggestion of Oerlemans and Van der Veen. Payne et al concluded that the reduction in the rate of isostatic adjustment increases the rate of ice sheet decay by calving. With the increase in sea level the ice sheet is in contact with the ocean for longer and experiences higher calving rates.

The discussion above has concerned the potential sensitivity of an ice sheet model to the treatment of isostasy. The following section concerns the reverse situation - namely the sensitivity of models of isostasy and of deduced isostatic parameter values to the treatment and history of ice sheets.

2.2 The Reconstruction of Ice Sheets for Isostatic Models

Sophisticated geophysical models of isostasy such as those derived by Peltier (1989) and Lambeck (1987) envisage a viscoelastic mantle rheology and a spherical self-gravitating earth to deduce the viscosity stratification of the inner earth. However, as the forcing for these earth models involves the history of ice sheet deglaciation, the issue of the influence of assumptions about the ice sheet is very important.

Arguably the best known ice sheet deglaciation chronology used in isostatic models is Peltier's 'ICE' series, which has been modified several times over the last few decades (Peltier & Andrews, 1976). As this thesis examines the sensitivity of the calculation of isostatic adjustment to assumptions relating to the representation of the ice sheets using the latest version of this chronology of ice extent (defined as ICE4G) the development of the ICE series is outlined. The first chronology (defined as ICE1) was generated using the isochron map of Bryson et al (1969) for the Laurentide ice sheet and that of Zonneveld (1973) for the Fennoscandian ice sheet. The vertical thickness profile of the ice sheets was assumed to be parabolic, with total volumes derived from Shepard's (1963) eustatic sea level curve. Wu and Peltier (1983) suggested that ICE1 is a sufficiently accurate deglaciation chronology for the deduction of realistic earth model parameters by comparing the model generated prediction of relative sea level to observations. Upon the determination of earth model parameters that

best predicted the relative sea level, Wu and Peltier assumed that the residual error was due to the inaccuracies in the deglaciation chronology. This assumption was based on the argument that near the centre of the former ice sheets the isostatic adjustment can be separated into an adjustment-amplitude (that depends on the ice sheet thickness) and an adjustment-rate (that depends on the mantle viscosity). They claimed that the ice sheet history and isostatic adjustment can be decoupled so that the ice sheet deglaciation chronology can be modified to produce an improvement in the prediction of the relative sea level data. Using ICE1, the modification process first attempts to deduce the best mantle viscosity profile which fits the relative sea level and free air gravity anomaly data. The gravity data was used as an indication of the present day state of isostatic disequilibrium in formerly glaciated regions (Walcott, 1970). When the viscosity profile that most realistically reproduced the observations was found the ice sheet thicknesses and extents were manually adjusted (thus creating the ICE2 chronology) until the sea level and gravity data was reconciled. With ICE2 Wu and Peltier found that although the model prediction of relative sea level data close to the ice sheets matched the observations better than when using ICE1, the relative sea level data far from the ice sheet (in New Zealand and Brazil) showed an anomaly of 2 kyr in response time. This anomaly in the far field data was attributed to the lack of consideration of the eustatic sea level contribution from other ice sheets such as Antarctica. Peltier (1988) found that by adding a delayed Antarctic deglaciation and by using a thick lithosphere in his model, the far field relative sea level data could be reconciled with the ICE2 chronology. However Nakada and Lambeck (1987) used a global spherical harmonic model to show the far field relative sea level calculations were sensitive to the finite element methodology used by Peltier. Nakada and Lambeck were able to reconcile the far field relative sea level data without using a thick lithosphere model.

Tushingham and Peltier (1991) developed the ICE3G deglaciation chronology by constraining the ice sheet history only with the near field relative sea level data and ignoring the free air gravity data. There is considerable justification for this. James (1992) suggested that isostatic disequilibrium is at

most responsible for 30% of the observed free air gravity anomaly over formerly glaciated regions. James proposed that the residual anomaly is caused by effects such as mantle convection. Le Meur (1996) concluded that for an isostatic model of adjustment over Northern Europe it is difficult to reconcile present day free air gravity data with present day radial velocity data.

The procedure used by Tushingham and Peltier to derive ICE3G was to infer earth model parameters and adjust the ice sheet thicknesses so that the agreement with the *near* field relative sea level data was as close as possible. Then both the near and far field relative sea level data was used to test the realism of the deglaciation chronology (Tushingham & Peltier, 1991). Nineteen iterations between earth model parameters and ice sheet thicknesses were used in deriving ICE3G. The corrections were made manually at every iteration to the ice sheet thicknesses and the ice sheet extent. The fit at some near field sites was still not complete. In North America between Nova Scotia and Cape Cod the fit to some sites was within experimental error while at other sites it was not. Tushingham and Peltier suggested that the ice sheet model resolution was too low to fully reproduce the deglaciation process.

To test the accuracy of ICE3G Tushingham and Peltier (1991) compared the model-generated changes in eustatic sea level to those calculated on the basis of $\delta^{18}O$ and coral reef data. In the Huon Peninsula in Papua New Guinea the observed eustatic sea level rise was 130 m since the last glacial maximum (Chappell & Shackleton, 1986), whereas ICE3G suggested 115 m and ICE2 suggested 97 m. The Northern Hemisphere ice sheets represented in ICE3G were thinner than in ICE2 but ICE3G included an Antarctic deglaciation chronology with volume change equivalent to a eustatic sea level contribution of 26 m.

Other authors have used ICE3G as a deglaciation chronology producing ambiguous overall results. James and Lambert (1993) used the ICE3G deglaciation chronology and convolved it with James' (1991) calculation of the horizontal deformation associated with isostatic adjustment to compare predictions of present day horizontal surface velocities with VLBI data. They found a reasonable match to the observations. The result suggests that ICE3G is a realistic model of the chronology of ice sheet deglaciation since the last ice age. However

Fang and Hager (1996) used a continuous radially-dependent viscosity model (as opposed to the stratified viscosity model of Tushingham and Peltier) to compare relative sea level predictions from ICE1 combined with the Antarctic deglaciation chronology of Nakada and Lambeck (1987) with those generated from ICE3G. Fang and Hager concluded that ICE1 has a better overall fit to the relative sea level data than ICE3G, suggesting that the iterative process used to generate ICE3G has to some extent been biased by the stratified viscosity assumption.

Relative sea level data is used to generate ICE3G and its accuracy is therefore dependent on the spatial distribution of the data. Following the publication of additional relative sea level data, Peltier (1994) developed the ICE4G deglaciation chronology using ICE3G as an initial estimate and iteratively modifying the earth model and ice sheet deglaciation chronology three times. In this chronology Peltier also introduced a time-dependent shoreline migration which Johnson (1993) argued is important in the calculation of relative sea level. The calculation of eustatic sea level change using ICE4G shows an excellent correspondence to that observed at New Guinea and Barbados (Peltier, 1994).

The ICE series is the only deglaciation chronology where the ice sheet thicknesses are modified iteratively to reconcile the relative sea level data. Lambeck (1993b) studied the glacial history of the British Isles, assuming several different deglaciation chronologies separately with ice sheet thicknesses computed through the non-linear rheology approximation of Paterson (1971) for an ice sheet with a realistic flow law. Lambeck argued that as this approximation generates a profile which is linearly dependent on the central ice sheet thickness, the ice sheet thicknesses could be linearly rescaled to be thicker or thinner while still retaining a realistic profile. Lambeck invoked the notion of an ice sheet rescaling factor β and considered it as a parameter of the model with a value that can be determined through agreement with the relative sea level data. Instead of using an iterative technique Lambeck conducted a parameter space search of the earth model parameters and β. Using this technique Lambeck argued that there is no circularity of argument in deducing the ice sheet thick-

nesses and earth model parameters. Another advantage of a parameter space search is that an estimate can be made of the sensitivity of the earth model and ice sheet deglaciation chronology to the parameters themselves (Lambeck, 1993c). For example a reduced lithospheric rigidity in the model allows a thinner ice sheet to satisfy the relative sea level data (Lambeck et al., 1996). The trade-off between ice sheet thickness and lithospheric rigidity occurs because a thin lithosphere allows a greater deflection and a thinner ice sheet is required to produce the correct isostatic deflection.

Breuer and Wolf (1995) used several different histories of ice sheet extent (assuming parabolic thickness) to constrain uplift in the Svalbard Archipelago to determine whether there is evidence for lateral heterogeneity in the structure of the earth. They found only a weak sensitivity of mantle viscosity to the assumed ice sheet history. However in a subsequent paper using a higher resolution ice sheet chronology Kaufmann and Wolf (1996) concluded that the estimate of lithospheric rigidity varied strongly with changes to the deglaciation chronology. Sigmundsson's (1991) study of post-glacial adjustment in Iceland concluded that there can be a certain amount of parameter trading between ice sheet thickness and mantle viscosity. This result was due in part to the rapid uplift found in the region producing a best estimate of mantle viscosity 2 orders of magnitude lower than the customary 10^{21} Pa s (Sigmundsson, 1991). Sigmundsson's result indicates that Peltier's assertion that the characteristic behaviour of relative sea level data can be separated into an ice-dependent adjustment amplitude and a viscosity-dependent adjustment rate may not be correct for regions of low mantle viscosity. Han and Wahr (1995) analysed the relative sea level data in the Hudson Bay region of Canada to assess the preference of the data for a particular mantle viscosity profile. They found that changing the thickness and timing of the imposed ice sheet changes the isostatic adjustment rate, in opposition to Peltier's assertion. They concluded that the inference of the earth's viscosity profile depends on the assumed deglaciation chronology.

2.3 Coupled Earth/Ice-Sheet Models

Oerlemans and Van der Veen's (1984) primary thesis on the effect of glacial isostasy on the behaviour of ice sheets is that isostasy accelerates both the advance and retreat of ice sheets over a glacial cycle. This property was proposed as an important non-linear mechanism in the accurate simulation of the growth and decay of ice sheets in response to orbitally induced radiation changes (Pollard, 1978). The Milankovitch theory of ice ages suggests that ice sheet behaviour is dominated by changes in incident radiation associated with the earth's cyclical orbital variations of period 21, 23 and 41 kyr. However the global change in ice volume reflected as a global eustatic sea level change (see Figure 4.1 for Chappell and Shackleton, 1986) is distinctly sawtoothed in form with an overall 90 kyr advance and 10 kyr retreat over a glacial cycle. It has been suggested that glacial isostasy modulates the ice sheet behaviour so that the cyclic orbital radiation changes produce the observed sawtooth pattern of advance and retreat (Pollard, 1982). This possible modulation of the ice sheet behaviour generated early interest in the coupling of ice sheet and isostatic models.

One of the first studies to couple realistic ice sheet dynamics with isostatic adjustment ignores the solar radiation forcing and reduces the ice sheet dynamics and 'thin channel flow' earth model to a zero dimensional formulation (Ghil & Le Treut, 1981). In their study Ghil and Le Treut imposed a latitude dependent snow line so that the ice sheet experiences net ablation below a certain elevation and net accumulation above it. This is shown schematically in Figure 2.1. Ghil and Le Treut concluded that, for certain ratios of the asthenospheric density to diffusivity, self sustained oscillations in ice sheet volume are generated. They found that the mechanism for the oscillation is that, during ice sheet growth, isostatic adjustment reduces the elevation of the sheet until it moves below the snow line and experiences net ablation, thereby reducing the ice thickness. The ice sheet continues to decay until it is small enough for isostatic adjustment to bring the ice sheet above the snow line so that accumulation dominates and the ice sheet starts to grow. The Ghil and Le Treut model did not display ice volume oscillations at the 100 kyr period

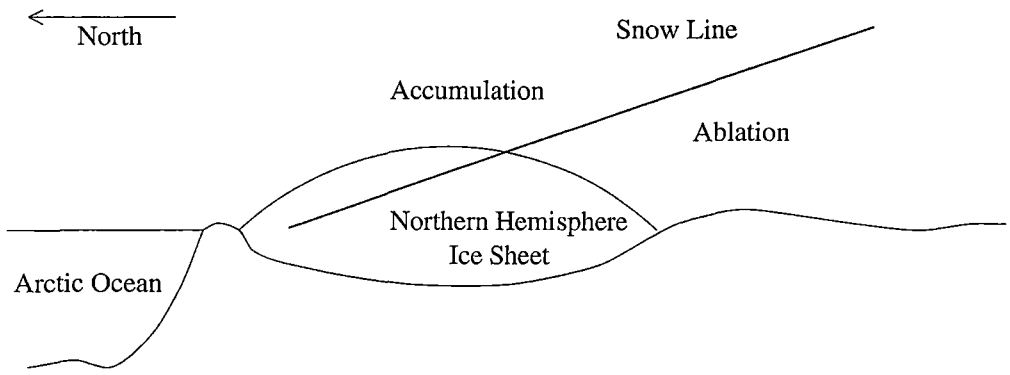

Fig. 2.1: Latitude dependence of snow line elevation and corresponding ice sheet accumulation/ablation.

characteristic of the Pleistocene era. Furthermore the asthenospheric diffusivity and density were considered as separate parameters in the model formulation. In reality the diffusivity is a function of density. The combinations of diffusivity and density for which self-sustained oscillations do occur in the model are not realistic.

Oerlemans (1980) was able to simulate the 100 kyr cycles of ice volume using a forcing of time varying accumulation and a physically-parametrised local bedrock adjustment model with a fixed decay time of 30 kyr. Most authors consider this decay time to be overly long (for example Saltzmann and Verbitsky, 1992), with a figure of 3 kyr considered more appropriate (Peltier, 1980). Smaller values of the decay time were considered in the study but Oerlemans found that only the 30 kyr value generated the 100 kyr cycle. Birchfield et al (1981) used the solar insolation data of Berger (1978) to calculate accumulation changes over the ice sheet. Using the same ice and earth model as Oerlemans but a decay time of 3 kyr, Birchfield et al were able to simulate successfully the 100 kyr cycle of ice volume changes. Pollard (1982) noted that although the coupled models of Oerlemans (1980) and of Birchfield et al (1981) reproduced the 100 kyr cycles, the amplitude of ice volume changes generated by the models were less than those suggested from $\delta^{18}O$ marine core records. Pollard (1982) was able to increase the ice volume changes by using a thin channel flow earth model. Birchfield and Grumbine (1985) used a different model of isostasy comprising an elastic lithosphere overlying a viscoelastic half-space. They reported

a reduced magnitude of growth and decay of the ice sheet, and attributed the reduction to the inclusion of the lithosphere. However the reasons why ice sheet growth and decay is exaggerated using a thin channel flow model compared to a half-space model were outlined previously in this chapter. This exaggeration explains why Pollard reported increased ice sheet volume changes using a thin channel flow model compared to Oerlemans and Birchfield et al (who used a physically-parametrised isostatic adjustment model) and Birchfield and Grumbine (who used a half-space adjustment model). Le Meur and Huybrechts (1996) noted that the prediction of isostatic adjustment is similar between a localised isostatic adjustment model and a viscoelastic half-space adjustment model.

Peltier (1982) noted that the results of the models of Birchfield et al (1981) and Oerlemans (1980) fit the ice volume record even though these models use a simple representation of isostasy. He further noted that only a small range of prescribed decay times generated the observed 100 kyr cycles of ice volume changes. As more realistic models of isostasy predict that the rate of isostatic adjustment should depend on the spatial scale of the ice sheet (Cathles, 1975), Peltier suggested that the use of a constant decay time is inappropriate when the ice sheet advances and retreats through a glacial cycle. Peltier (1982) simplified his spherical viscoelastic earth model and combined it with a one dimensional ice sheet model to represent the earth/ice-sheet system as a single differential equation. The equation suggests that the coupled system could be modelled as a damped simple harmonic oscillator with non-linear forcing. Peltier's findings agreed with those of Oerlemans in that the damping factor in the differential equation that determined the ice sheet response could only produce 100 kyr cycles for unrealistically large values of the isostatic decay time. De Blonde and Peltier (1991) compared the ice volume changes obtained by combining a model of ice sheet dynamics with a number of different isostatic models including a thin channel model and a spherical viscoelastic earth model. They explained the success of the thin channel flow model in reproducing the observed 100 kyr cycles in terms of its decay time dependence on spatial scale. When the ice sheet advances towards its maximum extent De Blonde and Peltier found that

the decay time increases towards the 30 kyr value used by Oerlemans. With the long decay time the isostatic adjustment rate is reduced and the ice sheet can remain longer in a region of net ablation so that a significant amount of ice is lost. In a half-space model the decay time is inversely proportional to the spatial scale of the ice sheet (Cathles, 1975). For this model at maximum extent the isostatic adjustment is fast so that the ice sheet quickly responds to the increased ablation by rising above the snow line, thereby reducing the magnitude of ice volume change. De Blonde and Peltier suggested that the conclusion of Oerlemans and Van der Veen (1984) that isostasy enhances the advance and retreat of ice sheets is only valid when using the thin channel flow approximation.

There are two papers of particular relevance to the present study. Lingle and Clark (1985) coupled a one dimensional model of an ice stream to a three dimensional viscoelastic half-space isostatic model to study the sensitivity of the modelled ice stream 'E' in West Antarctica to several different isostatic schemes. They concluded that the response of the earth to a thinning ice stream serves to delay the retreat of the ice stream grounding line. This is because ice sheet calving caused by an increase in eustatic sea level (associated with deglaciation of the Northern Hemisphere ice sheets) is counteracted by the isostatic uplift of the earth beneath the ice stream. In a model without isostasy the ice stream is flooded allowing a faster rate of ice sheet calving and grounding line retreat. This result of Lingle and Clark (1985) agrees with that of Payne et al (1989) who used a thin channel flow model in association with a model of the West Antarctic Peninsula ice sheet. These combined results suggest that this behaviour is not limited to the thin channel flow model.

The other paper of particular relevance to the present study concerns the results of coupling a model of the Antarctic ice sheet with a sophisticated model of glacial isostasy (Le Meur & Huybrechts, 1996). LeMeur and Huybrechts conducted a study of the sensitivity of the ice sheet model of Huybrechts (1992) to various isostatic schemes. Over a glacial cycle Le Meur and Huybrechts found that the thin channel flow isostatic model generated the most unrealistic changes in ice volume. Out of the set of simple models the physically-parametrised

constant decay time model coupled with an elastic lithosphere most resembled the sophisticated spherical viscoelastic model.

3. THE EARTH MODEL

This section outlines the manner in which the isostatic adjustment of the earth is represented in the present study. A limited-area flat-earth model domain is used so as to be consistent with the ice sheet model.

The neglect of the earth's sphericity can be important. Wolf (1984) suggests that for ice sheets the size of the Laurentide the neglect of the curvature of the earth underestimates the isostatic adjustment at the ice sheet edge by up to 40% compared to spherical models. Also changes in relative sea level can only be computed to first-order as globally consistent gravitational hydro-eustatic loading cannot be calculated. The first-order representation of the relative sea level equation defines change in relative sea level as the sum of glacio-isostatic adjustment, hydro-isostatic adjustment and spatially uniform (not gravitationally consistent) hydro-eustatic change.

Amelung and Wolf (1994) suggest that a flat earth model is preferable to a global spherical model that does not incorporate gravitational self consistency in the relative sea level equation. They also argue that global models which do not consider the gravitational anomaly associated with the change in surface shape of the earth (incremental gravitational force) are less realistic than flat earth models which ignore this feature. Thus the error in assuming a flat earth model tends to be cancelled by the fact that it does not treat changes in the force of gravity associated with changes in the surface shape and loading of the earth.

The structure of the earth envisaged in this model comprises a uniform elastic lithosphere overlying a viscoelastic mantle. The mathematical formulation is described in the following sections.

3.1 The Lithosphere

Barrel (1914) introduced the term 'lithosphere' to represent the strong outer layer of the earth under which the more viscous mantle flowed to maintain isostatic compensation. The differential equation governing the ultimate regional equilibrium deflection of the lithosphere resulting from the application of a surface load is (Brotchie & Silvester, 1969)

$$D_r \nabla^4 \varphi + \rho_m g \varphi = Q \tag{3.1}$$

where φ is the deflection of the lithosphere due to the application of the load, ρ_m is the mantle density, g is the acceleration due to gravity and Q is the applied load. Q can represent either the glacio- or hydro-isostatic loading

$$Q = \begin{cases} \rho_i g h & \text{glacio-isostasy} \\ \rho_{sw} g d & \text{hydro-isostasy} \end{cases} \tag{3.2}$$

where h is the ice thickness, ρ_i is the density of ice, d is the water depth, and ρ_{sw} is the density of sea water. D_r in Equation 3.1 is the 'flexural rigidity' of the lithosphere, related to the 'effective elastic thickness' of the lithosphere by the equation

$$D_r = \frac{E H_l^3}{12(1-\sigma^2)} \tag{3.3}$$

In this equation E is Young's modulus, H_l is the 'effective elastic thickness' of the lithosphere and σ is Poisson's ratio. There are several different definitions of the thickness of the lithosphere. The 'effective elastic thickness' of the lithosphere is defined by Anderson (1995) as the thickness of an elastic uniform plate that has the same elasticity of the lithosphere and duplicates the flexural shape of the lithosphere upon application of a geological load.

The first term on the left hand side of Equation 3.1 represents the force due to the flexure of the elastic lithospheric plate in partial support of the load. If the thickness of the lithosphere is zero Equation 3.1 reduces to the Archimedean equation for a mass floating on a fluid. Thus the second term in Equation 3.1 represents the buoyancy of the mantle that partially supports the load. The manner in which Equation 3.1 is solved in this study is through

Fourier decomposition. The two-dimensional Fourier Transform is defined as

$$\tilde{f}(k_x, k_y) = \int_{-\infty}^{\infty} \int_{-\infty}^{\infty} f(x, y) e^{-2\pi i(k_x x + k_y y)} dx dy \tag{3.4}$$

where k_x is the wavenumber in the x direction, k_y is the wavenumber in the y direction, $f(x, y)$ is the original field in the spatial domain and $\tilde{f}(k_x, k_y)$ is the Fourier transformed field. In the Fourier Domain the ratio of ice thickness to induced deflection for an ice sheet load is

$$\frac{\tilde{\varphi}}{\tilde{h}} = \frac{\rho_i g}{D_r k^4 + \rho_m g} \tag{3.5}$$

where $k^2 = {k_x}^2 + {k_y}^2$. The use of the Fourier technique to obtain an equilibrium deflection is demonstrated for the Antarctic ice sheet in Figures 3.1 and 3.2. The ice sheet thickness in Figure 3.1 is converted to the equilibrium isostatic deflection shown in Figure 3.2. The elasticity of the lithosphere acts to spread

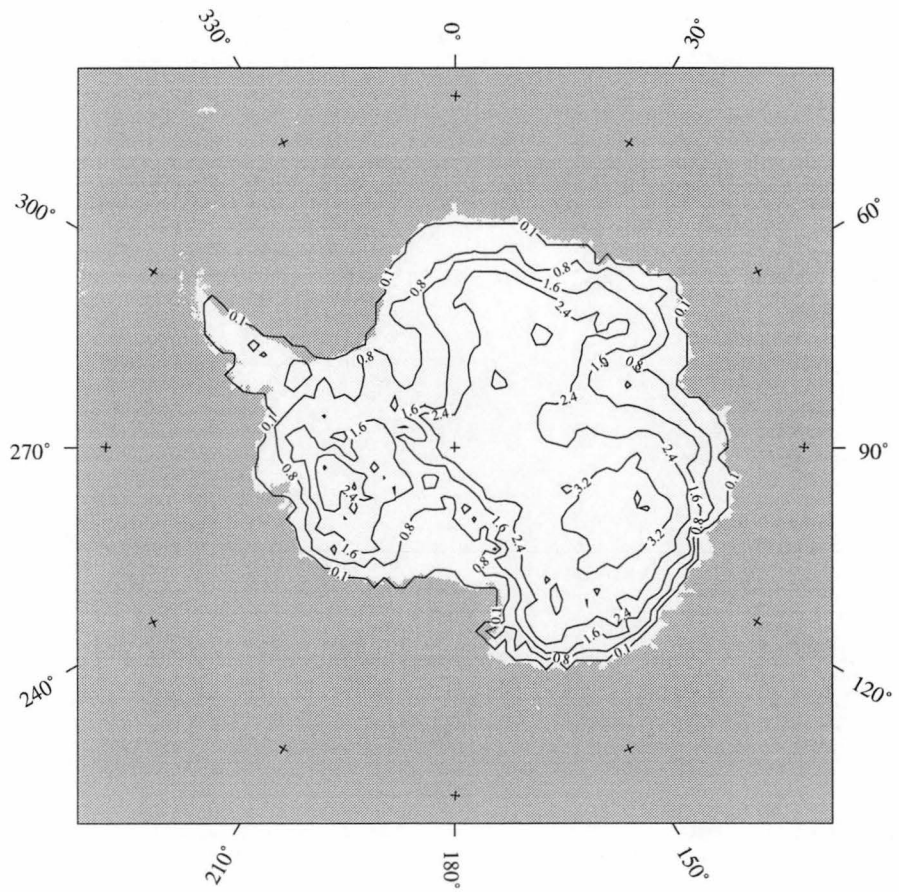

Fig. 3.1: Antarctic ice sheet thickness (km) at the present day.

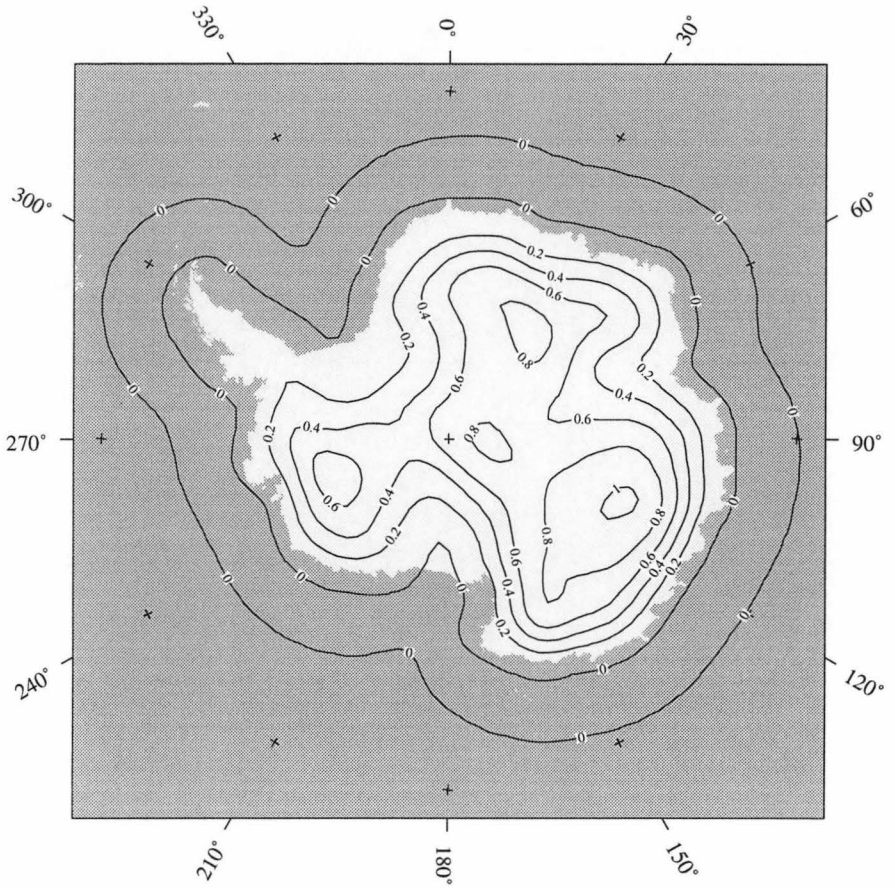

Fig. 3.2: Equilibrium Antarctic lithospheric deflection (km) corresponding to the ice load of the present day.

the weight of the load over the surrounding region. Equation 3.5 demonstrates the dependence of the lithospheric deflection on the spatial scale of the load. In simple terms, for small ice sheets ($k \to \infty$) there is no deflection and for large ice sheets ($k \to 0$) the deflection is at maximum. This is the classic 'low pass filter' behaviour of the lithosphere associated with Equation 3.1 (Cathles, 1975).

Anderson's definition of the effective elastic thickness of the lithosphere requires a definition of the horizontal surface profile of the earth in the absence of a geological load. This is because the flexural shape of the lithosphere can only be defined as the difference in topography with and without the application of the load. Assuming present day isostatic equilibrium (that is to say the deflection is complete) the 'reference bed' defined as the profile of the surface

of the earth in the absence of loading is given by

$$b_{pd} = b_0 + \varphi_{pd} \tag{3.6}$$

where b_{pd} is the bedrock elevation at the present day, b_0 is the 'reference bed' and φ_{pd} is the isostatic deflection caused by the present day ice sheet. The general approach in ice sheet modelling is to assume present day isostatic equilibrium under the ice sheet and use Equation 3.6 to generate a reference bed. As the loading configuration of the ice sheet changes it is no longer in isostatic equilibrium because there is a change in the equilibrium profile. The actual surface profile of the earth moves toward the new equilibrium. The magnitude of disequilibrium at any time is measured by the difference between the surface at that time and the new equilibrium elevation. The assumption of present day isostatic equilibrium used in this study is questionable but is used in the absence of a more feasible and practical alternative. The effect of the assumption of present day isostatic equilibrium is considered in Chapter 4.

The rate of change with time of the surface profile is governed by the response of the earth's mantle. The mathematical formulation of the mantle response is discussed in the next section.

3.2 The Mantle

The response time of ice sheets is faster than the response time of isostatic adjustment. Huybrechts (1992) notes that ice sheets can adjust to environmental changes with a response time of hundreds of years. Cathles (1975) notes that the characteristic response time for glacial isostatic adjustment is thousands of years. Thus when the ice sheet changes the subsequent isostatic adjustment of the earth moves more slowly towards the equilibrium value. For a changing ice sheet the isostatic disequilibrium at any time is given by the following equation

$$disequilibrium = (b - (b_0 + \varphi)) \tag{3.7}$$

where b is the value of the bedrock elevation at the given time, φ is the ultimate equilibrium isostatic deflection associated with the ice sheet loading at the given time and b_0 is the elevation of the reference bed. The usual approach

to representing the mantle in ice sheet modelling is to assume that the earth responds to disequilibrium through viscous thin channel flow (see the literature review). The uplift rate associated with a viscous thin channel is given by Van Bremmelen and Berlage (1935) as

$$\frac{db}{dt} = D_a \nabla^2 (b - (b_0 + \varphi)) \tag{3.8}$$

where D_a is the 'asthenospheric diffusivity', related to channel viscosity and depth by

$$D_a = \frac{\rho_m g H^3}{3\eta} \tag{3.9}$$

where H is the channel depth and η is the channel viscosity.

As it is the adjustment rate that is proportional to the disequilibrium, a phase lag occurs between disequilibrium and subsequent isostatic adjustment. The preferred manner of quantifying this phase lag is by defining a decay time of adjustment (see again the literature review) which is defined as the time taken for the earth to adjust $\frac{1}{e}$ of its former equilibrium depression following the instantaneous removal of a load. Huybrechts (1990a) and Payne et al (1989) relate the asthenospheric diffusivity to the decay time by

$$\tau = \frac{L^2}{D_a} \tag{3.10}$$

where τ is the decay time, L is the 'characteristic length scale' of the applied ice load and D_a is the asthenospheric diffusivity. The so called 'characteristic length scale' of the ice sheet is most often quoted as the ice sheet diameter (Huybrechts, 1990a; Letreguilly et al., 1991).

There is an inherent scale dependency in Equation 3.8 due to the divergence operator. The thin channel flow model predicts that the earth responds to an applied load by shifting mantle material laterally from underneath the ice sheet to beyond its edge. For viscous flow the rate at which the earth adjusts therefore depends on the distance between the interior of the ice sheet and its edge. To model the process accurately it is therefore important to be aware of the dimension of the ice sheet and adjust the asthenospheric diffusivity so that a realistic adjustment decay time is reproduced. If the assumed value of asthenospheric diffusivity is too small for the ice sheet the decay time is increased and

the isostatic adjustment is too slow. If the asthenospheric diffusivity is too high for the ice sheet size the isostatic adjustment is too fast. Table 3.1 shows the values of asthenospheric diffusivity used by various authors in ice sheet models. Despite the wide variety in the scale of ice sheets considered (column 2) similar values for the asthenospheric diffusivity are used in all the models. As the spatial scale of the Fennoscandian ice sheet is much less than the Antarctic ice sheet the peripheral bulge of a few hundred metres reported by Letreguilly and Ritz (see the literature review) is almost certainly a result of using a diffusivity which is too low.

D_a (m^2 yr^{-1})	Ice Sheet	Author
1.0×10^8	Global	Marsiat (1994)
0.5×10^8	Antarctica	Huybrechts (1992)
0.5×10^8	Greenland	Letreguilly et al (1991)
0.4×10^8	Fennoscandia	Letreguilly and Ritz (1993)
0.35×10^8	Antarctica	Payne et al (1989)
0.35×10^8	Svalbard Archipelago	Siegert and Dowdeswell (1995)
0.35×10^8	Laurentide	Arnold and Sharp (1992)

Tab. 3.1: Values of asthenospheric diffusivity used in various ice sheet models.

For the Antarctic ice sheet Huybrechts (1992) suggests a characteristic length scale of 1000 km and an asthenospheric diffusivity of 0.5×10^8 m^2 yr^{-1} with a resulting decay time of 20 kyr. Cathles (1975) suggests that the decay time of isostatic adjustment is closer to 3 kyr. Cathles' analysis uses a Fourier decomposition so that the decay time for a load of wavenumber k is given by

$$\tau(k) = \frac{1}{D_a k^2} \tag{3.11}$$

This decay time dependence assumes in its derivation that the characteristic length scale of the ice sheet is much larger than the channel depth. Cathles uses matrix propagator techniques to show that the decay time τ for flow in a

channel of arbitrary depth H is given by

$$\tau(k) = \frac{2\eta k}{\rho_m g} \frac{(C)^2 + (kH)^2}{CS - kH} \tag{3.12}$$

where C=cosh(kH) and S=sinh(kH). If the ice sheet diameter is greater than the channel depth ($kH \ll 1$) Equation 3.12 can be reduced by first-order Taylor expansion to

$$\tau(k) = \frac{2\eta k}{\rho_m g} \frac{3}{2(kH)^3} = \frac{3\eta}{\rho_m g H^3} \frac{1}{k^2} = \frac{1}{D_a k^2} \tag{3.13}$$

which is the decay time for thin channel flow already quoted in Equation 3.11.

If the ice sheet diameter is small compared with the channel depth ($kH \gg 1$) the transcendental terms dominate and Equation 3.12 becomes

$$\tau(k) = \frac{2\eta k}{\rho_m g} \tag{3.14}$$

This is the decay time associated with half-space flow derived initially by Haskell (1935). The isostatic submergence peripheral to retreating ice sheets predicted by the thin channel model and cited as a reason for its validity by Officer et al (1988) can also be produced by a half-space earth model with viscosity stratification with depth. Davis and Mitrovica (1996) report that the position of the submergence peripheral to the ice sheet is a sensitive indicator of lower mantle viscosity. For an earth model where the viscosity is stratified between the upper and lower mantle, Cathles (1975) reports a decay time of

$$\tau(k) = \frac{2\eta_{lm} k}{\rho_m g} \frac{C^2 + (kD)^2 (1-\nu) + 2\, CS\, \nu + S^2 \nu}{C^2 + S^2 + kD \left(\nu - \frac{1}{\nu}\right) + SC \left(\nu + \frac{1}{\nu}\right)} \tag{3.15}$$

where $\nu = \eta_{um}/\eta_{lm}$ is the ratio of the upper mantle viscosity to the lower mantle viscosity, η_{lm} the lower mantle viscosity and D the depth of the upper mantle.

By using the decay times given in Equations 3.11, 3.14 and 3.15 an isostatic model representing thin channel, half-space and stratified half-space flow can be generated. The isostatic model used in this thesis is simple compared to the more detailed geophysical models of Lambeck (1993b) and Peltier (1996b) which include effects such as the earth's sphericity and treatment of the core/mantle boundary. However the model formulation in the present work is sophisticated enough to reproduce the qualitative features of glacial isostasy (Peltier, 1980).

The next section confirms that the numerical implementation of these concepts in the present thesis is valid by comparing predictions in simple, radially-symmetric situations where solutions by alternate means can be generated.

3.3 Model Validation

3.3.1 Time-Independent Forcing

The numerical procedure to handle isostasy in this thesis relies on discrete techniques such as truncated Fourier integrals and finite difference solutions to differential equations. Given that the solutions are not exact it is important to test the earth model in situations where solutions by alternate means can be generated for comparison. Here the earth model is applied to a situation where a radially-symmetric parabolic profile ice sheet is imposed so that Hankel-transformed solutions can be found which are very close to purely analytic.

The zeroth order Hankel Transform of a function $f(r)$ is defined by

$$\tilde{f}(k) = \int_0^\infty f(r) r J_0(rk) dr \tag{3.16}$$

where $\tilde{f}(k)$ is the transformed function and J_0 is the zeroth order Bessel function. The Hankel transform of a parabolic profile ice sheet with normalised central height is given by Sneddon (1951) as

$$\tilde{h}(k) = \frac{2}{k^2}\left(\frac{2J_1(kR)}{kR} - J_0(kR)\right) \tag{3.17}$$

where J_1 is the Bessel function of the first-order and R is the radius of the ice sheet. Breuer and Wolf (1995) note that although the form of this parabolic profile ice sheet is not that produced using the plastic rheology assumption, it can be used as a reasonable first-order approximation to a realistic ice sheet profile. The equilibrium deflection of the lithosphere that arises from the application of an ice sheet of parabolic profile can be determined by using $\tilde{h}(k)$ of Equation 3.17 in Equation 3.5 and inverting to the spatial domain. On a surface with no topography and flat reference bed the equilibrium deflection is given by:

$$\varphi(r) = b(r) = \int_0^\infty \frac{2\rho_i g R \left(\frac{2J_1(kR)}{kR} - J_0(kR)\right) J_0(kr)}{k(D_r k^4 + \rho_m g)} dk \tag{3.18}$$

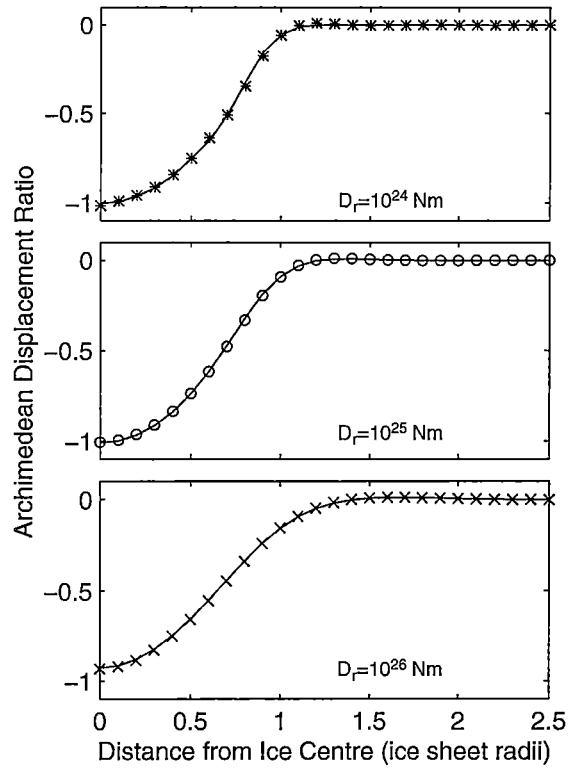

Fig. 3.3: Steady state deformation of a parabolic profile ice sheet for various lithospheric rigidities. Solid lines represent the Fourier solution and symbols represent the Hankel solution. Archimedean displacement ratio is the deflection profile divided by the ratios of density of ice and the earth's mantle.

There is no purely analytic solution to Equation 3.18 and a numerical integration is required. The algorithm developed by Anderson (1979) was modified to perform the integration. The deflections calculated by this integration are shown by the symbols in Figure 3.3 for various values of the lithospheric rigidity D_r. An ice sheet radius of 1000 km is used in the calculation. The deflections are linearly rescaled by $\frac{\rho_m}{\rho_i}$ (Archimedean displacement) so that values close to one are obtained near the centre of the ice sheet. Figure 3.3 also shows cross sections of the deflection calculated using the the two-dimensional Fourier technique of the present model (see Equations 3.4 and 3.5) as the solid lines near the symbols. The two techniques give values of deflection that agree closely. With a reduced value of the lithospheric rigidity the ability of the discrete Fourier inversion to capture the higher frequency components is diminished. Nevertheless the fit between the earth model and the Hankel transform solution for

$D_r = 10^{24}$ N m is still very good.

3.3.2 Time-Dependent Forcing

The time-independent model validation in the previous section concludes that the correct equilibrium deflection is generated by the two-dimensional Fourier method of the present thesis. However the two-dimensional Fourier method is also involved in calculating the time-dependent adjustment and a validation of the response of the mantle to changes in surface loading is also required. As with the previous section a comparison is made between the Fourier technique used in the present thesis and a radially symmetric solution based on Hankel transforms.

The validation performed here is for an instantaneous removal of the ice sheet load so that the bedrock adjustment at time t can be determined by Hankel transforming Equations 3.8 and 3.14 for both the thin channel flow and half-space flow models. Dealing specifically with the thin channel flow model, if the load is removed instantaneously after equilibrium deflection has been achieved, Equation 3.8 becomes

$$\frac{db}{dt} = D_a \nabla^2 b \tag{3.19}$$

noticing that the initial condition (using Equation 3.18) is

$$b(r,0) == \int_0^\infty \frac{2\rho_i g R \left(\frac{2J_1(kR)}{kR} - J_0(kR)\right) J_0(kr)}{k(D_r k^4 + \rho_m g)} dk \tag{3.20}$$

By Hankel Transforming Equation 3.19 one can obtain the already quoted Equation 3.11 as follows:

$$\frac{d\tilde{b}}{dt} = D_a \nabla^2 \tilde{b} = -D_a k^2 \tilde{b} \tag{3.21}$$

Integration of this equation yields

$$\int \frac{d\tilde{b}}{\tilde{b}} = \int -D_a k^2 dt \tag{3.22}$$

and therefore

$$\tilde{b}(k,t) = \tilde{b}(k,0) e^{-D_a k^2 t} = \tilde{b}(k,0) e^{\frac{-t}{\tau}} \tag{3.23}$$

where

$$\tau = \frac{1}{D_a k^2} \tag{3.24}$$

In the wavenumber domain the deflection is governed by a simple exponential decay determined by Equation 3.11

$$b(r,t) = \int_0^\infty \frac{2\rho_i g R \left(\frac{2J_1(kR)}{kR} - J_0(kR)\right) e^{-D_a k^2 t} J_0(kr)}{k(D_r k^4 + \rho_m g)} dk \tag{3.25}$$

The comparison between the Fourier and Hankel technique for thin channel flow is illustrated in Figure 3.4, where earth surface profiles are shown at three times (1,5 and 10 kyr) after the instantaneous unloading. The Hankel solutions are shown as stars (1 kyr), circles (5 kyr), and crosses (10 kyr). The corresponding solutions using the Fourier technique are illustrated by the solid lines. The match between the Fourier and Hankel solutions is very good.

For an earth model representing half-space flow the decay time of Equation 3.14 is substituted in Equation 3.25 to obtain:

$$b(r,t) = \int_0^\infty \frac{2\rho_i g R \left(\frac{2J_1(kR)}{kR} - J_0(kR)\right) e^{\frac{-\rho_m g t}{2\eta k}} J_0(kr)}{k(D_r k^4 + \rho_m g)} dk \tag{3.26}$$

Figure 3.5 shows profiles for the same instantaneous unloading and same geometry but for the case of half-space flow (see Equation 3.14). Again the match between the Hankel and Fourier calculations is very good. Comparison of Figures 3.4 and 3.5 show that the peripheral submergence predicted by the thin channel model (at about 1.5 ice radii from the centre) does not occur in the half-space model. There is no viscosity stratification in the half-space model and it predicts an inward migration of the peripheral bulge.

3.3.3 *Viscoelasticity*

In the previous discussion the mantle is assumed to have a viscous rheology. However authors such as Peltier (1974) and Lambeck (1993b) contend that Maxwellian viscoelasticity is a more appropriate rheology for the inner earth. The general technique of modelling a viscoelastic rheology is to solve the elastic equations of deformation in the Laplace transform domain and then invert the

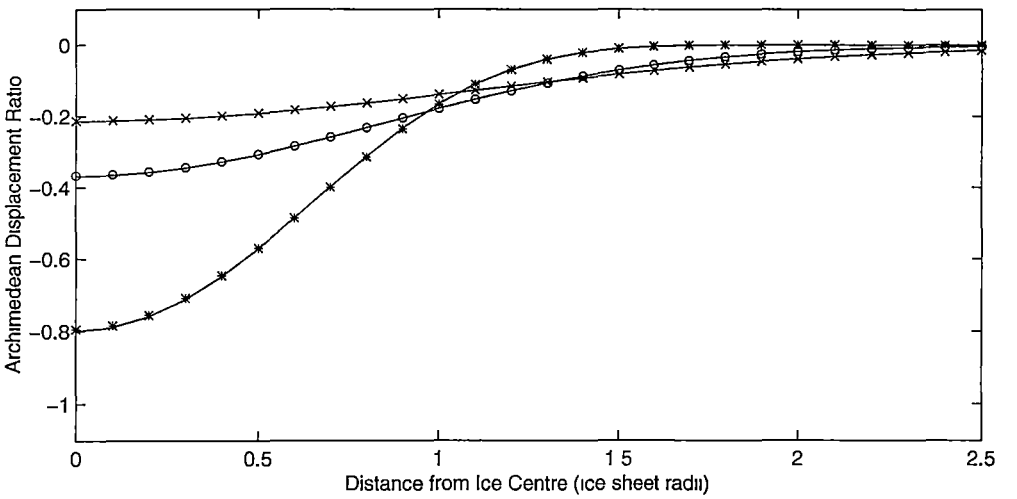

Fig. 3.4: Surface profile of earth for instantaneous unloading and thin channel flow at 1, 5 and 10 kyr after unloading. Solid lines represent the Fourier solutions and symbols represent the Hankel solutions. Archimedean displacement ratio is the deflection profile divided by the ratios of density of ice and the earth's mantle.

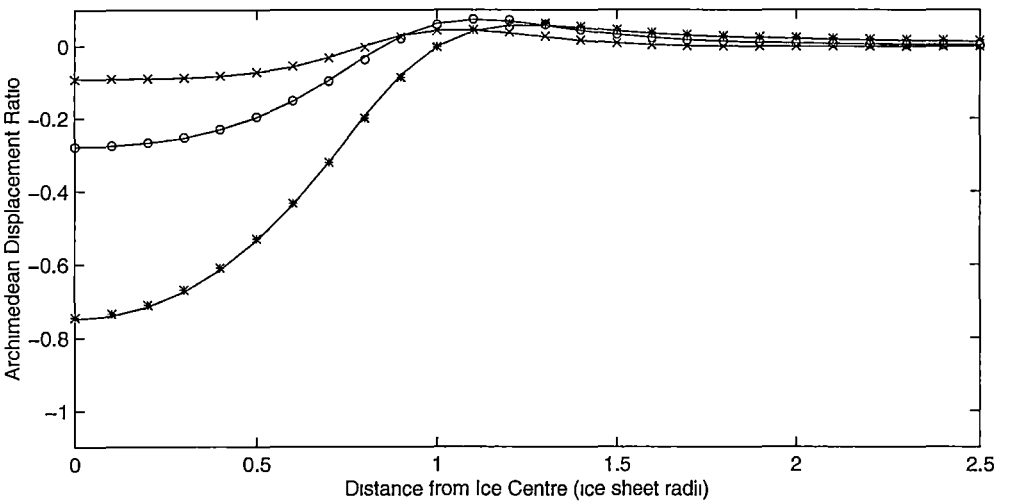

Fig. 3.5: Surface profile of earth for instantaneous unloading and half-space flow at 1,5 and 10 kyr after unloading. Solid lines represent the Fourier solution and symbols represent the Hankel solution. Archimedean displacement ratio is the deflection profile divided by the ratios of density of ice and the earth's mantle.

solutions for different values of the transform parameter to derive the corresponding viscoelastic equations (Mitrovica & Peltier, 1992). Due to computational considerations a simpler process of solution for the viscoelastic case is used in the present thesis. The viscous and elastic equations of motion are solved separately at each model time step using the technique of Cathles (decoupled viscoelasticity). In particular at each model time step the disequilibrium is calculated (Equation 3.6) and an elastic response computed. The elasticity of the earth is considered uniform with depth so that the elastic response to the disequilibrium is given by:

$$\Delta\tilde{b} = \frac{\rho_m g(\tilde{b} - (\tilde{b_0} + \tilde{\varphi}))}{2\mu k} \tag{3.27}$$

where μ is the shear modulus of elasticity, defined by:

$$\mu = \frac{E}{2(1+\sigma)} \tag{3.28}$$

The elastic response is subtracted from the disequilibrium at each time step and the change due to viscous flow is calculated. In essence, the surface disequilibrium is adjusted by an instantaneous elastic relaxation followed by a viscous response.

McKenzie (1967) points out that ignoring the earth's elasticity leads to an underestimate of its viscosity. Cathles (1975) estimates that the difference between calculating the viscoelastic response using his technique and using a Maxwellian viscoelastic rheology is of the order of 3%. The rest of the present section concerns a recalculation of this comparison. The comparison between these two forms of elasticity is achieved by generating solutions of Maxwellian viscoelasticity using the Hankel transform technique and comparing them to those derived using the Fourier technique for decoupled viscoelasticity (from Equation 3.27).

Wu (1993) states that for a Maxwellian viscoelastic half-space without a lithosphere the instantaneous *application* of a disk load is adjusted according to:

$$b(r,t) = \int_0^\infty \frac{\rho_i g R \left(1 + \frac{2\mu k}{\rho_m g}(1 - e^{\frac{-\rho_m g \mu t}{\eta(\rho_m g + 2\mu k)}})\right) J_0(kr) J_1(kR)}{\rho_m g + 2\mu k} dk \tag{3.29}$$

The Hankel transform of a disk ice load (Heaviside step function) is given by (Bracewell, 1965)

$$\tilde{h}(k) = R\frac{J_1(kR)}{k} \tag{3.30}$$

For such a case Wu's equation can be easily modified to accommodate both the presence of a lithosphere and the parabolic profile ice sheet of Equation 3.17. That is:

$$b(r,t) = \int_0^\infty \frac{\rho_i g R\left(1 + \frac{2\mu k}{\rho_m g}(1 - e^{-\frac{\rho_m g \mu t}{\eta(\rho_m g + 2\mu k)}})\right)\left(\frac{2J_1(kR)}{kR} - J_0(kR)\right)J_0(kR)}{(\rho_m g + 2\mu k)(k(D_r k^4 + \rho_m g))}dk \tag{3.31}$$

Equation 3.31 can be used to assess the difference between Maxwellian viscoelasticity (using Hankel transforms) and decoupled viscoelasticity (using the two-dimensional Fourier technique used in the present study and Equation 3.27). Because an instantaneous ice sheet loading has the greatest initial disequilibrium of any ice sheet history, this difference between Maxwellian and decoupled viscoelasticity indicates the maximum error between the two viscoelastic models. Figure 3.6 shows the differences for 3 separate times after instantaneous loading. The symbols appear to be reversed from those of Figures 3.4 and 3.5 because an instantaneous loading (not unloading) is being considered. The Pearson r correlation coefficient between the Maxwellian (symbols) and decoupled (solid lines) viscoelastic solutions is 0.972 at 1 kyr, 0.976 at 5 kyr and 0.982 at 10 kyr. As the disequilibrium reduces with time the decoupled (two-dimensional Fourier) viscoelastic model prediction converges with the Maxwellian (Hankel transform) viscoelastic model prediction. The decoupled viscoelastic model initially underestimates the Maxwellian viscoelastic model (1 kyr) but after this time it overestimates the Maxwellian model. The differences between the two methods are always less than 3%.

The case of loading instantaneous unloading is also considered. The Maxwellian response to the instantaneous removal of a parabolic ice sheet is given by (Cathles, 1975):

$$b(r,t) = \int_0^\infty \frac{2\rho_i g R\left(\frac{2J_1(kR)}{kR} - J_0(kR)\right)e^{\frac{-\rho_m g t}{2\eta k}}(1 - \frac{\rho_m g}{2k\mu})J_0(kr)}{k(D_r k^4 + \rho_m g)}dk \tag{3.32}$$

Comparison with the decoupled viscoelastic (Fourier) prediction is made in

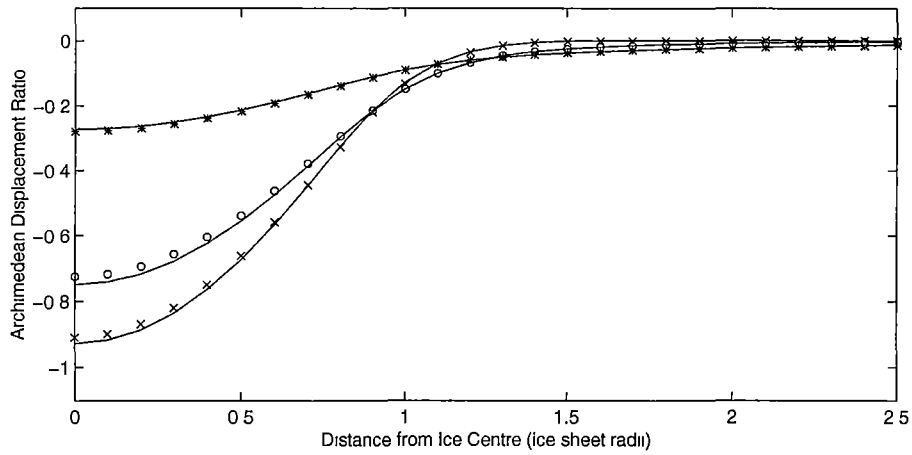

Fig. 3.6: Surface profile of earth for instantaneous loading and half-space flow at 1,5 and 10 kyr after loading. Solid lines represent the decoupled viscoelastic (Fourier) solution and symbols represent the Maxwellian viscoelastic (Hankel) solution. Archimedean displacement ratio is the deflection profile divided by the ratios of density of ice and the earth's mantle.

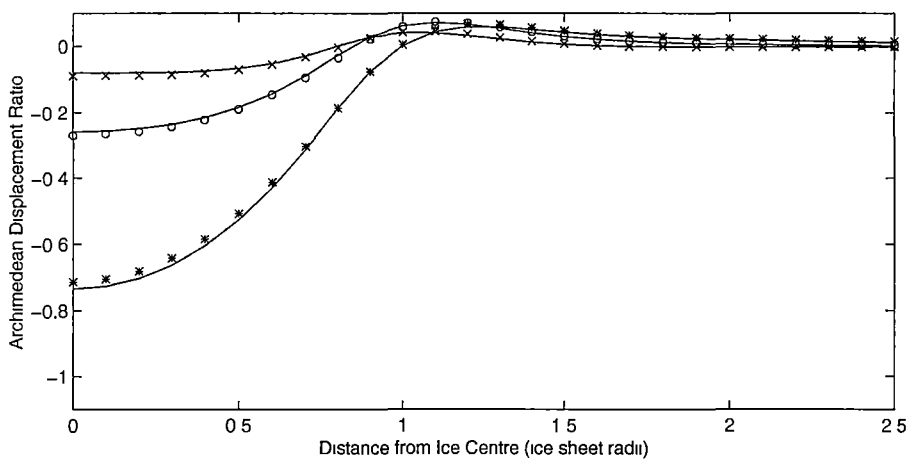

Fig. 3.7: Surface profile of earth for instantaneous unloading and half-space flow at 1,5 and 10 kyr after unloading. Solid lines represent the decoupled viscoelastic (Fourier) solution and symbols represent the Maxwellian viscoelastic (Hankel) solution. Archimedean displacement ratio is the deflection profile divided by the ratios of density of ice and the earth's mantle.

Figure 3.7. The correlation coefficients for the different deflection predictions shown in Figure 3.7 are 0.974 at 1 kyr, 0.980 at 5 kyr and 0.984 at 10 kyr. As in Figure 3.6 the decoupled viscoelastic solution underestimates the Maxwellian adjustment at 1 kyr and overestimates the adjustment at 5 and 10 kyr. There is also an improvement between the model prediction as the disequilibrium is reduced. This suggests that for a realistic loading history a decoupled viscoelastic rheology agrees with a Maxwellian viscoelastic rheology to within 3%.

4. THE ANTARCTIC ICE SHEET

The purpose of this chapter is to examine the sensitivity of an Antarctic ice sheet model to different schemes representing isostatic adjustment. Le Meur and Huybrechts (1996) studied this sensitivity and concluded that differences in ice sheet behaviour are observed when using different earth models. However for each earth model they also found that realistic changes in the earth model parameters themselves effect the ice sheet behaviour. This chapter is concerned primarily with the effect on an Antarctic ice sheet model of changes in earth model parameters over a larger range than examined by Le Meur and Huybrechts.

The sparseness of relative sea level data around Antarctica and the generally poor understanding of its behaviour at the end of the last ice age make it difficult to infer the most realistic isostatic model parameters. In this section no attempt is made to determine the most realistic isostatic model parameters. The prime objective is simply to determine the sensitivity of the ice sheet model to those parameters.

4.1 The Antarctic Ice Sheet Model

Over the last 160 kyr the Antarctic ice sheet is considered to have been most effected by changes in eustatic sea level and by surface accumulation (Budd & Smith, 1982). An explanation of the ice sheet model, originally formulated by Jenssen (1977) and used in the present study, is necessary so that the process by which the isostatic model modifies the ice sheet behaviour can be understood.

The model computes ice thickness changes with time from the continuity equation:

$$\frac{\partial h}{\partial t} + \nabla . F = A^t \tag{4.1}$$

where h is the ice thickness, F is the ice mass flux and A^t is the surface ac-

cumulation. This equation involves local ice accumulation/ablation and the divergence of ice flow. The ice velocities due to sliding and deformation are determined from the ice thickness, the basal shear stress and the bedrock depth, coupled with the ice flow parameters derived from the observed velocities of real ice sheets. That is, deformational velocity is given by:

$$V_{def} = k_{def} h^{n+1} (\rho_i g \alpha)^n \tag{4.2}$$

where V_{def} is the deformational velocity, n and k_{def} are the flow law parameters of the ice sheet, ρ_i is the density of ice, g is the acceleration due to gravity and α is the surface slope of the ice sheet elevation. The sliding velocity is given by:

$$V_{sld} = k_{sld} \frac{\rho_i g \alpha h}{\zeta + (z^*(1 + \kappa z^*))^2} \tag{4.3}$$

where V_{sld} is the sliding velocity; k_{sld}, ζ and κ are constants derived empirically from observations and z^* is the thickness of the ice which is above sea level.

The initial required input data are the present day spatial distribution of bedrock topography, initial ice sheet thickness, surface snow accumulation and yearly averaged temperature at sea level. The time-dependent input data required to drive the model are input eustatic sea level and snow accumulation change. The eustatic sea level change determines the amount of calving that occurs at the edge of the ice sheet. The snow accumulation change determines the input of ice over the surface of the ice sheet. The time-dependent eustatic sea level change used in this study is from Chappell and Shackleton (1986) and is illustrated in Figure 4.1. The changes in surface accumulation are derived from the temperature change record of the Vostok ice core after the style of Budd and Jenssen (1989). The Vostok ice core data is from Jouzel et al (1987) and the calculated equivalent accumulation change is shown in Figure 4.2. The fractional accumulation change from its present day value derived from the Vostok site is assumed to be representative of accumulation changes over the entire ice sheet. This means that time-dependent accumulation changes in the interior of East Antarctica are low in magnitude compared to the changes in coastal regions and in West Antarctica. (Observations show that the present day accumulation is low in the interior of East Antarctica compared to coastal regions and West Antarctica). The accumulation rate also varies with changes

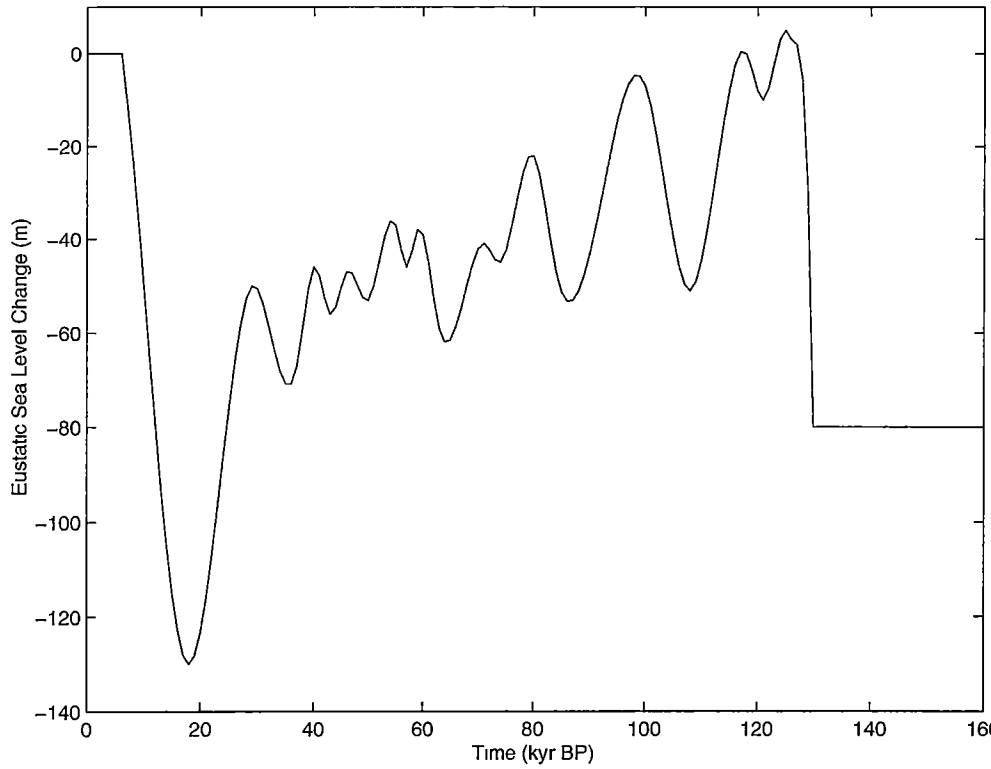

Fig. 4.1: Variation in sea level (Chappell and Shackleton, 1986).

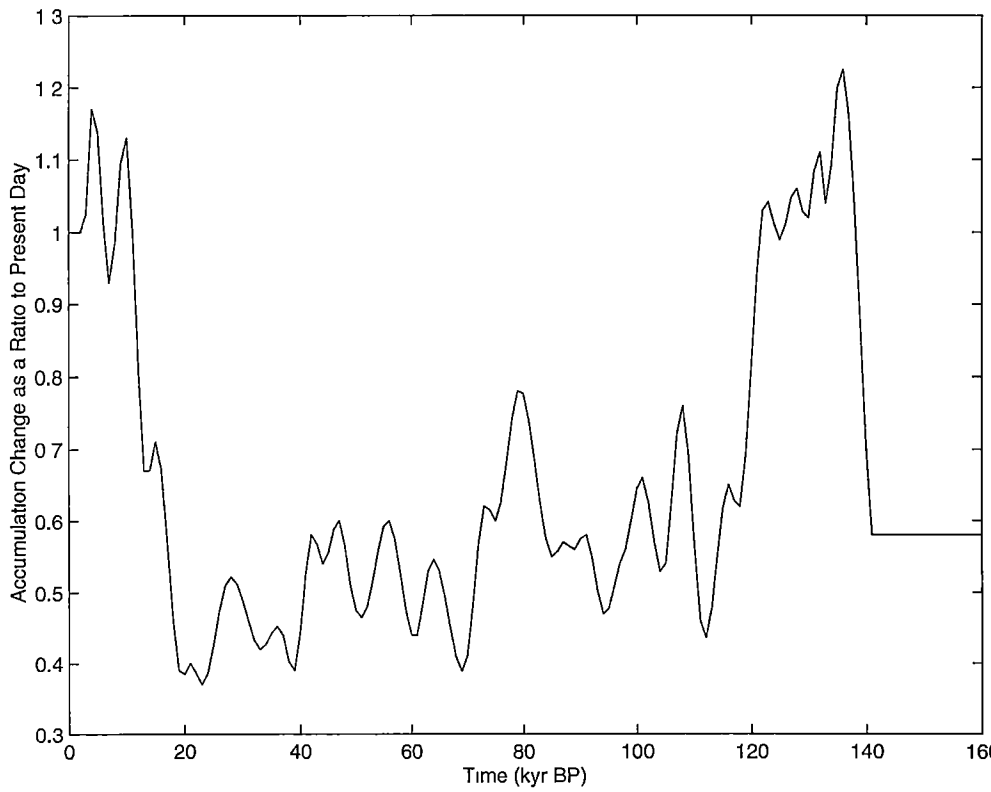

Fig. 4.2: Variation in surface accumulation (Jouzel et al, 1987).

in the local ice sheet elevation. In particular, each 1 km increase in the ice sheet elevation halves the input accumulation over the region:

$$A^t = A_p 2^{ln(2)(E_p - E^t)} \tag{4.4}$$

where A^t and E^t are respectively the accumulation and surface elevation at any time and A_p and E_p are respectively the present day values of accumulation and surface elevation. This accumulation dependence on elevation is a strong control on the ice sheet elevation and isostatic adjustment. Ablation is not considered in the model as present day Antarctica does not experience a significant amount of ablation. As the last 160 kyr were characterised by generally colder temperatures than today, the neglect of ablation is not considered significant.

4.2 The Equilibrium Situation

To separate the dynamic behaviour of the ice sheet from the isostatic behaviour of the earth an equilibrium ice sheet is used as the initial condition as in Huybrechts (1990a). The equilibrium ice sheet configuration is generated by running the ice sheet model to steady state using the initial values of the accumulation and eustatic sea level change. Thus the ice sheet is in dynamical equilibrium at the start of the time-dependent glacial cycle simulation.

The elevation and bedrock topography defined as the equilibrium state of the Antarctic ice sheet are shown in Figures 4.3 and 4.4. To generate this equilibrium state an implementation of isostasy is required. The earth model used to generate the equilibrium ice sheet uses an elastic lithosphere with rigidity of 10^{25} N m and a viscoelastic uniform mantle of 10^{21} Pa s viscosity. In all of the following model runs, the time-dependent forcing of the ice sheet is held constant for the first 20 kyr (see Figures 4.1 and 4.2 at the period 160 to 140 kyr BP). For that initial 20 kyr period therefore, the differences in behaviour of the ice sheets are attributable to the different isostatic models. In all cases the time-dependent forcing of the ice sheet is only applied after the first 20 kyr.

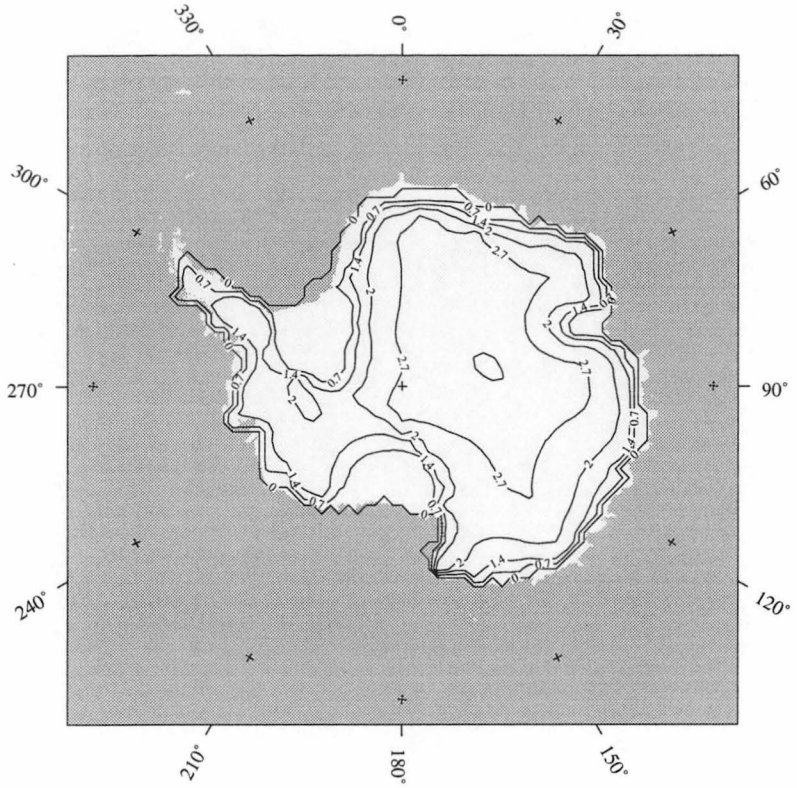

Fig. 4.3: Ice sheet elevation (km) of Antarctica defined as the equilibrium state.

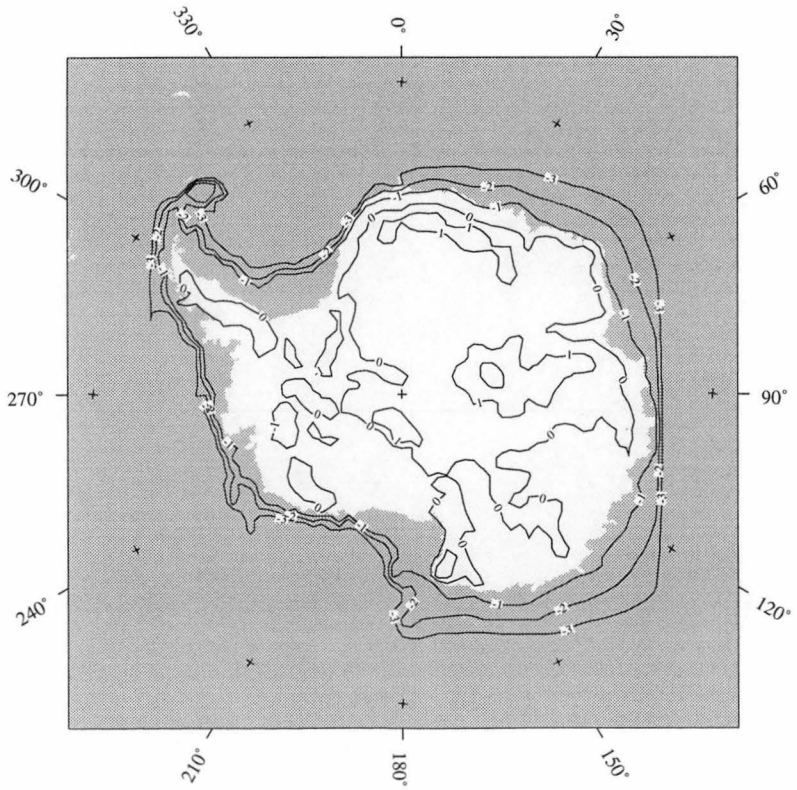

Fig. 4.4: Bedrock topography (km) of Antarctica defined as the equilibrium state.

4.3 The Inclusion of Glacial Isostasy in Antarctic Ice Sheet Models

To examine the first-order effect of isostasy two extreme isostatic adjustment schemes are used. The first is an instantaneous isostatic adjustment calculated in such a manner that the earth is always in isostatic equilibrium with the ice sheet. In other words it is equivalent to assuming an inviscid viscosity for the mantle. A lithospheric rigidity of 10^{25} N m is used to define the instantaneous isostatic deflection. The second model is a rigid earth with no isostatic adjustment. This model is equivalent to assuming an infinite viscosity for the mantle. These two models can be considered extremes of the adjustment process.

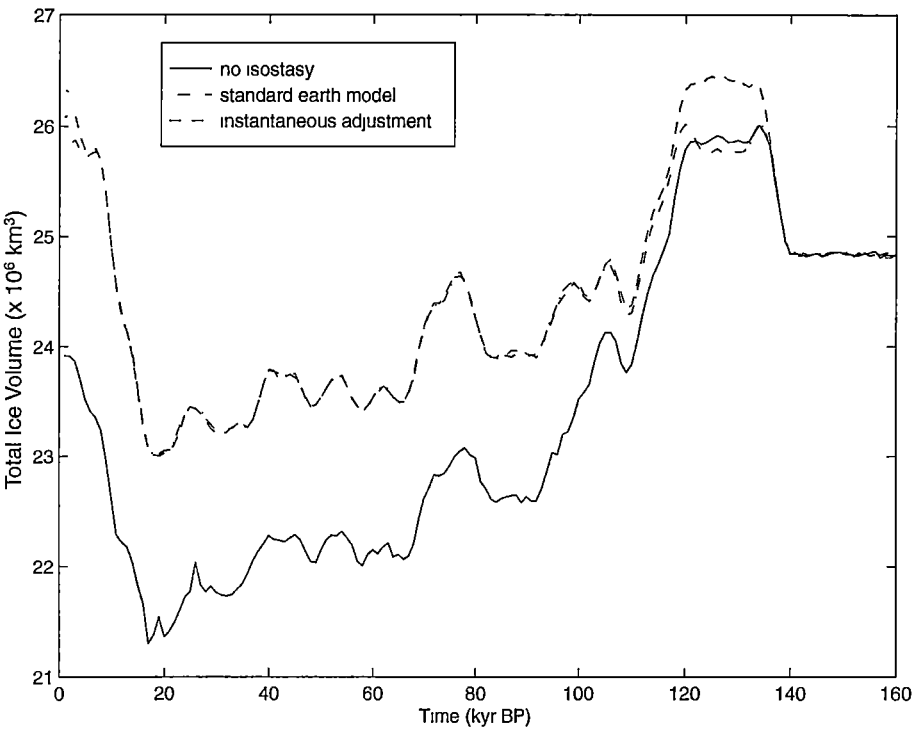

Fig. 4.5: Time-dependent change in the total volume of ice on Antarctica for the 'no isostasy' model, the 'instantaneous isostasy' model and the standard earth model.

Figure 4.5 shows the time-dependent changes in the total volume of ice for the two extreme earth models. The output from an additional earth model with lithospheric rigidity of 10^{25} N m and uniform mantle viscosity of 10^{21} Pa s is also shown. This model has parameter values inferred from studies of glacial isostasy and is referred to in the rest of this chapter as the 'standard earth model'. The

most extreme feature of Figure 4.5 is the gradual loss of ice beginning at 120 kyr BP for the 'no isostasy' model compared to the other models. Figure 4.6 shows the model prediction of the present day surface elevation of the Antarctic ice sheet for the standard earth model and Figure 4.7 shows the elevation profile for the 'no isostasy' model. From these figures it can be seen that the smaller total present day ice volume predicted by the 'no isostasy' model is due to the disappearance of ice in West Antarctica.

Figure 4.8 shows the model-predicted difference in bedrock elevation at the present day between the standard earth model and the 'no isostasy' model. Because the initial bedrock elevation is identical for the two earth models and the elevation for the 'no isostasy' model does not change with time it therefore also shows the change in the bedrock elevation between the beginning and end of the standard earth model run. The region has uplifted over 200 m in Marie Byrd Land (210° E) as a result of changes to the ice sheet. For the standard earth model the effect of isostasy is to stabilise the ice sheet. This result is in agreement with the work of Lingle and Clark (1985) and Payne et al (1989) discussed in the literature review. During a period of low accumulation rate or high eustatic sea level the retreating ice is stabilised by an isostatic adjustment which uplifts and grounds the ice to prevent further calving. For the 'no isostasy' model the West Antarctic ice sheet is flooded and most of the ice sheet calves into the ocean. Figure 4.4 shows that the bedrock elevation beneath West Antarctica is predominantly below sea level where the ice sheet is most sensitive to eustatic sea level changes.

Figure 4.5 shows that the ice volumes of the standard earth model are for the most part very similar to those of the 'instantaneous adjustment' model. This would suggest that for most of the model run the standard earth model is close to being in isostatic equilibrium. This results from the fact that the ice sheet model forcing is small enough that large changes in isostatic equilibrium and subsequent feedbacks in ice sheet dynamics do not occur. However, Figure 4.5 also suggests that the standard earth model is not in isostatic equilibrium at the present day. The assumption that the Antarctic ice sheet is in present day isostatic equilibrium is used to generate the reference bed used in the present

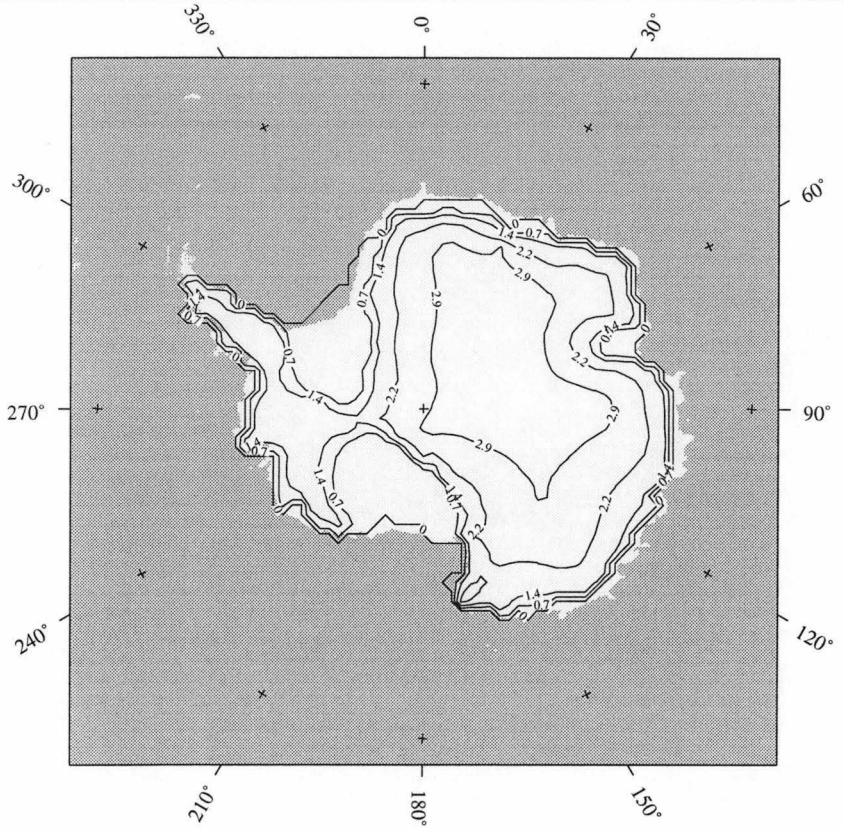

Fig. 4.6: Predicted surface elevation (km) of Antarctica at present day after the 160 kyr run of the standard earth model.

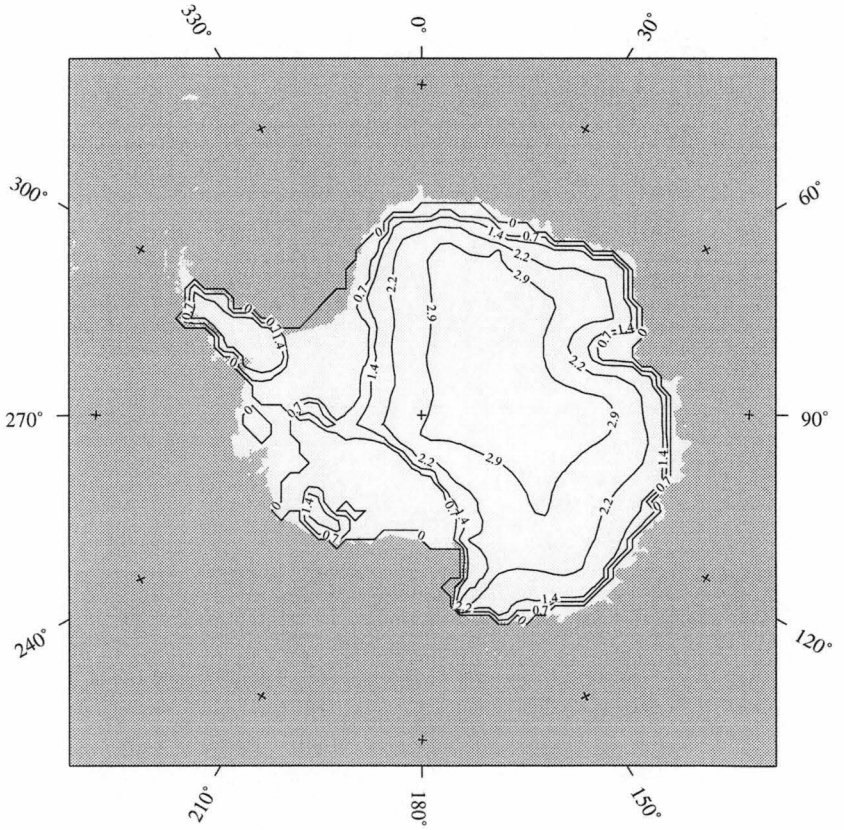

Fig. 4.7: Predicted surface elevation (km) of Antarctica at present day after the 160 kyr run of the 'no isostasy' model.

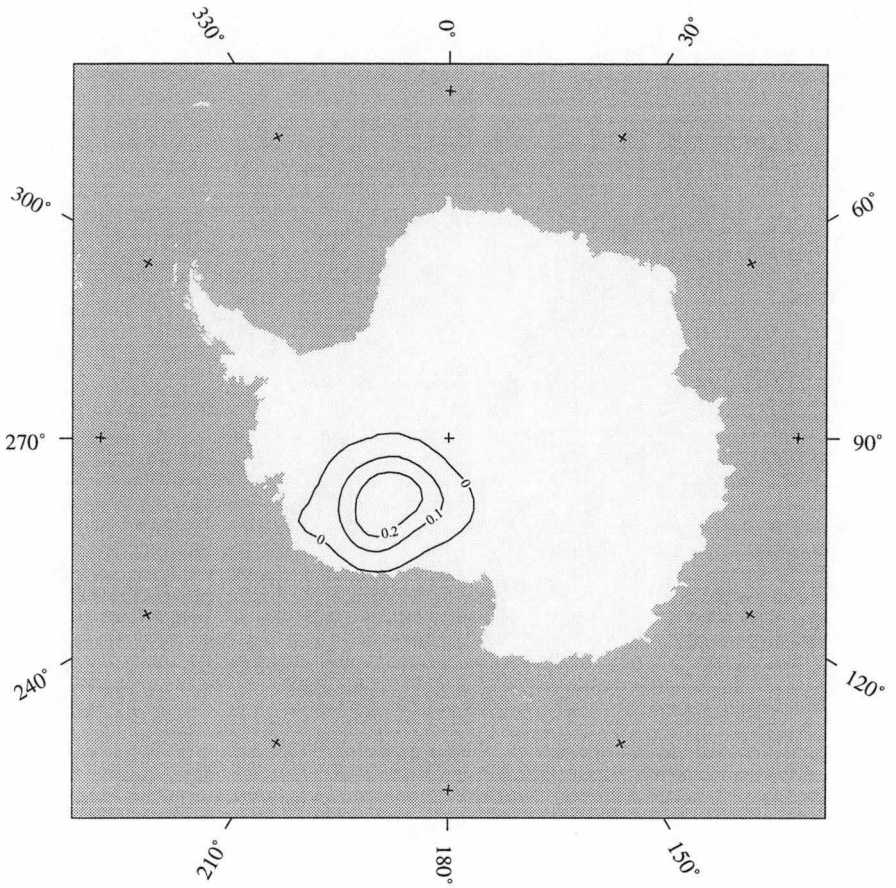

Fig. 4.8: Difference in bedrock elevation (km) at the present day between the standard earth model and the 'no isostasy' model.

study (see Section 3.1). At the end of this chapter an examination of the effect of this assumption on ice sheet dynamics is made.

4.4 Comparison with the Thin Channel Flow model

For comparison with the standard earth model a viscous thin channel model with asthenospheric diffusivity 0.5×10^8 m^2 yr^{-1} and rigidity 10^{25} N m was used to represent isostasy in the ice sheet model. This value of diffusivity is from Huybrechts (1990a). The total ice volume generated using this model over a glacial cycle is shown in Figure 4.9 together with that of the standard earth model and that of the 'instantaneous adjustment' model. The figure shows that the thin channel model has more ice than the standard earth model between 140 and 120 kyr BP and from 10 kyr BP to the present day. It has less ice

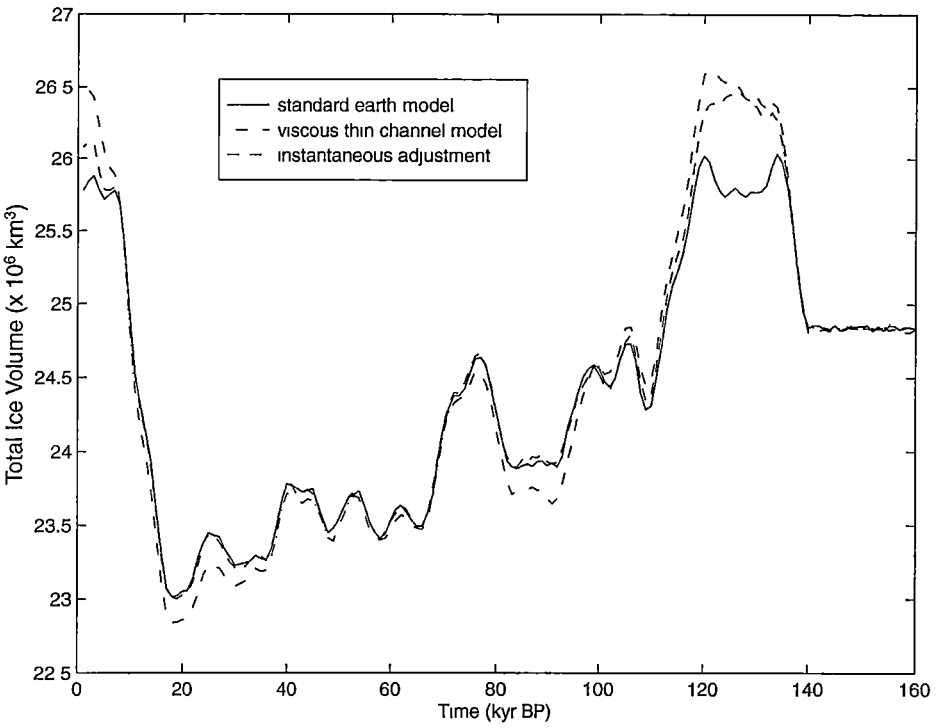

Fig. 4.9: Time-dependent change in the total volume of ice for the standard earth model, the thin channel model and the 'instantaneous adjustment' model.

than the standard earth model between 120 and 10 kyr BP. For the first 20 kyr of the model run the total ice volumes for the models are indistinguishable. Isostatic equilibrium is maintained for this period because the ice sheet is in steady state and the deflection is determined only by the lithospheric rigidity (which is 10^{25} N m for all models).

The decay times for the thin channel and standard earth models specified by Equations 3.11 and 3.14 are shown as a function of wavenumber in Figure 4.10. The Fourier spectrum of the ice thickness distribution of the Antarctic ice sheet is also displayed as a dimensionless power histogram to show the range of decay times used in the ice sheet model calculation.

Figure 4.10 shows a direct dependence of decay time with ice sheet size for the thin channel model and an inverse dependence for the standard earth model. For the dominant wavenumber range of the Antarctic ice sheet ($k \approx 10^{-3}$ km^{-1}) the decay time is larger for the thin channel model than the standard earth model. As the decay time is larger for the thin channel model the isostatically

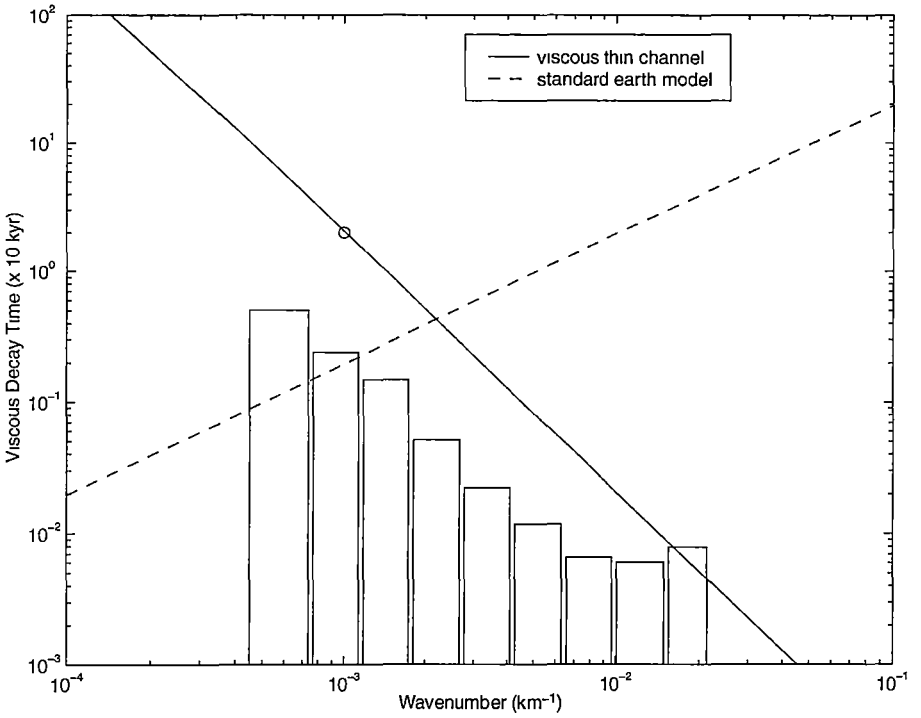

Fig. 4.10: Decay time as a function of wavenumber for the thin channel and standard earth models. Huybrechts' decay time for Antarctica (referred to in Chapter 3) is circled. The histogram represents the wavenumber range for the ice thickness distribution of the Antarctic ice sheet considered in this study.

induced ice sheet changes are slower. This is shown in Figure 4.9 from the fact that between 140 and 120 kyr BP and between 10 kyr BP and the present day the standard earth model and the 'instantaneous adjustment' model volumes are no longer changing but the thin channel volume is still increasing.

Differences in decay time dependence for the different earth models also give differences in isostatic adjustment. Figure 4.11 shows locations around the Antarctic coast where model predictions of isostatic adjustment over the last 15 kyr BP are shown in Figure 4.12. The thin channel model predicts a pattern of emergence at all sites while the standard earth model (half-space) predicts in general something of a submergence. The standard earth model produces a greater magnitude of adjustment for this period than the thin channel model.

In terms of overall generated ice sheet volume, Figure 4.9 shows that the thin channel flow model can be considered a reasonable first-order approximation to the viscoelastic half-space model. This result agrees with Le Meur

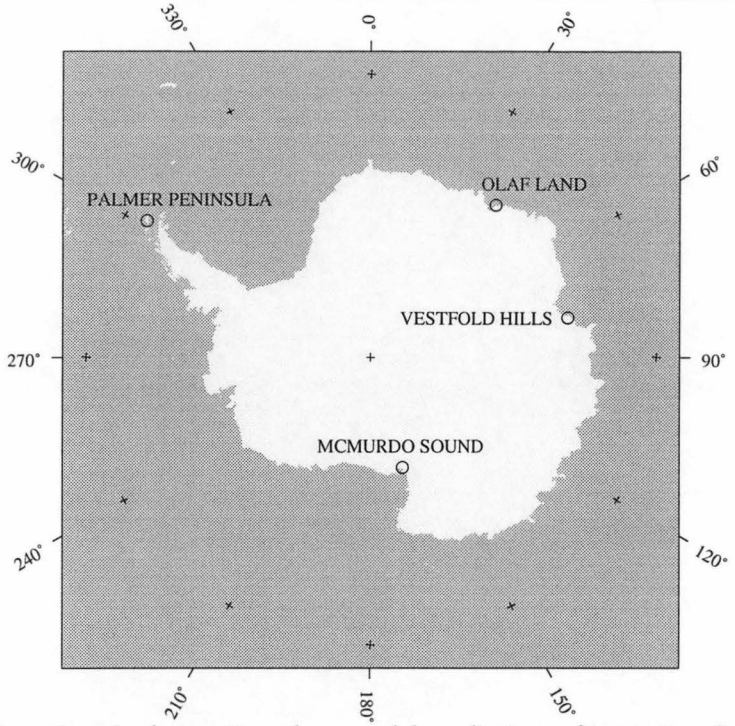

Fig. 4.11: Locations in Antarctica where model predictions of isostatic adjustment are shown in Figure 4.12.

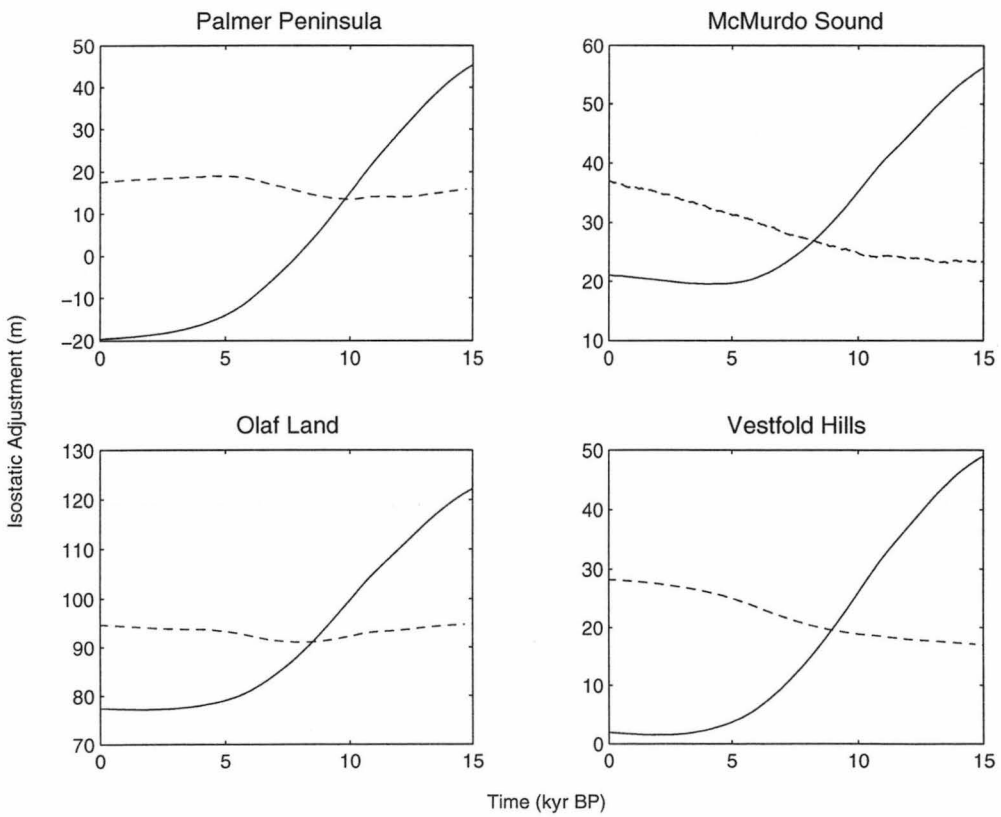

Fig. 4.12: Model predicted isostatic adjustment for the last 15 kyr BP at selected locations. Solid line represents the standard earth model and dashed line represents the thin channel model.

and Huybrechts (1996). However Figure 4.12 shows that the isostatic adjustment prediction should not be used to constrain the behaviour of the ice sheet when the thin channel flow approximation is used (for example see Siegert and Dowdeswell, 1995).

Le Meur and Huybrechts conclude that changes in the value of the earth model parameters produce changes in the ice sheet of the same order of magnitude as obtained when using different earth models. In the following sections the effect on the ice dynamics of changes to the earth model parameters is examined.

4.5 Mantle Viscosity

To examine the importance of changes in mantle viscosity the ice sheet model was used with the viscoelastic half-space isostatic adjustment model with viscosities of 10^{20} Pa s, 10^{21} Pa s (the standard earth model) and 10^{22} Pa s. Figure 4.13 shows that greater ice volumes are associated with lower viscosities. This result is to be expected in light of the behaviour of the 'instantaneous adjustment' and 'no isostasy' models considered previously. The results of Figure 4.13 make the point that viscosities less than 10^{21} Pa s are already so low that they can virtually be regarded as in isostatic equilibrium. That is, the behaviour is similar to the 'instantaneous adjustment' model. Cathles (1975) notes that decoupled viscoelastic earth models tend to overestimate the value of mantle viscosity. For the results here Cathles suggestion means that for the earth model used in this study a value of 10^{21} Pa s is an underestimate.

Mantle viscosity is the prime control on the time-dependent response of the mantle towards isostatic equilibrium. A decrease in mantle viscosity increases the rate of isostatic adjustment and decreases the magnitude of isostatic disequilibrium. A decrease in mantle viscosity therefore generates a more stable ice sheet because during periods of retreat the ice sheet is brought more rapidly above sea level so that calving is reduced.

Figure 4.14 shows the isostatic adjustment for the locations shown in Figure 4.11. The 10^{22} Pa s model has a continuous pattern of submergence while the standard earth model has a faster pattern of submergence followed by a slight

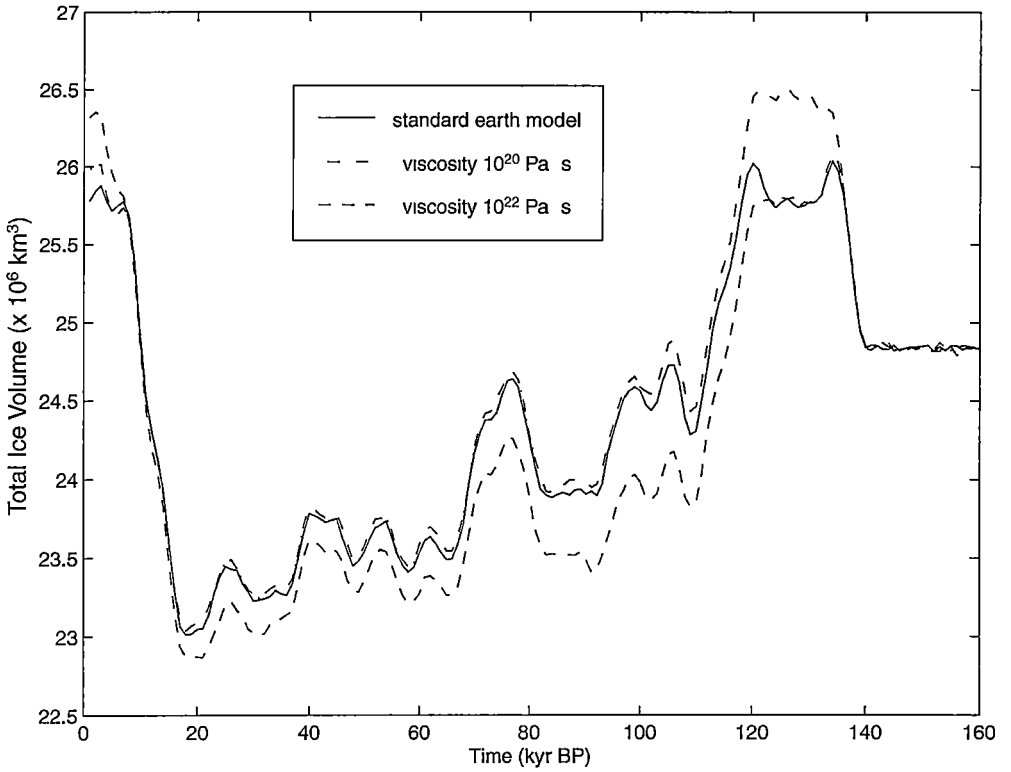

Fig. 4.13: Time-dependent change in the total volume of ice for the standard earth model (10^{21} Pa s), the 10^{20} Pa s viscosity model and the 10^{22} Pa s viscosity model.

emergence. The 10^{20} Pa s model is similar to the standard earth model but has a faster response, with emergence predicted for the last 7 kyr at Palmer Peninsula and the Vestfold Hills.

As the 10^{22} Pa s model has a slower response to ice sheet changes there is increased calving in West Antarctica that results from the lower ice sheet elevation in this region compared to the standard earth model. This is shown in Figure 4.14 where the model predicted bedrock elevation is 30 m higher at Palmer Peninsula for the 10^{22} Pa s model compared to the other models. The lower elevation in West Antarctica is also shown in Figure 4.15 where the elevation at Marie Byrd Land at 20 kyr BP is over 300 m higher for the standard earth model than for the 10^{22} Pa s model. On the other hand, and referring to Figure 4.13, the snow accumulation/elevation feedback ensures that the 10^{22} Pa s model generates a greater ice volume over the last 20 kyr than the standard earth model. The difference in ice sheet elevation between the standard and

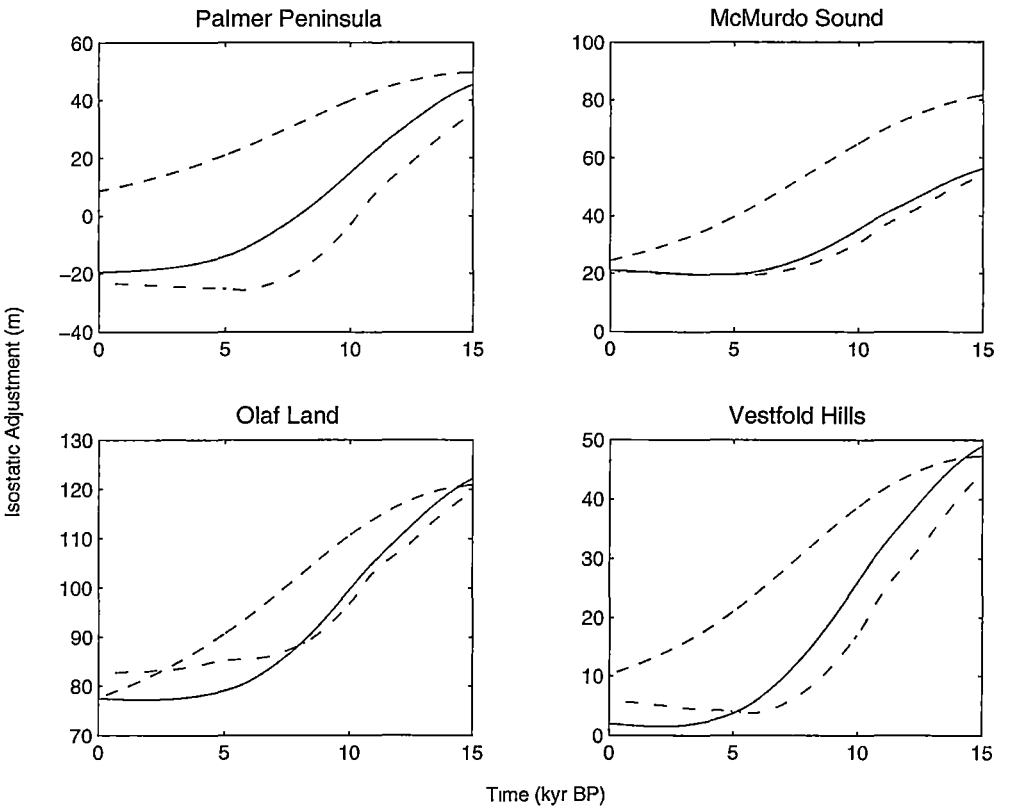

Fig. 4.14: Model predicted isostatic adjustment for the last 15 kyr BP at selected Antarctic locations. Solid line represents the standard earth model (10^{21} Pa s), dot-dashed line represents the 10^{20} Pa s viscosity model and dashed line represents the 10^{22} Pa s viscosity model.

10^{22} Pa s model at present day after the 160 kyr model runs is shown in Figure 4.16.

With regard to this behaviour over the last 20 kyr the 10^{22} Pa s model is similar to the viscous thin channel model. Both models have large decay times which decrease the stability of the ice sheet and increase calving. The reduced elevations in West Antarctica produce an increased accumulation and a thicker ice sheet at present day than the standard earth model.

The other feature of Figure 4.13 worthy of note is that the ice volumes are the same for the first 20 kyr of the run between 160 and 140 kyr BP. This reiterates the fact that in the absence of external forcing (as is the case for the first 20 kyr of all model runs) the isostatic equilibrium is not a function of the viscosity. It is however a function of lithospheric rigidity. This dependence is

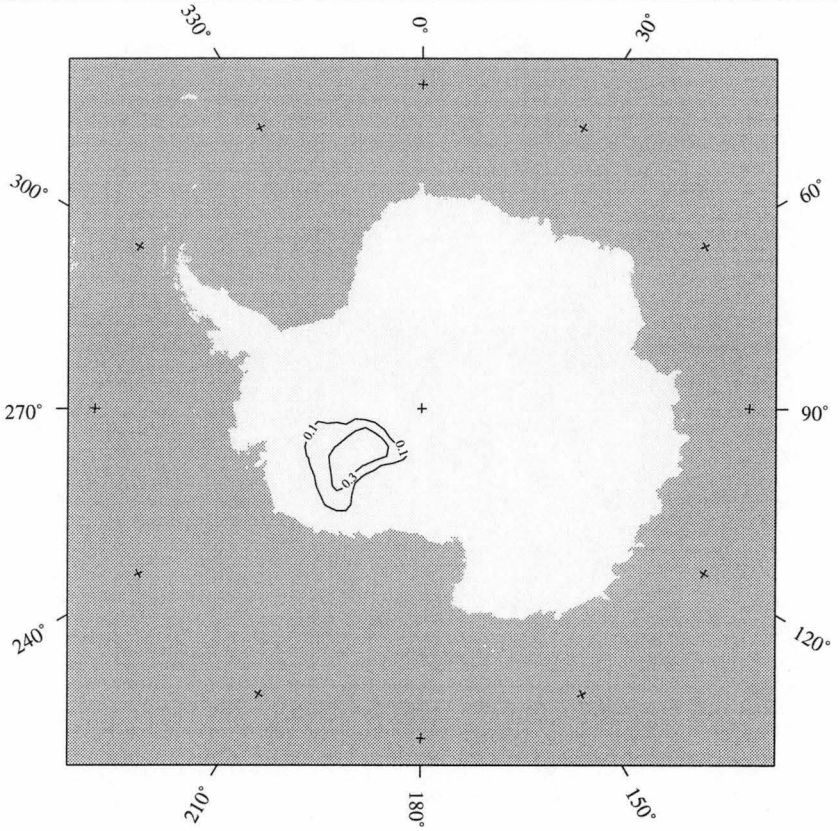

Fig. 4.15: Difference in ice sheet elevation (km) at 20 kyr BP between standard earth model and 10^{22} Pa s viscosity model.

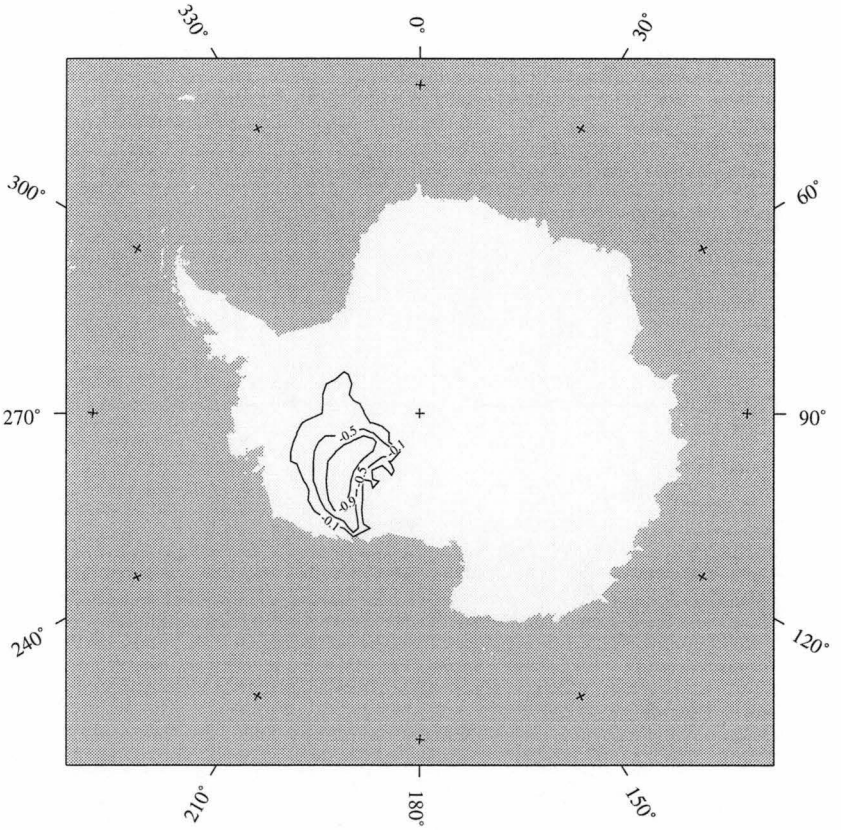

Fig. 4.16: Difference in ice sheet elevation (km) at the present day between standard earth model and 10^{22} Pa s viscosity model.

examined in the next section.

4.6 Lithospheric Rigidity

Equations 3.5 and 3.6 show that the lithospheric rigidity determines the equilibrium profile of the isostatic deflection. Le Meur and Huybrechts (1996) conclude that the lithosphere is the most important earth model feature to be used in ice sheet models. Figure 4.17 shows the time-dependent changes in total ice volume for ice sheets with lithospheric rigidities of 10^{24} N m, 10^{25} N m (standard earth model) and 10^{26} N m. The figure shows that the greater is the lithospheric

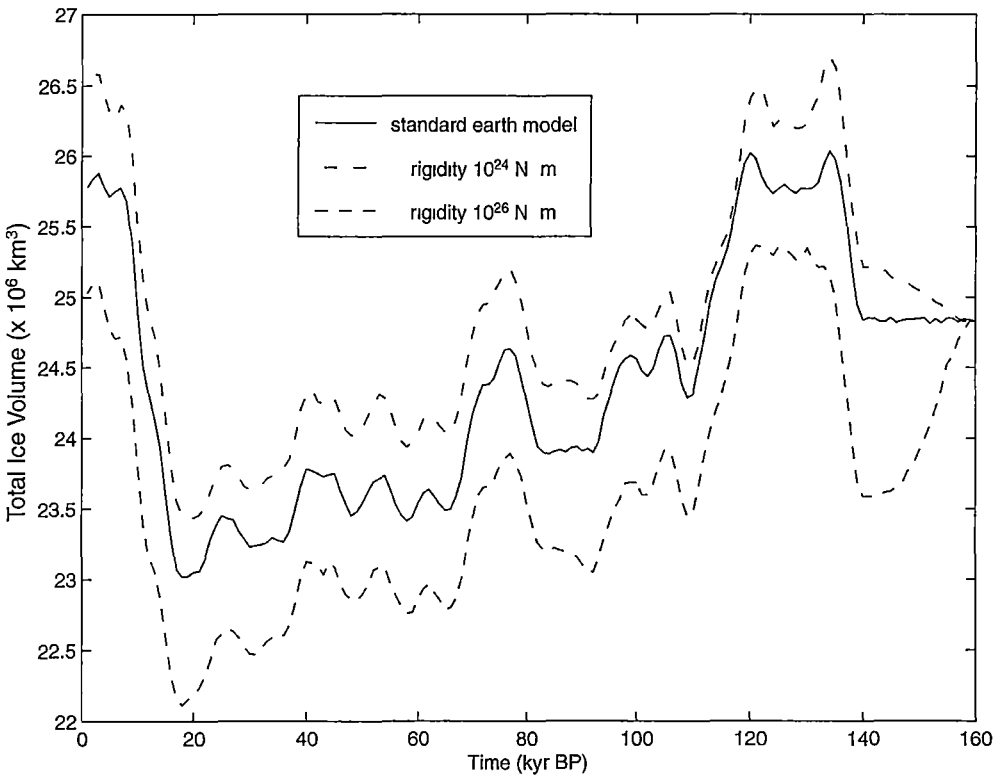

Fig. 4.17: Time-dependent change in the total volume of ice for the standard earth model (lithospheric rigidity equal to 10^{25} N m), the 10^{24} N m rigidity model and the 10^{26} N m rigidity model.

rigidity the less is the volume of ice generated over the period. Figure 4.18 shows the difference in ice sheet thickness between the 10^{26} N m model and the 10^{24} N m model at the present day. It shows that the lower lithospheric rigidity model (10^{24} N m) has generated more ice than the higher rigidity model (10^{26}

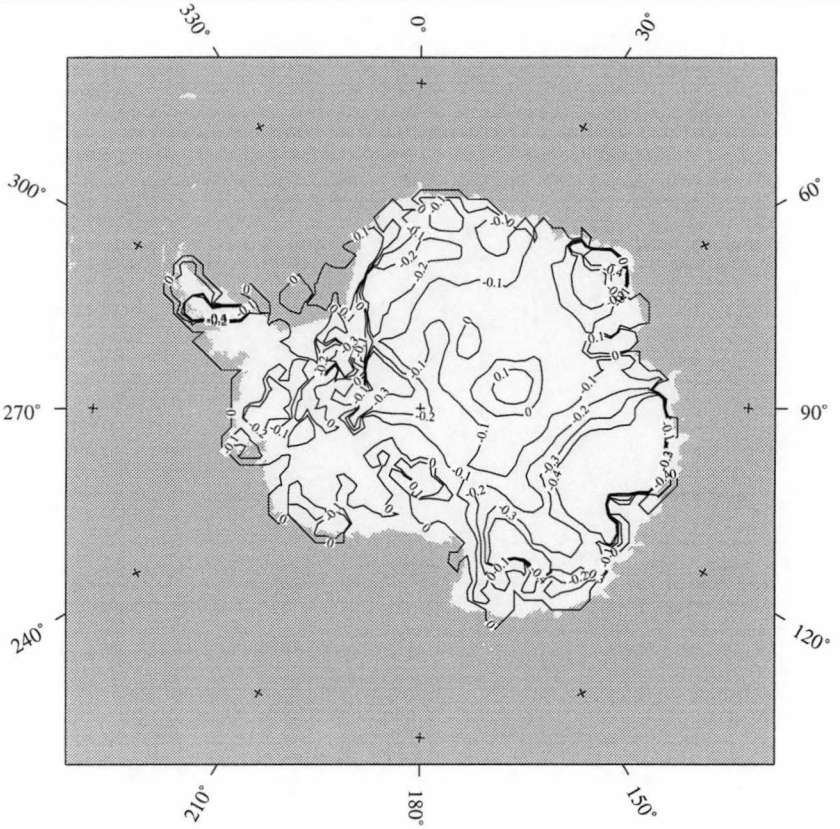

Fig. 4.18: Predicted difference in ice sheet thickness (km) at the present day between the 10^{26} N m rigidity model and the 10^{24} N m rigidity model.

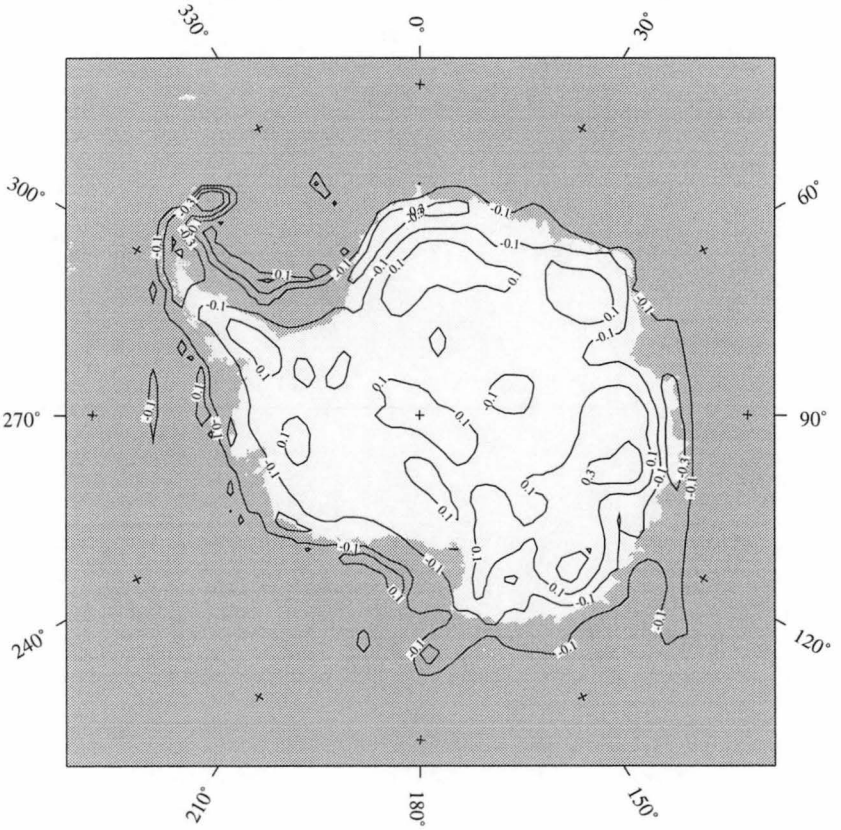

Fig. 4.19: Predicted difference in bedrock elevation (km) at the present day between 10^{26} N m rigidity model and 10^{24} N m rigidity model.

N m) over most of the ice sheet. That situation is reversed in central East Antarctica (60° E, 80° S). This location is where the East Antarctic ice sheet is at maximum elevation for the equilibrium situation (see Figure 4.3). The reversal occurs because because a greater value of the lithospheric rigidity produces a greater deflection in the centre of the continent because of the increased elasticity of the lithosphere. See also Figure 4.19 which shows the difference in predicted bedrock elevation of the two earth models at present day.

Figure 4.17 also shows that at the beginning of the model run (160 kyr BP) the ice volumes diverge before the time-dependent ice sheet model forcing begins. In the previous chapter it was shown that the magnitude of isostatic disequilibrium is a function of the lithospheric rigidity through the definition of the reference bed (Equations 3.6 and 3.7). The equilibrium configuration of the ice sheet used in the present study was generated using a lithospheric rigidity of 10^{25} N m. When a different value for the rigidity is used the ice sheet is not initially in isostatic equilibrium. If the new value of rigidity is greater than the original 10^{25} N m value the new equilibrium deflection profile is less than that used to generate the equilibrium configuration. This can be seen by noting the inverse dependence between equilibrium deflection and lithospheric rigidity in Equation 3.5. This means that to restore isostatic equilibrium the bedrock uplifts to the 'higher' profile generated by the larger value of deflection. With this uplift the ice sheet becomes thinner with a lower volume than that generated using the original 10^{25} N m value. For similar reasons a reduced value of lithospheric rigidity produces a larger ice sheet volume compared to that produced when using the original 10^{25} N m value.

The time-dependent isostatic adjustment at select locations for the three models examined in this section are shown in Figure 4.20. This figure shows that although the adjustment rates for the different models are similar the magnitudes differ from each other by up to 250 m. This results from the regional differences in ice sheet thickness near these sites.

Although the ice volumes generated here are artificial in the sense that the behaviour of the ice sheet is examined over order of magnitude changes in the isostatic parameters it is shown that the definition of the reference bed (from

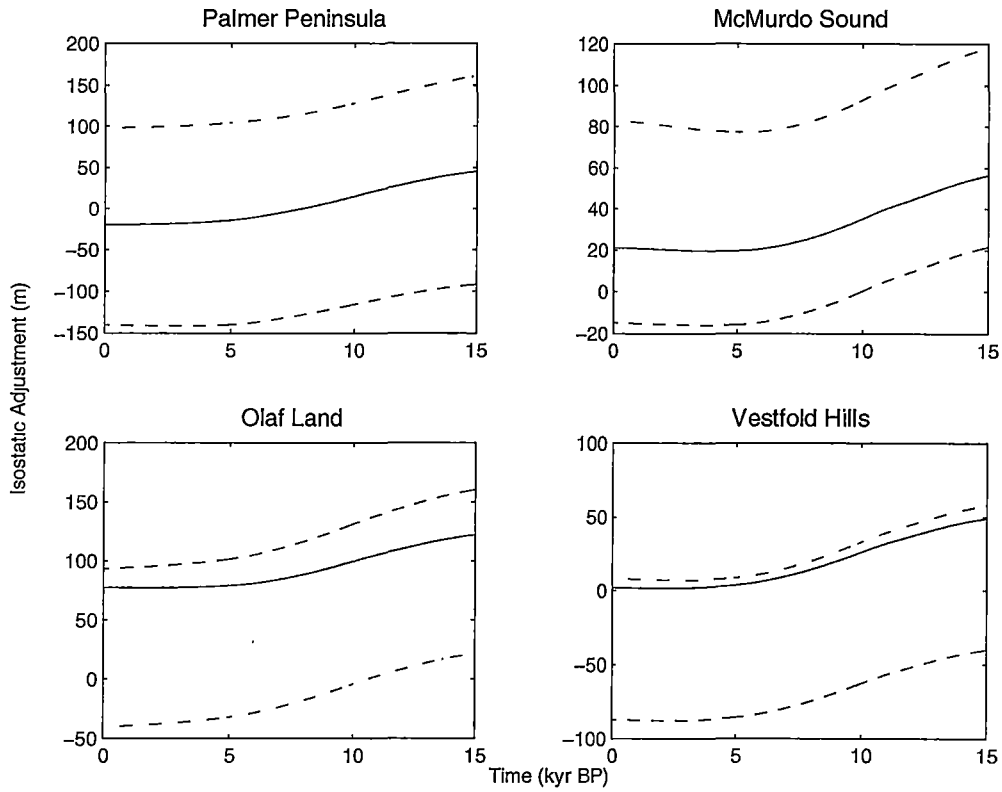

Fig. 4.20: Model predicted isostatic response for a last 15 kyr BP at selected locations. Straight line represents the standard earth model (10^{25} N m), dot-dashed line represents the 10^{24} N m rigidity model and dashed line represents the 10^{26} Pa s rigidity model.

Equation 3.6) has a strong control on ice sheet volume. The end of this chapter focuses on the effect of redefining the reference bed by using free air gravity anomaly data as an indication of present day isostatic disequilibrium.

4.7 Conclusions

The implications of this chapter can be separated into those pertaining to the choice of earth model and those pertaining to the earth model parameters. For the earth model it is shown that in terms of ice volume the thin channel flow model accelerates the advance and retreat of the Antarctic ice sheet compared to the viscoelastic half-space model. Oerlemans and Van der Veen use the thin channel flow approximation to conclude that the role of isostasy in ice sheet modelling is to accelerate the advance and retreat of ice sheets. The results of

the present study suggest that their conclusion is biased by the use of the thin channel model.

For the parameters themselves it is shown that an increase in either mantle viscosity or lithospheric rigidity serves to reduce the ice sheet volume. The mantle viscosity reduces the ice sheet volume because the reduction in isostatic adjustment rate decreases the ice sheet stability which leads to increased calving. As the adjustment rate is reduced the ice sheet remains in contact with the ocean for longer leading to increased loss. An increase in lithospheric rigidity also reduces the ice sheet volume because the increase in the reference bed elevation produces a reduced ice sheet thickness.

4.8 The Assumption of Present Day Isostatic Equilibrium

All of the ice sheet models discussed in the literature review assume present day isostatic equilibrium. This assumption is necessary for defining a reference bed profile through the use of Equation 3.6. Le Meur and Huybrechts (1996) conclude that this assumption is not likely to be true and in fact is not predicted by the ice sheet models in which it is used. The purpose of this section is to examine the sensitivity of the ice sheet model to the assumption of present day isostatic equilibrium. An approach based on the conclusion of Walcott (1970) and the work of Wu and Peltier (1983) that the free air gravity anomaly is representative of present day isostatic disequilibrium is used for the examination.

Figure 4.21 shows the free air gravity anomaly over Antarctica derived from the OSU91A geopotential model using the method of Rizos (1979). The dominant feature of Figure 4.21 is the anomaly north of the Ross ice shelf. It most likely results from a sideways force imposed by the Transantarctic Mountains (Stern & Ten Brink, 1989). For the present purpose Figure 4.21 is considered indicative of the present day isostatic disequilibrium over Antarctica. Although unrealistic this assumption is useful in defining a present day disequilibrium over the Antarctic continent. Using the approximation that the lithosphere is an infinite slab (James, 1992) the gravity anomaly shown in Figure 4.21 can be

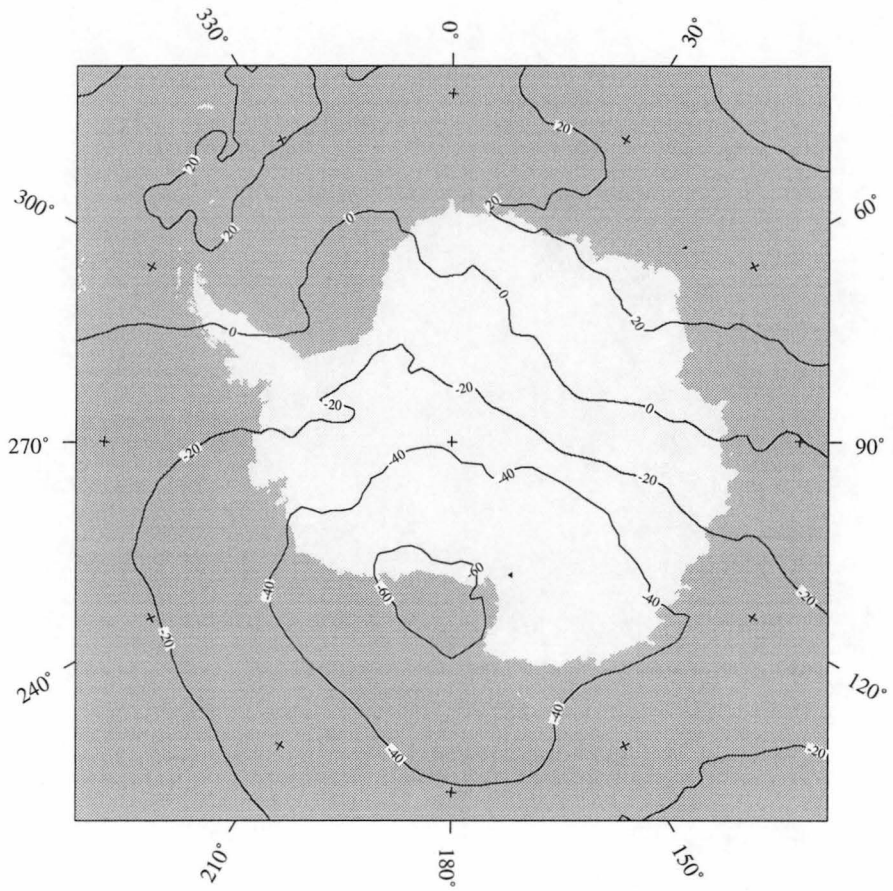

Fig. 4.21: Free air gravity anomaly (mgal) over Antarctica.

converted to a present day isostatic disequilibrium by:

$$\Delta h = -2\pi\rho_m G\Delta g \tag{4.5}$$

where Δh is the present day isostatic disequilibrium, ρ_m is the density of the earth's mantle, G is the gravitational constant and Δg is the gravity anomaly. Equation 4.5 suggests an approximate relation whereby 7 m of present day disequilibrium corresponds to every 1 mgal of gravity anomaly. For the high centred near the Ross ice shelf this equates to a remaining uplift required to produce isostatic equilibrium of over 430 m. However James (1992) suggests that current models of isostatic adjustment only predict 15 to 30% of the gravity anomaly in the North American region resulting from the Laurentide ice sheet deglaciation. Similarly Le Meur (1996) finds reconciliation of the total free air gravity anomaly with the present day vertical rebound velocities in the Northern

European region difficult. Assuming that the isostatic response in Antarctica to the retreat of ice is of the same order of magnitude as the response in North America to the Laurentide retreat, a figure of 65 to 130 m would be more appropriate for the Ross ice shelf high.

In this section the free air gravity data is used to redefine the reference bed discussed in the previous chapter. Equation 3.6 is used to define the reference bed elevation by assuming present day isostatic equilibrium. Using the gravity anomaly conversion to present day disequilibrium of Equation 4.5, Equation 3.6 can be redefined as:

$$disequilibrium_{pd} = (b_{pd} - (b_0 + \varphi_{pd})) \tag{4.6}$$

where $disequilibrium_{pd}$ is the present day isostatic disequilibrium in metres. The reference bedrock profile b_0 can therefore be redefined from Equation 4.6. Because there is uncertainty in the relation between free air gravity anomaly and remaining uplift (present day isostatic disequilibrium) two separate cases are examined. First it is assumed that only 15% of the gravity anomaly shown in Figure 4.21 results from present day isostatic disequilibrium. Second it is assumed that 30% of the gravity anomaly results from present day isostatic disequilibrium. Although the ICE4G deglaciation chronology suggests that Antarctica lost a substantial amount of ice (corresponding to a eustatic sea level rise of 20 m) between 9 and 4 kyr BP (Peltier, 1994) a value of 30% is still likely to be an overestimate.

The total ice volume generated over a glacial cycle for three cases of present day disequilibrium using the new reference bed profiles defined by Equation 4.6 are shown in Figure 4.22. (The third case corresponds to the standard earth model where the amount of present day disequilibrium is assumed to be zero). Incorporation of the present day isostatic disequilibrium term serves to increase the predicted ice sheet volume at all times. This is because the assumption of present day equilibrium underestimates the elevation of the reference bed so that a thinner ice sheet is required to produce isostatic equilibrium. Thus isostatic models that do not assume present day isostatic equilibrium are similar to models with a reduced value of lithospheric rigidity (see Section 4.6).

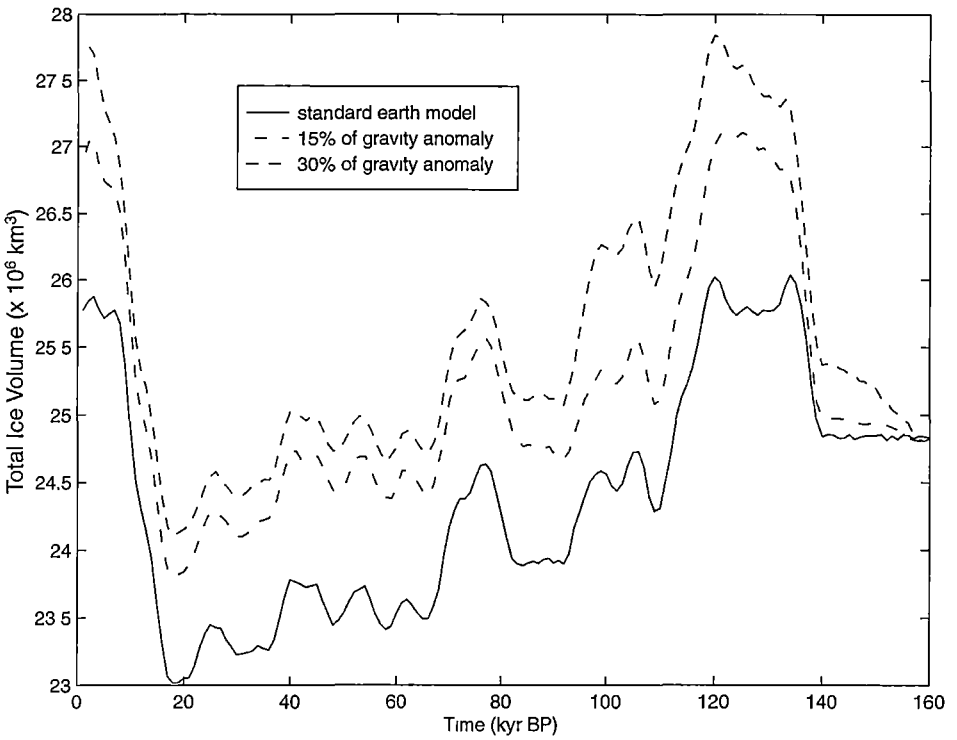

Fig. 4.22: Time-dependent change in the total volume of ice for the standard earth model (0%), the 15% gravity anomaly model and the 30% gravity anomaly model. For all models the standard earth model parameter values (10^{21} Pa s viscosity and 10^{25} N m rigidity) are used.

The significant point is that the assumption of present day isostatic equilibrium tends to reduce the magnitude of ice volume generated over a glacial cycle. The conclusion is valid as long as there is a positive (upwards) present day remaining uplift, regardless of its magnitude or distribution.

5. THE LAURENTIDE ICE SHEET

This and the following chapter are concerned with the two major Northern Hemisphere ice sheets where the available data on relative sea level change is more abundant than is the case for Antarctica.

The objectives are first to obtain the values of mantle viscosity and lithospheric rigidity in the isostatic model that most realistically reproduce the observed adjustment, and second to examine the sensitivity of the calculation to assumptions relating to the ice sheets.

5.1 Model Inputs

5.1.1 Relative Sea Level Data

The customary method to assess the realism of models of glacial isostasy is to compare model generated predictions of relative sea level with data from the Late Holocene relative sea level record. The data used in the present study is from Tushingham and Peltier (1991) and consists of 1888 individual sea level records from 392 sea level sites. The data age is in the range 15 to 0.3 kyr BP. From this global dataset only records with location in the model domain shown in Figure 5.1 are used. The model domain is an oblique-stereographic projection. It is a flat earth model which cannot take into account variations in sea level due to the gravitational attraction of the ice sheets. Thus only the last 7 kyr of Holocene relative sea level data can be used to constrain the isostatic model (Wu & Peltier, 1983). Circled sites in Figure 5.1 show locations where the entire record of sea level data have been excluded in the calculation because of the 7 kyr age restriction. 475 individual sea level records from 112 sites are used out of the 726 individual sea level records from 131 sites in the model domain. Relative sea level sites within 300 km of the model domain boundary

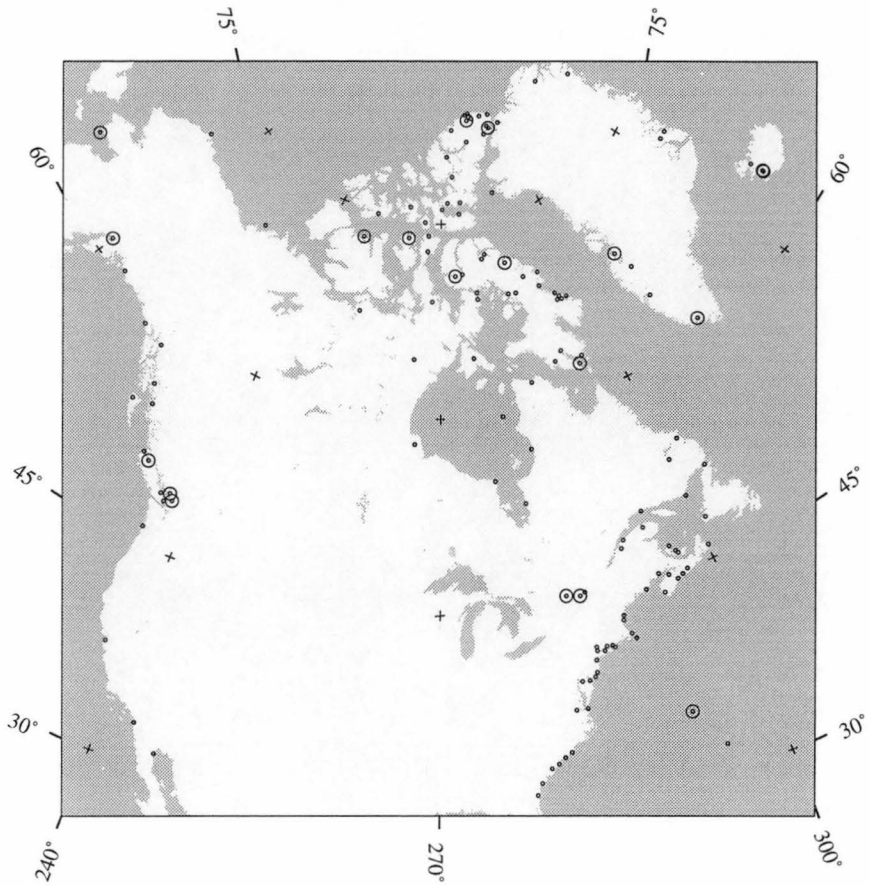

Fig. 5.1: Model domain and relative sea level data locations for the Laurentide ice sheet. Large circles indicate sites where data have been wholly excluded.

are also not used because of the periodicity of the Fourier technique used in the isostatic model.

5.1.2 Ice Sheet Deglaciation Chronology

Peltier's ICE4G deglaciation chronology (1994) is used here. It comprises 22 separate maps of ice extent at 1 kyr intervals from 21 kyr BP to the present day. The data is readily available in digital form with a grid resolution of 1° × 1°. As mentioned in the literature review ICE4G has been modified from its original sources (Bryson et al., 1969; Zonneveld, 1973) according to the qualitative features of the relative sea level data in the region. The ICE4G extent is shown here for 20 kyr BP (Figure 5.2), 10 kyr BP (Figure 5.3) and the present day (Figure 5.4). Although the ice extents shown in these figures

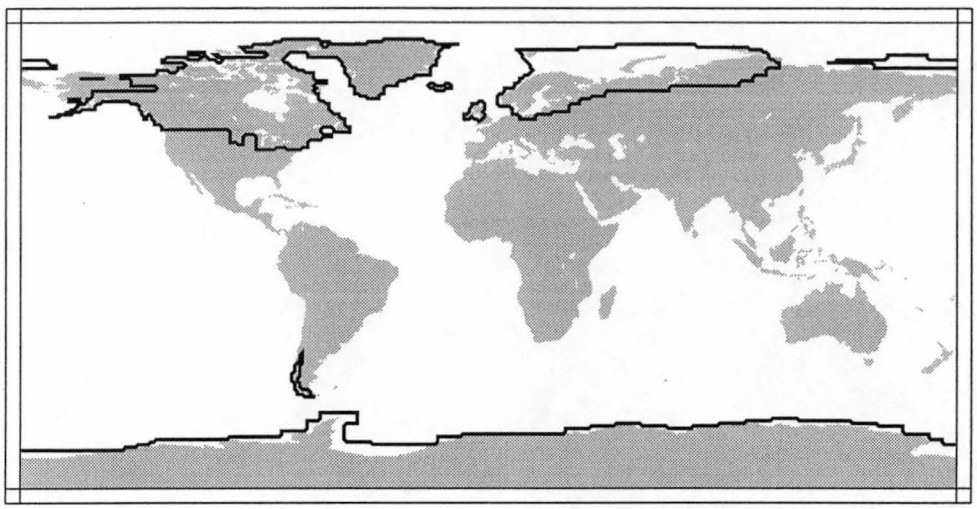

Fig. 5.2: ICE4G ice extent at 20 kyr BP.

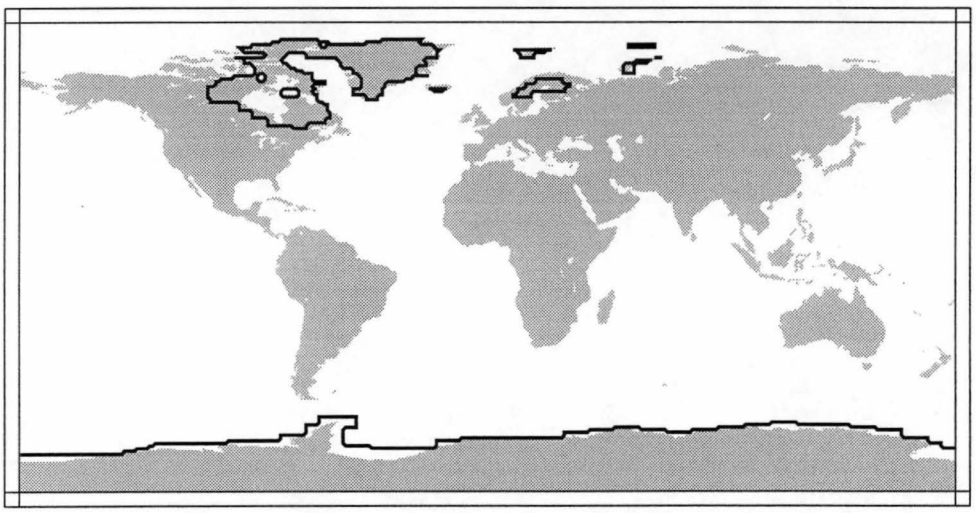

Fig. 5.3: ICE4G ice extent at 10 kyr BP.

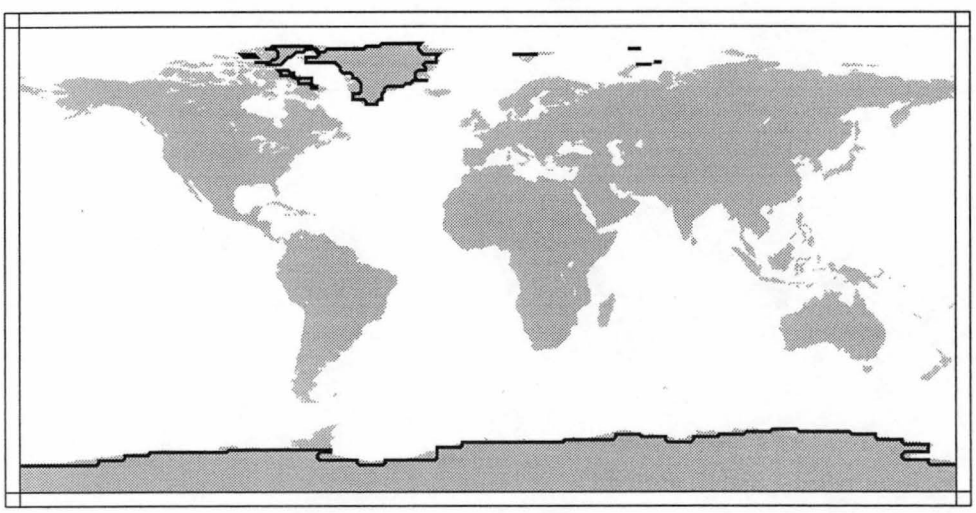

Fig. 5.4: ICE4G ice extent at the present day.

are assumed to be correct in the present study the ice thicknesses are considered to be 'unknown' and calculated along with the earth model parameters as in Lambeck (1993c).

One of the more straightforward techniques for reconstructing ice sheet thickness uses the plastic rheology approximation to generate ice sheets with a parabolic profile of thickness. To generate this profile the ice extent data of ICE4G is projected onto the model domain shown in Figure 5.1. The ice extent is then used as a boundary condition to solve for thickness using Reeh's (1982) equations for three-dimensional parabolic profile ice sheets. More sophisticated features such as multiple domed ice sheets (Peltier & Andrews, 1983), differences in ice sheet thickness due to geological variations in the region (Marshall et al., 1996) and isostatic adjustment are ignored using this technique, but the ice sheet chronology generated here is considered reasonable to first order. Figure 5.5 illustrates the ice sheet thickness calculated in the above manner for the maximum extent Laurentide ice sheet at 21 kyr BP. The total volume of the ice sheet shown in Figure 5.5 is 17×10^6 km^3. The difference in ice sheet volume between 21 kyr BP and the present day is equivalent to a eustatic sea level rise of 45 m.

A useful feature of the plastic rheology approximation is that because the ice sheets are parabolic a linear rescaling of thickness over the entire ice sheet ensures that it retains a parabolic profile. In the present study the method of Lambeck (1993b) is used. He defines a rescaling factor β which is adjusted to determine the most realistic overall thickness of the ice sheet that correctly predicts the observed relative sea level data in the region.

5.1.3 Eustatic Sea Level

As the model is a flat-earth limited-area projection the predicted relative sea level changes can only be computed to first-order since the gravitational attraction of the oceans to the ice sheets is ignored. The relative sea level changes in the present study result from glacio-isostatic, hydro-isostatic and hydro-eustatic changes. For the hydro-eustatic component the curve of Chappell and Shackleton (1986) illustrated in Figure 4.1 is used. The model itself predicts the

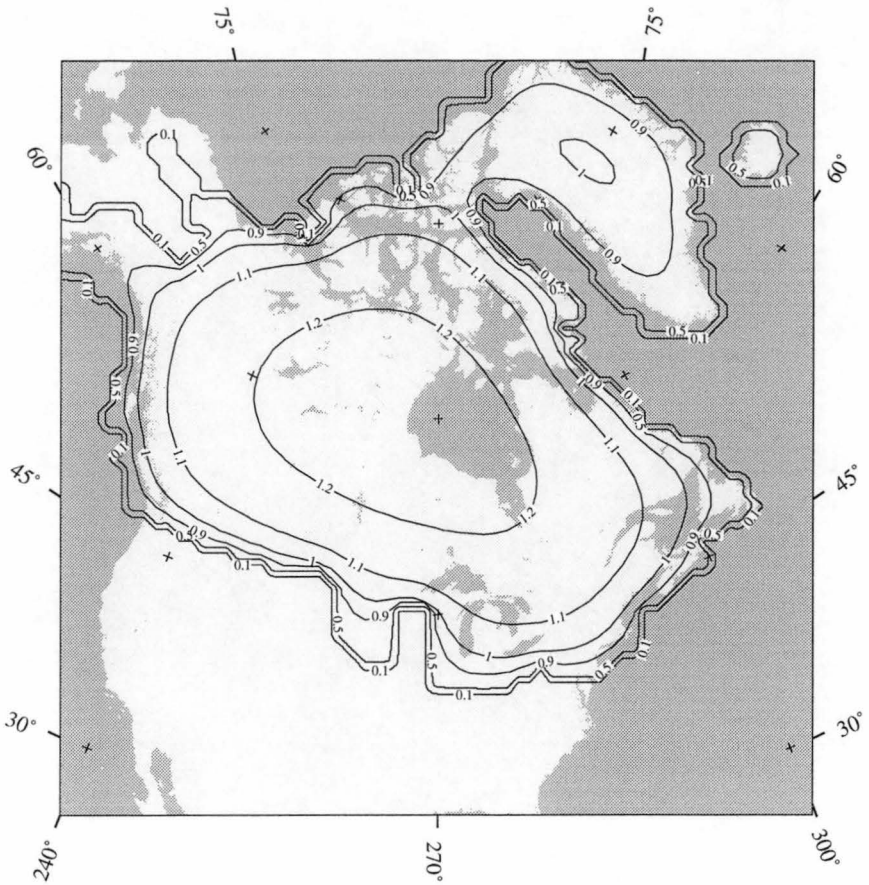

Fig. 5.5: Parabolic profile ice sheet thickness at maximum extent (21 kyr BP).

glacio-isostatic and hydro-isostatic changes.

5.1.4 *Initial Conditions*

Although the retreat of the Laurentide ice sheet from 21 kyr BP to the present day is reasonably well constrained, the behaviour of the ice sheet prior to the last glacial maximum is more uncertain. As an indication of global ice volume the eustatic sea level curve of Chappell and Shackleton suggests reasonably broad scale glaciation prior to 21 kyr BP. Budd and Smith (1987) conclude that it is likely that the ice sheets were neither in isostatic nor dynamic equilibrium at 21 kyr BP.

To simulate this isostatic disequilibrium at 21 kyr BP the isostatic model timing is set so that for the first 21 kyr the ICE4G ice extent chronology is reversed. This reversal attempts to simulate an advance. After this advance the

following 21 kyr simulates retreat to present day. Peltier (1982) suggests that for the characteristic decay times of isostatic adjustment the assumption that at 21 kyr BP the ice sheets are in isostatic equilibrium is not seriously limiting. Le Meur's (1996) contrast between the assumption of isostatic equilibrium at 21 kyr BP and a sawtooth-like ice sheet advance and decay (to emulate the Pleistocene ice volume changes) suggests that the maximum difference in isostatic adjustment for these models is 20 m at the centre of the ice sheet. Le Meur further reports that from 21 kyr BP onwards this difference diminishes so that at present day there is almost no difference in the isostatic response. It is therefore assumed that the results generated here are not significantly effected by the 21 kyr 'advance' at the start of the model run.

The elevation of the continental surface topography of the North American region before the last ice age is also uncertain. In this study an iterative scheme based on the 'near linearity' of isostatic adjustment is used. As a first approximation present day topography is used as the initial condition with the ice sheet growing and retreating over this topography. With the decay times associated with glacial isostasy the model prediction of present day topography at the end of one model run of 42 kyr (21 kyr 'backwards' and 21 kyr 'forwards') is then lower than observed. To account for this difference the residual between the observed and predicted present day topography is added to present day topography and the time-dependent run repeated with the new, higher topography used as the initial condition. This process is repeated several times so that the prediction of present day topography converges towards observation. The model is considered to be reasonable when the predicted and observed present day topography agrees at each model point to within 10 cm. Normally less than four iterations are required to achieve this convergence although the choice of earth model parameters effects the convergence rate through the decay time variation.

5.2 Minimum Variance and Least Squares Variance

Comparison of relative sea level data with the isostatic model prediction allows the most realistic values of earth model parameters to be determined. In this study the method of comparison used initially was the minimum variance technique of Lambeck (1993c). The technique for finding the minimum in the variance is simply to try a range of values for the earth model parameters (that is to say a process of parameter space search). This technique ensures that the parameters determined as most realistically representing the isostatic adjustment are not dependent on the values of other earth model parameters. This technique also allows the sensitivity of the model behaviour to the parameter values to be examined.

Lambeck varies the parameters of the model to determine values that minimise the variance defined as follows:

$$Variance = \sqrt{\frac{1}{N}\sum_{i=1}^{m}\sum_{j=1}^{n}\left(\frac{RSL_{mod}(\theta_i,\phi_i,t_j) - RSL_{obs}(\theta_i,\phi_i,t_j)}{\Delta RSL_{obs}(\theta_i,\phi_i,t_j)}\right)^2} \qquad (5.1)$$

where $RSL(\theta_i, \phi_i, t_j)$ is the sea level height (either modelled or observed) with respect to present day at longitude θ_i and latitude ϕ_i on the surface of the earth at time t_j. $\Delta RSL_{obs}(\theta_i, \phi_i, t_j)$ is the measurement error for the sea level observation, m is the number of sea level sites in the model domain, n is the number of occurrences of sea level data at each particular site and N is the total number of sea level records. Note that the discrepancy between model prediction and observation is weighted by the measurement error in the observation.

The minimisation technique using this definition of variance was not successful using the present viscoelastic half-space isostatic model. Figure 5.6 shows the model predicted relative sea level amplitudes plotted against the observations for those earth model parameters (mantle viscosity and lithospheric rigidity) that produce the lowest variance. There is a general pattern of underestimation (that is to say $|RSL_{mod}| < |RSL_{obs}|$) of relative sea level. It results from the use of uniform hydro-eustatic loading and from neglecting sea level data older than 7 kyr BP.

In the relative sea level data there is a general correlation between sea level

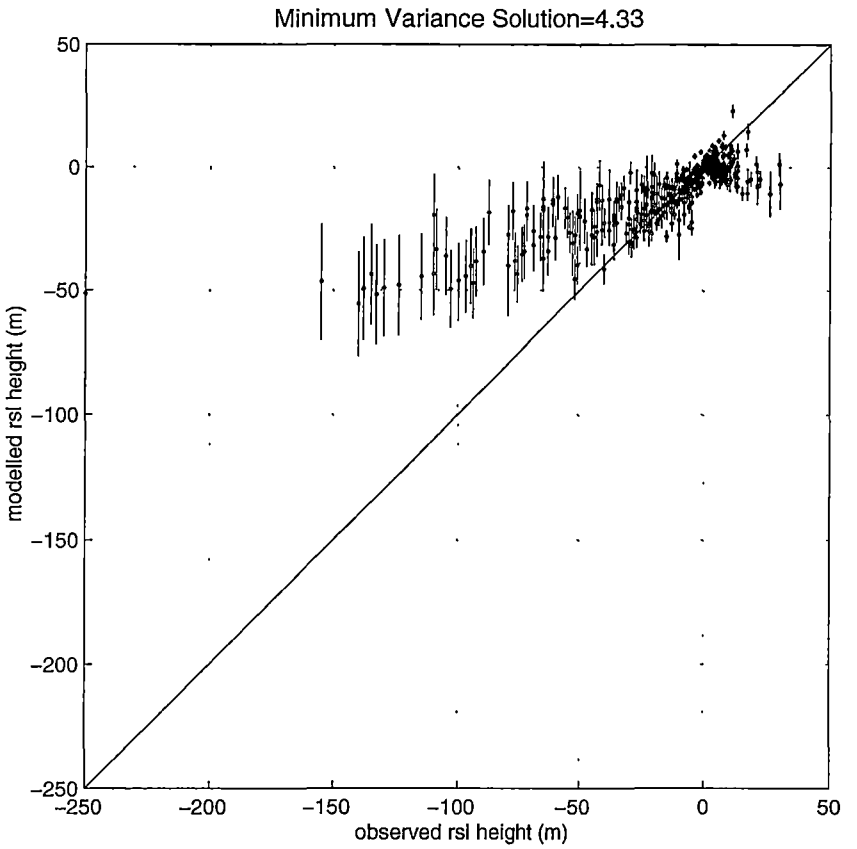

Fig. 5.6: Observed and predicted relative sea level heights for 'best fit' earth model parameter values using the Lambeck (1993c) definition of variance.

data age, amplitude and observation error. The amplitude and error correlation is shown graphically by the variation of the error bars in Figure 5.6. This is presumably because processes such as erosion are more uncertain for older sea level data so that an accurate determination of sea level amplitude is more difficult. Equation 5.1 accounts for the observational error by weighting the data according to its uncertainty. Most of the data concerns small sea level changes of amplitude less than 25 m that have occurred over the last 3 to 4 kyr BP. The minimum variance calculation therefore tends to satisfy younger sea level data at the expense of the older sea level data. This can be seen by reference to Figure 5.6.

The problem is a significant shortcoming of the minimum variance technique in the present context. As a consequence the least squares procedure of Wu and Peltier (1983) is adopted in the present study where the variance is defined

as follows:

$$Variance = \sqrt{\frac{1}{N}\sum_{i=1}^{m}\sum_{j=1}^{n}\left(RSL_{mod}(\theta_i,\phi_i,t_j) - RSL_{obs}(\theta_i,\phi_i,t_j)\right)^2} \qquad (5.2)$$

Equation 5.2 is the same as Equation 5.1 except that the observation error is not accounted for. As the observational error is generally proportional to the relative sea level amplitude the use of Equation 5.2 biases the calculation by emphasising the level of agreement for sea level data with large amplitude. This bias partially counteracts the bias created by using only sea level data with age less than 7 kyr BP.

The next section explores the parameter space of the model using Equation 5.2 as the definition of variance to determine the most realistic earth model parameters.

5.3 Least Squares Variance

In this section the parameter space search is used to determine the values of four model parameters that most realistically reproduce the observed relative sea level data in the model. These are the lower mantle viscosity, the upper mantle viscosity, the lithospheric rigidity and the ice sheet rescaling factor β. In parameter space units of log to base 10, the resolution of the parameters used in the parameter space search is 0.4 steps in the lower mantle viscosity, upper mantle viscosity and lithospheric rigidity. In linear units the resolution is 0.1 for the ice sheet rescaling factor β. Earth model parameter values in the range 10^{20} to 10^{22} Pa s for the viscosity and 10^{24} to 10^{26} N m for the lithospheric rigidity are examined.

The result of the parameter space search for the lower and upper mantle viscosities is shown in Figure 5.7. In this case the lithospheric rigidity was *fixed* at 10^{25} N m and the upper mantle viscosity, lower mantle viscosity and β were varied. For each choice of viscosities shown in Figure 5.7 a range of values for β was considered. The viscosities in Figure 5.7 refer to a situation where β gives a minimum variance.

Figure 5.7 shows a minimum in the parameter space of the model for a lower mantle viscosity of 1.5×10^{21} Pa s and upper mantle viscosity of 1.5×10^{21} Pa s

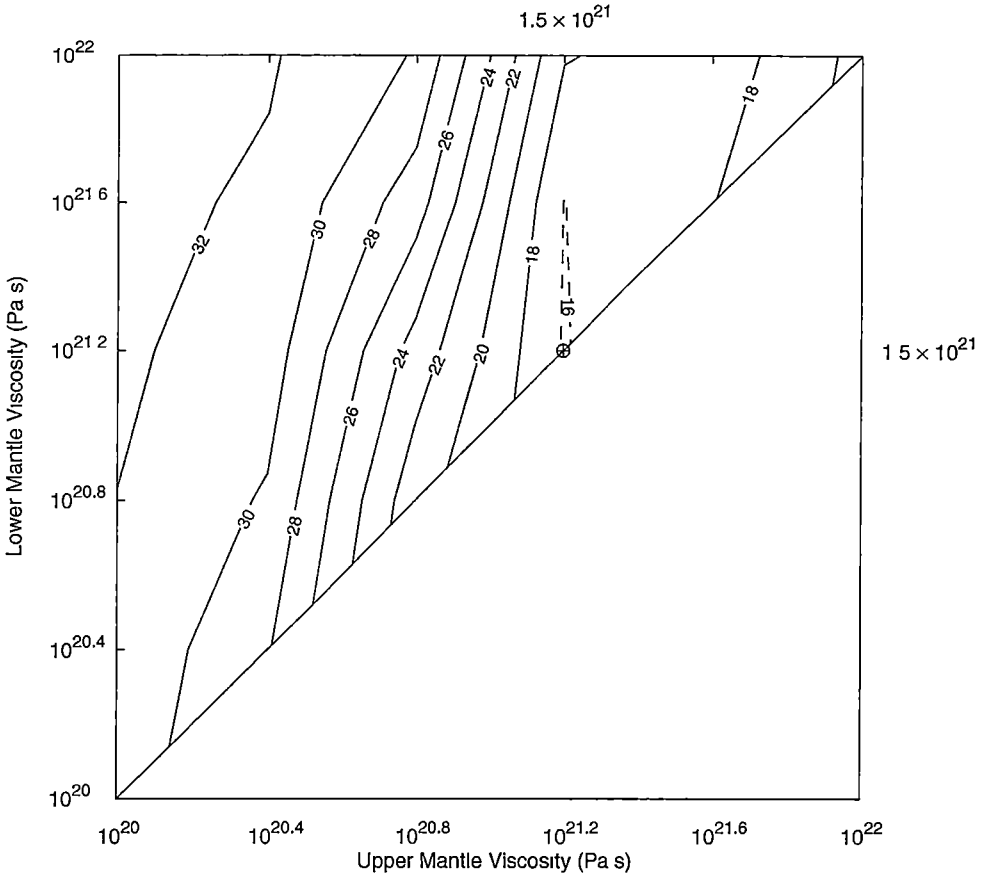

Fig. 5.7: Parameter space for 3 layer earth model with upper mantle and lower mantle viscosities as searching parameters. The minimum in parameter space is shown by ⊕ with corresponding earth model parameter values shown in exponential notation at top and right hand side of axes. Note that from pressure arguments the viscosity of the lower mantle must be greater than the viscosity of the upper mantle and hence there are no contours to the right of the diagonal line of equal viscosities.

(in other words it is suggesting a best fit is a uniform mantle viscosity). The contouring in Figure 5.7 is predominantly vertical suggesting that the upper mantle viscosity is a more sensitive parameter than the lower mantle viscosity. The minimum in the variance is produced for $\beta = 0.9$. The determination of the value of β for this particular set of earth model parameters is shown explicitly in Figure 5.8. This means that the dimensions of the ice sheet that most realistically reproduces the observed relative sea level data is such that at maximum extent the total ice volume of the ice sheet is 15×10^6 km^3. This

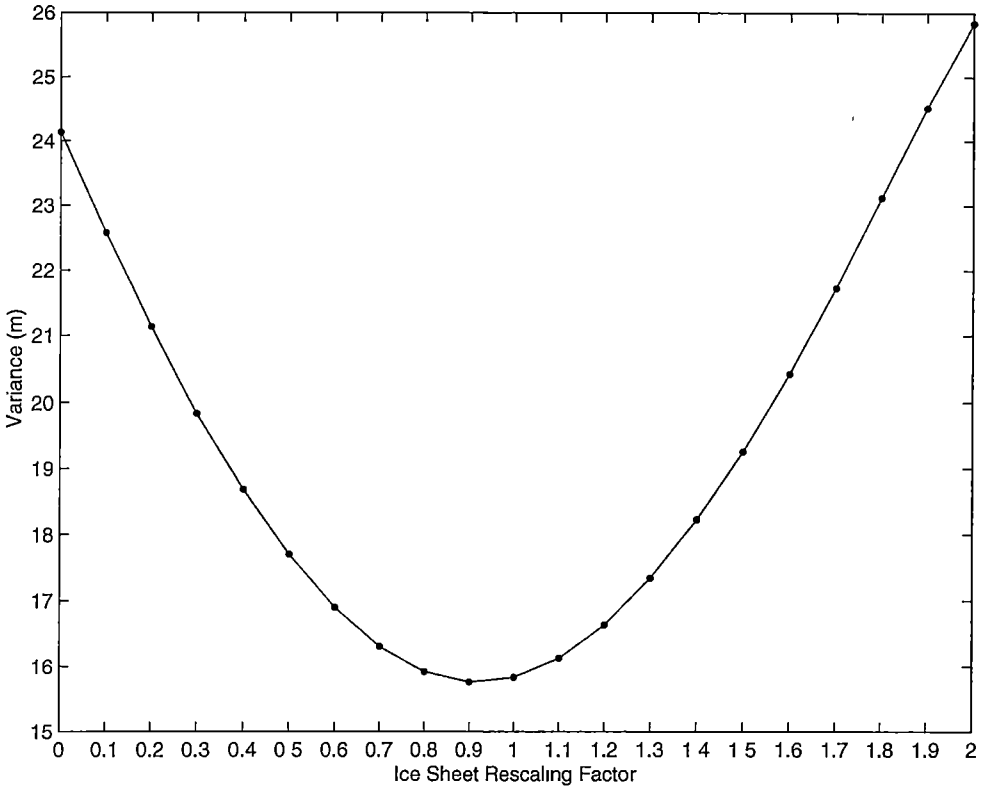

Fig. 5.8: Variance as a function of ice sheet rescaling factor β for uniform mantle viscosity of 1.5×10^{21} Pa s and lithospheric rigidity of 10^{25} N m. Minimum variance occurs for $\beta = 0.9$.

volume corresponds to a eustatic sea level contribution from deglaciation of the ice sheet of 40 m.

Assuming the upper and lower mantle viscosities are equal, the results of a parameter space search of viscosity and lithospheric rigidity are given in Figure 5.9. The minimum variance occurs for a uniform mantle viscosity of 1.5×10^{21} Pa s and a lithospheric rigidity of 1.5×10^{25} N m. In this case the value of β for the ice sheet that best reproduces the observed relative sea level data is 0.8. This value corresponds to a total ice sheet volume of 14×10^6 km^3 at maximum extent and a corresponding eustatic sea level contribution of 35 m. The minimum in rigidity is extremely shallow. The spatial scale of the ice sheet is so large that the lithospheric rigidity plays a minor role in the adjustment. Note that in Figure 5.9 the minimum variance is greater than the minimum in Figure 5.7 because the lithospheric rigidity in Figure 5.7 was fixed at 10^{25} N m.

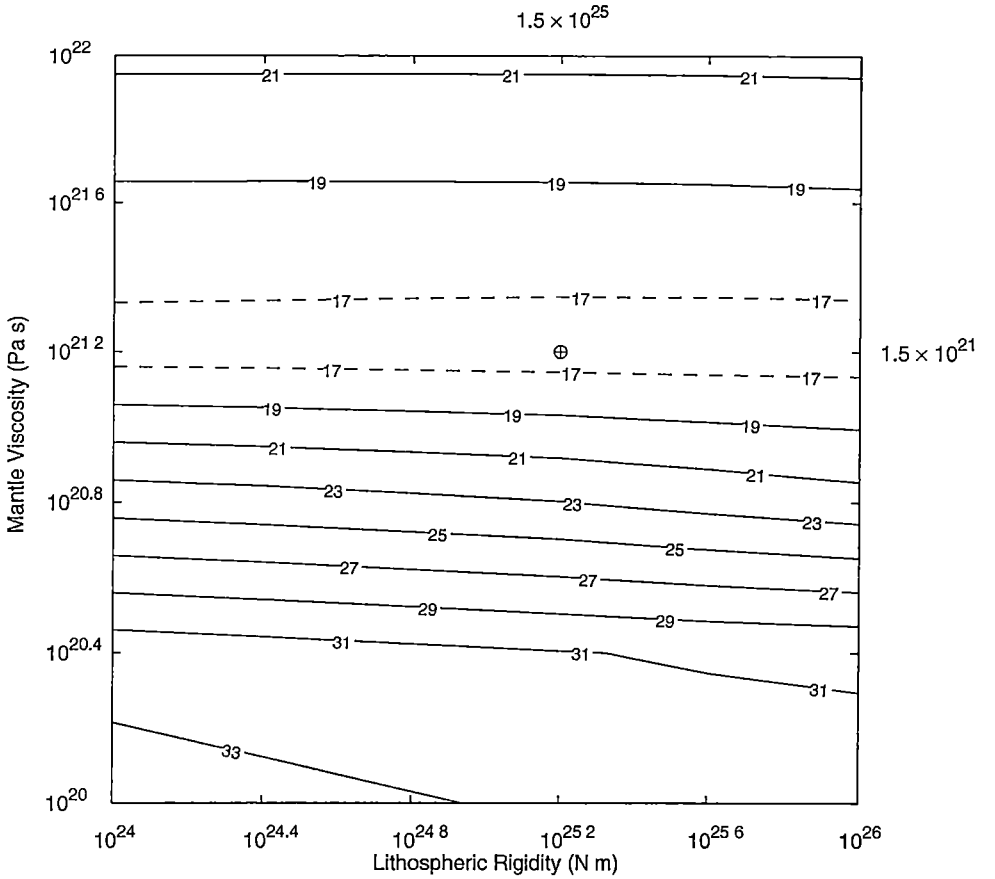

Fig. 5.9: Parameter space for 3 layer earth model with upper mantle viscosity and lithospheric rigidity as searching parameters. The minimum in parameter space is shown by ⊕ with corresponding earth model parameter values shown in exponential notation at top and right hand side of axes.

This highlights the problem of consistency of parameter resolution. The same parameter space search was conducted at higher resolution in viscosity and rigidity (the resolution of β was held at 0.1). The higher resolution (better by a factor of four) in units of log to base 10 was in steps of 0.1 for both viscosity and rigidity. The low resolution results are important in showing that at least one minimum occurs within the range of parameter space being considered. There was also an additional step incorporated in the technique while conducting the increased resolution parameter space search. For the minimum in parameter space a value of β is found which most realistically reproduces the observed changes in relative sea level. If $\beta \neq 1$, the ice sheet thicknesses associated with the ice sheet chronology (see Section 5.1.2) are multiplied by β and the

parameter space search was reconducted. The process was repeated until the minimum in the parameter space search occurred for $\beta = 1$. The reason for this modification is that the second part of this chapter compares the results generated using the parabolic profile deglaciation chronology with an alternate deglaciation chronology where β must be set to 1. This condition is necessary in order to ensure consistency of the physics relating the gradient of the ice sheet to velocities. The process of refining the ice sheet thicknesses until $\beta = 1$ also ensures that both deglaciation chronologies are determined to an equal degree of precision.

Figure 5.10 is the higher resolution version of Figure 5.7. The best fit model prediction has a lower mantle viscosity of 3×10^{21} Pa s and an upper mantle viscosity of 2×10^{21} Pa s. With the lower mantle viscosity held at 3×10^{21} Pa s Figure 5.11 shows the results of the parameter space search for the upper mantle viscosity and lithospheric rigidity. With β forced to 1 the total volume of the ice sheet at maximum extent is 14×10^6 km^3.

In summary the values of the earth model parameters which most realistically reproduce the relative sea level data where $\beta = 1$ are outlined in Table 5.1.

Model Parameter	Best Fit Value
Lower Mantle Viscosity	3×10^{21} Pa s
Upper Mantle Viscosity	2×10^{21} Pa s
Lithospheric Rigidity	1×10^{25} N m
Ice Sheet Volume at Maximum Extent ($\beta = 1$)	14×10^6 km^3
Variance	15.6 m

Tab. 5.1: Best fit earth model parameters using parabolic profile approximation to generate deglaciation chronology.

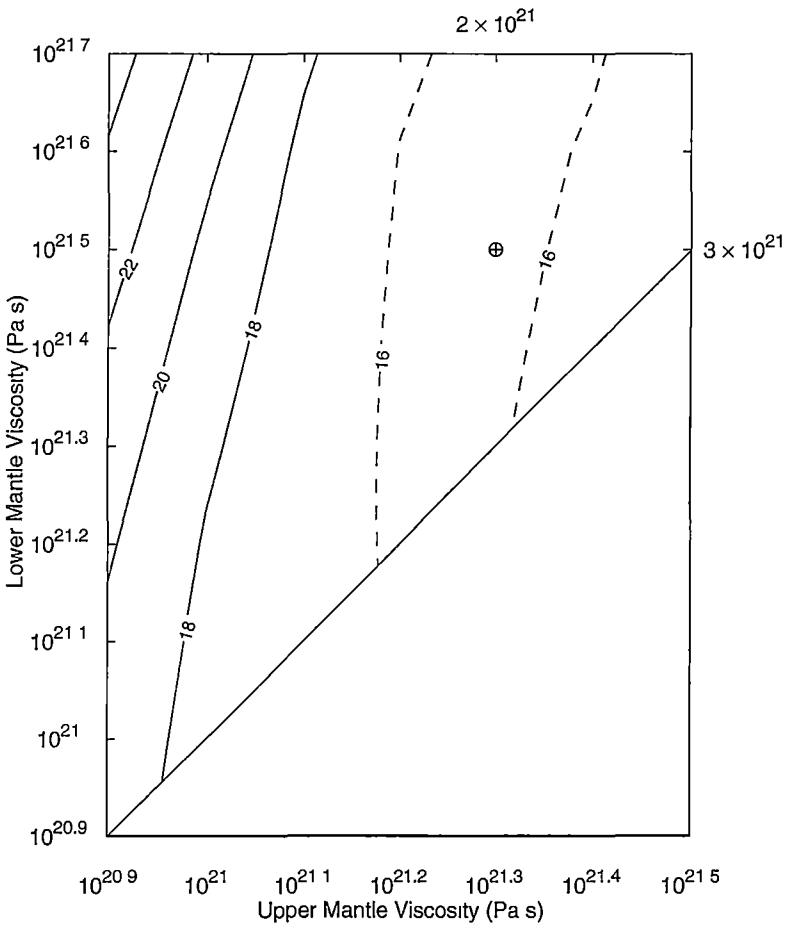

Fig. 5.10: Parameter space for 3 layer earth model with upper and lower mantle viscosities as searching parameters. The minimum in parameter space is shown by $\oplus$ with corresponding earth model parameter values shown in exponential notation at top and right hand side of axes. Note that from pressure arguments the viscosity of the lower mantle must be greater than the viscosity of the upper mantle and hence there are no contours to the right of the diagonal line of equal viscosities.

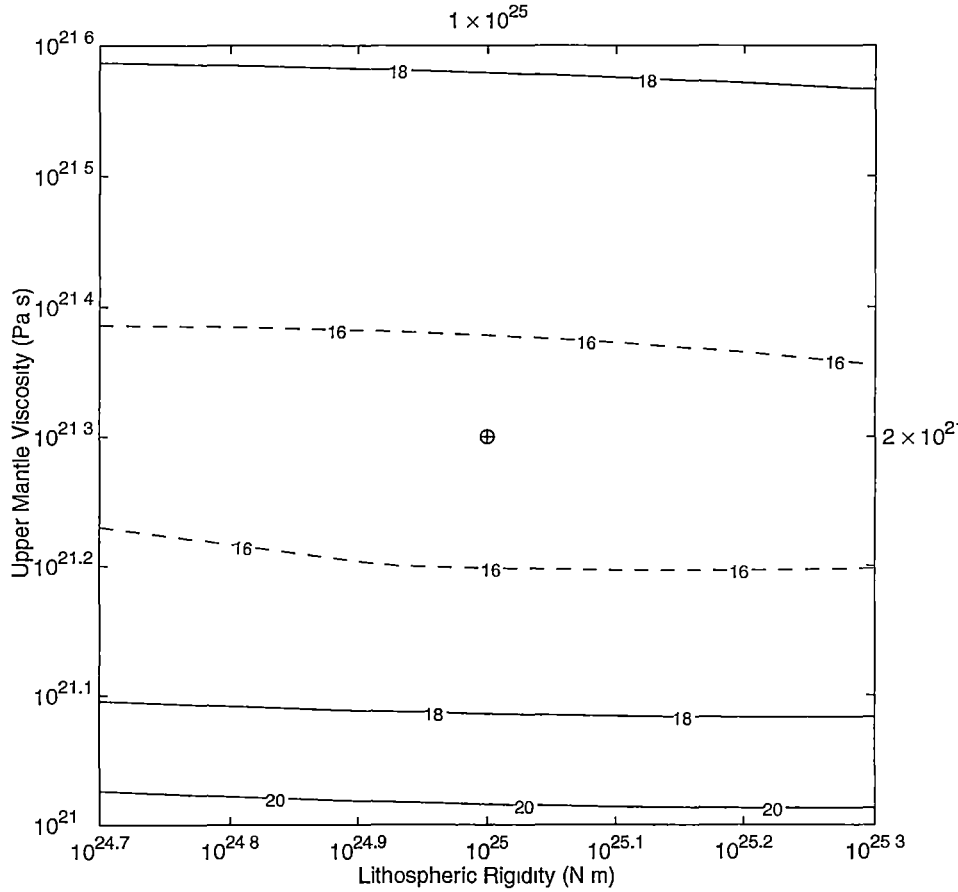

Fig. 5.11: Parameter space for 3 layer earth model with upper mantle viscosity and lithospheric rigidity as searching parameters. The minimum in parameter space is shown by ⊕ with corresponding earth model parameter values shown in exponential notation at top and right hand side of axes.

5.4 Effect of Parabolic Profile Ice Sheet Thickness Assumption on Relative Sea Level Prediction

Figure 5.12 compares the observed changes in relative sea level with the changes in relative sea level predicted by the isostatic model with the minimum variance parameters of Table 5.1. The correlation coefficient between prediction and observation is 0.87. The match is better for the large amplitude relative sea level heights than was found using the minimum variance technique referred to in Section 5.2. However Figure 5.12 shows that observed relative sea levels less than -100 m are underestimated by the model ($|RSL_{mod}| < |RSL_{obs}|$) with the worst match being for the -250 m amplitude at James Bay. Also most observed sea level data less than -50 m are underestimated. Between 0 and -50 m the majority of observed relative sea level data are overestimated (that is to say $|RSL_{mod}| > |RSL_{obs}|$). This pattern of under- and over-estimation is reinforced by the error histogram shown in Figure 5.13. Note the skewness whereby the largest errors are associated with underestimations.

The geographic distribution of errors is shown in Figure 5.14. The column heights are proportional to the time integrated errors for each site. The model prediction of relative sea level at each station is shown in Appendix A. The light shaded columns represent underestimation and dark shaded columns represent overestimation. The errors are dominated by the James Bay site in Hudson Bay. The figure shows that, in general, sites towards the centre of the former ice sheet (that is in Hudson Bay) are underestimated while sites closer to the ice edge (near Northern Canada and Eastern North America) are overestimated.

This distribution of under- and over-estimation does not result from the neglect of the sphericity of the earth. Wolf (1984) showed that flat earth models underestimate rather than overestimate sea levels at sites near the periphery of ice sheets.

The most likely reason for the geographic pattern of over and underestimation is the assumption of parabolic profile ice sheet *thickness*. For present day ice sheets such as Antarctica and Greenland it is the ice sheet elevation which approximates a parabolic profile. The calculations of Paterson (1971) used to

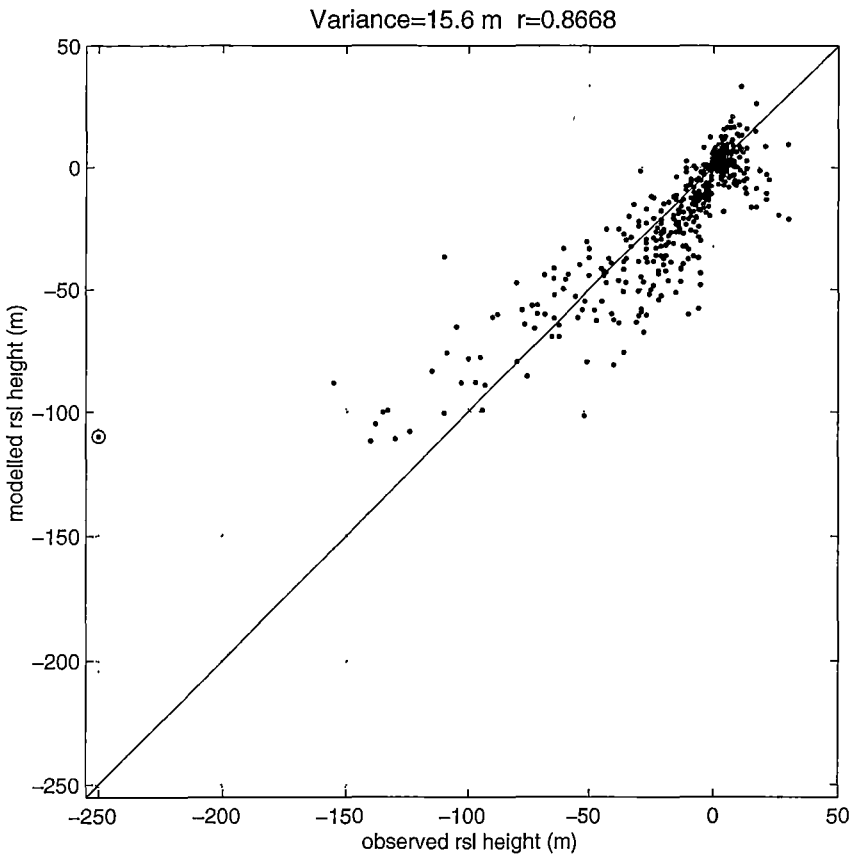

Fig. 5.12: Observed and predicted relative sea level heights for best fit earth model. Underestimation at James Bay for $RSL_{obs} = -250$ m is circled.

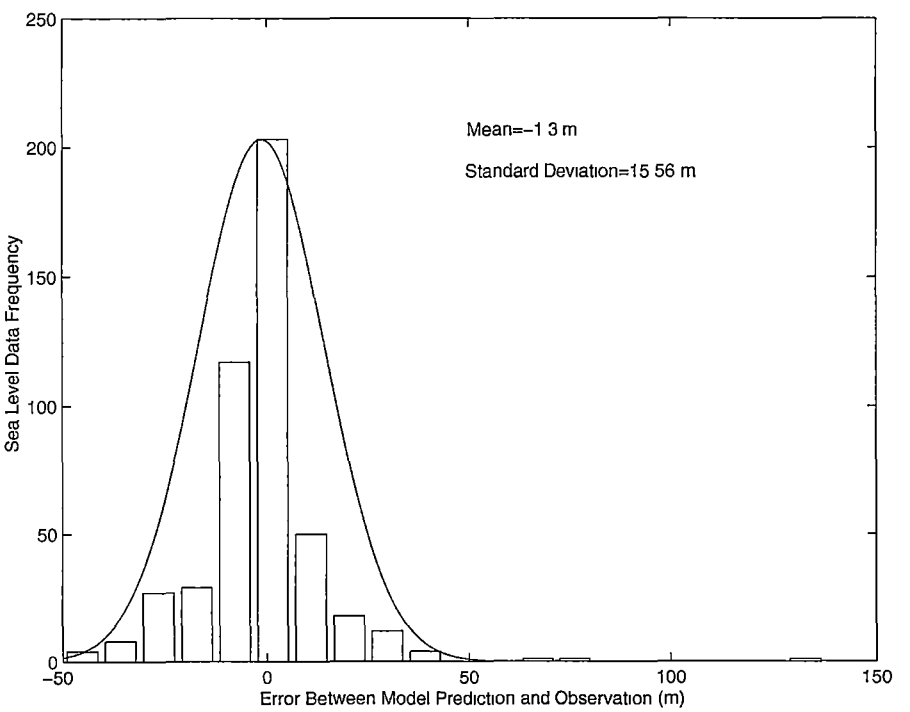

Fig. 5.13: Frequency distribution of misfit between modelled and observed relative sea level data. To the right of 0 corresponds to underestimation and to the left of 0 corresponds to overestimation.

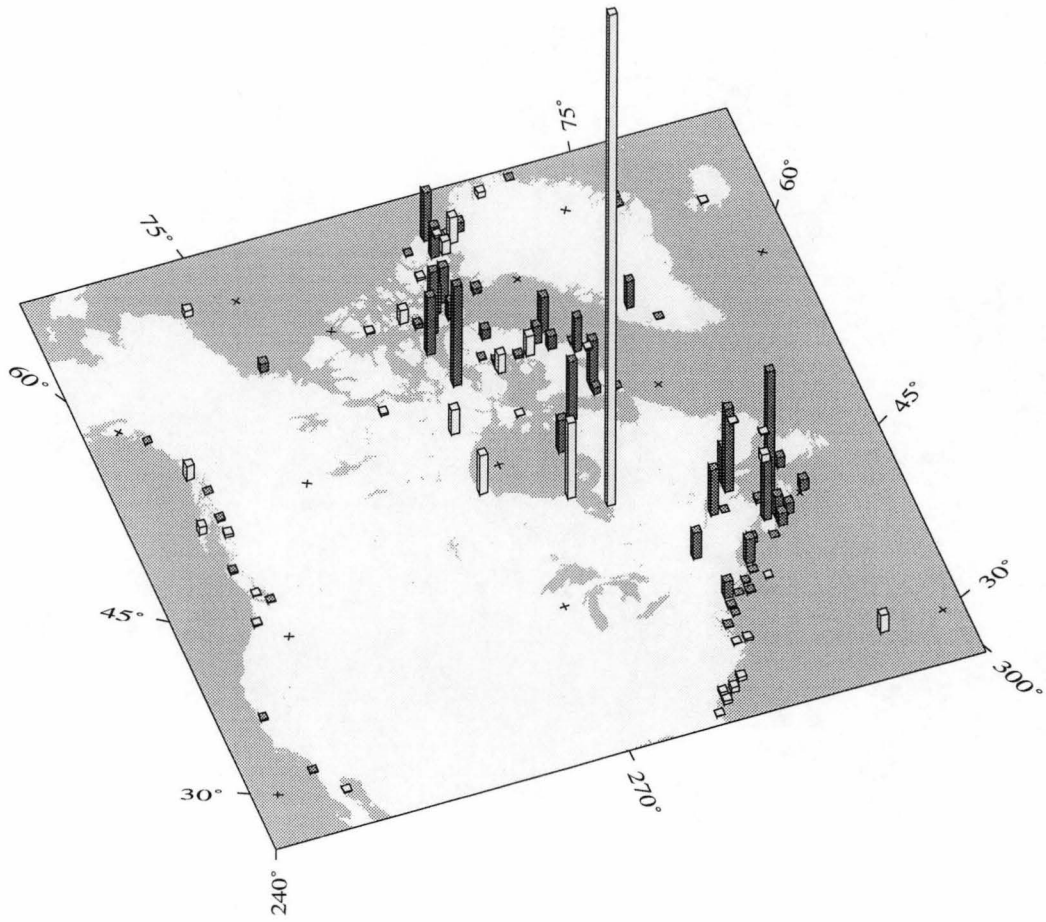

Fig. 5.14: Geographic distribution of error between observed and predicted sea level heights at individual sea level locations.

generate ice sheets with a parabolic profile assume a) that the ice sheet is resting on a flat bed, and b) that there is no isostatic adjustment. Clearly neither assumption is valid in the present study. In other words the geographical distribution of error shown in Figure 5.14 suggests that the misfit in the sea level data could be systematically the result of poor representation of the ice sheet deglaciation chronology when one makes the assumption of parabolic profile ice sheet thickness. In order to overcome this problem, it is necessary to use an ice sheet model where elevations and thicknesses are calculated explicitly. This is done in the following sections using the time-dependent ice sheet model (the Jenssen model) described in the previous chapter.

5.5 Ice Sheet Model Output as Isostatic Model Input

In the following sections the Jenssen ice sheet model is used to generate ice sheet thickness. The ice sheet thickness is used in much the same way as in the previous section. The time-dependent chronology of thickness generated using the time-dependent ice sheet model allows a parameter space search for upper and lower mantle viscosities, lithospheric rigidity and β to be conducted. In this case, β is a scaling factor for the thickness of the ice sheets generated by the time-dependent ice sheet model. The primary motivation for this exercise is to compare the results of the parameter space search for the earth model parameters. In this manner the sensitivity of the inference of earth model parameters to the assumed form of the ice sheet deglaciation chronology can be examined.

5.6 Ice Sheet Model Input Data

In order to use the ice sheet model the average annual accumulation rate and average annual temperature over the domain must be provided as input data at each yearly time step. The present day averages were obtained from the climatology atlas of Shea (1986) and are shown in Figures 5.15 and 5.16. This atlas is derived from 30 years of station data which were averaged and interpolated onto a global $2.5° \times 2.5°$ grid. The model calculates the average accumulations and temperatures at any time by making use of the lapse rate of temperature and accumulation with elevation as described in the previous chapter.

For this particular study the model ice extent is constrained to resemble ICE4G in a manner similar to the basal drag model of Fisher et al (1985). Using the accumulation distribution shown in Figure 5.15 the ice extent is imposed over the ice sheet model domain such that the thickness of any ice that develops outside the area defined by ICE4G is set to zero. The retreat of the ice from 21 kyr BP to the present day is modelled year by year by linearly interpolating the ice extents defined by ICE4G at each of its 1 kyr intervals. This technique is crude compared to letting the ice sheet model determine its own extent but it ensures that the ice extent matches that of ICE4G. It is assumed that the

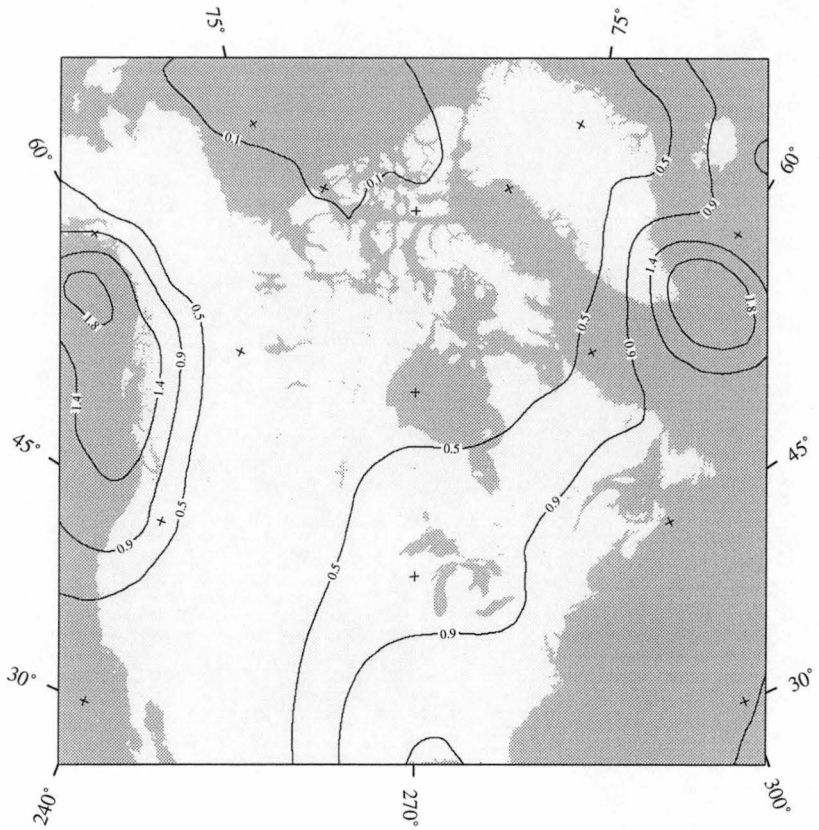

Fig. 5.15: Annual precipitation (m yr^{-1}) over North America (Shea, 1986).

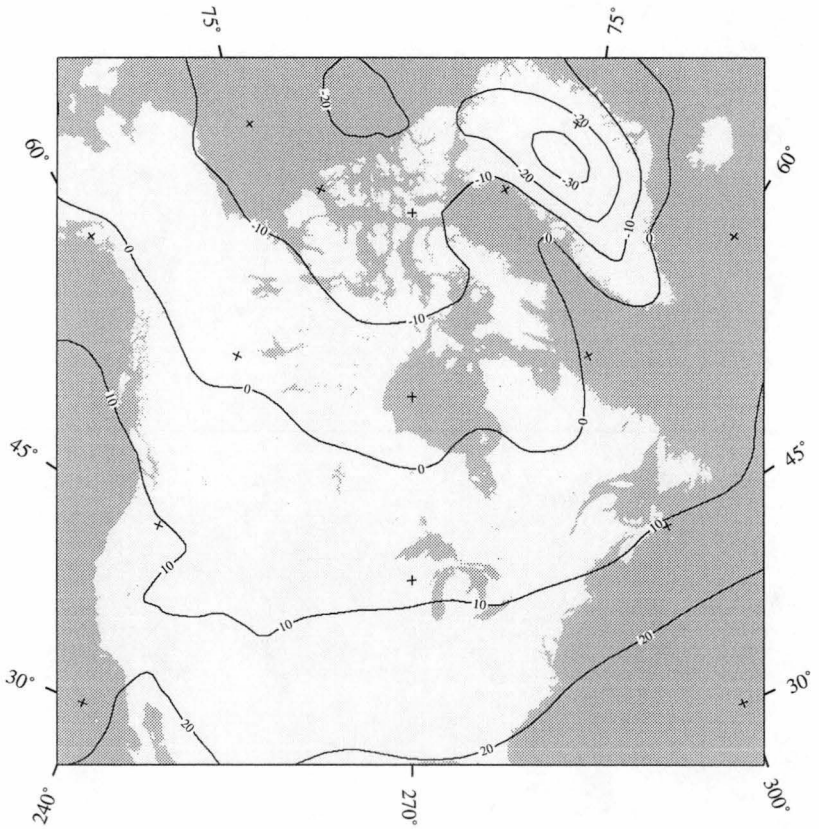

Fig. 5.16: Annual mean temperature (°C) over North America (Shea, 1986).

errors arising from this artificial constraint on ice sheet extent will be 'built into' the recovered value of β. Alternately it is also possible to use the ice sheet model to generate steady state reconstructions of ice sheet thickness for each of ICE4G's time series using the same procedure as for the equilibrium Antarctic situation in the previous chapter. However this procedure was not used in the present study. This is because a steady state reconstruction assumes isostatic equilibrium. Generated in this way, it is thought that the inference of the earth model parameters would be unduly biased by the isostatic equilibrium assumption.

A major modification to the time-dependent ice sheet model is the increase in the value of the coefficients relating shear stress to deformational velocities. The Laurentide ice sheet is considered to have been more temperate than the Antarctic ice sheet, so the coefficients were increased by a factor of 3 as suggested by Budd and Smith (1987).

5.7 *Results using Time-Dependent Ice Sheet Model*

As an initial exercise the time-dependent ice sheet model was coupled to the isostatic model with a uniform mantle viscosity of 10^{21} Pa s and a lithospheric rigidity of 10^{25} N m (standard earth model). Time-dependent reconstructions of ice sheet thickness were generated. The iterative technique to constrain the model to produce the observed continental surface topography at present day (outlined in Section 5.1.4) was also used in the time-dependent reconstruction of ice sheet thickness. The profile of the generated ice sheet thickness at 21 kyr BP is shown in Figure 5.17. It is important to note that because there is no surface ablation (melt) in this model the generated ice sheet thicknesses are overestimated. The total volume of the ice sheet shown in Figure 5.17 is 35×10^6 km^3. The deglaciation of this volume would yield a sea level rise of 95 m.

The time-dependent thicknesses (of which Figure 5.17 is an example) were then used as the ice sheet deglaciation chronology in order to conduct a parameter space search. Figure 5.18 shows the results for a search of uniform mantle viscosity and lithospheric rigidity. The minimum variance occurs for a

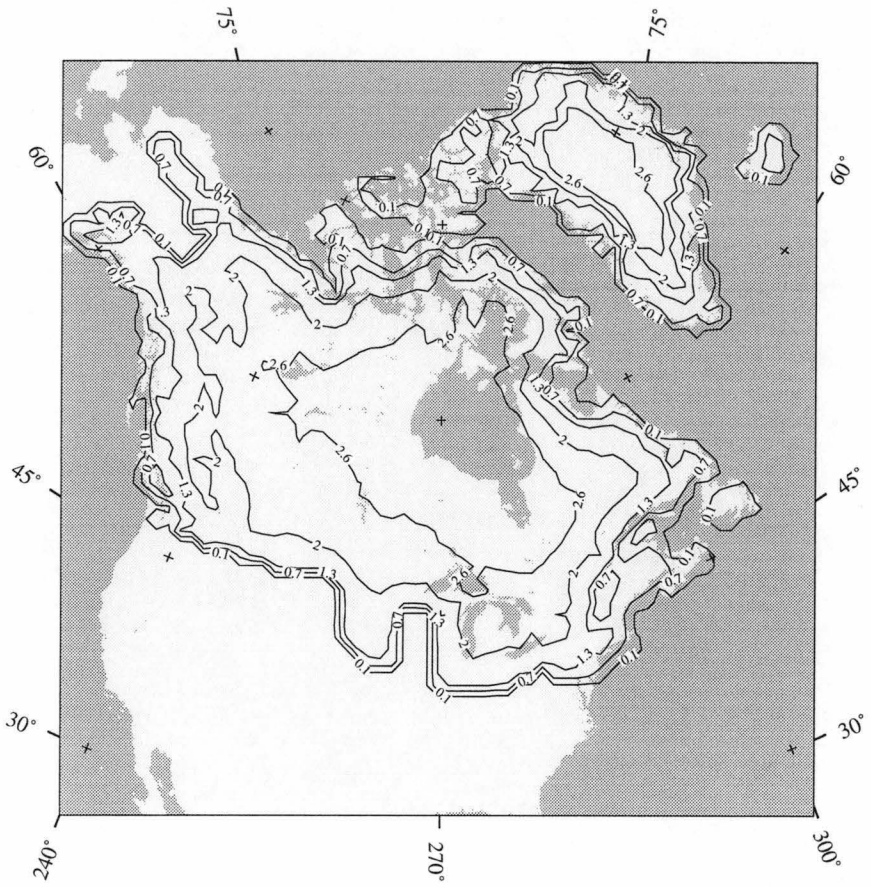

Fig. 5.17: Ice sheet thickness (km) at 21 kyr BP generated as a first approximation using the time-dependent ice sheet model and ICE4G chronology of ice extent

uniform mantle viscosity of 1.5×10^{21} Pa s and a lithospheric rigidity 1.5×10^{25} N m. These are the same values deduced when using the parabolic profile ice sheet shown in Figure 5.9. However the minimum occurs for $\beta = 0.4$ which corresponds to an ice sheet volume at maximum extent of 14×10^6 km^3. For a parabolic profile ice sheet model the value of $\beta = 0.4$ is entirely legitimate, as the ice sheet still has a parabolic profile. However for the time-dependent ice sheet model a value of β which is not unity corresponds to an unrealistic ice sheet. This is because the velocities of the ice sheet are dependent on the thicknesses through the continuity equation. Therefore the ice sheet chronology generated using the time-dependent ice sheet model must recover a value of $\beta = 1$ from the parameter space search to be glaciologically realistic. The fact that β is not equal to 1.0 is understandable since there is effectively no ablation

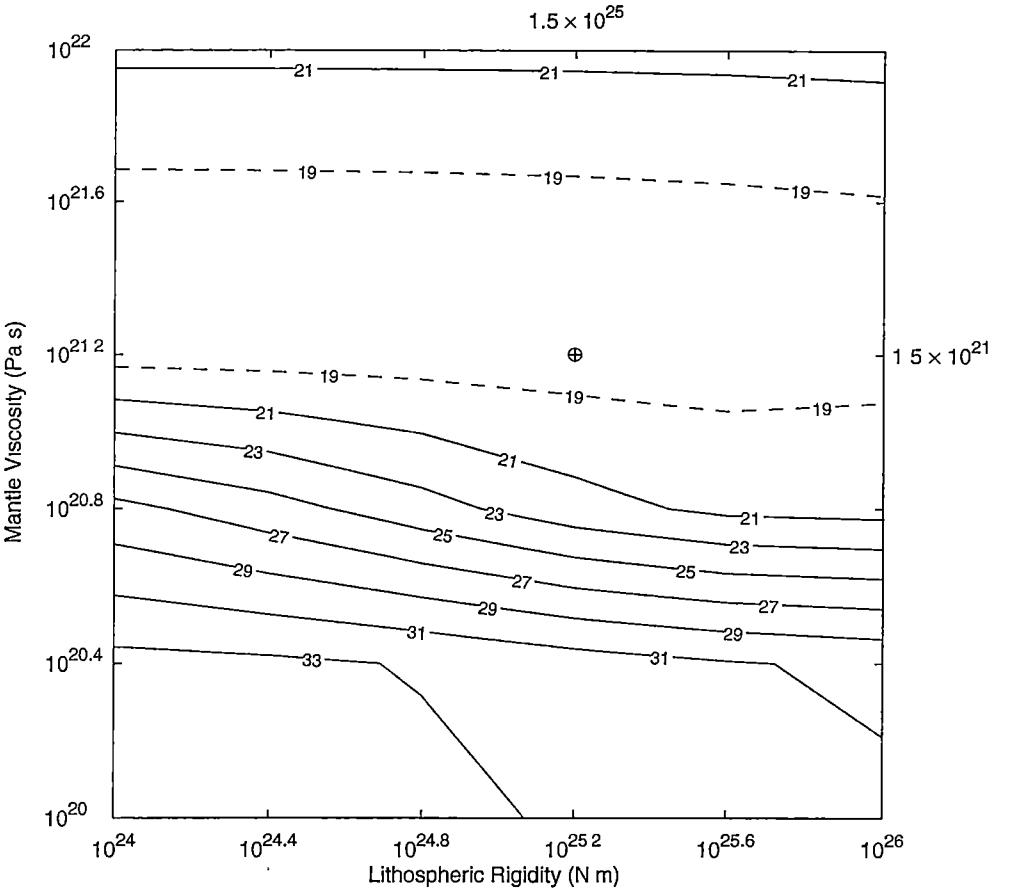

Fig. 5.18: Parameter space for an earth model with uniform mantle viscosity and lithospheric rigidity as searching parameters. The minimum in parameter space is shown by ⊕ with corresponding earth model parameter values shown in exponential notation at top and right hand side of axes.

in the ice sheet model, which in reality drives the retreat of the ice sheet. Budd and Smith (1987) conclude that ablation is the most important control on the growth and retreat of the Laurentide ice sheet.

For this reason the method chosen to constrain the ice sheet model to produce a chronology of thicknesses so that $\beta = 1$ is by adjusting the net accumulation rate (see Figure 5.15) over the ice sheet. This method allows the modelling of *net* accumulation (that is accumulation minus ablation) to be included in the ice sheet reconstruction.

The value of β indicates the rescaling magnitude for the input accumulation rate (accumulation rate $\propto \beta^8$). As a first approximation the accumulation is

adjusted to produce an ice sheet with a volume of 14×10^6 km^3 at maximum extent. This is the ice volume corresponding to $\beta = 0.4$ for the deglaciation chronology generated without accumulation rescaling. The parameter space search is then repeated with a new deglaciation chronology generated with this rescaled input accumulation. The iteration between β and accumulation is repeated until $\beta = 1$. By this means the parameter space search not only returns a value compatible with a realistic ice sheet, but also ensures that the deglaciation chronology is determined to the same precision as that determined for the parabolic profile ice sheet chronology. The results for the parameter space search (viscosity versus rigidity) with the accumulation rescaled so that $\beta = 1$ is shown in Figure 5.19.

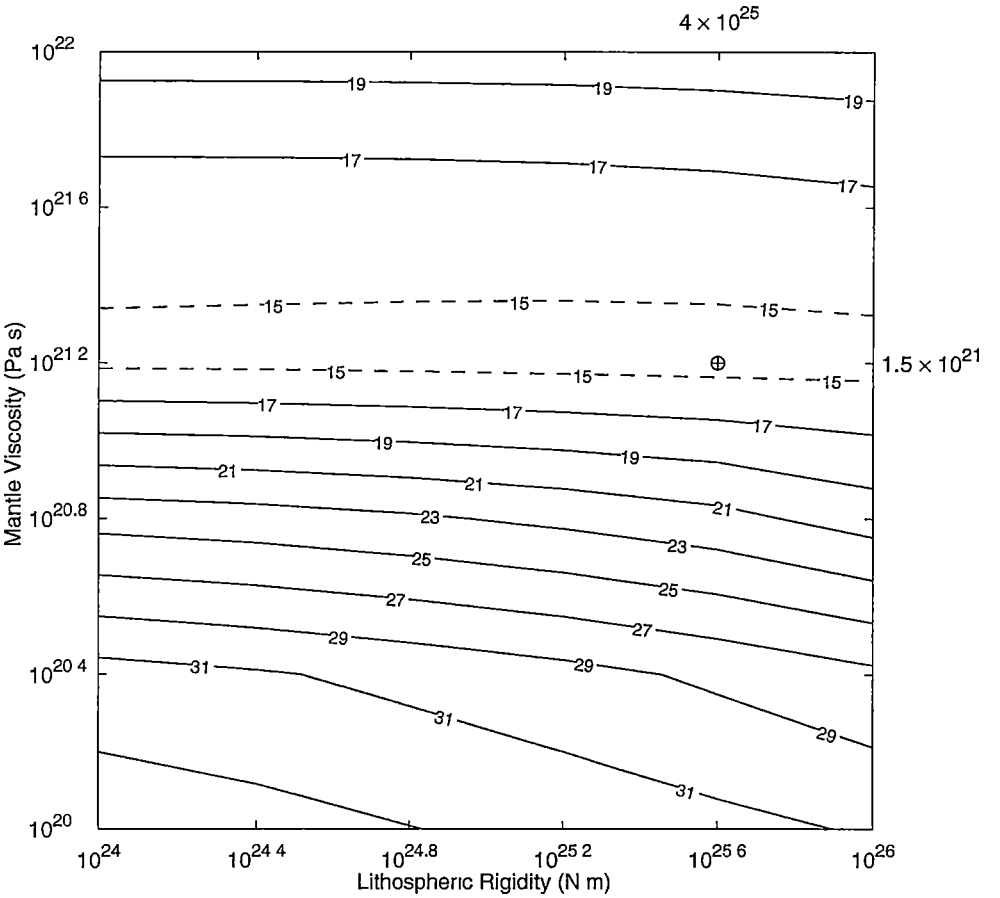

Fig. 5.19: Parameter space for an earth model with uniform mantle viscosity and lithospheric rigidity as searching parameters. The minimum in parameter space is shown by ⊕ with corresponding earth model parameter values shown in exponential notation at top and right hand side of axes.

The deglaciation chronology generated when using the accumulation rescaling described above produces a better fit to the relative sea level data than the unscaled deglaciation chronology. Figure 5.19 shows a minimum variance of less than 15 m compared to the 18 m of Figure 5.18. However the best fit lithospheric rigidity is shifted to 4×10^{25} N m. This best fit corresponds to an ice sheet thickness at maximum extent of 13×10^6 km^3. The higher value for the lithospheric rigidity suggests a level of parameter trading between ice sheet thickness and lithospheric rigidity.

The above procedure was repeated at higher resolution (steps of 0.1 in units of log to the base 10 in viscosity and rigidity). Figure 5.20 shows the results of the parameter space search for the lower and upper mantle viscosity. Figure 5.21 shows the results of the parameter space search for upper mantle viscosity and lithospheric rigidity. In all high resolution parameter space searches the accumulation was rescaled to produce a value for $\beta = 1$ for the minimum variance.

The best fit earth model parameter values vary slightly from those deduced from the low resolution parameter space search. They are in fact the same as those deduced from the deglaciation chronology using the parabolic profile assumption, although the value of the variance is smaller. They are summarised in Table 5.2.

Model Parameter	Best Fit Value
Lower Mantle Viscosity	3×10^{21} Pa s
Upper Mantle Viscosity	2×10^{21} Pa s
Lithospheric Rigidity	1×10^{25} N m
Ice Sheet Volume at Maximum Extent ($\beta = 1$)	13×10^6 km^3
Variance	13.6 m

Tab. 5.2: Best fit earth model parameters using time-dependent ice sheet model to generate deglaciation chronology.

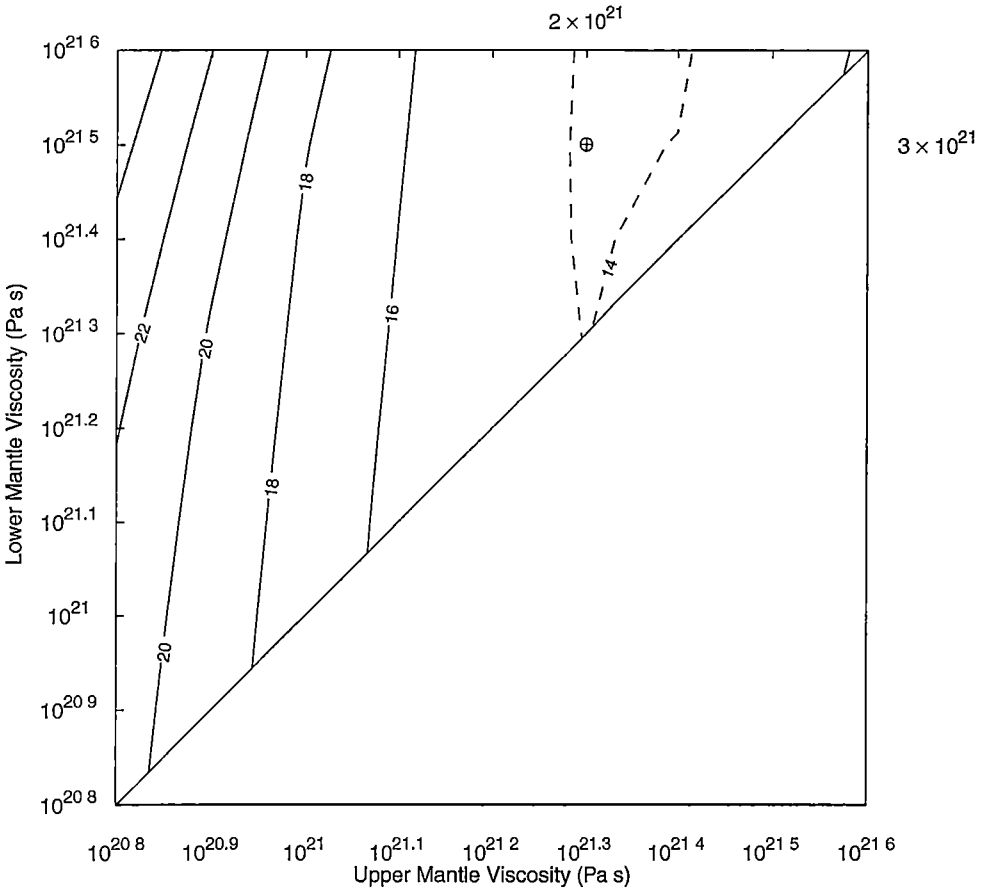

Fig. 5.20: Parameter space for 3 layer earth model with upper and lower mantle viscosity as searching parameters. The minimum in parameter space is shown by $\oplus$ with corresponding earth model parameter values shown in exponential notation at top and right hand side of axes. Note that from pressure arguments the viscosity of the lower mantle must be greater than the viscosity of the upper mantle and hence there are no contours to the right of the diagonal line of equal viscosities.

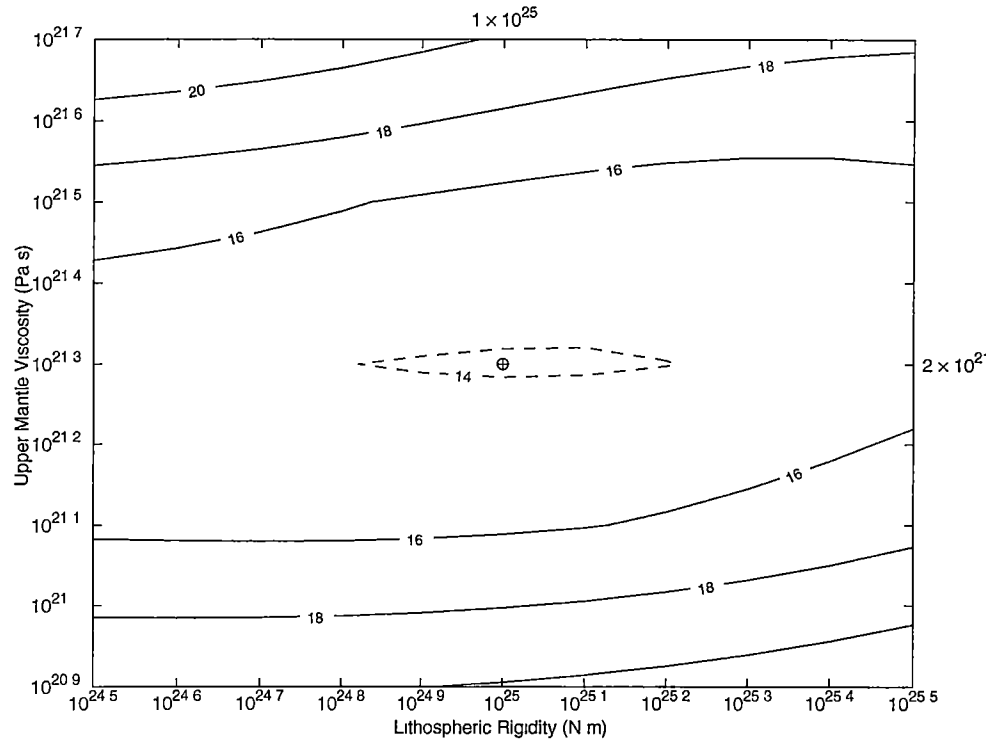

Fig. 5.21: Parameter space for 3 layer earth model with upper mantle viscosity and lithospheric rigidity as searching parameters. The minimum in parameter space is shown by $\oplus$ with corresponding earth model parameter values shown in exponential notation at top and right hand side of axes.

As a final iteration these values for the earth model parameters were used in the time-dependent ice sheet model to regenerate the ice sheet thickness chronology and then again conduct a parameter space search for the upper mantle viscosity and β. This procedure introduces a degree of circularity between the deduction of earth model parameters and ice sheet deglaciation chronology, but is used here only for consistency, as otherwise the deglaciation chronology that infers these parameters has been generated by using different values for the parameters. Ideally each choice of earth model parameters should be considered with a deglaciation chronology generated using the values of the earth model parameters under consideration. However this procedure is not feasible from computational considerations. The results from this iteration are presented in Figure 5.22 (the lower mantle viscosity and lithospheric rigidity are held constant at 3×10^{21} Pa s and 10^{25} N m respectively). The minimum variance is 13.6 m for $\beta = 1.0$ and an upper mantle viscosity of 2×10^{21} Pa s. The 'bulls eye' contouring pattern of Figure 5.22 suggests that at this parameter resolution the importance of β and the upper mantle viscosity is approximately equal.

Figure 5.23 shows the observed and predicted relative sea level amplitudes using the Table 5.2 parameter values. The balance between under- and overestimation is more even for this deglaciation chronology than for the parabolic profile deglaciation chronology. This is also demonstrated in Figure 5.24 where the histogram of error between prediction and observation is more balanced than for the parabolic profile ice sheet model shown in Figure 5.13.

Figure 5.25 shows the geographic distribution of error between model prediction and observation at the individual sea level sites (c.f. Figure 5.14 for the parabolic profile ice sheet calculations). Although the James Bay site is still underestimated, the magnitude of underestimation is reduced and other sites in Hudson Bay are overestimated by a small amount. Sites in Northern Canada are also generally underestimated whereas using the parabolic profile ice sheet deglaciation chronology they were predominantly overestimated. Overestimation in Eastern Canada occurs for both models.

In general Figure 5.25 shows a more random pattern of under- and overestimation than Figure 5.14 which suggests that there is less of a systematic

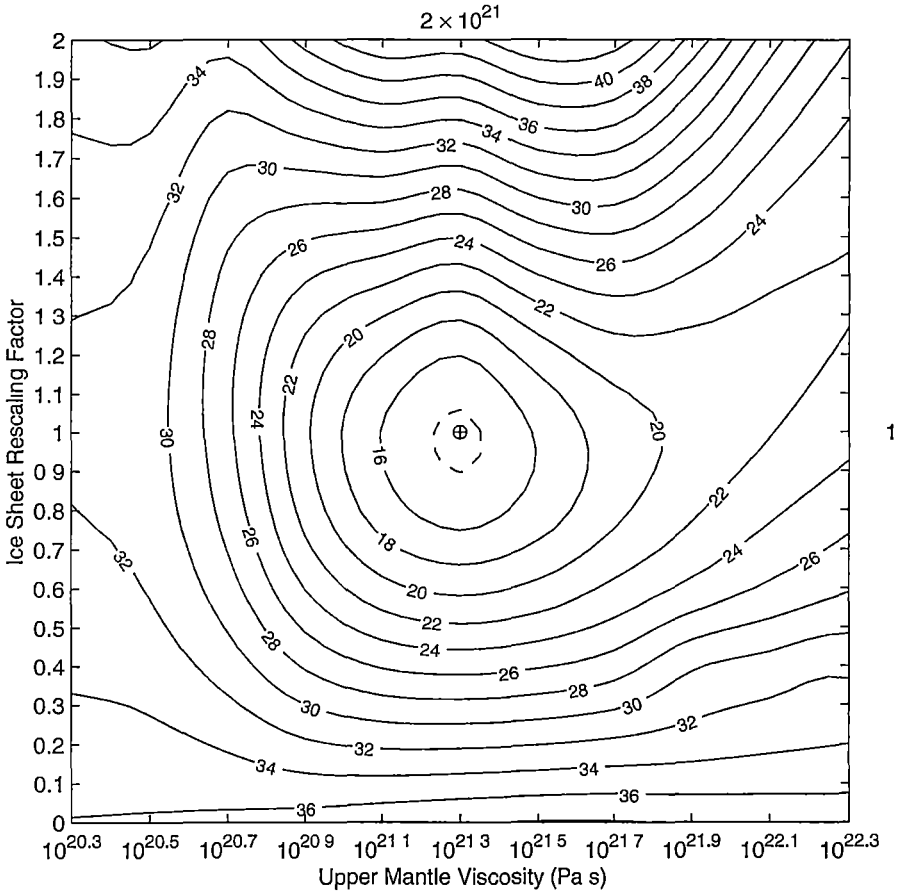

Fig. 5.22: Parameter space for 3 layer earth model with upper mantle viscosity and β searching parameters. The minimum in parameter space is shown by $\oplus$ with corresponding earth model parameter value shown in exponential notation at top of axes.

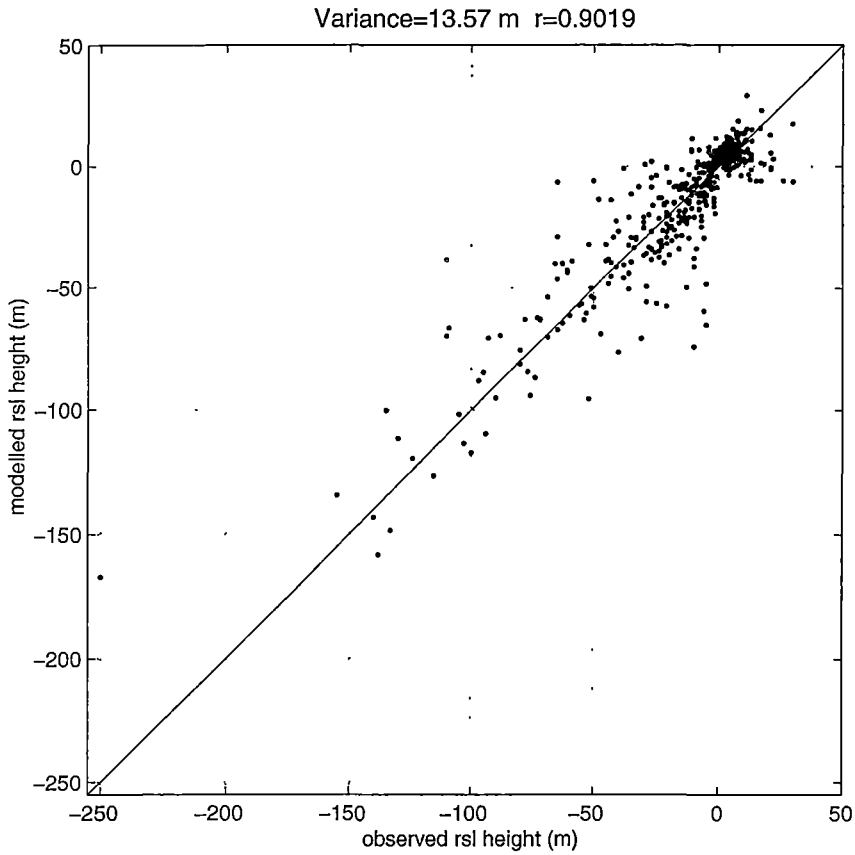

Fig. 5.23: Observed and predicted relative sea level heights for best fit earth model.

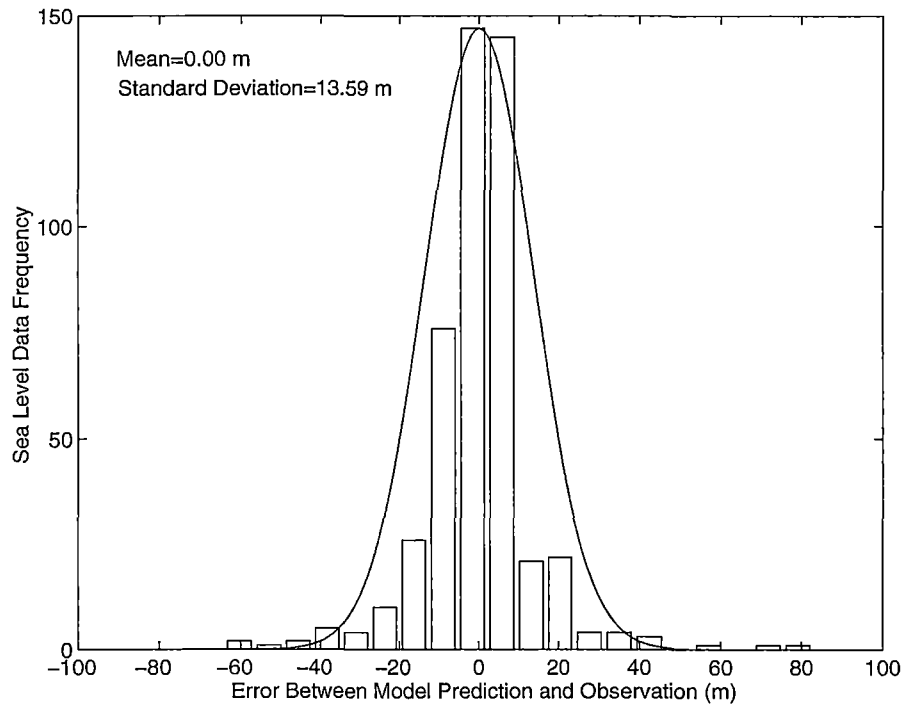

Fig. 5.24: Frequency distribution of misfit between modelled and observed relative sea level data. To the right of 0 corresponds to underestimation and to the left of 0 corresponds to overestimation.

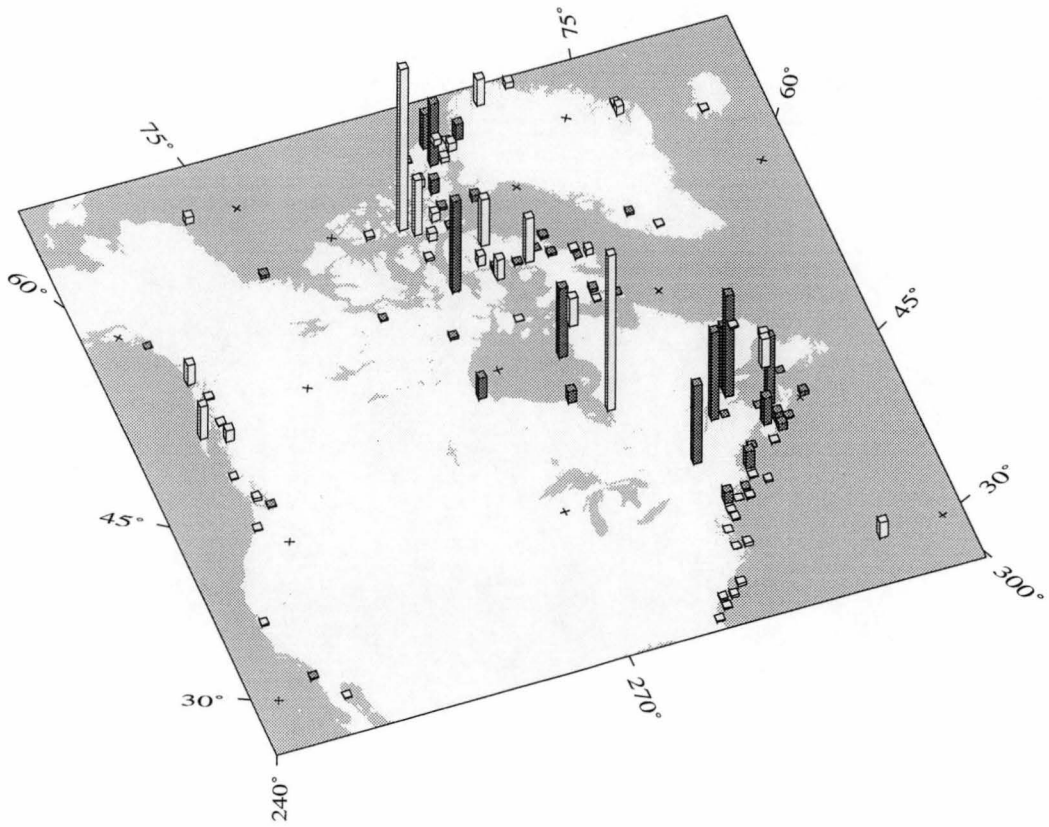

Fig. 5.25: Geographic distribution of error between observed and predicted sea level heights at individual sea level locations.

bias in the prediction of the relative sea level data using the time-dependent ice sheet model than the parabolic profile ice sheet model.

5.8 *Eustatic Sea Level Contributions of Deglaciation Chronologies*

Figure 5.26 shows the time-dependent change in ice sheet volume for the 'best fit' parabolic profile deglaciation chronology (that is to say the parabolic profile chronology rescaled to produce the lowest variance) and the time-dependent change in ice sheet volume for the 'best fit' Jenssen ice sheet model deglaciation chronology. The volumes have been converted to represent a first-order eustatic sea level contribution. The curves are reasonably similar. The accumulation rescaling used in the time-dependent ice sheet model implies an ablation rate over the region which is 90% of the accumulation.

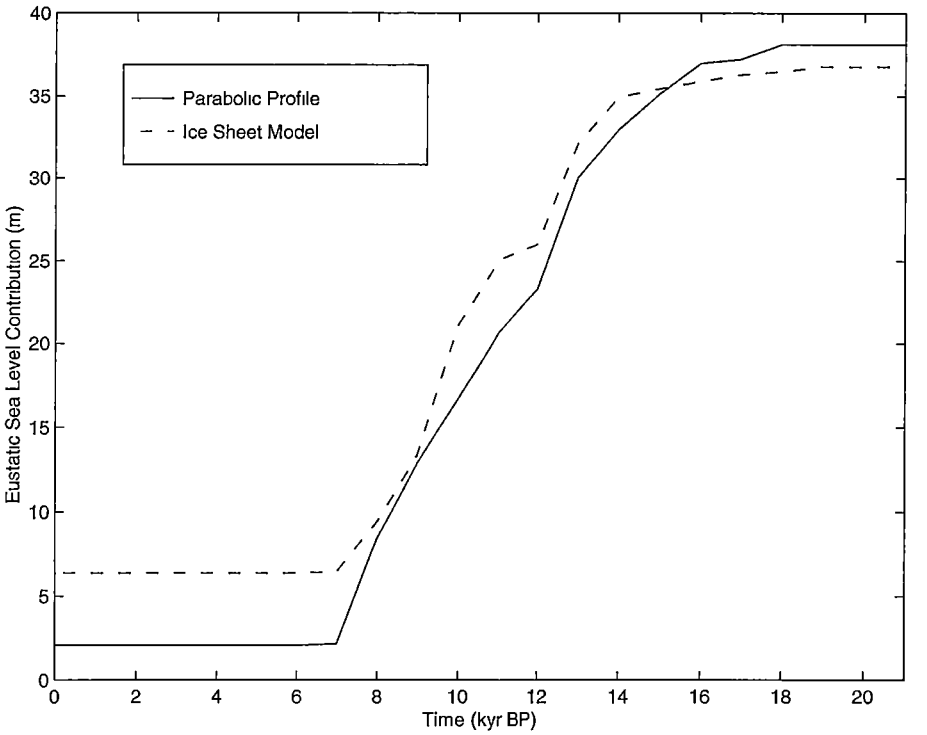

Fig. 5.26: Equivalent eustatic sea level contribution of both ice sheet deglaciation chronologies as a function of time.

5.9 Present Day Isostatic Adjustment

In this section a study is made of the influence of assumptions about the ice sheet reconstruction on the prediction of present day rate of isostatic adjustment and present day sea level change. Figure 5.27 shows the model-predicted present day adjustment rate calculated using the parabolic profile ice sheet model and Figure 5.28 shows the model predicted present day adjustment rate calculated using the time-dependent ice sheet model. Although the broad scale features of present day uplift velocity are similar for both models there are differences in detail.

The tide gauge data that record the present day changes in sea level are from the Permanent Service for Mean Sea Level, which collects monthly and annual mean values of sea level from approximately 1600 stations (Spencer & Woodworth, 1993). The method of selection of records from this data set for the present study follows Peltier (1996a) in that only sites along the east coast of North America (where tectonic activity is minor) are used. Of these only

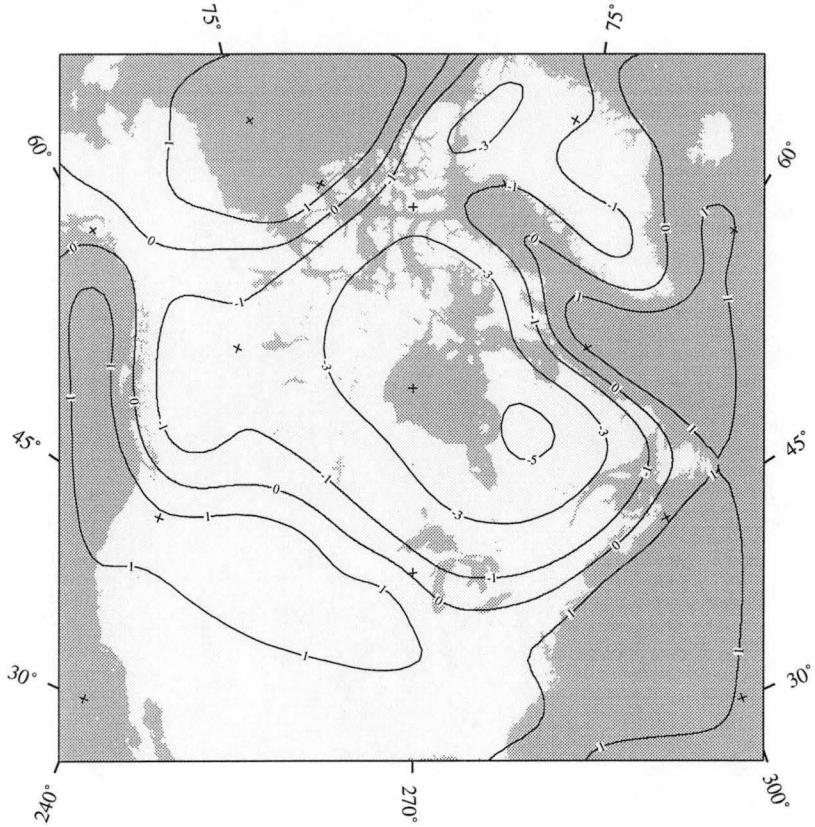

Fig. 5.27: Present day uplift rate (mm yr^{-1}) calculated using parabolic profile ice sheet model.

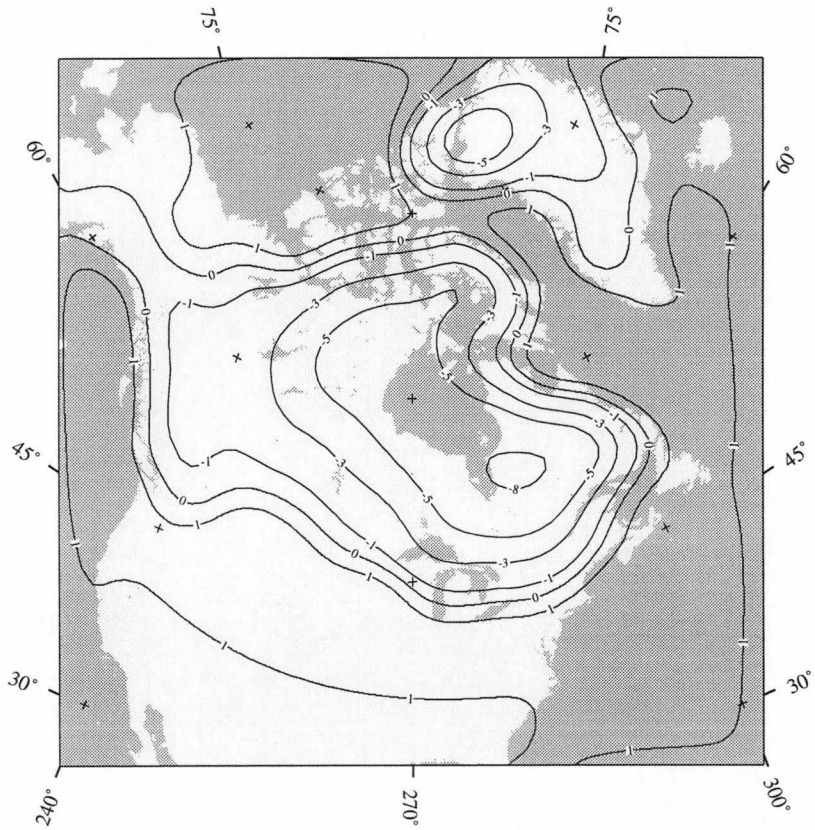

Fig. 5.28: Present day uplift rate (mm yr^{-1}) calculated using time-dependent ice sheet model.

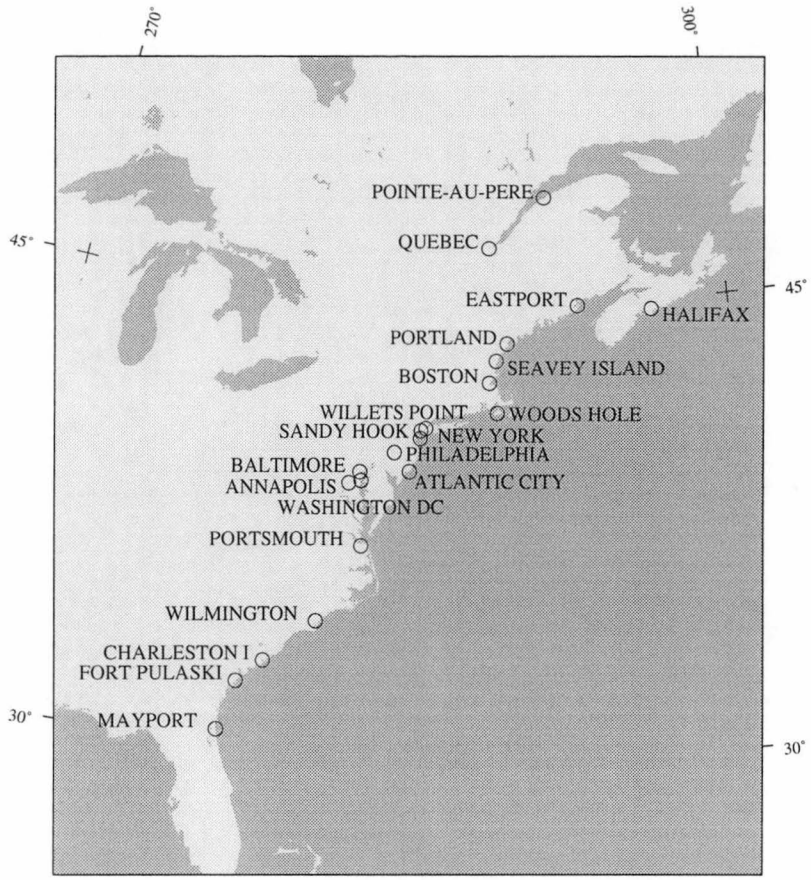

Fig. 5.29: Location of present day tide gauge stations.

records of duration longer than 50 years are used. The 50 year duration criterion minimises the effect of inter-decadal oceanographic variability. The locations of the sea level stations considered in the present study are shown in Figure 5.29. The present day observed sea level rises and the predicted present day isostatic adjustment rate at these stations is shown in Figure 5.30.

As a first-order estimate of sea level change attributable to changing ocean volume, the predicted adjustment rate of both models is subtracted from the actual sea level change shown at each station. Figure 5.30 suggests a present change change in sea level due to changes in ocean volume of 1.95 ± 0.61 mm yr^{-1} for the parabolic profile ice sheet model and 1.52 ± 0.65 mm yr^{-1} for the time-dependent ice sheet model. The prediction of present day sea level change is 0.5 mm yr^{-1} higher for the parabolic profile ice sheet model than the time-dependent ice sheet model.

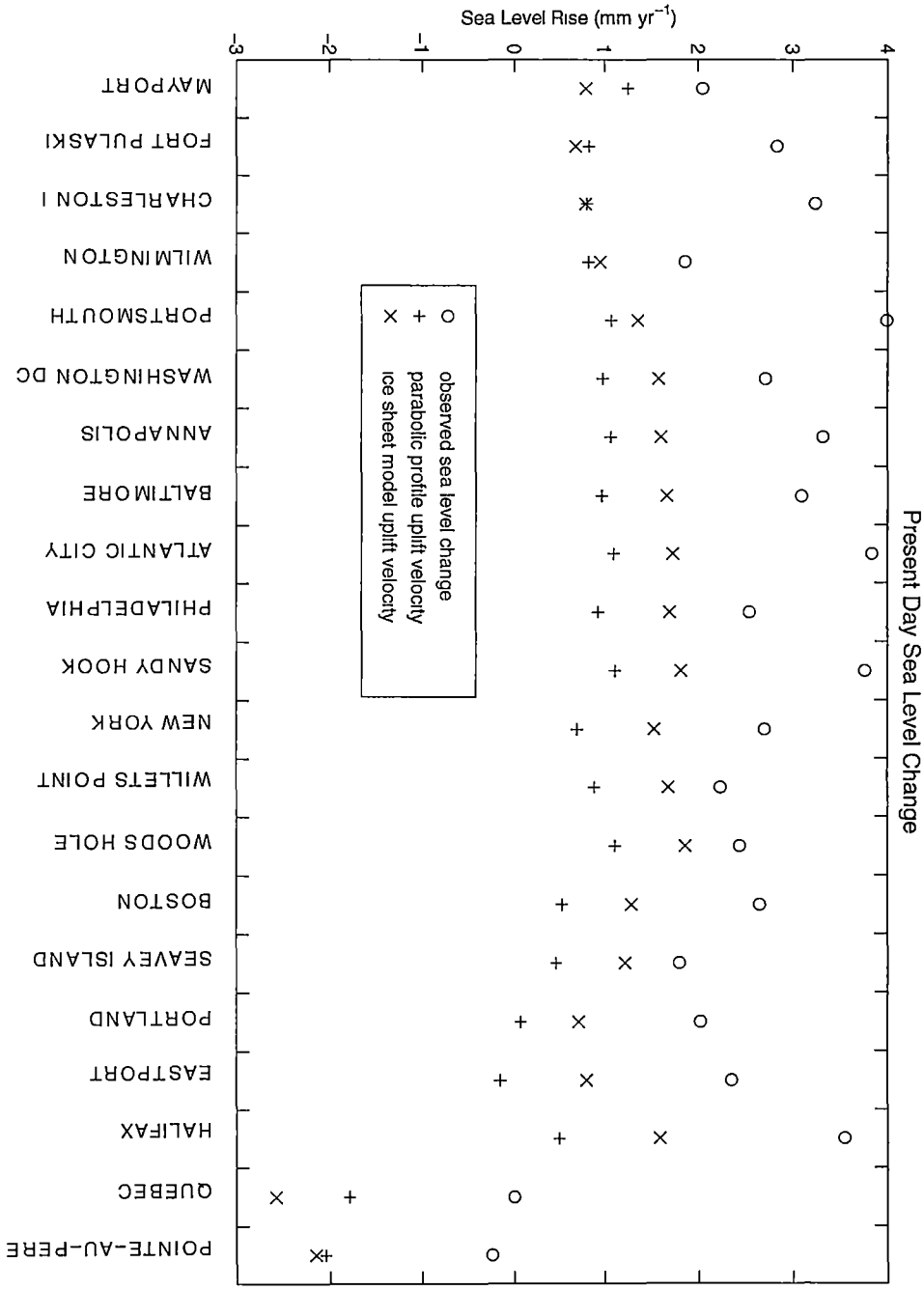

Fig. 5.30: Observed sea level change and model predicted adjustment velocity for ice sheet model generated deglaciation chronology (r=0.8382) and parabolic profile ice sheet chronology (r=0.8276).

This study is simplistic in its calculation of corrected present day sea level change and it is likely that a method that accounts for the spatial density of tide gauge stations such as that of Nakiboglu and Lambeck (1991) is more appropriate given the natural variability in the observed present day data (see Figure 5.30). However the point remains that the predicted uplift velocities are sufficiently different using the two different ice sheet chronologies to show that calculation of present day sea level change is sensitive to the form of the assumed ice sheet.

5.10 Conclusions

Despite the differences in ice sheet deglaciation chronologies the earth model parameters and eustatic sea level contribution of the ice sheets derived using the two models are similar. It is not clear if these parameters are suitable for use in other regions. Also the robustness of the technique using the time-dependent ice sheet model to generate a deglaciation chronology for the isostatic models has not been examined. Therefore the next chapter repeats the process for the Fennoscandian ice sheet. The purpose is primarily to examine the extent to which the results of the present chapter can be generalised.

6. THE FENNOSCANDIAN ICE SHEET

The previous chapter examined the retreat of the Laurentide ice sheet to determine the earth model parameters that most realistically simulate the observed isostatic adjustment in the region. This chapter repeats the process for the Fennoscandian ice sheet.

Figure 6.1 shows the model domain and relative sea level data locations. Again data of age older than 7 kyr BP are excluded from the calculation. Also

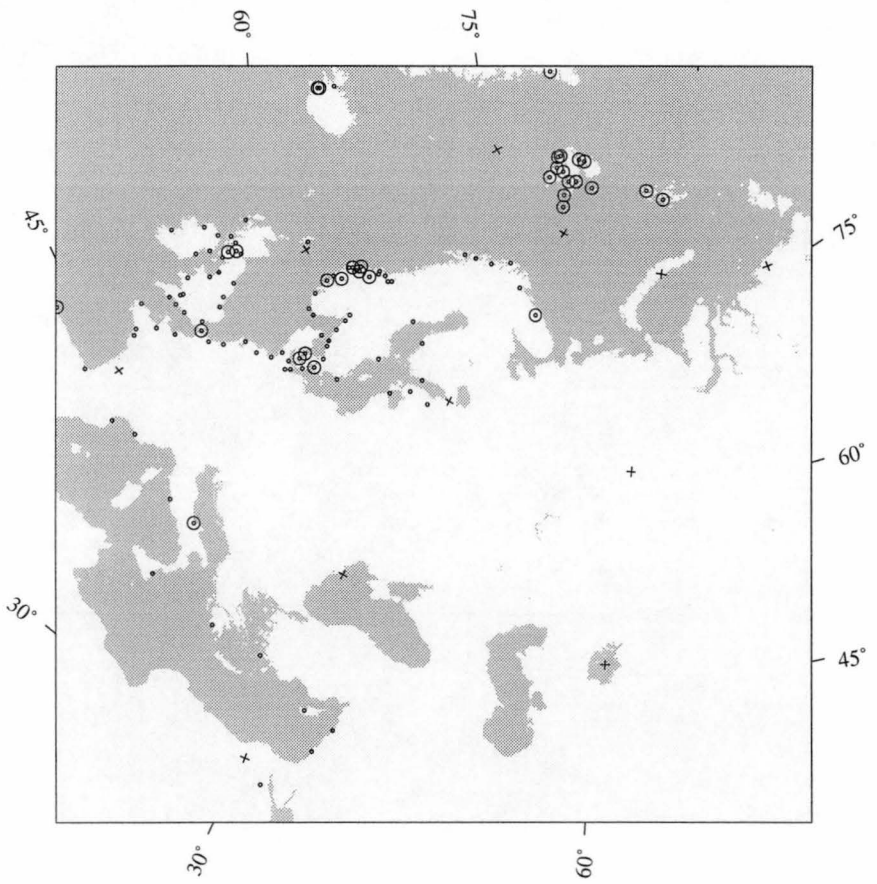

Fig. 6.1: Model domain and relative sea level data locations for the Fennoscandian ice sheet. Large circles indicate sites where data have been wholly excluded.

data from the Svalbard Archipelago is excluded because of its proximity to the edge of the model domain.

According to Mitrovica et al (1994) the isostatic adjustment of the Laurentide ice sheet plays an appreciable role in the adjustment in Northern Europe as the ice sheets are only 45° of longitude distant from each other. In the present work the effect of the Laurentide adjustment on the Fennoscandian ice sheet is not considered.

6.1 Parabolic Profile Ice Sheet Model

Figure 6.2 shows the Fennoscandian ice sheet at its maximum extent calculated assuming a parabolic profile of thickness and using the ice extent data of ICE4G. A full coverage of the Barents Sea is assumed. This is controversial (Siegert & Dowdeswell, 1995) as Kaufmann and Wolf (1996) suggest only partial coverage. Figure 6.3 shows the results of a high resolution parameter space search using the calculated chronology of thickness with lithospheric rigidity fixed at 10^{25} N m. The lower and upper mantle viscosities are the searching parameters. The minimum variance occurs for higher mantle viscosities than for the Laurentide ice sheet. These higher viscosities are 4×10^{21} Pa s for the upper mantle and 6×10^{21} Pa s for the lower mantle.

Figure 6.4 shows the results of a search with the lower mantle viscosity held at 6×10^{21} Pa s and the upper mantle viscosity and lithospheric rigidity considered unknown. The agreement with the relative sea level data is marginally improved by a reduction of the lithospheric rigidity to 5×10^{24} N m.

The values of the earth model parameters that most realistically reproduce the relative sea level data where $\beta = 1$ are outlined in Table 6.1.

These 'best fit' earth model parameters differ from those determined for the Laurentide adjustment. The viscosities are larger, and the rigidity of the lithosphere is smaller. In a discussion of the isostatic adjustment of the British Isles Lambeck et al (1996) suggest that a larger value of mantle viscosity can be accommodated by using a larger value of lithospheric rigidity. The increase in mantle viscosity determined here is associated with a *reduced* value of lithospheric rigidity.

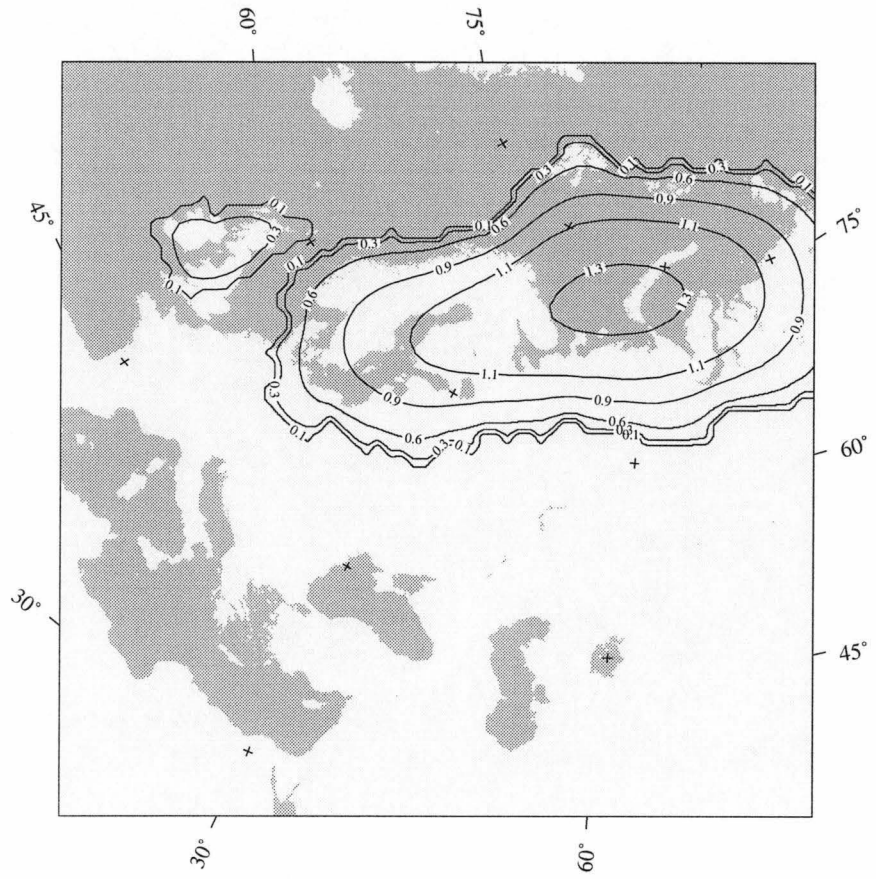

Fig. 6.2: Parabolic profile ice sheet reconstruction at maximum extent (21 kyr BP) derived from ICE4G.

Model Parameter	Best Fit Value
Lower Mantle Viscosity	6×10^{21} Pa s
Upper Mantle Viscosity	4×10^{21} Pa s
Lithospheric Rigidity	5×10^{24} N m
Ice Sheet Volume at Maximum Extent ($\beta = 1$)	7×10^{6} km^3
Variance	9.6 m

Tab. 6.1: Best fit earth model parameters using parabolic profile approximation to generate deglaciation chronology.

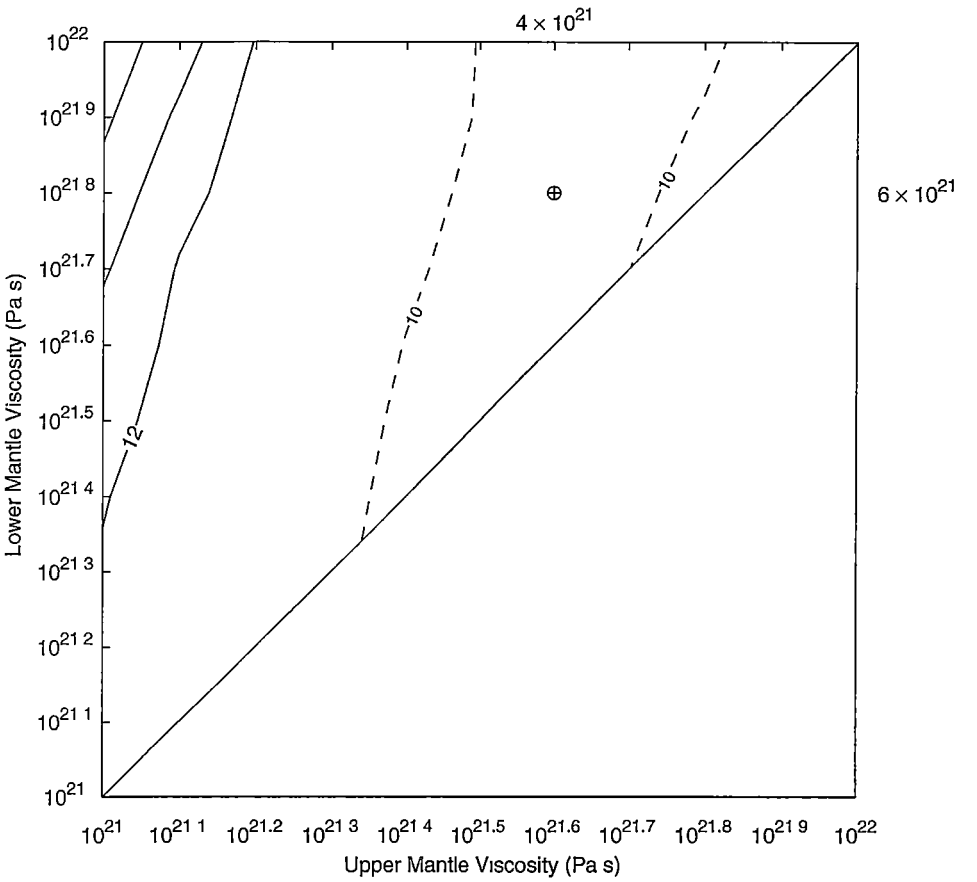

Fig. 6.3: Least Squares Variance solution space for 3 layer earth model with upper mantle and lower mantle viscosities as searching parameters. The minimum in parameter space is shown by $\oplus$ with corresponding earth model parameter values shown in exponential notation at top and right hand side of axes. Note that from pressure arguments the viscosity of the lower mantle must be greater than the viscosity of the upper mantle and hence there are no contours to the right of the diagonal line of equal viscosities.

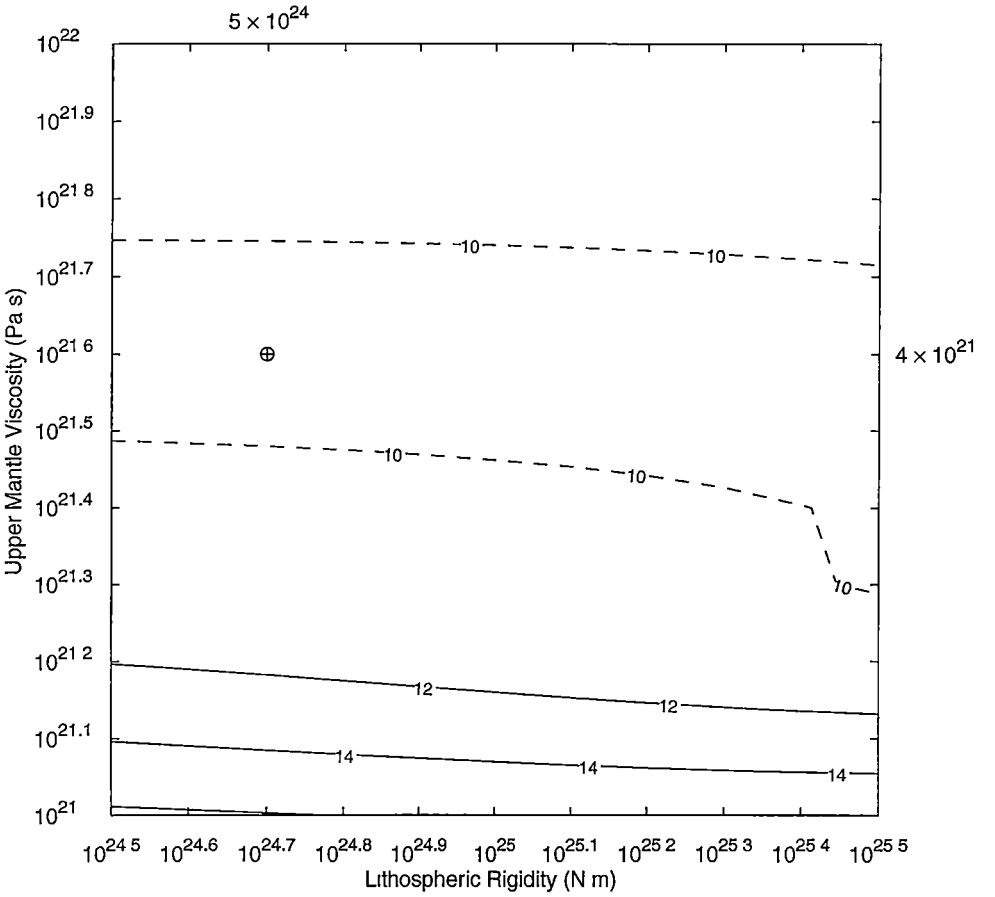

Fig. 6.4: Least Squares Variance solution space for 3 layer earth model with upper mantle viscosity and lithospheric rigidity as searching parameters. The minimum in parameter space is shown by ⊕ with corresponding earth model parameter values shown in exponential notation at top and right hand side of axes.

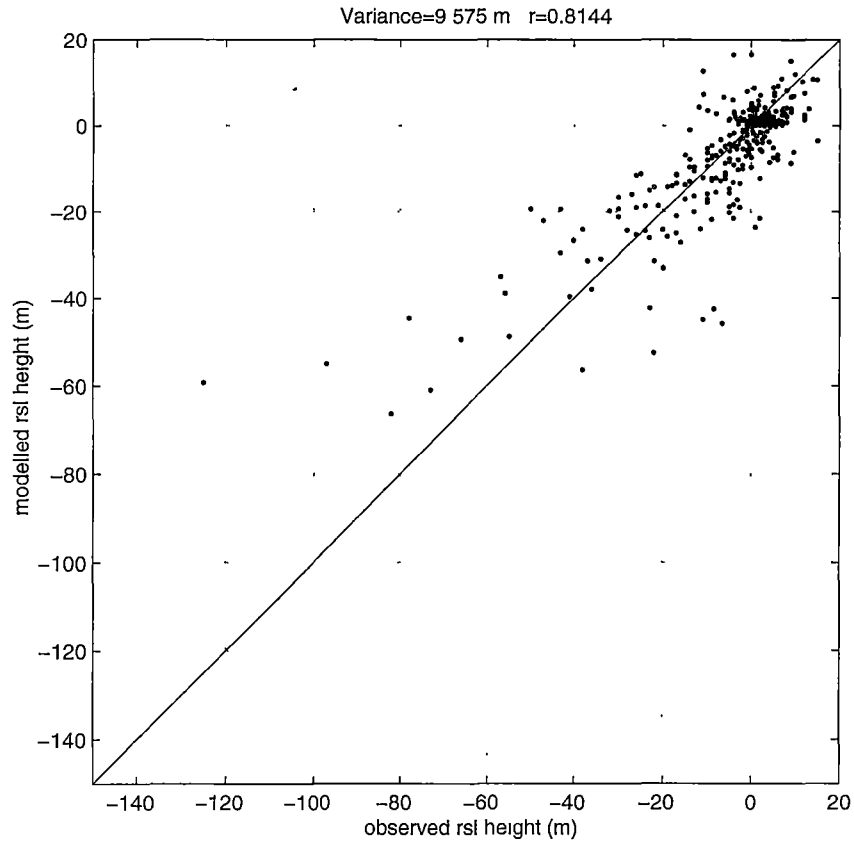

Fig. 6.5: Observed and predicted relative sea level heights for best fit earth model using parabolic profile ice sheet deglaciation chronology.

According to the ICE4G data which drives the model the Fennoscandian ice sheet disappeared almost completely by 9 kyr BP. This means that the relative sea level data (which because of the assumption of uniform hydro-eustatic loading can only be used if it is younger than 7 kyr BP) concerns a period when a considerable amount of isostatic rebound has already occurred. In other words the range of observed sea level change is less, and as a consequence the accuracy of the calculated earth parameters is reduced. In these circumstances it is easier to 'trade' viscosity against rigidity to obtain a best fit at a different position in parameter space.

Figure 6.5 shows the observed and predicted relative sea levels for the earth model parameters given in Table 6.1. The underestimation of large amplitude sites is not as obvious as in the case of the Laurentide adjustment. Although sites where the sea level change is less than -40 m are underestimated, sites with

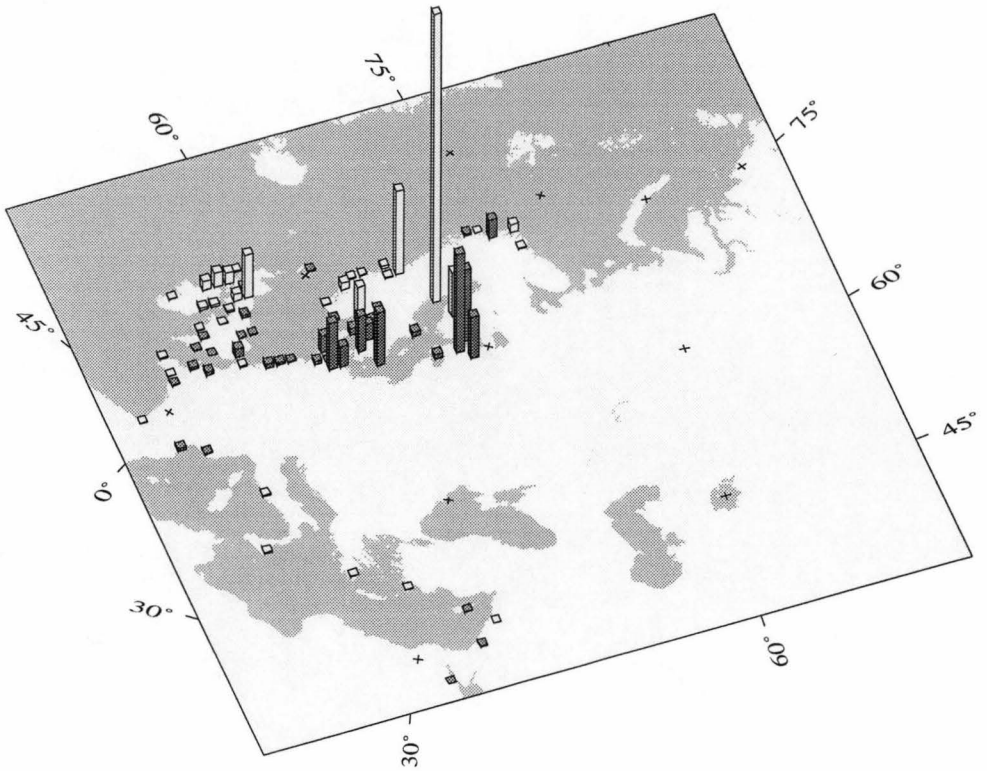

Fig. 6.6: Geographic distribution of error between observed and predicted sea level heights at individual sea level locations using parabolic profile ice sheet chronology.

changes greater than -40 m are not generally overestimated. The reduction in variance compared to the Laurentide adjustment is a consequence of the generally smaller values of relative sea level change.

The Fennoscandian ice sheet is smaller than the Laurentide and has greater gradients of thickness. The previous chapter suggested that for a parabolic profile thickness ice sheet, the relatively flat shape of the ice sheet produces underestimation in the interior (for example at James Bay). As the slope of a parabolic profile ice sheet in the interior increases with decreasing ice sheet size, the underestimation is not as great for the smaller ice sheet.

The geographic distribution of error shown in Figure 6.6 shows underestimation near the Gulf of Bothnia and overestimation near St Petersburg and near Berlin. The data and model prediction used to generate Figure 6.6 is given

in Appendix B.

Although the ICE4G deglaciation chronology shows the last stages of retreat around the Gulf of Bothnia (see Figure 5.3 in the previous chapter), at 21 kyr BP the parabolic profile reconstruction places the ice sheet summit near Novaya Zemlya in the Barents Sea (see Figure 6.2). Other deglaciation chronologies (for example Peltier, 1996b) reconstruct the ice summit at maximum extent directly over the Gulf of Bothnia. Although the summit migrates to the Gulf of Bothnia during retreat (through the ice extent) the isostatic deflection is still reduced and relative sea level amplitude underestimated.

6.2 Time-Dependent Ice Sheet Model

As in the previous chapter the time-dependent ice sheet model was used to reconstruct the ice sheet thicknesses by using β to rescale the input accumulation. Figures 6.7 and 6.8 show the accumulation rate and mean temperature for the model domain. Figure 6.9 shows the results of a parameter space search with ice sheet deglaciation chronology generated by the time-dependent ice sheet model. The upper and lower mantle viscosities are the searching parameters and the lithospheric rigidity is fixed at 10^{25} N m. The mantle viscosity that most realistically reproduces the observed relative sea levels is uniform with a value of 1.3×10^{21} Pa s. This result differs significantly from that generated using the parabolic profile ice sheet model (see Table 6.1).

Figure 6.10 shows the results for the time-dependent ice sheet model reconstruction with the upper mantle viscosity and lithospheric rigidity as the unknown parameters. The contour lines are not predominantly horizontal as for the Laurentide ice sheet but have a slight gradient suggesting that the lithosphere has a more important role in the Fennoscandian adjustment. The best fit lithospheric rigidity is 2×10^{25} N m. Table 6.2 shows the values of best fit for the isostatic model using the time-dependent ice sheet model.

Because the minima of Figures 6.9 and 6.10 are very shallow, it is conceivable that a deglaciation chronology with earth model parameters of higher viscosity and lower rigidity could produce comparable results with those shown here.

The observed and predicted relative sea levels for the time-dependent ice

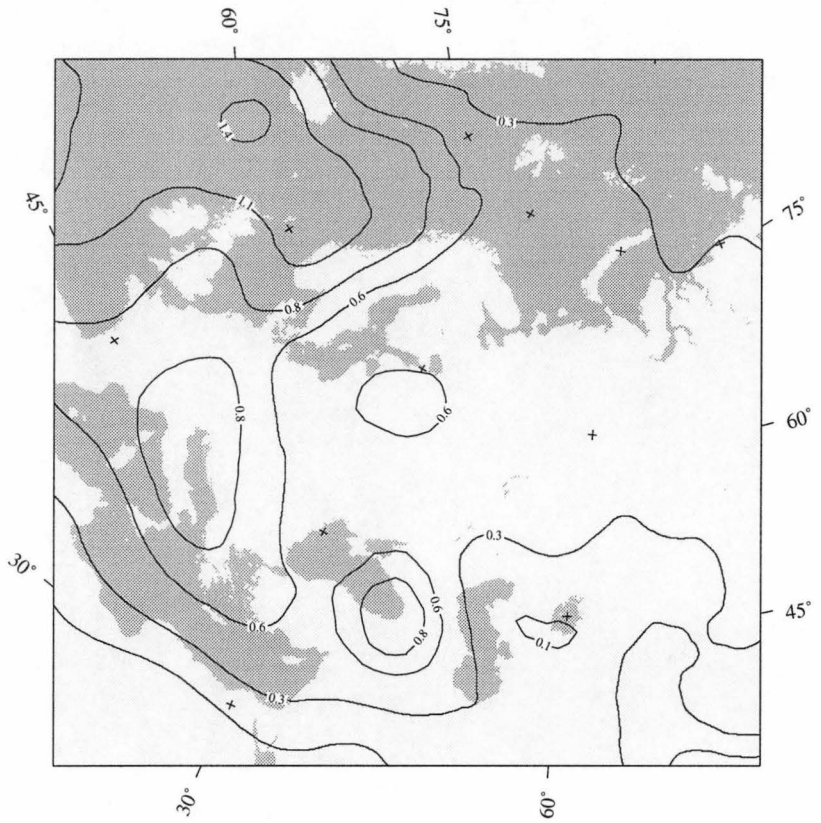

Fig. 6.7: Annual precipitation (m yr^{-1}) over Northern Europe (Shea, 1986).

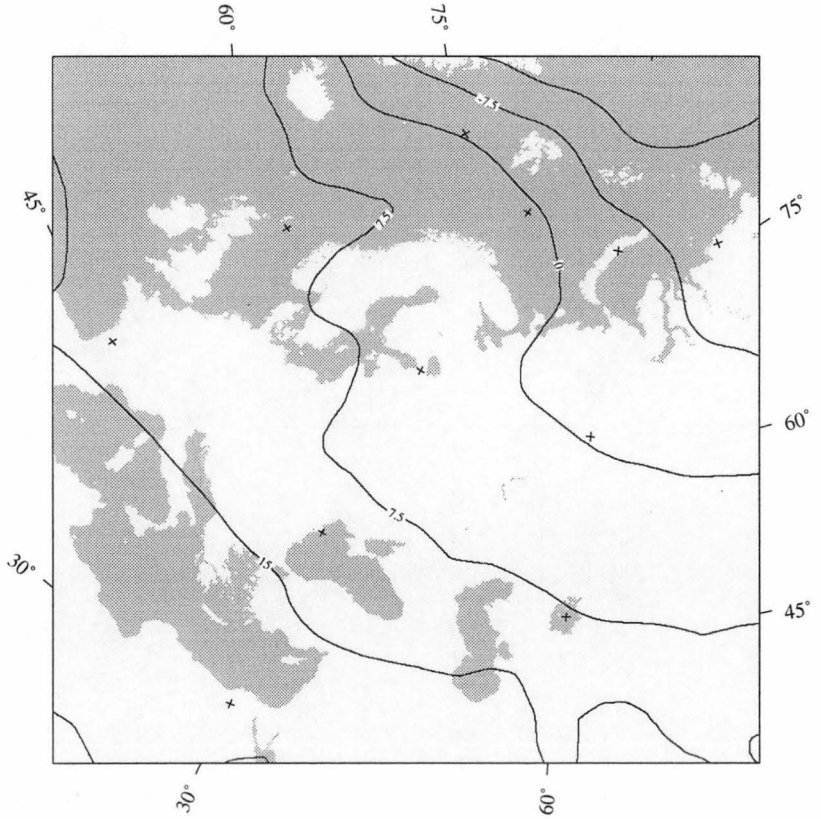

Fig. 6.8: Annual mean temperature (°C) over Northern Europe (Shea, 1986).

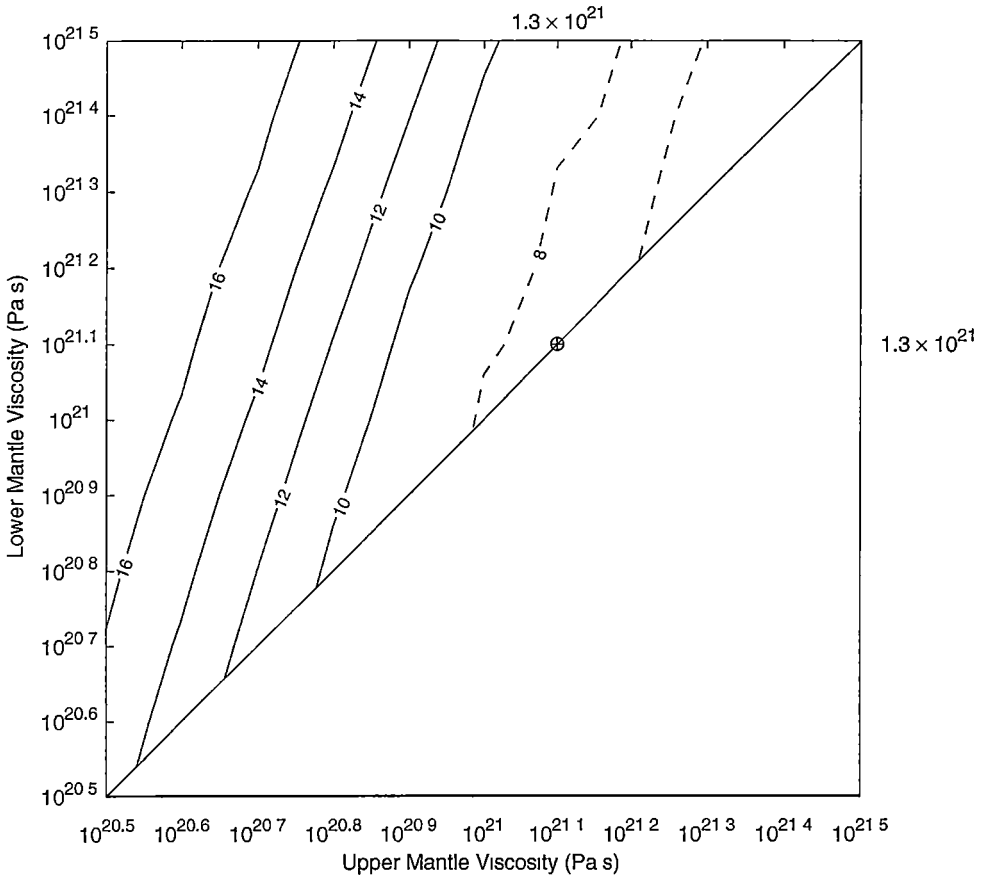

Fig. 6.9: Parameter space for 3 layer earth model with upper mantle and lower mantle viscosities as searching parameters. The minimum in parameter space is shown by ⊕ with corresponding earth model parameter values shown in exponential notation at top and right hand side of axes. Note that from pressure arguments the viscosity of the lower mantle must be greater than the viscosity of the upper mantle and hence there are no contours to the right of the diagonal line of equal viscosities.

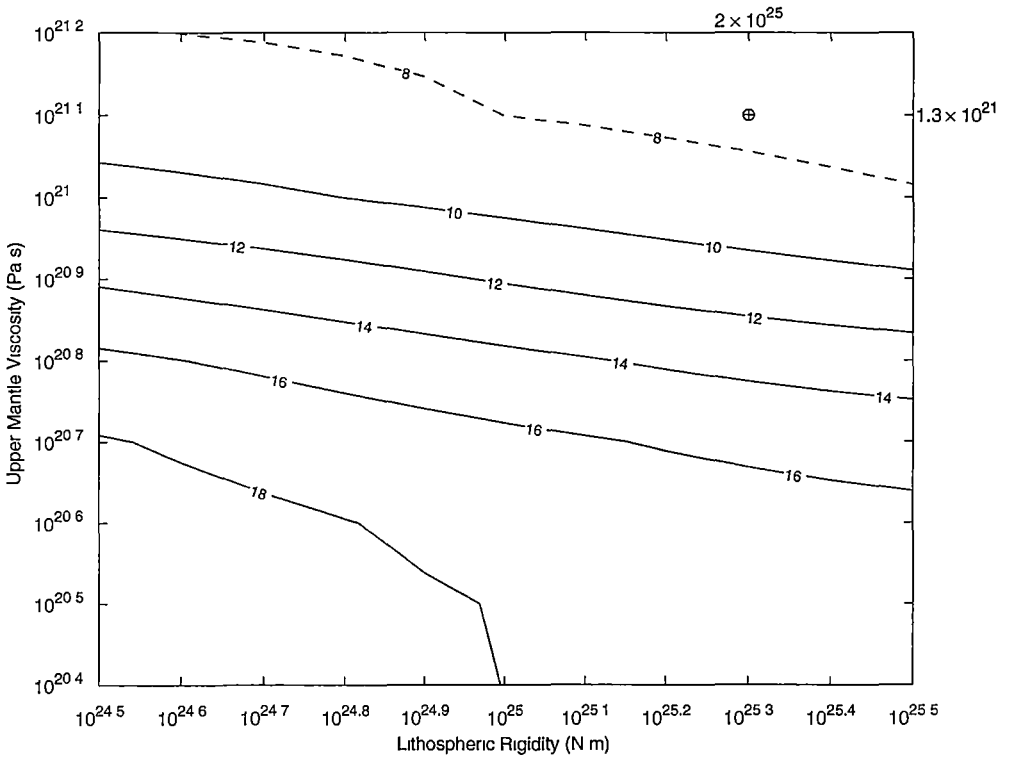

Fig. 6.10: Parameter space for 3 layer earth model with upper mantle viscosity and lithospheric rigidity as searching parameters. The minimum in parameter space is shown by $\oplus$ with corresponding earth model parameter values shown in exponential notation at top and right hand side of axes.

Model Parameter	Best Fit Value
Lower Mantle Viscosity	1.3×10^{21} Pa s
Upper Mantle Viscosity	1.3×10^{21} Pa s
Lithospheric Rigidity	2×10^{25} N m
Ice Sheet Volume at Maximum Extent ($\beta = 1$)	3×10^{6} km^3
Variance	7.6 m

Tab. 6.2: Best fit earth model parameters using time-dependent ice sheet model to generate deglaciation chronology.

sheet model deglaciation chronology are shown in Figure 6.11. The variance is lower than produced with a parabolic profile ice sheet deglaciation chronology.

Referring to Figure 6.12, the mean of the error between prediction and observation is +1.08 m suggesting that on average the model underestimates the relative sea level data.

The geographic distribution of error is shown in Figure 6.13. There are several differences from the calculation using the parabolic profile ice sheet shown earlier in Figure 6.6. The most notable difference is the reduction in underestimation of sea levels at Angermanland in the Gulf of Bothnia compared to the parabolic profile deglaciation chronology. This improvement is to be expected considering the misplacement of the ice sheet summit in the parabolic profile ice sheet model. Figure 6.13 shows that the overestimation near St Petersburg is still a feature for the time-dependent ice sheet model but the overestimation to the south-west near Berlin is reduced. Referring to Figure 6.6 the prediction of sea level height for the parabolic and time-dependent ice sheet models are similar for the British Isles. As the model resolution is 100 km the ice sheet model is too coarse to be appreciably different from the parabolic profile ice sheet model in this region.

Referring to Figure 6.14 and comparing it with similar calculations (Figure 5.22) for the Laurentide adjustment, it can be seen that the minimum for the

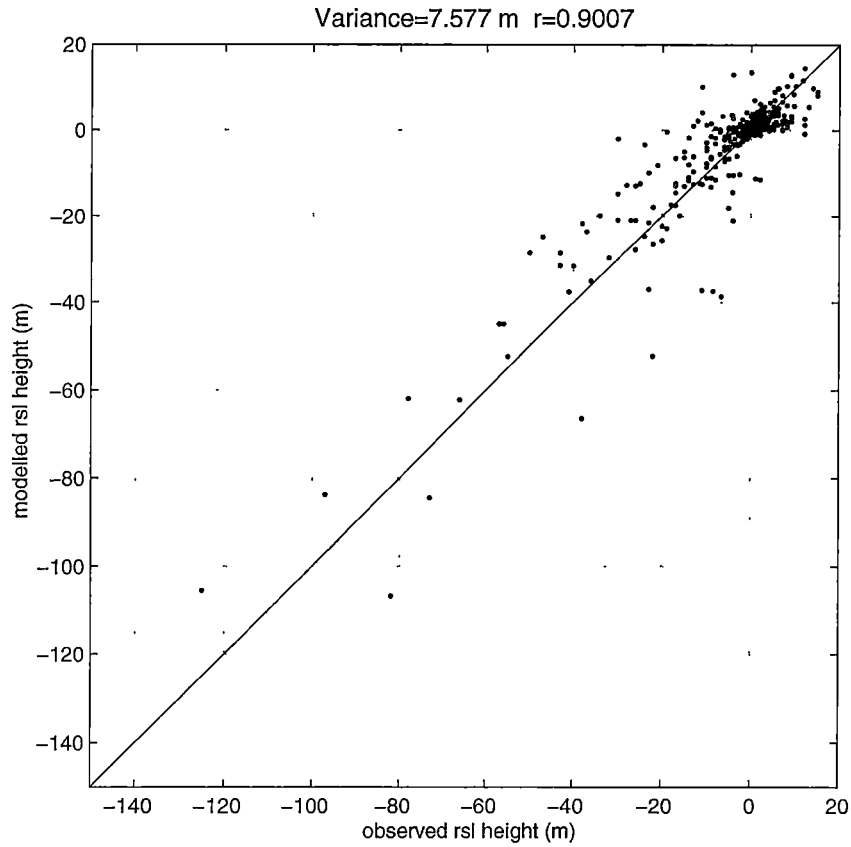

Fig. 6.11: Observed and predicted relative sea level heights for best fit earth model using time-dependent ice sheet model deglaciation chronology.

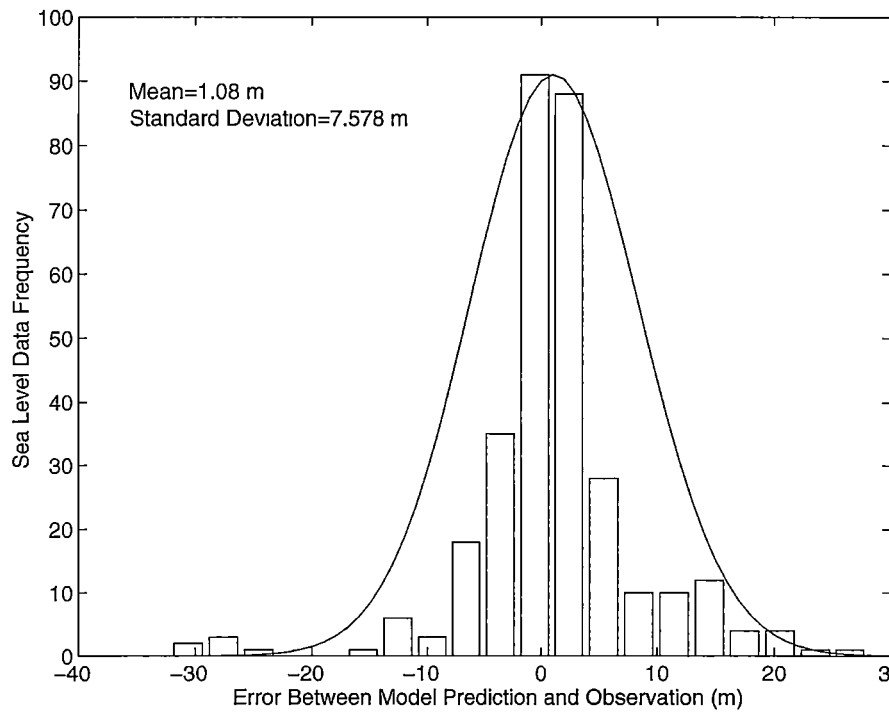

Fig. 6.12: Frequency distribution of misfit between modelled and observed relative sea level data. To the right of 0 corresponds to underestimation and to the left of 0 corresponds to overestimation.

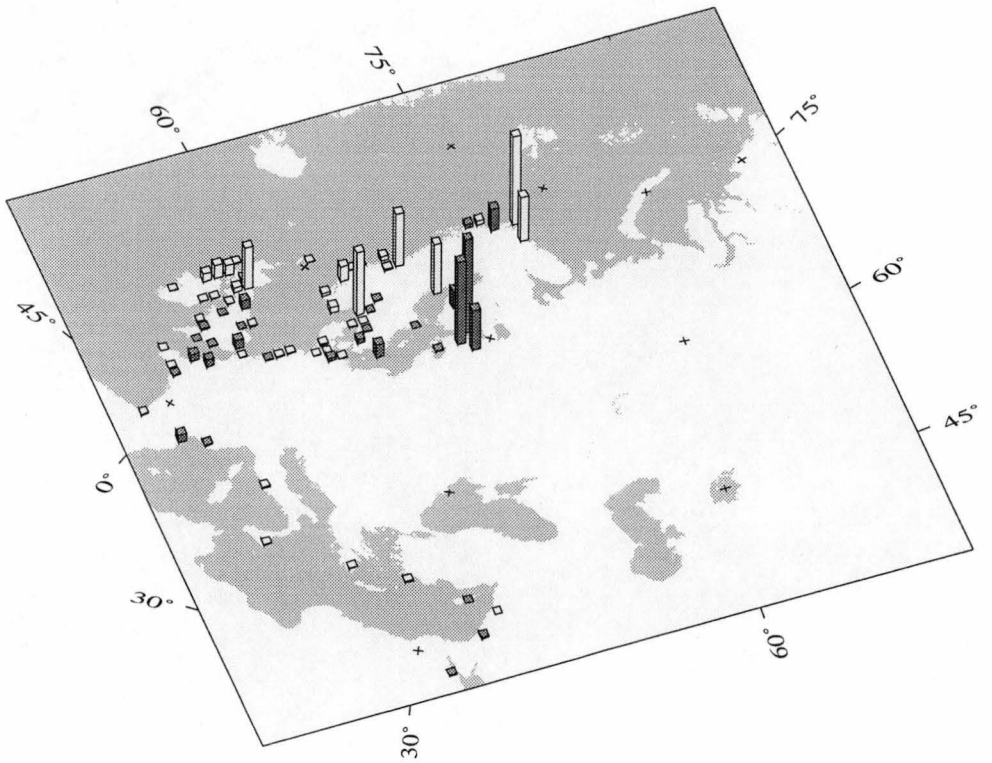

Fig. 6.13: Geographic distribution of error between observed and predicted sea level heights at individual sea level locations.

Fennoscandian ice sheet is not as well defined as for the Laurentide. Figure 6.14 suggests that with small changes to the deglaciation chronology could produce best fit parameters with larger mantle viscosities and larger ice sheet thicknesses. For the Laurentide adjustment a circular pattern ('bull's eye') between β and mantle viscosity is inferred, suggesting that the parameters play an equal role in the prediction of relative sea level amplitude. However in Figure 6.14 a minima 'tail' is found with a reduced gradient towards a larger mantle viscosity and thicker ice sheet. This suggests that although the mantle viscosity and β are still equally important in the prediction of relative sea level data the ability of the model to infer the most appropriate earth model parameters is reduced. Figure 6.14 therefore reports the level of parameter trading between ice sheet thickness and mantle viscosity in the prediction of relative sea level. Despite this parameter trading the least squares variance solution for the time-dependent

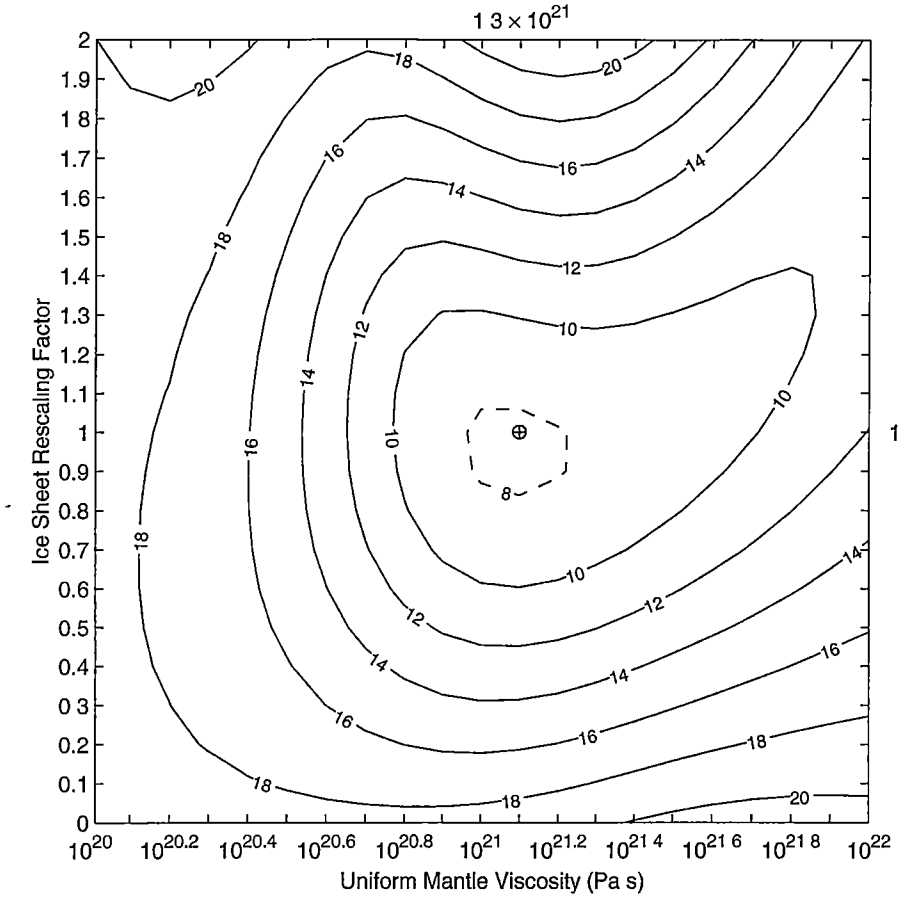

Fig. 6.14: Parameter space for 2 layer earth model with β and uniform mantle viscosity as searching parameters. The minimum in parameter space is shown by $\oplus$ with corresponding earth model parameter value shown in exponential notation at top of axes.

ice sheet model is minimal for the earth model parameters given in Table 6.2. This was verified by a thorough parameter space search in the range of values near those determined using the parabolic profile ice sheet deglaciation chronology. This verification was conducted because Lambeck et al (1996) caution that inappropriate earth model parameters can be derived from a parameter space search that is not exhaustive.

6.3 Present Day Isostatic Adjustment

Again comparison is made between the observed rate of present day sea level change and the predicted present day isostatic adjustment of the best fit isostatic models with different deglaciation chronologies. Figure 6.15 shows the predicted present day adjustment velocity using the parabolic profile ice sheet chronology and Figure 6.16 shows the present day velocity predicted using the time-dependent ice sheet model chronology. Significant differences result from using different earth model parameters. Davis and Mitrovica (1996) report that the prediction of the present day isostatic adjustment of the earth is highly sensitive to the value assumed for the lower mantle viscosity. With the large differences in lower mantle viscosity reported between the parabolic and time-dependent ice sheet chronologies the differences between Figures 6.15 and 6.16 are to be expected.

Figure 6.17 shows the locations of the 59 tide gauge stations used in the calculation of present day sea level change. The only criterion used in station selection was that only records with duration greater than 50 years were used. The observed present day rate of sea level change of the stations is presented in ascending order in Figure 6.18. The predicted uplift velocities of the models at these locations are also shown.

The predicted present day change in sea level due to changes in ocean volume is 0.23 ± 1.93 mm yr^{-1} for the time-dependent ice sheet model and -0.91 ± 1.23 mm yr^{-1} for the parabolic profile model. The high value of standard deviation for these predictions suggest that neither model reliably predicts the present day behaviour of the earth. The differences in prediction result from both the different earth model parameters and different deglaciation chronologies.

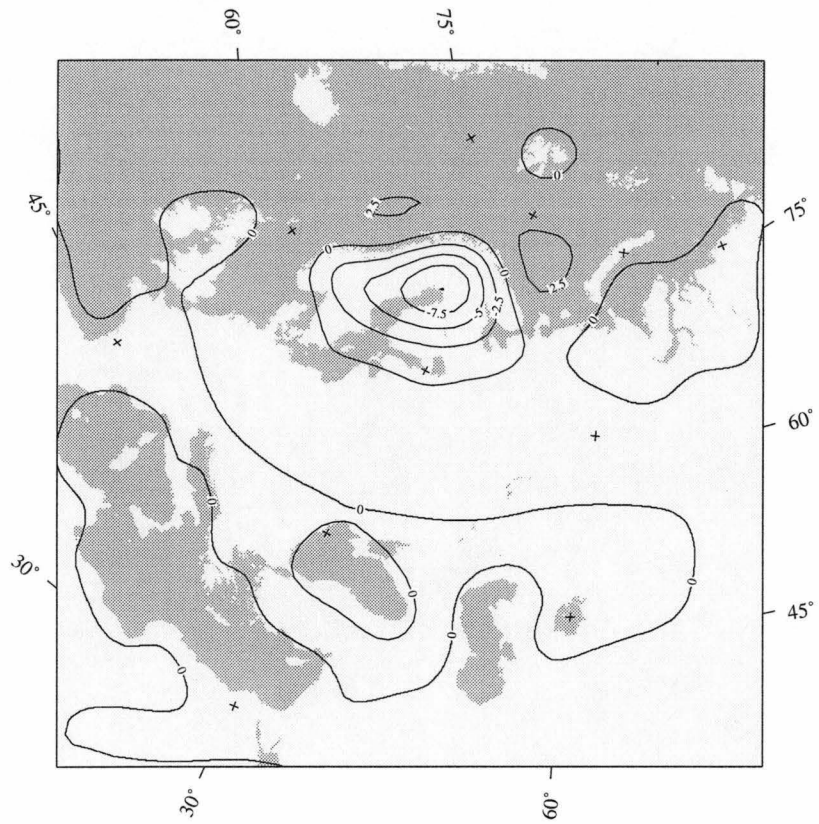

Fig. 6.15: Present day uplift rate (mm yr^{-1}) for parabolic profile ice sheet model.

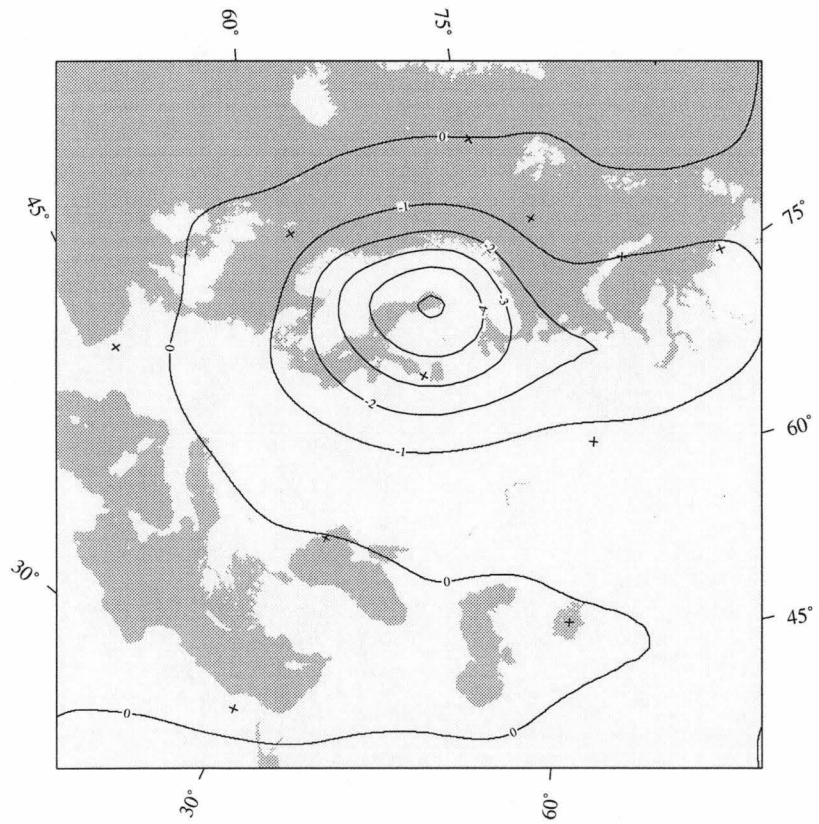

Fig. 6.16: Present day uplift rate (mm yr^{-1}) for time-dependent ice sheet model.

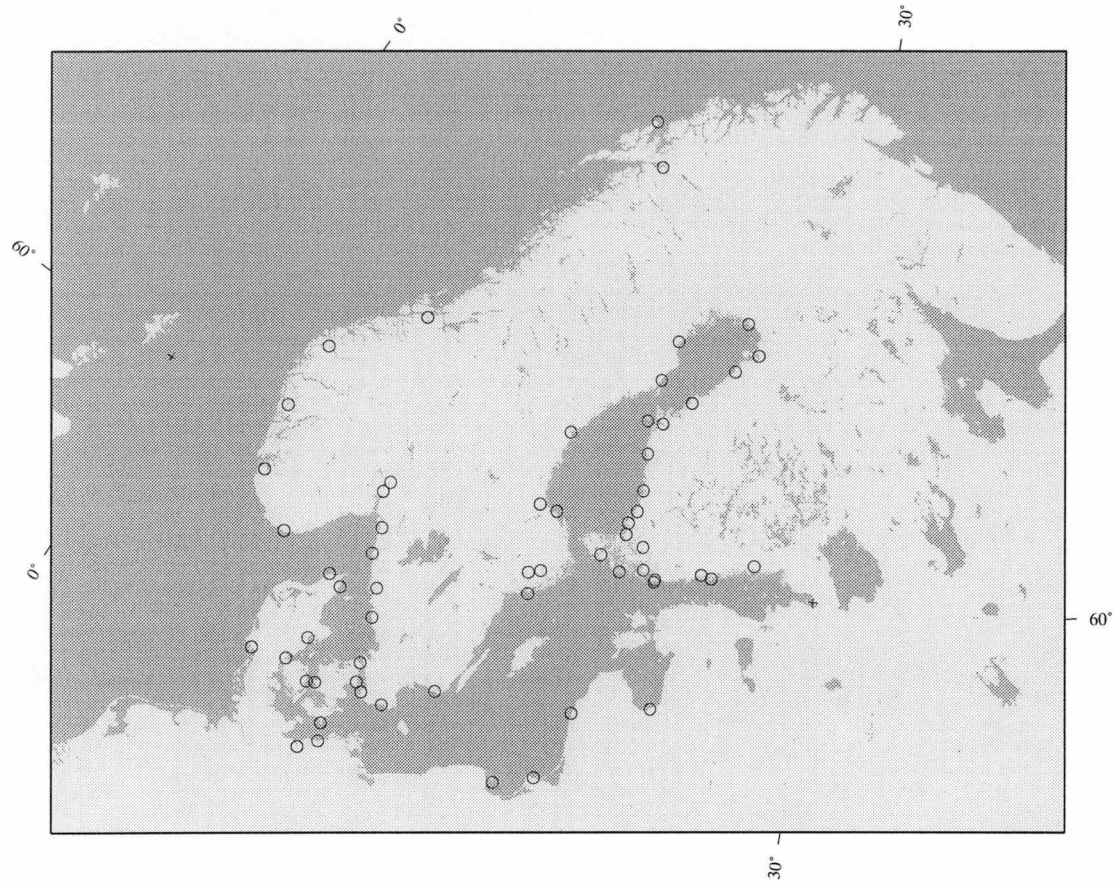

Fig. 6.17: Location of present day tide gauge stations.

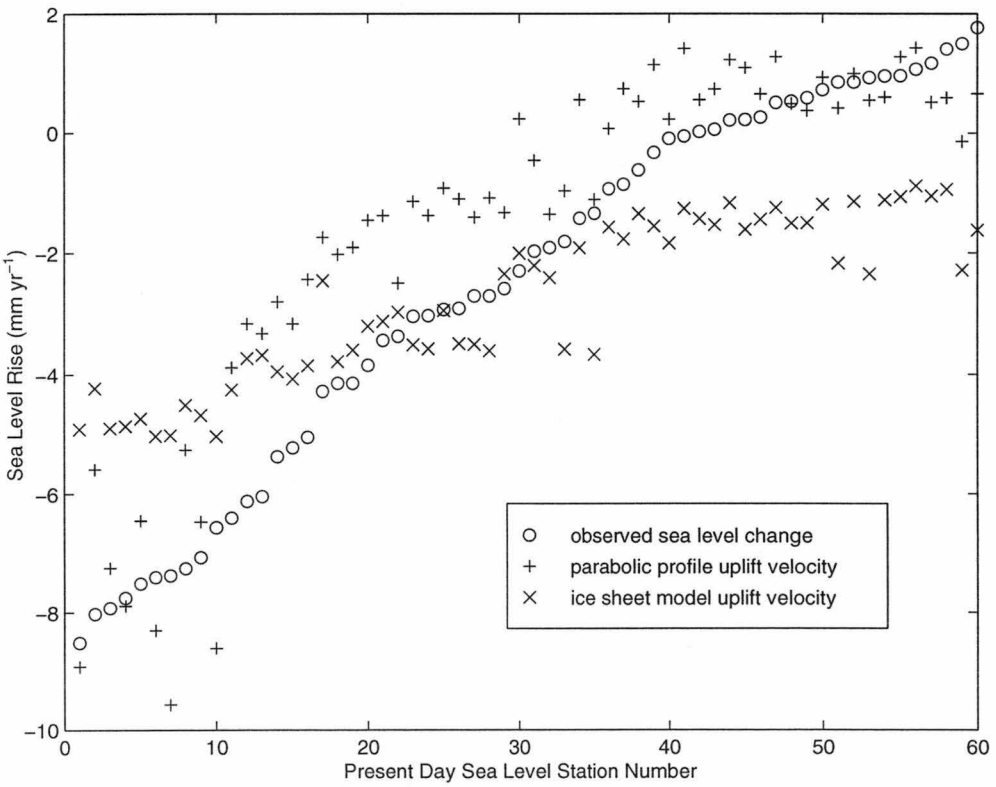

Fig. 6.18: Observed sea level change and model predicted adjustment velocity for ice sheet model generated deglaciation chronology (r=0.9278) and parabolic profile ice sheet chronology (r=0.9180).

6.4 Conclusions

This chapter has examined the isostatic adjustment following the retreat of the Fennoscandian ice sheet. It has shown that the results of the previous chapter cannot be generalised. For the Fennoscandian ice sheet the calculation of isostatic adjustment is sensitive to the assumed form of the ice sheet deglaciation chronology. This could result from the fact that the Fennoscandian ice sheet retreated comparatively early, so that a precise determination of earth model parameters based on relative sea level observations is more difficult than is the case for the Laurentide adjustment. It could also result from the different locations of the ice sheet summits at maximum extent (in the previous chapter the ice sheet summits for the parabolic and time-dependent ice sheet chronologies are approximately coincident).

Han and Wahr (1995) note that until recently the earth model parameter values reported by Peltier using a refined ice sheet deglaciation chronology suggest only a minor viscosity stratification between the upper and lower mantle, whereas most models that assume a parabolic profile ice sheet deglaciation chronology report a more substantial mantle viscosity stratification. The results in this chapter suggest some level of parameter trading between the ice sheet form used in the calculation and the lower mantle viscosity. However this was not found using the time-dependent ice sheet model with the Laurentide ice sheet reconstruction. Mitrovica (1996) points out that for the Northern European adjustment widely varying estimates of mantle viscosity have been made.

Both sets of values of earth model parameters found in this chapter differ from those of the previous chapter. This result could reflect the inadequacy of using a flat earth model for ice sheets of different scales. Alternately this result could suggest that there is some degree of lateral heterogeneity in earth model parameters between different regions. The next chapter examines the effect of a lateral heterogeneity of lithospheric rigidity for the Antarctic ice sheet.

7. VARIABLE LITHOSPHERIC RIGIDITY

The previous two chapters attempted to infer realistic earth model parameters by simulating the isostatic adjustment observed in North America and Northern Europe. It was found that the best fit parameters were different for the two regions. This result presumably reflects a lateral heterogeneity of the earth so that the model parameters should vary as a function of geographic location. This chapter deals with the Antarctic ice sheet and considers lateral heterogeneity of lithospheric rigidity.

The assumption of lateral homogeneity in the interior of the earth has been questioned by Breuer and Wolf (1995) and Kaufmann and Wolf (1996). In their studies relative sea level data from the Svalbard Archipelago were used to examine the sensitivity of individual sites to deviations in earth model parameters. The inference of regional variation of lithospheric rigidity in particular is of interest for Antarctic ice sheet models because Stern and Ten Brink (1989) suggest that East and West Antarctica have different lithospheric rigidities. They find that West Antarctica has a lithospheric thickness 5 times less than that of East Antarctica. The results of Chapter 4 show that this thickness structure would ensure the generation of more ice in West Antarctica over a glacial cycle. As the ICE4G deglaciation chronology suggests over 20 m of eustatic sea level contribution from change of the Antarctic ice sheet since the last ice age (Peltier, 1994), and the time-dependent model simulations in Chapter 4 generate -7 m, any mechanism that is capable of allowing the model to generate more ice in Antarctica throughout the last ice age is of interest.

Figure 7.1 is adapted from Drewry (1982) and shows the cratonic structure of Antarctica. West Antarctica is composed of 4 separate fragments all of much smaller size than the East Antarctic craton. It is understandable given this distribution that West Antarctica has a wide distribution of crustal thicknesses.

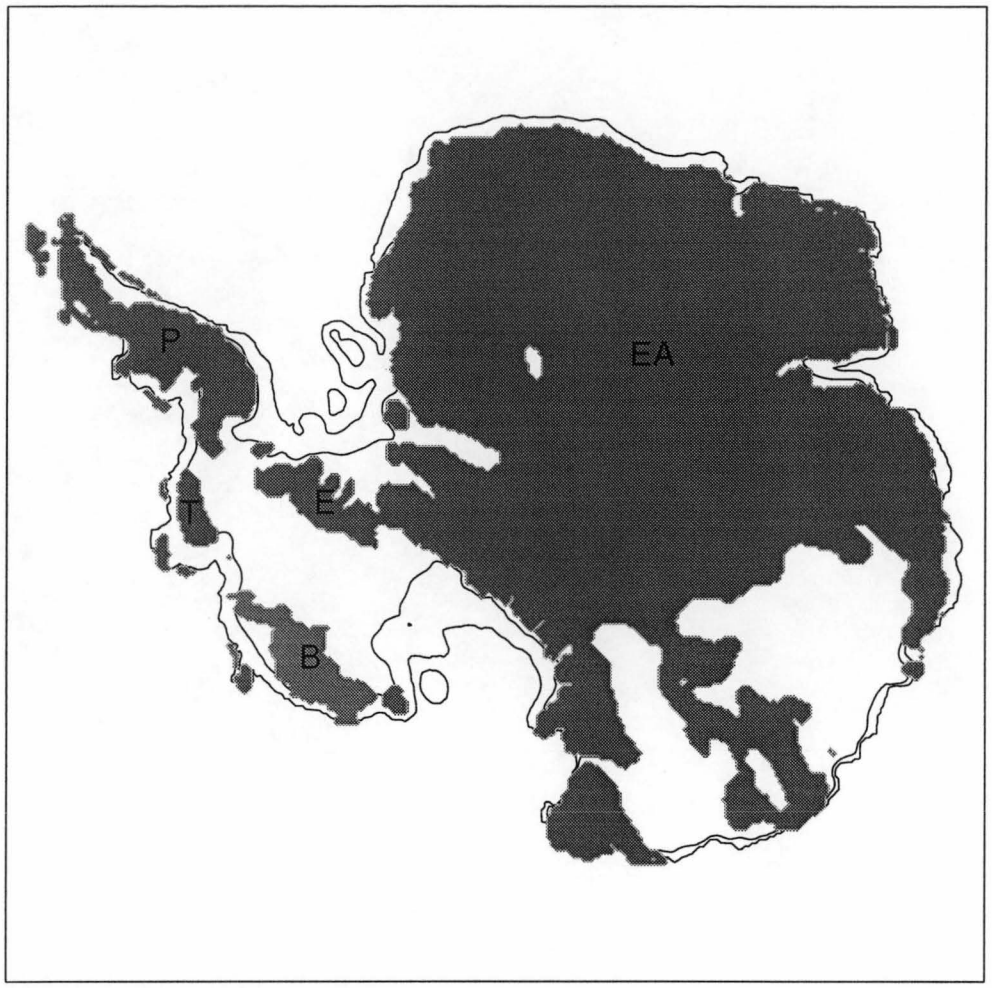

Fig. 7.1: Cratonic structure of Antarctica. EA=East Antarctica, E= Ellsworth Block, P=Antarctic Peninsula, T=Thurston Block, B=Marie Byrd Land Block.

7.1 Method

Equation 3.1 in Chapter 3 is the differential equation governing the deflection of a uniform thickness lithosphere under an applied load. Equation 3.1 is a special case of the more general equation (Egan, 1992):

$$\nabla^2(D_r\nabla^2\varphi) + \rho_m g\varphi = Q \tag{7.1}$$

This is not a constant coefficient differential equation and is therefore not easily susceptible to solution by Fourier methods. It can be solved by sparse matrix methods as follows.

Equation 7.1 can be expressed in finite difference form as

$$\nabla^2 D_{i,j} \nabla^2 \varphi_{i,j} + \rho_m g \varphi_{i,j} = Q_{i,j} \tag{7.2}$$

or as an operator equation

$$[\nabla^2 D_{i,j} \nabla^2 + \rho_m g] \varphi_{i,j} = Q_{i,j} \tag{7.3}$$

Defining A as the operator in the square brackets, this equation (that is Equation 7.1) inverts to:

$$\varphi_{i,j} = A^{-1} Q_{i,j} \tag{7.4}$$

The deflection φ can be calculated at each time step by calculating the load Q through Equation 3.2 in Chapter 3 and solving for φ.

Equation 7.5 shows the matrix of non-zero coefficients for the differential operator A. The position of the of the non-zero entries results from using the nine-point, double-spaced, centred finite difference form of the divergence operator in Equation 7.1 taken from Abramowitz and Stegun (1965).

$$\begin{bmatrix}
0 & 0 & 0 & 0 & \varphi_{i,j+4} & 0 & 0 & 0 & 0 \\
0 & 0 & 0 & 0 & \varphi_{i,j+3} & 0 & 0 & 0 & 0 \\
0 & 0 & \varphi_{i-2,j+2} & \varphi_{i-1,j+2} & \varphi_{i,j+2} & \varphi_{i+1,j+2} & \varphi_{i+2,j+2} & 0 & 0 \\
0 & 0 & \varphi_{i-2,j+1} & \varphi_{i-1,j+1} & \varphi_{i,j+1} & \varphi_{i+1,j+1} & \varphi_{i+2,j+1} & 0 & 0 \\
\varphi_{i-4,j} & \varphi_{i-3,j} & \varphi_{i-2,j} & \varphi_{i-1,j} & \varphi_{i,j} & \varphi_{i+1,j} & \varphi_{i+2,j} & \varphi_{i+3,j} & \varphi_{i+4,j} \\
0 & 0 & \varphi_{i-2,j-1} & \varphi_{i-1,j-1} & \varphi_{i,j-1} & \varphi_{i+1,j-1} & \varphi_{i+2,j-1} & 0 & 0 \\
0 & 0 & \varphi_{i-2,j-2} & \varphi_{i-1,j-2} & \varphi_{i,j-2} & \varphi_{i+1,j-2} & \varphi_{i+2,j-2} & 0 & 0 \\
0 & 0 & 0 & 0 & \varphi_{i,j-3} & 0 & 0 & 0 & 0 \\
0 & 0 & 0 & 0 & \varphi_{i,j-4} & 0 & 0 & 0 & 0
\end{bmatrix} \tag{7.5}$$

The values for the non-zero entries of matrix A in Equation 7.5 are as follows

$$\begin{aligned}
\varphi_{i,j} &= 16\rho_m g \Delta x^4 + 28 D_{i,j} - 2(D_{i,j+2} + D_{i,j-2} + D_{i+2,j} + D_{i-2,j}) + \\
&\quad 2(4D_{i,j} - D_{i+2,j} - D_{i-2,j} - D_{i,j+2} - D_{i,j-2}) \\
\varphi_{i,j\pm1} &= \mp 10(D_{i,j+1} - D_{i,j-1}) \\
\varphi_{i\pm1,j} &= \mp 10(D_{i+1,j} - D_{i-1,j}) \\
\varphi_{i\pm1,j\pm1} &= 2(D_{i+1,j+1} + D_{i-1,j-1} - D_{i-1,j+1} - D_{i+1,j-1}) \\
\varphi_{i,j\pm2} &= D_{i,j+2} - 10 D_{i,j} + D_{i,j-2} + (D_{i+2,j} + D_{i-2,j} - 2D_{i,j})
\end{aligned}$$

$$
\begin{aligned}
\varphi_{i\pm2,j} &= D_{i+2,j} - 10D_{i,j} + D_{i-2,j} + (D_{i,j+2} + D_{i,j-2} - 2D_{i,j}) \\
\varphi_{i\pm1,j+2} &= -2(D_{i,j+1} - D_{i,j-1}) \\
\varphi_{i\pm2,j-1} &= -2(D_{i,j+1} - D_{i,j-1}) \\
\varphi_{i\pm1,j-2} &= 2(D_{i,j+1} - D_{i,j-1}) \\
\varphi_{i\pm2,j+1} &= 2(D_{i,j+1} - D_{i,j-1}) \\
\varphi_{i,j\pm3} &= \pm2(D_{i,j+1} - D_{i,j-1}) \\
\varphi_{i\pm3,j} &= \pm2(D_{i,j+1} - D_{i,j-1}) \\
\varphi_{i\pm2,j\pm2} &= 2D_{i,j} \\
\varphi_{i\pm4,j} &= D_{i,j} \\
\varphi_{i,j\pm4} &= D_{i,j}
\end{aligned}
$$

where Δx is the finite difference grid spacing in both the x and y direction. In order to solve Equation 7.4 the non-zero coefficients listed above are converted to single column matrix form so that the resulting sparse matrix can be used to calculate the equilibrium deflection φ. The solution for φ involves LU factorisation of the matrix A through threshold pivoting. Boundary conditions are imposed so that at the model boundary the deformation and its first three spatial derivatives are set to zero. Although these boundary conditions are somewhat arbitrary they do not strongly effect the isostatic adjustment in the interior of the model domain.

Equation 7.4 is difficult to verify against analytic solutions but its prediction of equilibrium deflection for a uniform lithospheric rigidity allows comparison with the Fourier methods described in Chapter 3. Figure 7.2 shows the calculated equilibrium deformation using the sparse matrix inversion technique and assuming a uniform lithospheric rigidity of 10^{25} N m. Figure 3.2 in Chapter 3 is the same calculation using the Fourier technique. The correlation coefficient between the two predictions is 0.9994 suggesting that the inverse matrix technique is reasonable for uniform thickness models. Figure 3.2 has a smoother pattern of deformation than Figure 7.2. This is primarily due to the fact that the Fourier technique assumes a smooth and continuous surface function.

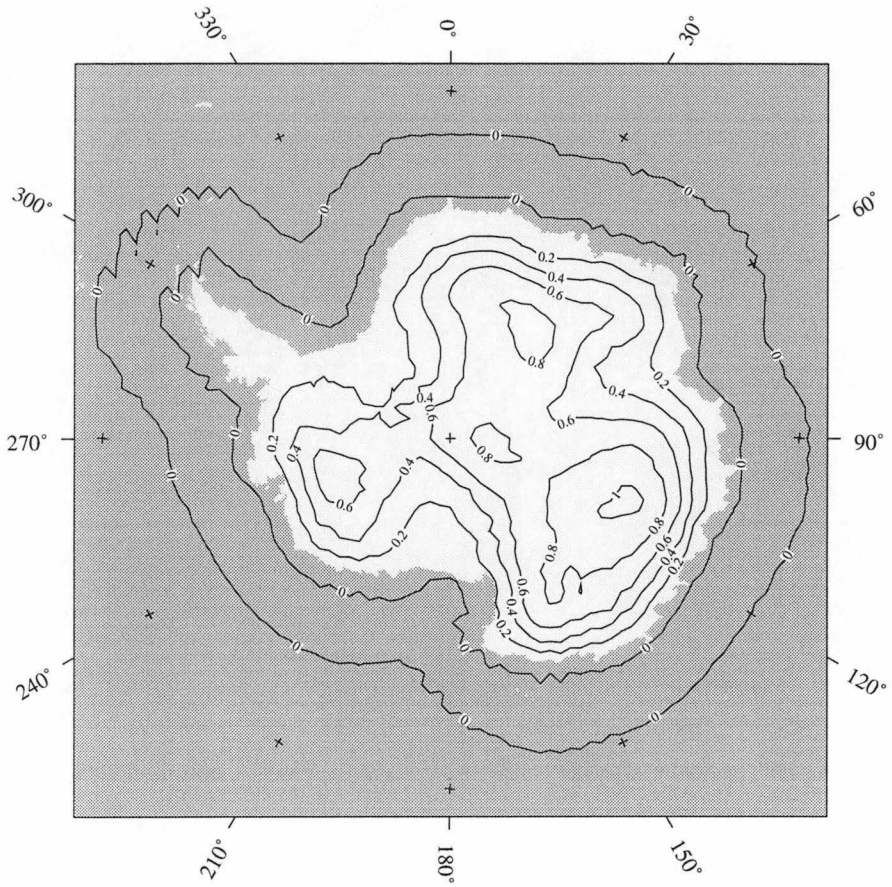

Fig. 7.2: Equilibrium deflection (km) calculated for Antarctic ice sheet using finite difference sparse matrix methods.

7.2 Data

In order to utilise the theory outlined in the previous section a representation of the structure of the lithospheric rigidity beneath Antarctica is required. Anderson (1995) notes that there are several differing interpretations of the definition of the lithosphere (and the 'effective elastic thickness' of the lithosphere H_l) with both mechanical and thermal properties being used to define its thickness. In this study the crustal thickness map of Figure 7.3 (from Demenitskaya and Ushakov, 1966) derived from gravity and seismic data is used to generate the lithospheric rigidity profile over the Antarctic continent. The high values in West Antarctica correspond with the cratonic structure of the region shown in Figure 7.1.

Figure 7.3 is not a map of lithospheric thickness but of crustal thickness. It

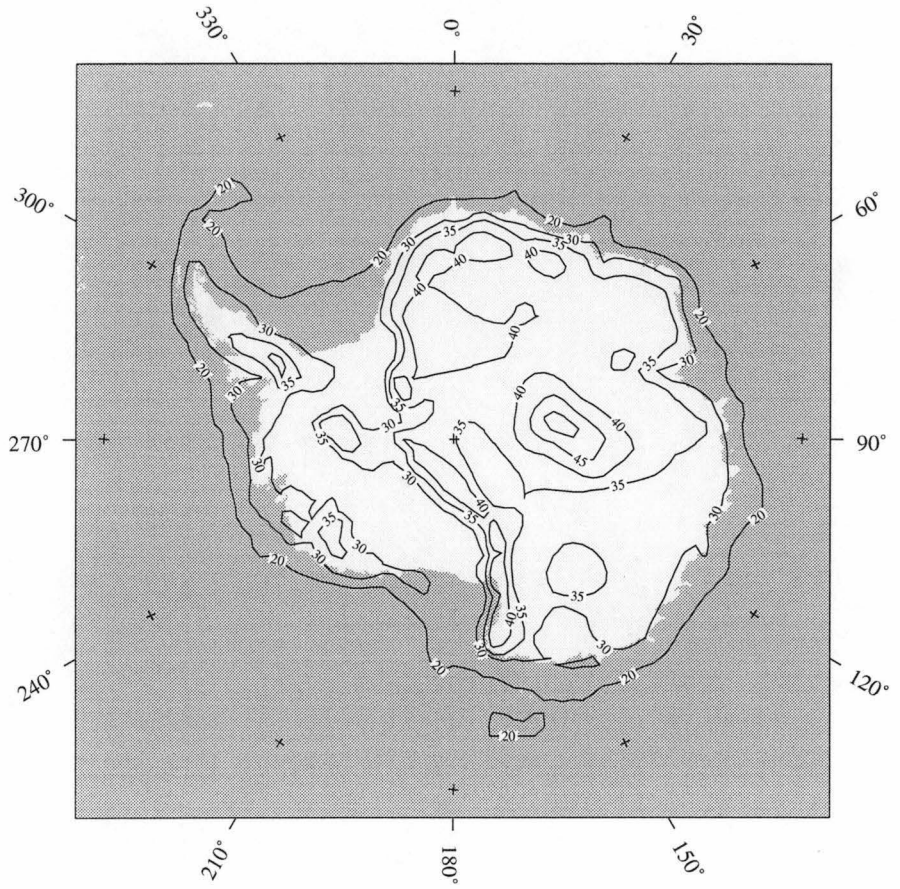

Fig. 7.3: Crustal thickness (km) of Antarctica (Demenitskaya and Ushakov, 1966).

has three major problems in the present context. First, the gravity data used to generate the crustal thicknesses were derived using the assumption of present day isostatic equilibrium, which Chapter 4 shows may not be appropriate. Second, the crustal thickness values derived from seismic refraction data depend on the local geology of the Antarctic region and may not indicate crustal variations. Third, there is no well defined relation between crustal thickness and lithospheric thickness.

The Demenitskaya and Ushakov crustal thicknesses display the high thickness in East Antarctica and low thickness in West Antarctica suggested by Stern and Ten Brink. This feature, and the lack of a more realistic alternative, are the primary reasons for its use in the present study.

On geological time scales it is thought that there is indeed a relation between the thickness of the crust and the thickness of the lithosphere (Kusznir

& Karner, 1985). Two simple monotonic relations are assumed here. The first is that lithospheric thickness is directly proportional to crustal thickness. The second is that lithospheric thickness is equal to crustal thickness plus a constant. Although neither of these relations produce the differences in rigidity between East and West Antarctica suggested by Stern and Ten Brink, they are used because it is difficult to justify more complex relations between crustal and lithospheric thickness. Both of these relations are explored and analysed in the following.

7.3 ◦ Modelling the Antarctic Ice Sheet using a Laterally Heterogeneous Lithosphere Model

7.3.1 Lithospheric thickness directly proportional to crustal thickness

In this section proportionality coefficients of 2, 3 and 4 between crustal and lithospheric thickness are assumed. Thus given a value for crustal thickness, one can calculate lithospheric thickness and then lithospheric rigidity from Equation 3.3. Table 7.1 shows the minimum, maximum and average values of the lithospheric thicknesses and corresponding rigidities when they are derived in this manner. The table shows that for the 'crust × 3' case the average rigidity is fairly close to the customary value of 10^{25} N m.

model	$\min(H_l)$	$\max(H_l)$	$\overline{H_l}$	$\min(D_r)$	$\max(D_r)$	$\overline{D_r}$
crust × 2	45	102	70	1×10^{24}	2×10^{25}	5.1×10^{24}
crust ×3	68	154	105	4×10^{24}	5×10^{25}	1.7×10^{25}
crust ×4	90	205	140	1×10^{25}	1×10^{26}	4.1×10^{25}

Tab. 7.1: Minimum, maximum and average values of the effective elastic thickness (km) and lithospheric rigidity (N m) used in the case of direct proportionality between the crust and lithosphere.

The geographic distribution of rigidities calculated in this way was used to generate the sparse matrix A of Equation 7.4. The equilibrium deflection φ calculated using Equation 7.4 was then used to calculate the isostatic disequi-

librium through Equation 3.7. The disequilibrium was then used to force the decoupled viscoelastic half-space isostatic adjustment model described in Chapter 3. In turn this representation of isostatic adjustment was coupled to the time-dependent ice sheet model described in Chapter 4. The overall coupled model was run over a glacial cycle 160 kyr long.

The equilibrium ice sheet configuration defined in Chapter 4 (Section 4.2) was not used as the initial condition. The results of Chapter 4 show that the initial state of isostatic equilibrium for the ice sheet model is sensitive to the choice of lithospheric rigidity through the definition of the reference bed (see Section 4.6). Therefore the present day situation of the Antarctic ice sheet was used as the initial condition for the model runs. The time-dependent input data on accumulation and eustatic sea level are identical to those described in Chapter 4. A uniform mantle viscosity of 2×10^{21} Pa s was assumed. This value is considered to be reasonable in the light of the results of the previous chapters.

Figure 7.4 shows the time-dependent change in total ice volume for the three different relations between crustal and lithospheric thickness. The ice volume generated when using a uniform lithospheric rigidity of 10^{25} N m is also shown and is referred to as the standard earth model. The pattern of ice volume change is different to those in Chapter 4 where an equilibrium ice sheet profile was used as the initial condition. The change in ice volume between 20 kyr BP and the present day is about 2.5×10^6 km^3 for all cases except the 'crust $\times$ 2' model, where it is about 3.5×10^6 km^3.

There are two obvious features in Figure 7.4. At approximately 135 kyr BP the 'crust $\times$ 4' model has more ice than the other models, with this excess continuing for the next 60 kyr. After 70 kyr BP the 'crust $\times$ 4' ice volume lowers to that of the other models and stays in the midrange of model prediction for the rest of the simulation. The other feature is that at 60 kyr BP the 'crust $\times$ 2' model diverges from the others until at the present day it has 1×10^6 km^3 more ice than the other models.

Figure 7.5 shows the difference in ice sheet thickness between the 'crust $\times$ 4' model and the standard earth model at 80 kyr BP. The major ice volume

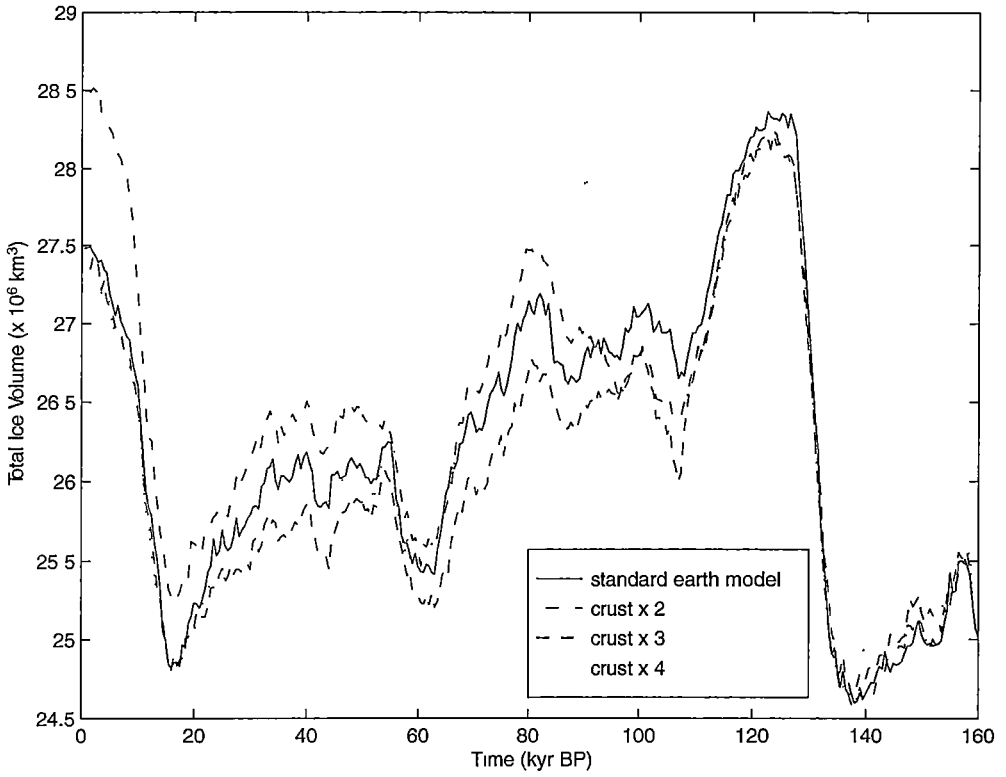

Fig. 7.4: Time-dependent change in the total volume of ice for the standard earth model, the 'crust × 2' model, the 'crust × 3' model and the 'crust × 4' model.

differences are around the Amery and Ronne ice shelves and the interior of West Antarctica. The Amery and Ronne ice shelves both float over shallow sea floors so that grounding occurs readily. Figure 7.6 shows the position of the ice sheet grounding line for the 'crust × 4' and standard earth models at 80 kyr BP. Comparing Figures 7.5 and 7.6 it is obvious that the differences in ice sheet volume are related to the differences in grounding line. The 'crust × 4' model grounds further out onto the continental shelf than the standard earth model. A similar correlation between the ice sheet thickness and grounding line position is found in a comparison of the 'crust × 2' model and the standard earth model at the present day.

The average rigidity for the 'crust × 2' model is less than that of the standard earth model. The average rigidity for the 'crust × 4' model is greater than that of the standard earth model. Both models generate a greater overall ice

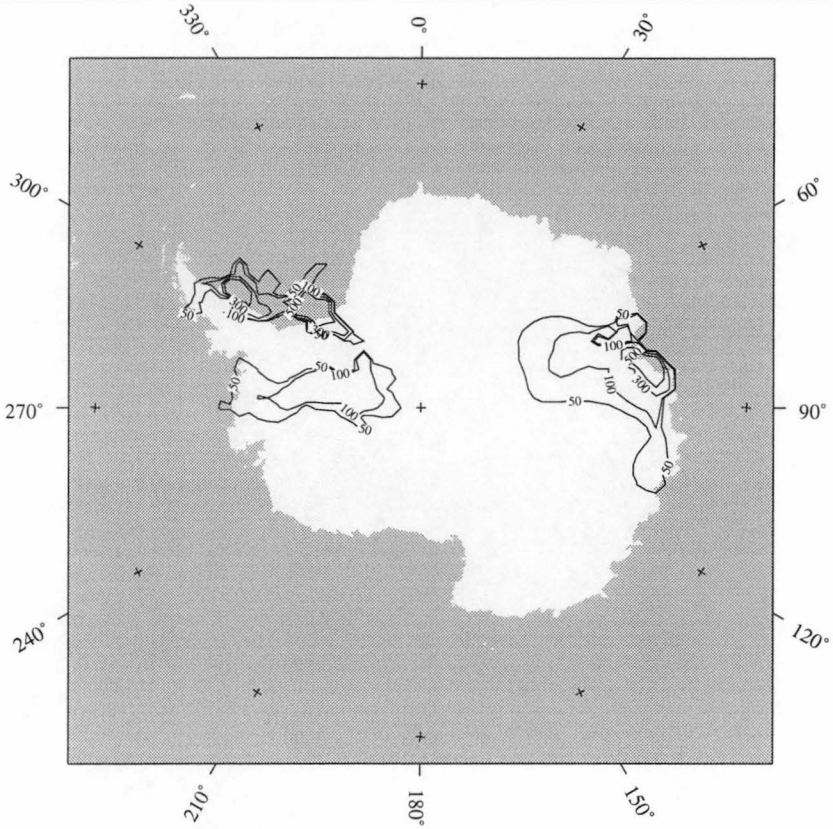

Fig. 7.5: Difference in ice sheet thickness (m) between the 'crust × 4' model and the standard earth model at 80 kyr BP.

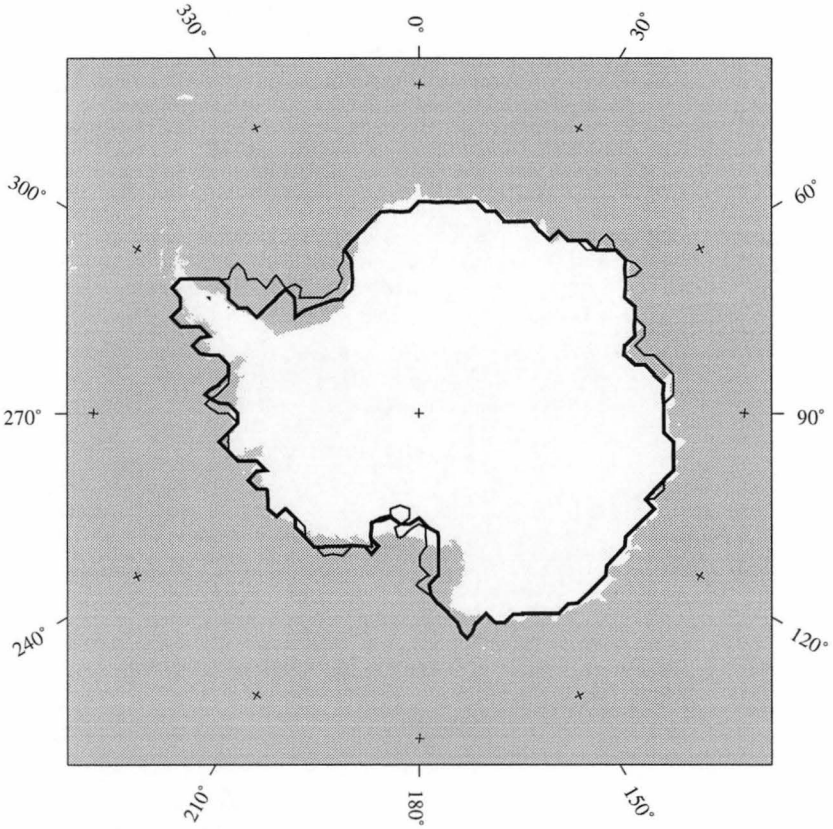

Fig. 7.6: Grounding lines for the 'crust × 4' model (thin line) and the standard earth model (thick line) at 80 kyr BP.

volume than the standard earth model for most of the glacial cycle. This result conflicts with Chapter 4 which concludes that the generated ice volume is inversely proportional to the lithospheric rigidity. It should be noted that the initial conditions for the model differ here from those used in Chapter 4. In that chapter the equilibrium situation is defined by generating a steady state profile of the ice sheet using a uniform lithospheric rigidity of 10^{25} N m. Here the equilibrium situation is not used and the reference bed is generated using each assumed distribution of lithospheric rigidity. This is the reason the ice volumes do not diverge significantly from each other at the start of the model run as occurs in Chapter 4 (Figure 4.17).

7.3.2 Lithospheric thickness equal to crustal thickness plus constant

In this section lithospheric thickness is assumed to be equal to crustal thickness plus a constant. Three cases are examined where the constant value is 30, 50 and 70 km. Table 7.2 outlines the main statistical features of these three cases.

model	$\min(H_l)$	$\max(H_l)$	$\overline{H_l}$	$\min(D_r)$	$\max(D_r)$	$\overline{D_r}$
crust + 30 km	53	82	65	2×10^{24}	8×10^{24}	4.1×10^{24}
crust + 50 km	73	102	85	6×10^{24}	2×10^{25}	9.1×10^{24}
crust + 70 km	93	122	105	1×10^{25}	3×10^{25}	1.7×10^{25}

Tab. 7.2: Minimum, maximum and average values of the effective elastic thickness (km) and lithospheric rigidity (N m) used when the lithospheric thickness is equal to the crustal thickness plus a constant.

As in the previous section the values of the constant were chosen so that the corresponding average rigidities span the 'standard' 10^{25} N m value that was found to be appropriate for uniform rigidity models. The generation of lithospheric rigidities was calculated in the same manner as for the linear proportionality models.

Figure 7.7 shows the predicted variation in total ice volume for the three different relations between crustal and lithospheric thickness. The 'crust + 30

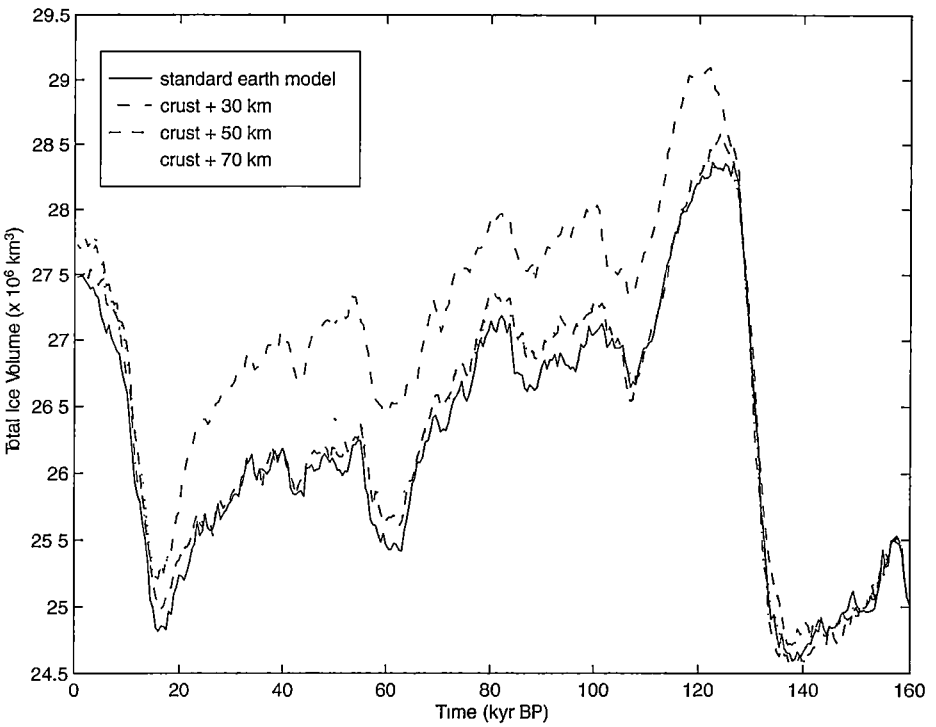

Fig. 7.7: Time-dependent change in the total volume of ice for the standard earth model, the 'crust + 30 km' model, the 'crust + 50 km' model and the 'crust + 70 km' model.

km' model generates an ice sheet volume between 120 kyr BP and 20 kyr BP which is about 1×10^6 km^3 larger than the other models. The other cases, which include the standard earth model, are very similar to each other. Figure 7.8 shows the geographic distribution of ice sheet thickness difference between the 'crust + 30 km' model and the uniform lithospheric thickness model at 80 kyr BP. As in the linearly proportional case the major difference in ice volume occurs near the Ronne ice shelf in West Antarctica. The difference near the Amery ice shelf which appeared in the linearly proportional case (see Figure 7.5) is absent. Figure 7.9 shows the grounding lines at 80 kyr BP for the standard earth model and for the 'crust + 30 km' model. The 'crust + 30 km' model has ice grounded further out onto the continental shelf around the Ronne ice shelf than the standard earth model.

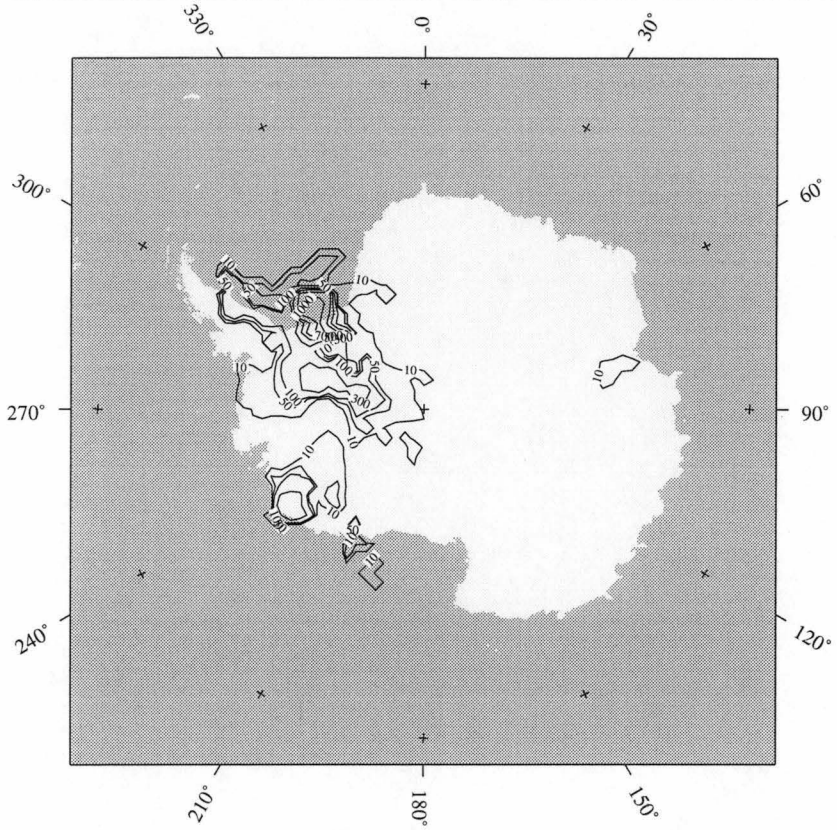

Fig. 7.8: Difference in ice sheet thickness (m) between the 'crust + 30 km' model and standard earth model at 80 kyr BP.

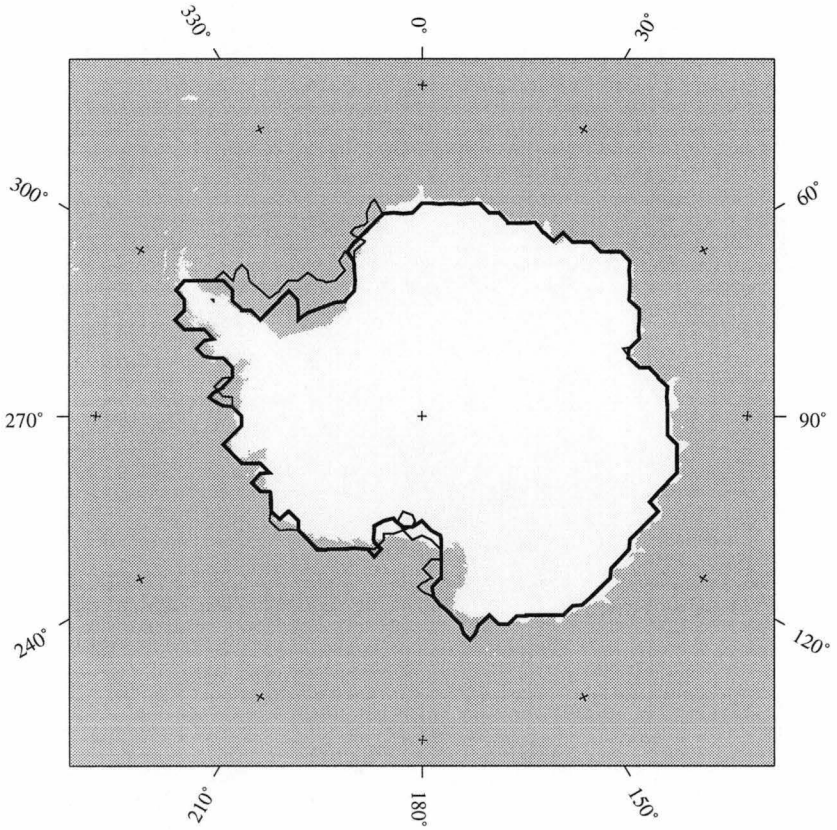

Fig. 7.9: Grounding lines for the 'crust + 30 km' model (thin line) and the standard earth model (thick line) at 80 kyr BP.

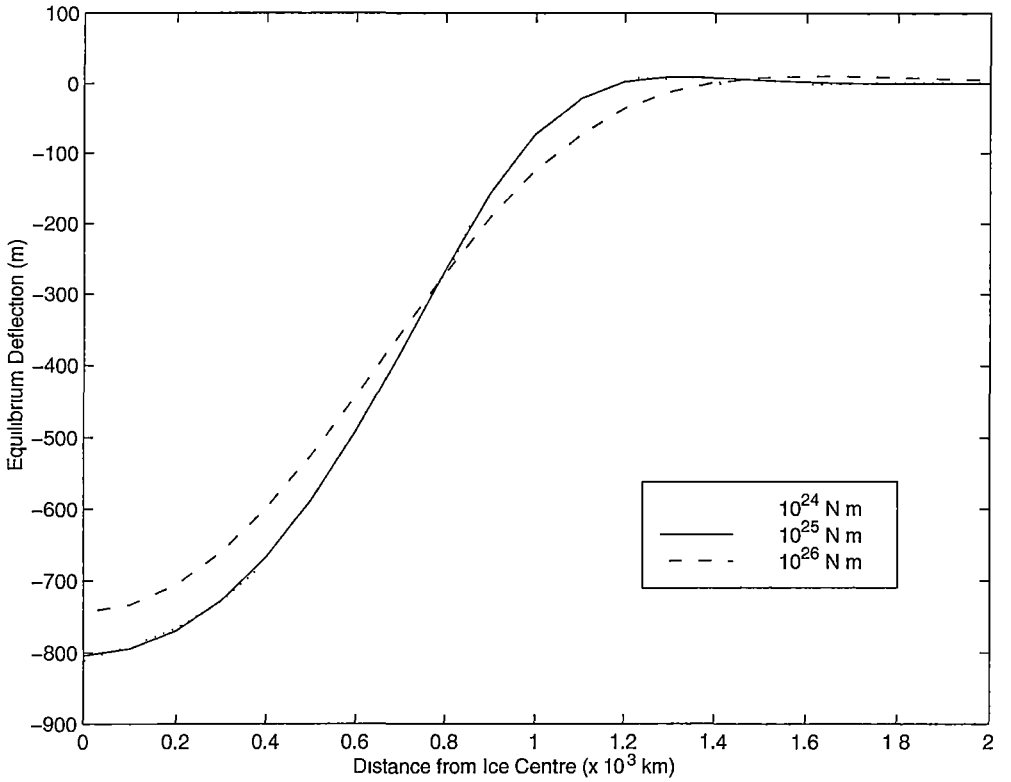

Fig. 7.10: Equilibrium deflection for a parabolic profile ice sheet for differing but uniform lithospheric rigidities.

7.4 Ice Volume Differences

It can be seen from Figures 7.4 and 7.7 that the ice volumes generated from the 'crust × 4','crust × 2' and 'crust + 30 km' models are at times much greater than that of the standard uniform thickness model. Referring to Tables 7.1 and 7.2, these turn out to be cases where the average value of lithospheric rigidity deviates most from the standard 10^{25} N m model.

Returning for a moment to the case of uniform lithospheric rigidity, Figure 7.10 is a similar calculation to that shown earlier in Figure 3.3. Basically it shows the different equilibrium deflection profiles caused by an ice sheet of parabolic profile, for three different values of lithospheric rigidity. In this case the dimensions of the ice sheet were chosen so as to resemble the Antarctic ice sheet (3 km central thickness and 1000 km radius).

The differences in deflection at the ice sheet edge due to the different rigidi-

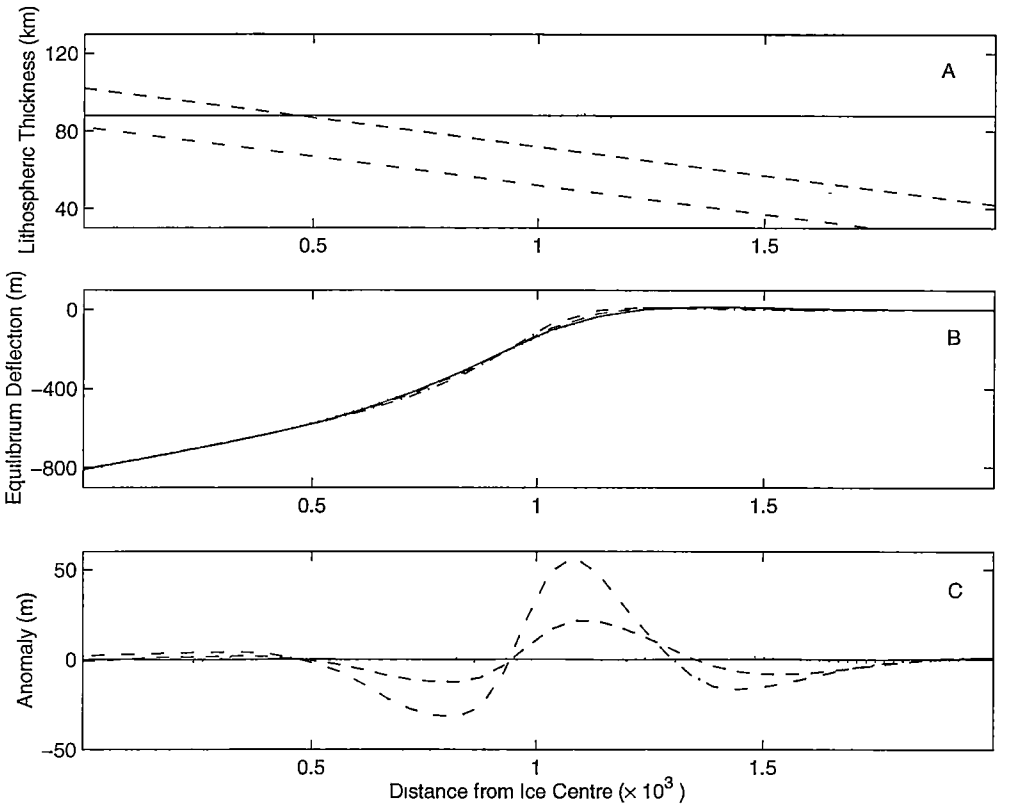

Fig. 7.11: Figure A shows the thickness distribution for each lithosphere model. The distribution is chosen to resemble the cases of crust plus a constant. Figure B shows the equilibrium deflection (m) from the application of the ice sheet. Figure C shows the deflection anomaly (m) from the uniform rigidity lithosphere model.

ties are of the order of 50-100 m. This difference is important because in the case of the Antarctic ice sheet the ice edge is effectively the grounding line in places such as the Amery and Ronne ice shelves. As both of these ice shelves are shallow, differences of 50-100 m at the grounding line can significantly effect the flow of the overall ice sheet.

Figure 7.11 B shows the equilibrium deflection calculated in the same manner as for Figure 7.10 but for non-uniform lithospheric thickness models with thickness distributions given in Figure 7.11 A. The thickness profiles were chosen to resemble the case where lithospheric thickness is assumed to be equal to crustal thickness plus a constant value. Figure 7.11 C presents the equilibrium deflection as an anomaly from that calculated for a uniform lithosphere model

with 10^{25} N m rigidity.

Figure 7.11 C shows that large differences in equilibrium deflection from the uniform model (of the order of 50 m) are predicted by the non-uniform rigidity models, both at the ice edge itself and also well outside the ice sheet edge. Figure 7.11 C is important because it shows that in general the maximum differences in the calculated equilibrium deflection occur to the front (that is outside) of the ice sheet. The positions of these maxima occur at 100 km beyond the ice sheet edge. For the present day Ronne and Amery ice shelves a distance of 100 km is well within the geographic extent covered by these shelves. For deflection differences of magnitude 50 m the maxima can enhance the ice shelf grounding by raising the sea floor elevation until contact with the base of the ice shelf occurs. With this enhanced grounding a greater volume of ice develops around the ice shelf.

Figure 7.12 shows a cross section of the Ronne ice shelf at different times for the uniform rigidity model and the 'crust × 4' model. At 160 kyr BP (the start of the model run) the ice shelves are the same. At 140 kyr BP the 'crust × 4' model experiences an enhanced grounding on the continental shelf compared to the uniform model. This enhanced grounding generates a thicker ice sheet at 80 kyr. However with the increase in sea level the shelf ungrounds for both models so that at present day the ice shelves are similar to each other.

7.5 Conclusions

An increase in ice sheet volume generated by the non-uniform models compared to the uniform model occurs only for 3 of the 6 non-uniform cases examined in the present study. These are the 'crust × 4' model (between 135 and 70 kyr BP), the 'crust × 2' model (between 60 kyr BP and the present day) and the 'crust + 30 km' model (between 120 and 20 kyr BP). These 3 cases have an average value of lithospheric rigidity significantly different from the standard 10^{25} N m uniform model (see Tables 7.1 and 7.2). That is, the advanced grounding shown by these three models could result from the fact that the average lithospheric rigidity is much too low or much too high.

However it is also true that the standard uniform value of 10^{25} N m has

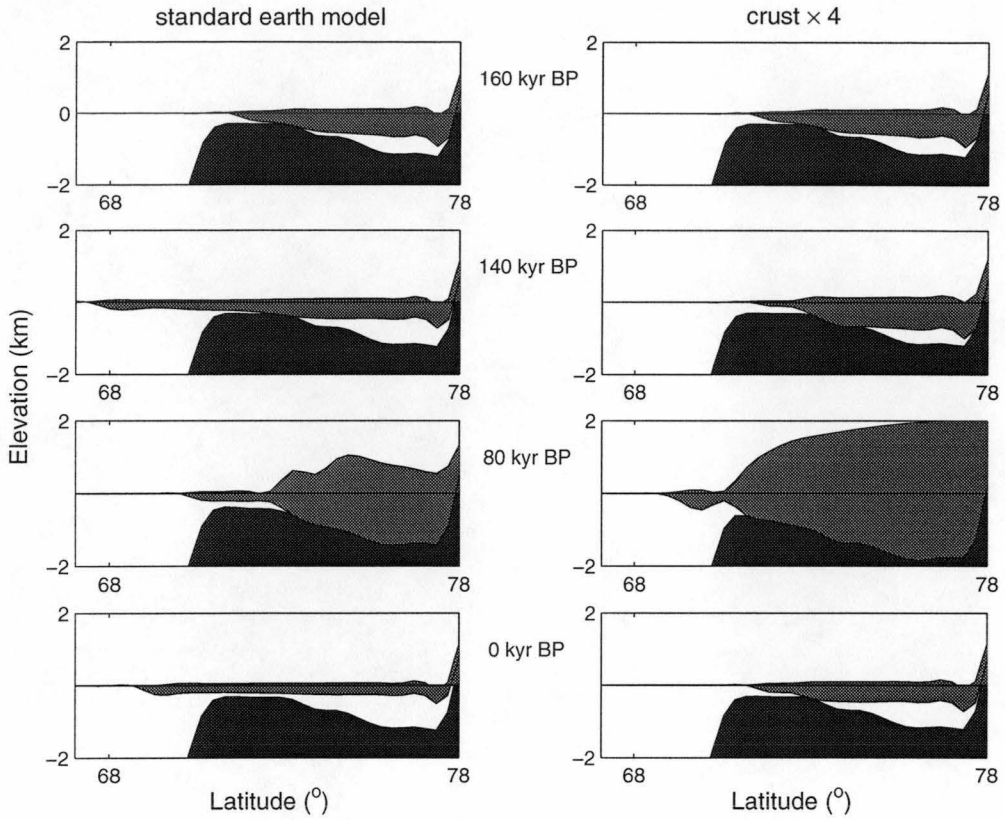

Fig. 7.12: Bedrock topography, ice shelf thickness and ice shelf elevation as a function of time for a cross section through the Ronne ice shelf. The continental shelf is the dark shading and the ice shelf is the light shading

been determined from observations of relative sea changes at coastal locations in continental margins. Observations further out towards the continental shelf are difficult because the data has been submerged by the increase in sea level since the last ice age. It is therefore possible that use of a lithospheric rigidity value close to 10^{25} N m could be inappropriate near the Ronne and Amery ice shelves. Kaufmann and Wolf (1996) report that for the Svalbard Archipelago values of lithospheric thickness between 0 and 200 km are found to satisfy the relative sea level data. The most general conclusion from the results presented here is that ice sheet models using isostatic schemes incorporating models of uniform lithospheric rigidity may underestimate the extent of ice shelf grounding.

8. ICE SHEETS AND SEA LEVEL

The Milankovitch theory of ice ages suggests that the summer solar insolation over the Northern Hemisphere dominates the advance and retreat of the Northern Hemisphere ice sheets with the corresponding change in sea level driving the Antarctic ice sheet in the Southern Hemisphere. The ice sheet changes are considered to be globally synchronous between hemispheres (Huybrechts, 1990b). This chapter describes an attempt to model the global situation of ice volume and eustatic sea level change since the last ice age. This is achieved by linking the Laurentide, Fennoscandian and Antarctic ice sheets through a common first-order representation of eustatic sea level change. There are two major reasons for this attempt. The first is to generate Northern Hemisphere ice sheets at 21 kyr BP without using the constraints on ice extent and eustatic sea level which were imposed in Chapters 5 and 6. The second is to examine the apparent underestimate of global eustatic sea level change that was found in those chapters. Lambeck (1993a) notes that 'best fit' global deglaciation chronologies used with sophisticated models of glacial isostasy underestimate global ice volume changes by up to 60 m. This chapter examines whether this underestimation could result from the neglect of realistic ice sheet dynamics in models of glacial isostasy.

8.1 Climatological Forcing

A global model of ice sheet changes and a climatological forcing scheme is required. For the present study a climatological forcing scheme is adopted from the radiation/albedo model of Budd and Smith (1981). They contend that the primary controls on the growth and retreat of the Northern Hemisphere ice sheets are the summer solar insolation inputs over the region and the albedo of the ice sheets themselves. The temperature changes in the region are calculated

from changes in solar insolation and ice sheet albedo, and these temperature changes are then used to determine the amount of ablation (surface melt) that occurs over the ice sheet. The equation used to calculate the temperature change over the ice sheet is

$$\Delta\theta(\phi,t) = \beta_1 \Delta R(\phi,t) - \beta_2 \frac{S(t)}{S_m} \tag{8.1}$$

where $\Delta\theta(\phi,t)$ is the temperature change from the present day, $\Delta R(\phi,t)$ is the summer insolation difference from the present day, $S(t)$ is the ice sheet surface area at time t, S_m is the maximum surface area of the ice sheet, β_1 is the constant of proportionality between radiation difference and temperature change, β_2 is the constant of proportionality between albedo change and temperature change and ϕ is Northern latitude.

The second term on the right hand side of Equation 8.1 represents the change in temperature that results from ice sheet albedo change. When the ice sheet is at maximum extent the temperature is lowered uniformly over the model domain by a value of β_2 (which has the units of °C). The maximum extent of the ice sheet is defined in the present study by the surface area of the ice sheets at 21 kyr BP in the ICE4G chronology (see Figures 5.5 and 6.2).

The first term on the right hand side of Equation 8.1 represents the change in temperature that results from the solar insolation difference. The insolation difference can be determined for any latitude and time by making use of the earth's variations in orbital eccentricity, precession and obliquity (Berger et al., 1993). For this study they are taken from Vernekar (1972) and are illustrated in Figure 8.1.

In the Budd and Smith model the temperature changes are used to specify changes in the elevation of the snow line (shown schematically in Figure 2.1 in the literature review) as a function of time. Equation 8.2 is used here to convert temperature changes to changes in the snow line elevation through the lapse rate

$$\Delta e(\phi,t) = -\frac{\Delta\theta(\phi,t)}{6.5} \tag{8.2}$$

where $\Delta e(\phi,t)$ is the change in the snow line elevation in kilometres. Absolute values for the present day snow line elevation have been determined empirically

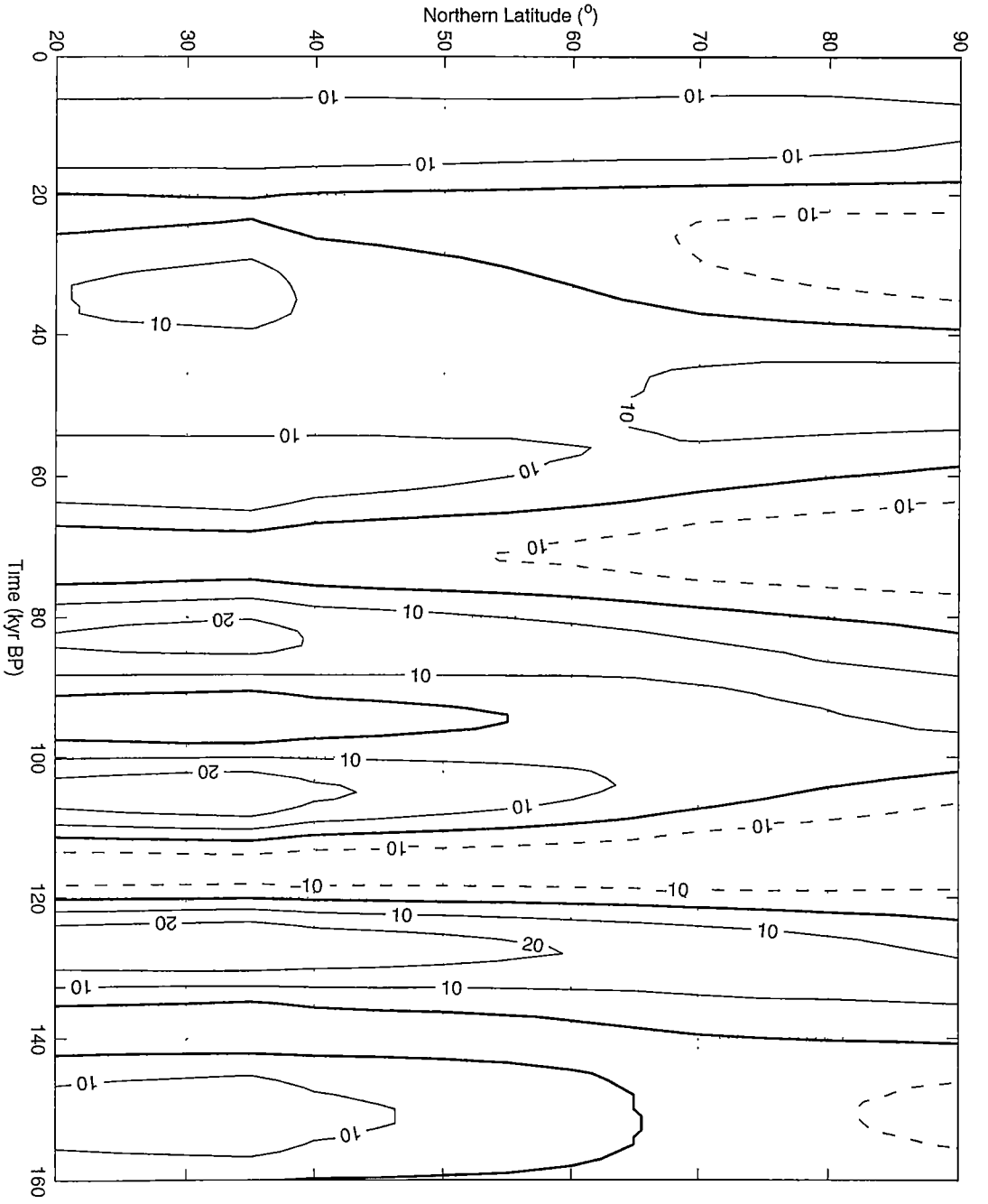

Fig. 8.1: Summer solar insolation difference (W m^{-2}) from the present day as a function of time (160 kyr BP to the present) and latitude.

as a function of latitude (Budd & Smith, 1981). Table 8.1 lists the elevations at which present day glaciers experience a 1 m yr^{-1} ablation rate, which for present purposes is defined as the snow line e_0.

The ablation rate is determined by the deviation of the snow line from its

Latitude (°)	e_0 (m)
90	0
80	500
70	900
60	1700
50	2600
40	4200
30	5100

Tab. 8.1: Latitude dependent elevation of the 1 m yr^{-1} ablation rate.

present day elevation from the following equation.

$$A(\phi, t) = 10^{\left(\frac{e_0 - e(t) - \Delta e(\phi, t)}{m}\right)} \tag{8.3}$$

where $A(\phi, t)$ is the ablation rate, e_0 is the present day snow line elevation, $e(t)$ is the ice sheet elevation, $\Delta e(\phi, t)$ is the change in the snow line calculated from Equation 8.2 and m=1200 m.

The climatological forcing scheme is summarised as follows. At each time step the ice sheet albedo and solar insolation changes are used to calculate the temperature change through Equation 8.1. This temperature change is then converted to a snow line elevation change according to Equation 8.2 and a corresponding change in the ablation rate through Equation 8.3. The ablation rate is then subtracted from the precipitation rate to produce a net accumulation rate of ice over the model domain. The precipitation rates used in the study are the same as used in Chapters 5 and 6.

This climatological forcing is used for the Northern Hemisphere ice sheets. For the Antarctic ice sheet ablation is considered to be minor and is neglected. The only factor considered to control the Antarctic ice sheet in this chapter is change in eustatic sea level. In this chapter the Laurentide and Fennoscandian ice sheets are driven by the climate forcing just described and the Antarctic ice sheet is coupled to them via first-order changes in eustatic sea level. The coupling method is outlined in the next section.

8.2 Coupling of Eustatic Sea Level

The most straightforward method of coupling the three ice sheets is to use the model domains shown in previous chapters and sum the eustatic sea level contributions from each ice sheet at each time step. This coupling ignores ice volume contributions from regions outside these particular model domains. However the three domains enclose most of the global ice extent defined in ICE4G. The ice sheet models are run synchronously and at each time step a eustatic sea level contribution from each ice sheet is determined. The overall sum of eustatic sea level change is then returned to each ice sheet model as a sea level height correction. The most serious shortcoming is the neglect of isostatic adjustment of ocean basins. Lambeck (1993a) estimates that the global eustatic sea level changes recorded at sites such as Papua New Guinea underestimate changes in global ice volume because ocean basin adjustment accounts for about 20 m of equivalent ice volume. This is because the influx of meltwater from the retreating ice sheets depresses the ocean floor. Thus the present study overestimates global eustatic sea level change by up to 20 m.

There is not necessarily a one-to-one relation between total ice sheet volume change and eustatic sea level change. The changes in volume referred to in previous chapters are of total ice volume. Ice that is floating or ice that is grounded below sea level does not contribute to eustatic sea level. The ice volume that contributes to a net eustatic sea level change is defined as the 'volume above floating'. For a column of ice grounded below sea level the ice volume that contributes to eustatic sea level change is:

$$V_{esl} = h + d\frac{\rho_{sw}}{\rho_i} \tag{8.4}$$

where V_{esl} is the volume of the column of ice above floating, h is the total height of the ice sheet column, d is the depth of the column below sea level, ρ_{sw} is the density of sea water and ρ_i is the density of ice.

In this manner changes in V_{esl} from one time step to the next represent a net exchange of water between the ocean and the ice sheet. By applying this equation at every grid point of the ice sheet it is possible to relate the net exchange of water to the ocean with the total volume of ice.

8.3 Initial Conditions

All model runs presented here simulate the time between 160 kyr BP and the present day. The initial conditions for the North American and Northern European continental surface topographies are the isostatic equilibrium profiles deduced from Chapters 5 and 6. These topographies are generally higher than the present day elevation of these regions. Budd and Smith point out that this is an important factor as the higher elevations produce 'seed' locations for glacier inception from which the ice sheets can grow. For the Antarctic ice sheet the equilibrium situation defined in Chapter 4 (see Figures 4.3 and 4.4) is used as the initial condition.

8.4 Isostatic Parameters

The earth model parameter values relevant to the Northern Hemisphere ice sheets derived in Chapters 5 and 6 are used in the present simulations. For the Antarctic ice sheet the standard earth model parameters suggested in the previous chapter (uniform 2×10^{21} Pa s mantle viscosity and uniform 10^{25} N m lithospheric rigidity) are used.

8.5 Results

Figure 8.2 shows the time-dependent changes in the volume of 'above floating' ice for each of the three linked ice sheets using the technique described above. The proportionality coefficients required when using Equation 8.1 were those of Budd and Smith (1981), namely $\beta_1 = 0.4°/\text{W m}^{-2}$ and $\beta_2 = 4.7°$.

The changes in Northern Hemisphere ice sheet volume show approximately 40 kyr cycles of ice sheet growth and decay. The 100 kyr cycle characteristic of the Pleistocene era is not produced in the simulation. As the 40 kyr obliquity period is most dominant in the insolation data (Figure 8.1) this result suggests that radiation forcing dominates the albedo feedback, and the proportionality constants need to be adjusted in order to provide a more realistic situation. As the Budd and Smith value of β_2 was derived from the output of a paleoclimate general circulation model it is likely to depend on the characteristics of that

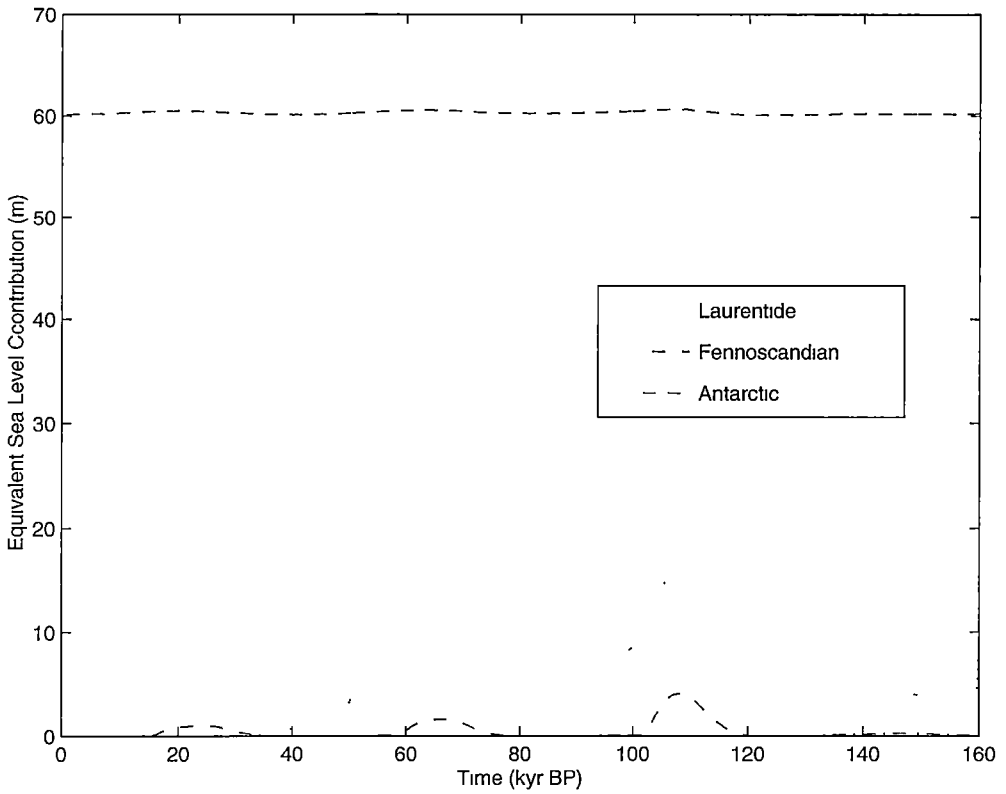

Fig. 8.2: Time-dependent change in 'above floating' ice volume as an equivalent eustatic sea level contribution for the Laurentide, Fennoscandian and Antarctic ice sheets with the β values of Budd and Smith (1981).

model. For this reason the value of β_2 was increased here for both Northern Hemisphere ice sheets until the observed 100 kyr ice advance and retreat was reproduced by the model. Figure 8.3 shows the changes with time of the ice sheet volume with $\beta_2 = 6.8°$ for the Laurentide ice sheet and $\beta_2 = 6.4°$ for the Fennoscandian ice sheet.

The ice sheet albedo acts as a positive feedback to the radiation changes. During periods of negative radiation change the temperature drops and the ice sheet advances. The increase in ice sheet surface area increases the albedo which decreases the temperature further. This amplification ensures that the ice sheet growth and retreat is sensitive to β_2.

Figure 8.3 suggests a total eustatic sea level contribution from the melting of the ice sheets since the last ice age (that is between 21 kyr BP and the present day) of 140 m. This value is 10 m higher than the value suggested by

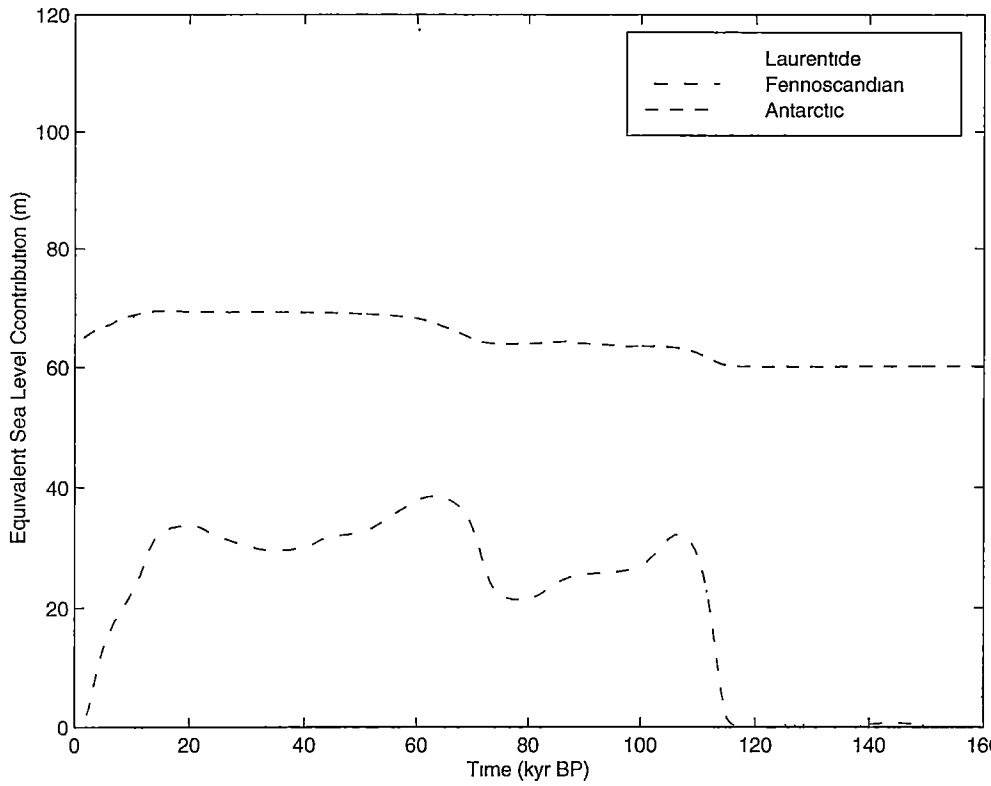

Fig. 8.3: Time-dependent change in 'above floating' ice volume as an equivalent eustatic sea level contribution for the Laurentide, Fennoscandian and Antarctic ice sheets with $\beta_2 = 6.8°$ for the Laurentide ice sheet and $\beta_2 = 6.4°$ for the Fennoscandian ice sheet.

Chappell and Shackleton, but is an underestimate by up to 10 m when one takes into account Lambecks' suggestion of a reduction in observed eustatic sea level due to ocean basin adjustment. The Antarctic ice sheet contributes only about 5 m to sea level change since the last ice age according to this simulation. In previous chapters the Antarctic ice sheet makes a negative contribution to sea level. This change suggests that for the Antarctic ice sheet model used in the present section the mass increase due to snow accumulation is less than the mass decrease due to calving at the ice sheet edge.

The timing of the changes in ice sheet volume shown in Figure 8.3 is not supported by the ICE4G ice extent chronology. The ICE4G data suggest that over the last 21 kyr BP the Fennoscandian ice sheet deglaciated before the Laurentide ice sheet. Figure 8.3 suggests that the Fennoscandian ice sheet continued

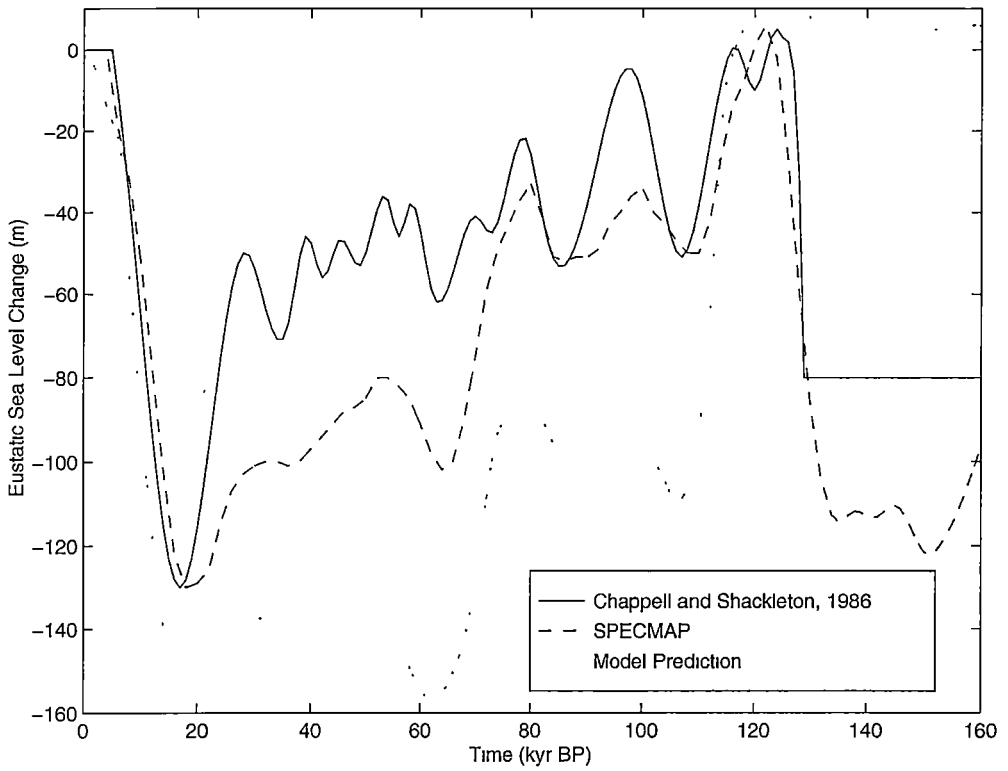

Fig. 8.4: Model predicted change in global eustatic sea level over the last glacial cycle using new values of β_2. Also shown are the global eustatic sea level curve of Chappell and Shackleton (1986) and the SPECMAP eustatic sea level curve (Martinson et al, 1987).

deglaciating well after the Laurentide ice sheet had completely retreated. It should also be noted from Figure 8.3 that the sawtooth waveform of ice sheet growth (from 110 kyr BP to 20 kyr BP) and retreat (20 kyr BP to 10 kyr BP) reflected in the global eustatic sea level curve of Chappell and Shackleton is not found in the present simulation.

8.5.1 Eustatic Sea Level Change

Figure 8.4 shows the model-predicted eustatic sea level change, the observed eustatic sea level change according to Chappell and Shackleton, and the observed eustatic sea level change of 'SPECMAP' (Martinson et al., 1987). In terms of the advance and retreat of the ice sheets the present model prediction is qualitatively more like the SPECMAP sea level data than the data of

Chappell and Shackleton. The 70 m drop in sea level at 70 kyr BP shown in the SPECMAP record is also a feature of the model used here. However the SPECMAP record still suggests a more sawtoothed form of ice sheet advance and retreat than the model. There is also a phase lag of a few kyr between the sea level highs and lows of SPECMAP and those of the model prediction. Chappell and Shackleton (1986) note that the uplift at the Huon Peninsula used to generate their eustatic sea level curve is more accurate for times of high sea level (for example at 6 kyr BP) than times of low sea level (for example at 18 kyr BP). For this reason the amplitudes of eustatic sea level change for the Chappell and Shackleton data are not well constrained.

8.5.2 Last Glacial Maximum

Figures 8.5 and 8.6 show the model predictions of the elevations of the Laurentide and Fennoscandian ice sheet at 21 kyr BP. The extents of both ice sheets are similar to those of ICE4G at the same time (see Figures 5.5 and 6.2). However for the Laurentide ice sheet the south-west corner extends further south than indicated by ICE4G. It is probable that the problem here is with the ICE4G dataset rather than the model, which can specifically simulate the influence of the Rocky Mountains. The model-simulated Laurentide ice extent coverage is also much more extensive in Alaska than suggested by ICE4G. In this case the problem is thought to be with the ice sheet model (as will be shown in the next section). In Figure 8.6 it is seen that the southernmost extent of the ice of the Fennoscandian ice sheet is apparently entirely determined by the latitude dependence of the snow line. The ice edge closely follows the 48 °N line of latitude. This is because the topography of the Northern European region is generally flatter than the North American region.

Both figures suggest that at this time of maximum extent (21 kyr BP) both Hudson Bay and the southern end of the Gulf of Bothnia experienced some degree of marine incursion. Most deglaciation chronologies reconstruct the ice sheet summits close to both Hudson Bay and the Gulf of Bothnia. In this study the present day surface topography is modified by the estimate of present day remaining uplift (obtained from the results of Chapters 5 and 6) to generate the

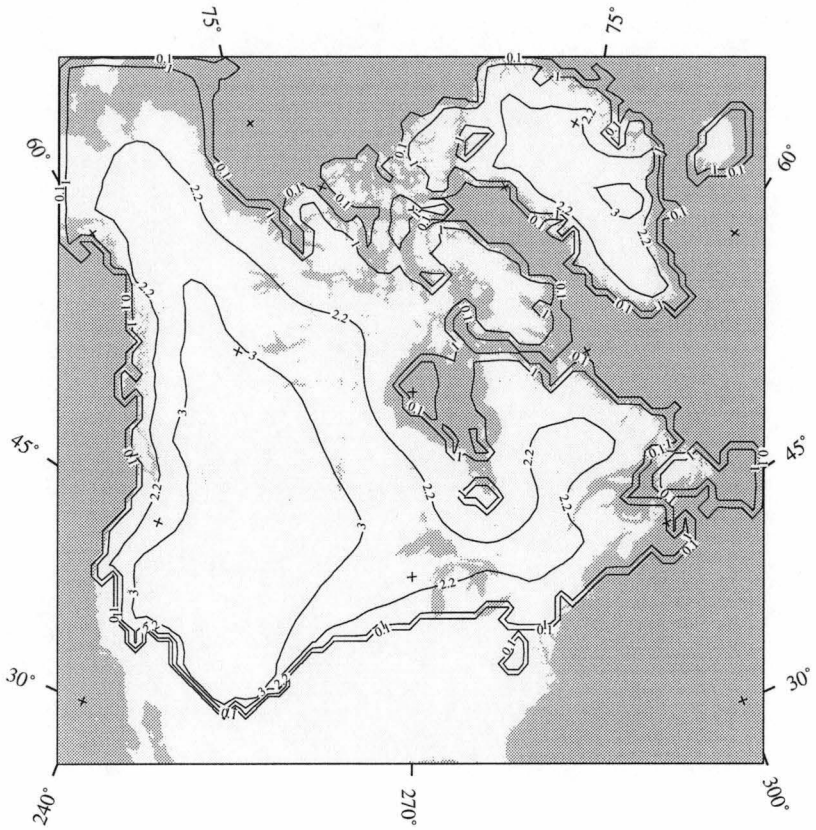

Fig. 8.5: Model prediction of Laurentide ice sheet elevation at 21 kyr BP.

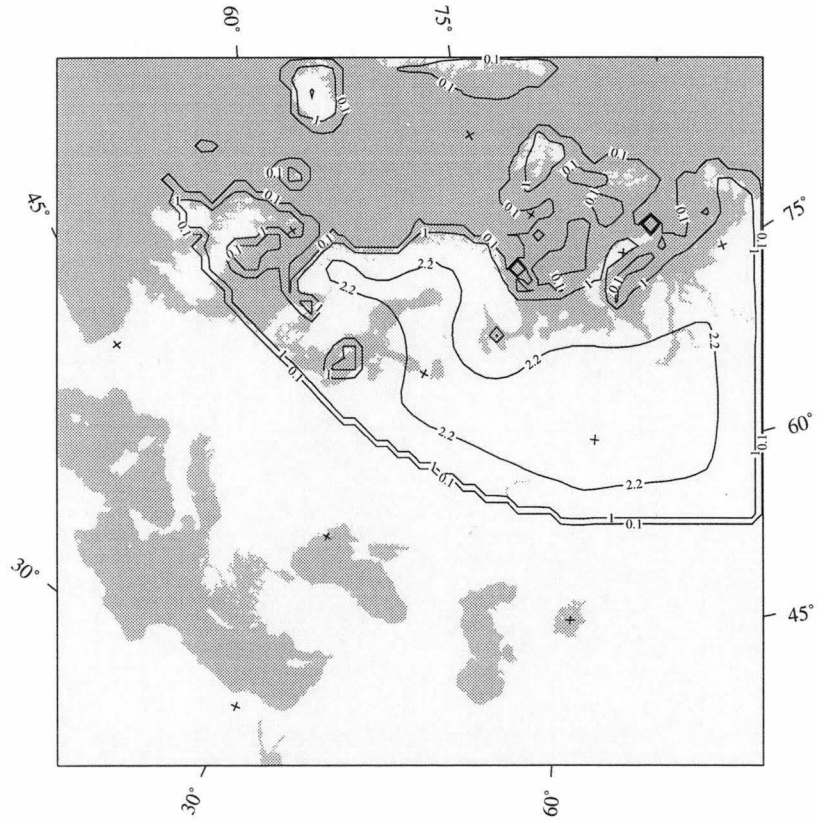

Fig. 8.6: Model prediction of Fennoscandian ice sheet elevation at 21 kyr BP.

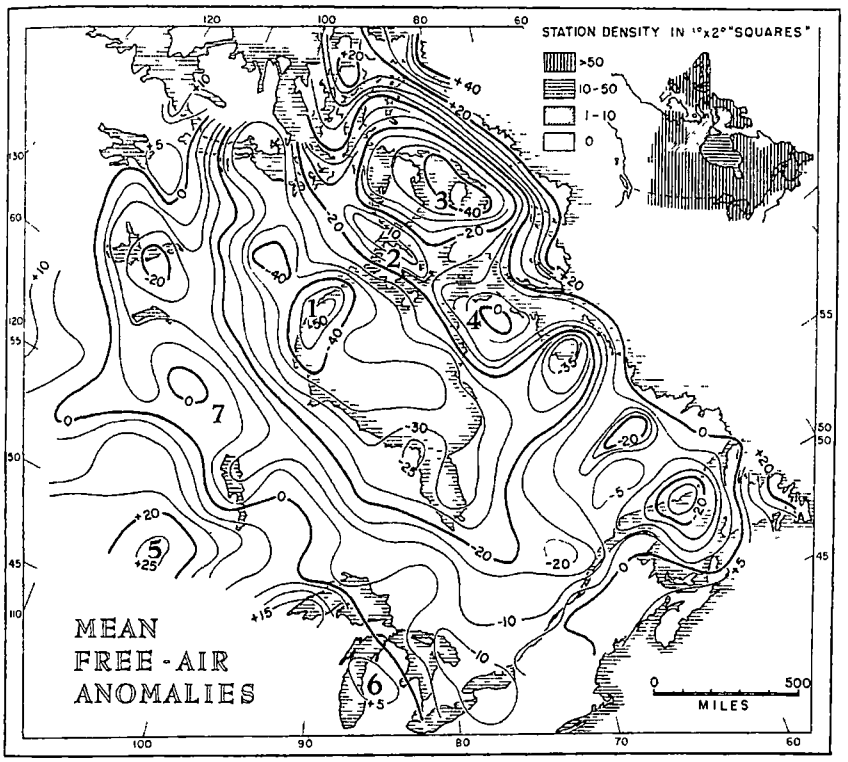

Fig. 8.7: Free air gravity anomaly (mgal) over North America from Walcott (1970).

isostatic equilibrium profile which is used as the initial conditions at 160 kyr BP according to Equation 3.6. For Hudson Bay this estimate is 50 m of remaining uplift for equilibrium. At 21 kyr BP the model predicts an eustatic sea level lowering of 140 m compared to the present day which (without accounting for isostasy) implies an elevation of at least 180 m above sea level at that time compared with present day sea level. Peltier (1982) concludes that there is about 300 m of remaining uplift for Ottawa Island in Hudson Bay. If he is correct it is therefore possible that the initial conditions relating to surface topography used in the present study underestimate the elevation at which isostatic equilibrium prevails. As at present the maximum depth of Hudson Bay is 400 m this possible underestimate could be responsible for the marine incursions shown in Figures 8.5 and 8.6. This underestimate is probably a result of not incorporating a realistic density profile of the inner earth in the isostatic model used in the present study. However the North American free air gravity anomaly map of Walcott (1970) shown in Figure 8.7 combined with the analysis

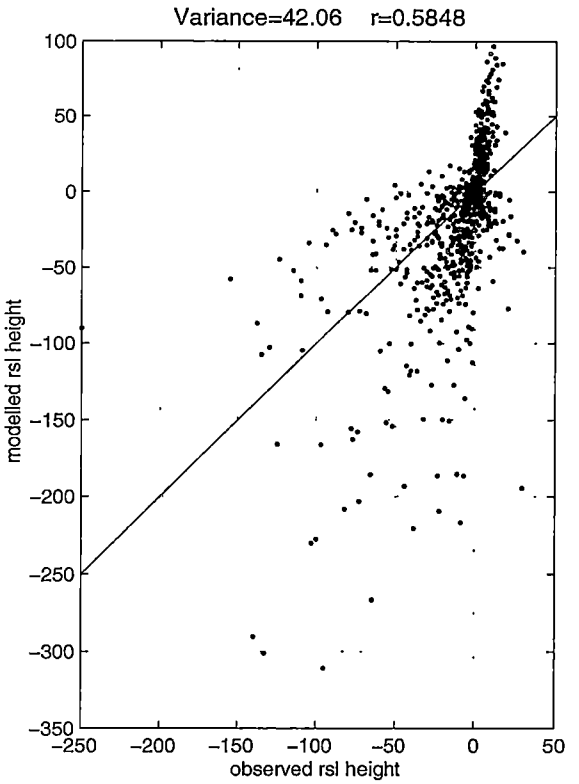

Fig. 8.8: Observed and predicted relative sea level heights for both the Laurentide and Fennoscandian isostatic adjustment.

presented in Chapter 4 (Equation 4.5) would suggest a value more like 100 m of remaining uplift in Hudson Bay. From amino acid analysis of shells in Southern Hudson Bay, Andrews et al (1983) suggest that the region was ice free at 35, 75 and 105 kyr BP. This finding would suggest that at these times the elevation of Hudson Bay was either close to or below sea level. The Andrews et al result is interesting considering that for the model prediction with $\beta_2 = 4.7°$ these times correspond to ice free conditions (see Figure 8.2).

8.5.3 Isostatic Adjustment

Figure 8.8 is a plot of the observed versus predicted relative sea level heights over the last 7 kyr for the observation points used in Chapters 5 and 6 (ie from the Laurentide and Fennoscandian ice sheets). The calculation used to generate Figure 8.8 is simpler than that presented in Chapters 5 and 6 because the iterative scheme used in those chapters to constrain the model to produce

the observed present day topography is not applicable in the present section. It should also be noted that in this section the model predicts its own eustatic sea level change instead of the observed change of Chappell and Shackleton used in Chapters 5 and 6. As the relative sea level change is the sum of isostatic and eustatic sea level changes the results of Figure 8.8 relate not just to the model prediction of isostatic adjustment but also to the model prediction of eustatic sea level change.

The correlation coefficient between prediction and observation in Figure 8.8 is 0.58, so the match is not statistically significant. There is a large degree of both under- and over-estimation. The overestimation is associated with regions of relatively thick ice and times of comparatively late deglaciation (see Figure 8.3). This is understandable given that the ice sheets are on average 4 times the volume of the 'best fit' chronologies generated in Chapters 5 and 6. The underestimation is associated with only partial ice coverage and the overall increased magnitude of eustatic sea level contribution (see the top right hand corner in Figure 8.8).

Figures 8.9 and 8.10 show the geographic distribution of error between the relative sea level prediction and observation shown in Figure 8.8. For the Laurentide adjustment most of the overestimation occurs in North-Western Canada and Alaska. Figure 8.5 shows that the climatology scheme used here predicts that this region was ice covered at 21 kyr BP whereas ICE4G suggests that it was mainly ice free (see Figure 5.5 in Chapter 5). The James Bay site is underestimated but sites in Western Hudson Bay are overestimated. The underestimation in Eastern Hudson Bay casts some doubt on the model prediction of marine incursion in Hudson Bay at 21 kyr BP. Underestimation also occurs along the south-east coast of America due to the increase in eustatic sea level change and only partial coverage of the region. Figure 8.5 suggests that the southeastern extent of the ice sheet only extends slightly past the Great Lakes at maximum extent. ICE4G suggests an ice sheet coverage further south (see Figure 5.5 in Chapter 5). The thicker ice sheet also produces a greater peripheral submergence in this region which contributes to the underestimation. Figure 8.10 shows that all of the adjustment in Northern Europe is overesti-

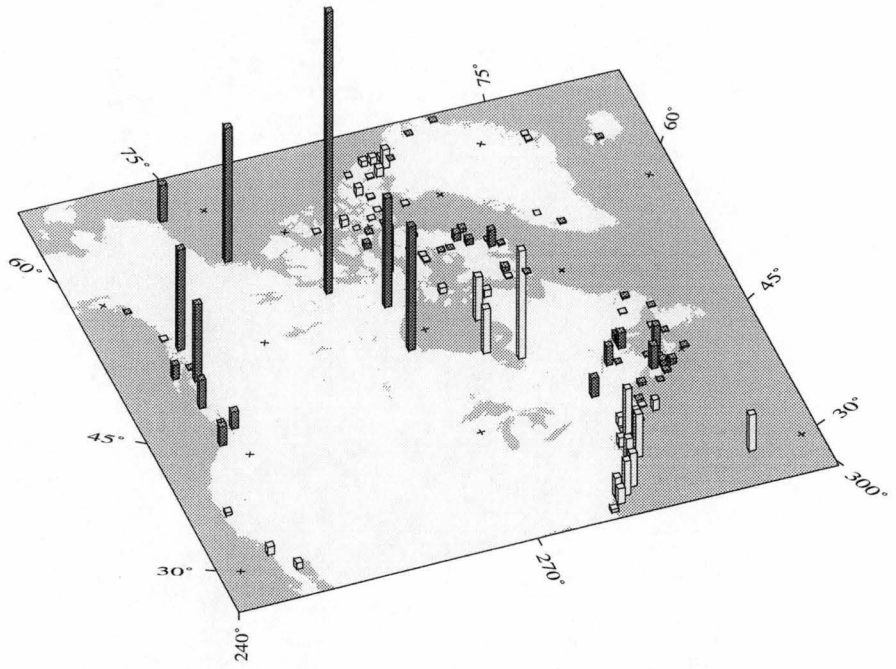

Fig. 8.9: Geographic distribution of error between observed and predicted sea level heights at individual sea level locations for the Laurentide ice sheet.

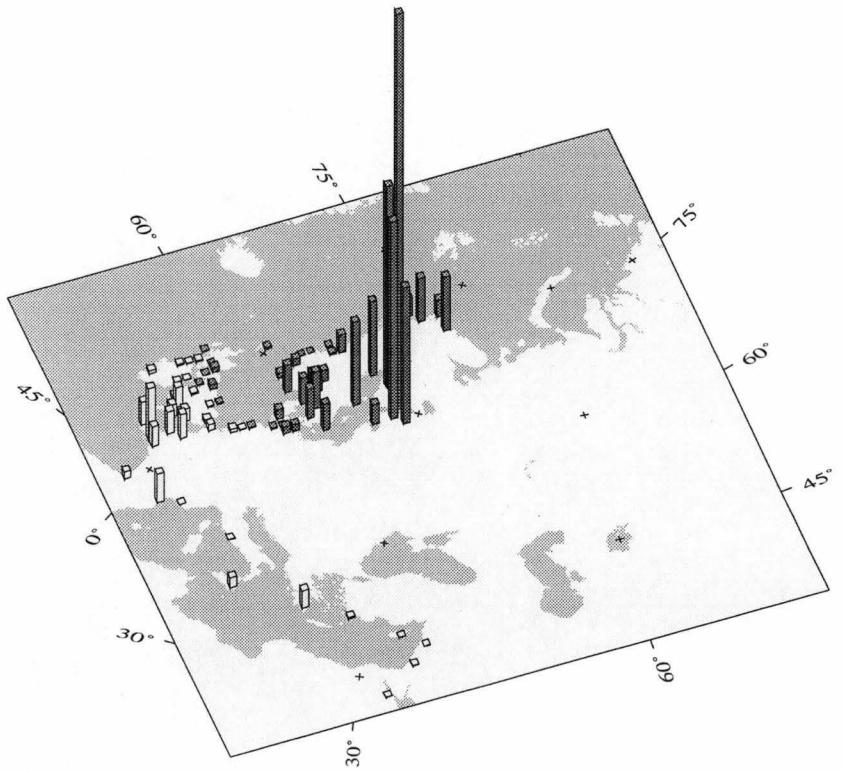

Fig. 8.10: Geographic distribution of error between observed and predicted sea level heights at individual sea level locations for the Fennoscandian ice sheet.

mated. This is due to a combination of a thicker ice sheet and later deglaciation. Near the United Kingdom there is underestimation. This is thought to be due to the increase in eustatic sea level and peripheral submergence resulting from the retreat of the thicker Fennoscandian ice sheet on mainland Europe.

8.6 Conclusions

The climatologically driven coupled model of the three combined ice sheets produces a good simulation of the eustatic sea level change over the last 21 kyr since the last ice age - that is a rise of the order of 130m. The model also produces an ice sheet extent at 21 kyr BP similar to that of ICE4G. However it does not produce good relative sea level changes (that is sea level change associated with isostatic adjustment) over the last 7 kyr for which the relative sea level data can be used. The relative sea level changes have the same order of magnitude as the observations, but have a greater spread of error than the model predicted relative sea level changes in Chapters 5 and 6. This is to be expected considering that the rigorous constraints imposed on the ice sheets in Chapters 5 and 6 are not imposed in the present model. Most of the relative sea level error associated with the climatologically driven model occurs because there are regions in the domain where the ice sheet is much thicker than that determined from the ICE4G constrained models. The comparison between observation and model prediction for the specific site of Churchill in Hudson Bay is shown in Figure 8.11.

The dot-dashed line in Figure 8.11 represents the model prediction of isostatic adjustment using the 'best fit' deglaciation chronology in Chapter 5. The solid line is the prediction of isostatic adjustment at Churchill using the climatology model used in this chapter. The overestimation at Churchill in this chapter results from an increased level of isostatic adjustment caused by an ice sheet which is too thick. The difference in isostatic deflection at 21 kyr BP is 200 m which suggests that the ice sheet thickness generated using the climatology model is 750 m too thick at this location. Figure 8.11 also shows that for the climatologically driven model the ice sheet thickness change starts at 14 kyr BP whereas for the ICE4G driven model the ice sheet thickness change

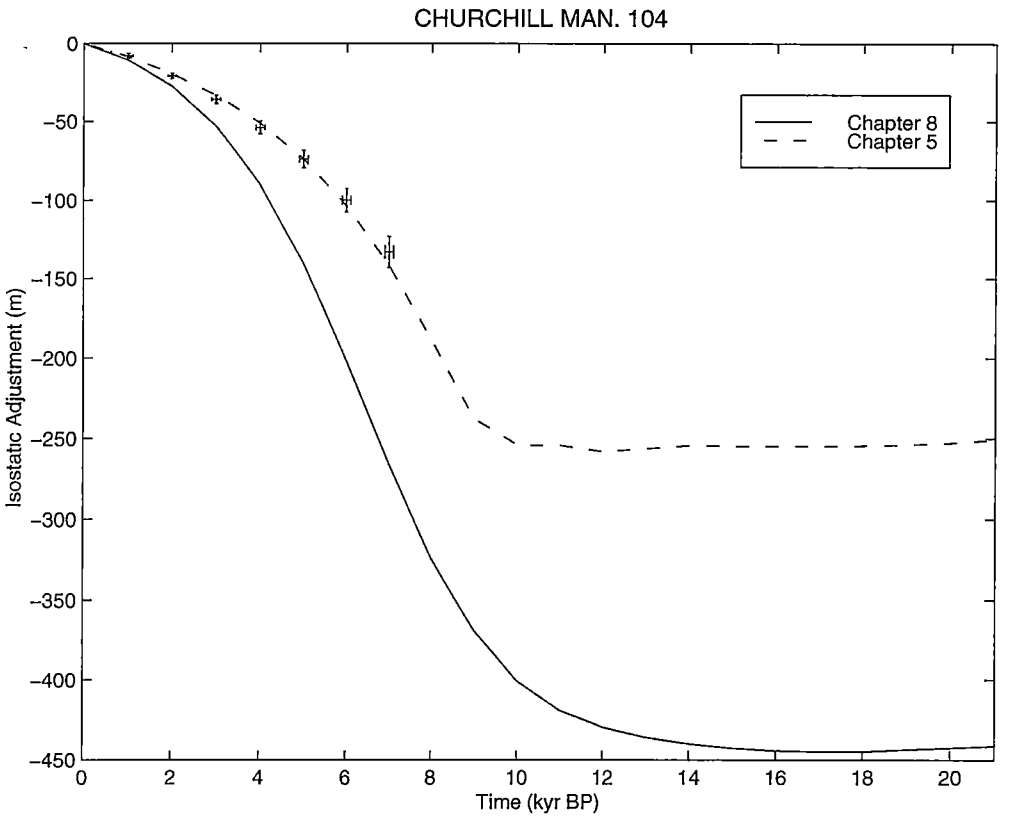

Fig. 8.11: Model prediction of isostatic adjustment at Churchill since the last ice age. Dot-dashed line is prediction from 'best fit' deglaciation chronology for the Laurentide ice sheet in Chapter 5. Solid line is the prediction of adjustment for the climatological model used in this chapter.

starts at 10 kyr BP.

This chapter, where the ice sheet model is driven using a realistic climatology scheme, has produced a reasonable reproduction of the observed eustatic sea level changes but a poor reproduction of the observed relative sea level changes. In Chapters 5 and 6 where the ice sheet model is driven using the ice extent changes, a good reproduction of relative sea level changes is found but with a poor reproduction of the eustatic sea level changes. There are at least four possible explanations for the differences.

First it is possible that the errors in relative sea level relate more to inaccuracies in the timing of ice sheet deglaciation rather than ice sheet size. Figure 8.11 shows that when the ice sheet model is forced by the ICE4G chronology of ice extent then large changes in ice volume only begin to occur at 10 kyr BP.

When the ice sheet model is forced by a realistic climatology then large changes in ice volume begin to occur at 14 kyr BP. The ICE4G forcing occurs at the ice sheet edge, whereas the climatological forcing occurs over the entire ice sheet surface. The results presented here for the Fennoscandian ice sheet, with late deglaciation (Figure 8.3) and overestimation (Figure 8.10) would suggest that the relative sea level overestimation could result from the timing of ice sheet deglaciation.

Second it is possible that the ice sheet volumes presented in Chapters 5 and 6 are reasonable, but there were additional large ice sheets on the earth's surface during the last ice age that are not included in the ICE4G deglaciation chronology. In this instance the ice sheet volumes determined in the present chapter would be too large. Grosswald (1988) estimates that the Northern Hemisphere ice sheet contribution to eustatic sea level was 160 m, but originated from ice sheets in North America, Northern Europe and also a large Eastern Siberian ice sheet. The ice sheet models of Marsiat (1994) and Fastook and Hughes (1991) predict that Siberia was fully glaciated at 21 kyr BP. However to be consistent with the results of Chapters 5 and 6, the Siberian ice sheet would have had a eustatic contribution to sea level of over 100 m. This volume would appear to be unrealistically large.

Third it is possible that for large changes in ice sheet volume the isostatic response of the earth at the end of the last ice age is non-linear. If for large changes the rate of isostatic response is proportional to some power of the disequilibrium it is possible that a large amount of adjustment had already taken place before relative sea level information was laid down in the geological record (Budd, personal communication). The eustatic sea level records of Chappell and Shackleton suggest that the ice sheets began to lose ice at 18 kyr BP whereas ICE4G only begins to show retreat at closer to 15 kyr BP. However Wu (1995) suggests that isostatic models with non-linear rheology underestimate the observed submergence peripheral to retreating ice sheets.

Fourth it is possible that the differences observed between the results here and the results of Chapters 5 and 6 originate from assumptions relating ice sheet surface area and ice sheet volume. Most deglaciation chronologies used

in isostatic models are generated assuming steady state behaviour of the ice sheet. This assumption means that ice thickness (and therefore volume) is proportional to ice sheet surface area. Budd and Rayner (1993) suggest that for realistic models of ice sheet dynamics ice volume changes lag behind ice sheet area changes by the order of about 2 kyr. There is also anecdotal evidence supporting this possibility from Clark et al (1978) who find an improved fit to the relative sea level data by delaying the Northern Hemisphere deglaciation by 2 kyr. It should be noted that the ice sheet volumes of Chapters 5 and 6 were generated by time-dependent changes in ice sheet extent only. The 'best fit' volumes were generated by using an ice sheet rescaling factor β, which was considered to be time-independent. It is possible that the Northern Hemisphere ice sheets were much thicker than as they are reconstructed in Chapters 5 and 6, but lost a substantial volume without a major change in surface area. ICE4G suggests that substantial changes in the surface area of the Laurentide ice sheet only occurred at 15 kyr BP.

9. CONCLUSIONS

A model of the Antarctic ice sheet is used in Chapter 4 to examine the effect of using different representations of isostasy. Table 9.1 shows how the ice volume generated over a glacial cycle is modified both by the choice of isostatic model and the values of parameters such and mantle viscosity and lithospheric rigidity. 'Ice volume' in this context refers to the difference in ice volume from the standard earth model which is averaged over the entire glacial cycle. This average difference is then divided by the standard earth model ice volume amplitude. The last column shows how each model differs from the standard earth model.

	viscosity (Pa s)	rigidity (N m)	earth model	Mean Difference from SEM (%)
1		10^{24}		14.1
2	0		'instantaneous'	3.4
3	10^{20}			2.2
4			thin channel	0.1
5	10^{21}	10^{25}	standard earth model (half space)	0
6	10^{22}			-6.7
7		10^{26}		-25.9
8	∞		'no isostasy'	-33.9

Tab. 9.1: Deviation in ice sheet volume from the standard earth model (5) for representations of isostasy (that is earth models) and earth model parameters. Blank spaces refer to the default use of standard earth model structure and/or standard earth model parameters.

Table 9.1 orders the list from the greatest to the least ice volume. Column 2 shows that the ice volume decreases with increasing viscosity. Column 3 shows that the ice volume decreases with increasing rigidity. In terms of these average ice volumes the model most resembling the standard earth model is the viscous thin channel model. This is because the calculation of column 5 in Table 9.1 uses time averaging, so that although the instantaneous ice volumes for the thin channel and half-space models are different the averages are similar. The question as to whether it is reasonable to use the computationally less expedient thin channel model in an ice sheet model therefore depends on the modelling aim. For ice sheet simulations over long periods of time Table 9.1 suggests that the thin channel model is a reasonable approximation to the viscoelastic half-space model. However for calculating eustatic sea level changes since the last ice age or predictions of the present day behaviour of ice sheets, Chapter 4 suggests that the assumption of thin channel flow unrealistically effects ice sheet behaviour.

Table 9.2 shows the values of the earth model parameters deduced in Chapters 5 and 6 from the modelling of the decay of the Laurentide (North American) and Fennoscandian (Northern European) ice sheets. In that modelling the ice sheet extent was defined by the ICE4G chronology and for each ice sheet two cases were considered. The first was where the ice sheet thickness was generated as a parabolic profile and the second was where the thickness was generated by the Jenssen three-dimensional ice sheet model. For the North American adjustment the recovered values of earth model parameters were the same for both cases. For the Northern European adjustment the recovered earth model parameters differed for each case. In Chapter 6 it is suggested that the greater level of parameter trading for the Fennoscandian ice sheet results from the region being ice free by 7 kyr BP so that the relative sea level data used to constrain the ice model is predominantly due to pure isostatic rebound. If this problem is to be pursued further the model must be extended to incorporate gravitational consistent hydro-eustasy. This would allow relative sea level data older than 7 kyr to be used. Note however that the results presented in this study for the Laurentide ice sheet agree with Peltier's assertion that isostatic adjustment

	Laurentide Parabolic	Laurentide Time Dependent	Fennoscandian Parabolic	Fennoscandian Time Dependent
Lower Mantle Viscosity (Pa s)	3×10^{21}	3×10^{21}	6×10^{21}	1.3×10^{21}
Upper Mantle Viscosity (Pa s)	2×10^{21}	2×10^{21}	4×10^{21}	1.3×10^{21}
Lithospheric Rigidity (N m)	1×10^{25}	1×10^{25}	5×10^{24}	2×10^{25}
Variance (m)	15.6	13.8	9.6	7.6
Correlation	0.87	0.90	0.81	0.90
Sea Level Change (mm yr^{-1})	1.95 ± 0.61	1.52 ± 0.65	0.23 ± 1.93	-0.91 ± 1.23

Tab. 9.2: Earth model parameters, fit to relative sea level data and prediction of present day sea level change for North American and Northern European adjustment.

can be separated into an ice-thickness-dependent adjustment amplitude and a mantle-viscosity-dependent adjustment rate.

Figure 9.1 shows the 'best fit' estimation of the Laurentide ice sheet elevation at maximum extent using the time-dependent (that is Jenssen) ice sheet model in Chapter 5. It is of interest that although the ice sheet *thickness* shown in Figure 5.17 in Chapter 5 has a single summit the corresponding ice sheet *elevation* shown here in Figure 9.1 is multiple domed. The debate over whether the Laurentide ice sheet had a single summit or multiple summits dates back to the arguments of Tyrell in 1898 and Flint in 1943 (Peltier & Andrews, 1983). The conclusions of the present work would support the multiple summit hypothesis. However the results of Chapter 8 suggest that caution should be used

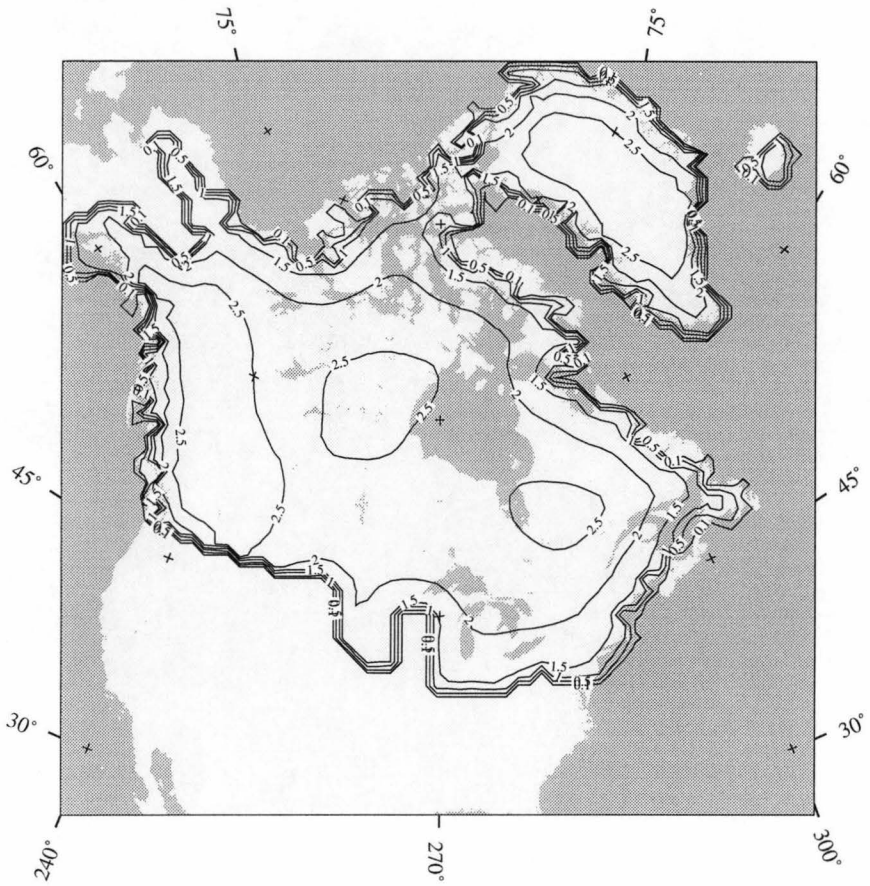

Fig. 9.1: Elevation of Laurentide ice sheet at maximum extent.

in estimating ice sheet elevation at 21 kyr BP using relative sea level data only since 7 kyr BP.

It has been found that the time-dependent (Jenssen) ice sheet model produces a better reproduction of the observed relative sea level changes than the parabolic profile ice sheet model. It is also important to note that the ice sheet deglaciation chronologies generated in Chapters 5 and 6 by the Jenssen model are glaciologically realistic as well as producing an improved prediction of relative sea level data (that is improved compared to the prediction using the parabolic profile ice sheet deglaciation chronology). Marshal et al (1996) observe that Peltier's 1994 ICE4G thickness estimations for the Laurentide ice sheet need to be adjusted from a 'blocky' distribution before they can be used in an ice sheet model. This would suggest that although the ICE4G thickness chronology produces an excellent fit to the relative sea level data it is lacking

in glaciological realism.

A peripheral issue is that despite the fact that the deglaciation chronologies were modified (either by thickness or surface accumulation) to produce best fit, the best correlation between observation and model prediction of relative sea level data is only 0.9 (see Table 9.2). This would suggest that there are features beyond the scope of this thesis that need to be considered in the prediction of relative sea level. In particular neither deglaciation chronology was able to reproduce the observed adjustment in Eastern Canada or near St Petersburg. A site-by-site comparison of the prediction of relative sea level data for both the 'best fit' parabolic and time-dependent ice sheet models are given in Appendix A (for the North American adjustment) and Appendix B (for the Northern European adjustment).

In Chapter 7 a method to incorporate a model of laterally varying lithospheric rigidity was presented. Table 9.3 shows how different representations of this lateral variation produce different volumes of ice averaged over a glacial cycle (cf Table 9.1). With the introduction of a variable lithospheric structure

	model	$\overline{H_l}$ (km)	$\overline{D_r}$ (N m)	Mean Difference from SEM (%)
1	crust × 4	140	4.1×10^{25}	16.2
2	crust + 30	65	4.1×10^{24}	11.5
3	crust + 70	105	1.7×10^{25}	3.1
4	crust + 50	85	9.1×10^{24}	2.7
5	standard earth model	88	1×10^{25}	0
6	crust × 3	105	1.7×10^{25}	-0.0
7	crust × 2	70	5.1×10^{24}	-0.1

Tab. 9.3: Deviation in total ice sheet volume from the standard earth model (5) for different earth models and earth model parameters.

the simple correspondence between increasing lithospheric rigidity and decreas-

ing ice sheet volume no longer holds. Instead it is found that changes to the grounding line occur near the major ice shelves as a result of the differences in crustal deflection towards the front of the ice sheet. The results of Chapter 7 must be considered tentative as a there is no clear indication of either the magnitude or spatial scale of lithospheric rigidity variability for the Antarctic continent apart from the local observations of Stern and Ten Brink (1989).

In Chapter 8 a climatologically driven global model of ice sheet growth and decay over a glacial cycle was implemented and adjusted to produce a reasonable eustatic sea level curve. 'Climatologically driven' means that the Northern Hemisphere ice sheets were driven by Milankovitch solar variations and were allowed to determine their own ice extent and ice thickness. They were linked to a model of the Antarctic ice sheet through a common eustatic sea level change. It was found that the model prediction of eustatic sea level was qualitatively more like the SPECMAP sea level observational data than the observational data of Chappell and Shackleton. However the calculated relative sea level changes near the Northern Hemisphere ice sheets were not good simulations of actual observations. Previous ice sheet modelling results (DeBlonde & Peltier, 1990; Fastook & Hughes, 1991; Marsiat, 1994) predict Northern Hemisphere ice sheet extents at 21 kyr BP that differ from those of ICE4G, particularly so for the Laurentide ice sheet. For the Fennoscandian ice sheet, previous predictions are closer to that of ICE4G but on the other hand they predict a major glaciation in Siberia (Letreguilly & Ritz, 1993; Marsiat, 1994).

Chapter 8 is somewhat speculative but it highlights how coupled models of ice sheets and isostatic adjustment can be used to constrain more tightly the processes associated with the last ice age. The relative sea level data was used to examine the realism of the ice sheet model prediction on a regional scale. It was also found that relative sea level data is not as strongly dependent on ice volume change as might be expected (since the ice sheets generated in Chapter 8 had about four times the volume of the ice sheets in Chapters 5 and 6 but did not predict as greatly differing relative sea level changes).

The ICE4G thickness chronology has been used to represent topography

changes in paleoclimate reconstructions using general circulation models of the atmosphere (Peltier, 1996b). A useful, iterative assessment of the validity of ICE4G would be to use the results of a general circulation model in association with an ice sheet model to see how closely the ICE4G chronology and isostatic adjustment is reproduced. As an intermediate step a coupled climate/ice-sheet model that can reproduce the time-dependent ice extent of ICE4G would go some way towards understanding the ice sheet dynamics of the last ice age.

This thesis has outlined the relationships between isostatic adjustment and ice sheet behaviour predominantly on the basis of differences in predictions by models. This has been necessary because a solid understanding of the key processes of ice sheet retreat and isostatic adjustment are difficult to quantify. The thesis has shown that coupling realistic models of glacial isostasy to realistic models of ice sheet dynamics serves to strengthen understanding and to place greater constraints on our understanding of the last ice age.

BIBLIOGRAPHY

Abramowitz, M. & I. Stegun, 1965. *Handbook of mathematical functions with formulas, graphs, and mathematical tables.* Dover Publications, New York.

Amelung, F. & D. Wolf, 1994. Viscoelastic perturbations of the Earth: significance of the incremental gravitational force in models of glacial isostasy. *Geophys. J. Int.*, **117**, 864–879.

Anderson, D. L., 1995. Lithosphere, Asthenosphere, and Perisphere. *Rev. Geophys.*, **33**(1), 125–149.

Anderson, W. L., 1979. Numerical integration of related Hankel transforms of orders 0 and 1 by adaptive digital filtering. *Geophysics*, **44**, 1287–1305.

Andrews, J. T., W. W. Shilts & G. H. Miller, 1983. Multiple deglaciations of the Hudson Bay Lowlands, Canada, since deposition of the Missinaibi (last-interglacial?) Formation. *Quat. Res*, **19**, 18–37.

Barrel, J., 1914. The strength of the Earth's crust. *J. Geol.*, **22**, 729–735.

Berger, A. L., 1978. Long-term variations of daily insolation and Quaternary climatic changes. *J. Atmos. Sci.*, **35**, 2362–2367.

Berger, A. L., M. F. Loutre & C. Tricot, 1993. Insolation and Earth's Orbital Periods. *J. Geophys. Res.*, **98**(2), 10341–10362.

Birchfield, G. E. & R. W. Grumbine, 1985. 'Slow' Physics of Large Continental Ice Sheets and Underlying Bedrock and Its Relation to the Pleistocene Ice Ages. *J. Geophys. Res.*, **90**(B13), 11294–11302.

Birchfield, G. E., J. Weertman & A. T. Lunde, 1981. A Paleoclimate Model of Northern Hemisphere Ice Sheets. *Quat. Res*, **15**, 126–142.

Bracewell, R. N., 1965. *The Fourier Transform and its Applications.* McGraw-Hill, New York.

Breuer, D. & D. Wolf, 1995. Deglacial land emergence and lateral upper-mantle heterogeneity in the Svalbard Archipelago-1. First results for simple load

models. *Geophys. J. Int.*, **121**(3), 775–788.

Brotchie, J. F. & R. Silvester, 1969. On Crustal Flexure. *J. Geophys. Res.*, **71**(2), 5240–5252.

Bryson, R. A., W. M. Wendland, J. D. Ives & J. T. Andrews, 1969. Radiocarbon isochrones on the disintegration of the Laurentide Ice Sheet. *Arc. Alp. Res.*, **1**, 1–14.

Budd, W. F. & D. Jenssen, 1989. The Dynamics of the Antarctic Ice Sheet. *Ann. Glaciol.*, **12**, 16–22.

Budd, W. F. & P. Rayner, 1993. Modelling ice sheet and climate changes through the ice ages. In *Ice in the Climate System* (edited by W. R. Peltier), volume 12, pp. 291–319. Springer-Verlag Berlin, NATO ASI Series.

Budd, W. F. & I. N. Smith, 1981. The Growth and retreat of ice sheets in response to orbital radiation changes. In *Sea Level, Ice and Climatic Change* (edited by I. Allison), volume 131, pp. 369–409. International Association of Hydrological Sciences.

Budd, W. F. & I. N. Smith, 1982. Large-Scale Numerical Modelling of the Antarctic Ice Sheet. *Ann. Glaciol.*, **3**, 42–49.

Budd, W. F. & I. N. Smith, 1987. Conditions for the Growth and Retreat of the Laurentide Ice Sheet. *Géograph. Phys. Quat.*, **41**, 279–290.

Cathles, L. M., 1975. *The viscosity of the Earth's mantle*. Princeton University Press, Princeton.

Chappell, J. & N. J. Shackleton, 1986. Oxygen isotopes and sea level. *Nature*, **324**(13), 137–140.

Clark, J. A., W. E. Farrell & W. R. Peltier, 1978. Global changes in postglacial sea level: a numerical calculation. *Quat. Res*, **9**, 265–278.

Daly, R. A., 1934. *The Changing World of the Ice Age*. Yale University, New York.

Davis, J. L. & J. X. Mitrovica, 1996. Glacial isostatic adjustment and the anomalous tide gauge record of eastern North America. *Nature*, **379**, 331–333.

DeBlonde, G. & W. R. Peltier, 1990. A model of late Pleistocene ice sheet growth with realistic geography and simplified cryodynamics and geody-

namics. *Clim. Dyn.*, **5**, 103–110.

DeBlonde, G. & W. R. Peltier, 1991. A One-Dimensional Model of Continental Ice Volume Fluctuations through the Pleistocene: Implications for the Origin of the Mid-Pleistocene Climate Transition. *J. Clim.*, **4**, 318–344.

Drewry, D. J., 1982. Antarctica Unveiled. *New Scientist*, pp. 246–251.

Egan, S. S., 1992. The flexural isostatic response of the lithosphere to extensional tectonics. *Tectonophysics*, **202**, 291–308.

Fang, M. & B. H. Hager, 1996. The sensitivity of post-glacial sea level to viscosity structure and ice-load history for realistically parametrised viscosity models. *Geophys. Res. Lett.*, **23**(25), 3787–3790.

Fastook, J. L. & T. J. Hughes, 1991. Changing ice loads on the Earth's surface during the last glaciation cycle. In *Glacial Isostasy, Sea-Level and Mantle Rheology* (edited by R. Sabadini, K. Lambeck & E. Boschi), volume 1, pp. 165–201. Kluwer Academic Publishers, Netherlands.

Fisher, D. A., N. Reeh & K. Langley, 1985. Objective reconstructions of the late wisconsinan Laurentide ice sheet and the significance of deformable beds. *Géograph. Phys. Quat.*, **39**(3), 229–238.

Fjeldskar, W. & L. Cathles, 1991. Rheology of Mantle and Lithosphere inferred from post- glacial uplift in Fennoscandia. In *Glacial Isostasy, Sea-Level and Mantle Rheology* (edited by R. Sabadini, K. Lambeck & E. Boschi), pp. 1–19. Kluwer Academic Publishers, Netherlands.

Ghil, M. & H. Le Treut, 1981. A Climate Model with Cryodynamics and Geodynamics. *J. Geophys. Res.*, **86**(C6), 5262–5270.

Grosswald, M. G., 1988. Antarctic-style ice sheet in the northern hemisphere: toward a new global glacial theory. *Polar. Geogr. Geol.*, **12**(4), 239–267.

Han, D. & J. Wahr, 1995. The viscoelastic relaxation of a realistically stratified Earth, and a further analysis of postglacial rebound. *Geophys. J. Int.*, **120**, 287–311.

Haskell, N. A., 1935. The Motion of a Viscous Fluid Under a Surface Load. *Physics*, **6**, 265–269.

Huybrechts, P., 1990a. A 3-D model for the Antarctic ice sheet: a sensitivity study on the glacial-interglacial contrast. *Clim. Dyn.*, **5**, 79–92.

Huybrechts, P., 1990b. The Antarctic Ice Sheet during the last glacial-interglacial cycle: A three dimensional experiment. *Ann. Glaciol.*, **14**, 115–119.

Huybrechts, P., 1992. *The Antarctic ice sheet and environmental change: a three-dimensional modelling study*, volume 99. Ber. Polarforsch., Bremen, Germany.

James, T. S., 1991. *Post-glacial Deformation.* Princeton University, Unpublished Ph.D. dissertation.

James, T. S., 1992. The Hudson Bay Free-air gravity anomaly and glacial rebound. *Geophys. Res. Lett.*, **19**(9), 861–864.

James, T. S. & A. Lambert, 1993. A comparison of VLBI Data with the ICE-3G Glacial Rebound Model. *Geophys. Res. Lett.*, **20**(9), 871–874.

Jenssen, D., 1977. A three dimensional polar ice-sheet model. *J. Glac.*, **18**(80), 373–389.

Johnston, P., 1993. The effect of spatially non-uniform water loads on the prediction of sea-level change. *Geophys. J. Int.*, **114**, 615–634.

Jouzel, J., C. Lorius, J. R. Petit, C. Genthon, N. I. Barkov, V. M. Kotlyakov & V. M. Petrov, 1987. Vostok ice core: a continuous isotope temperature record over the last climatic cycle (160,000 years). *Nature*, **329**, 402–408.

Kaufmann, G. & D. Wolf, 1996. Deglacial land emergence and lateral upper-mantle heterogeneity in the Svalbard Archipelago-2. Extended results for High Resolution load models. *Geophys. J. Int.*, **127**(1), 125–140.

Kusznir, N. & G. Karner, 1985. Dependence of the flexural rigidity of the continental lithosphere on rheology and temperature. *Nature*, **316**, 138–142.

Lambeck, K., 1993a. Glacial rebound and sea-level change: an example of a relationship between mantle and surface processes. *Tectonophysics*, **223**, 15–37.

Lambeck, K., 1993b. Glacial rebound of the British Isles- 1. Preliminary model results. *Geophys. J. Int.*, **115**, 941–959.

Lambeck, K., 1993c. Glacial rebound of the British Isles- 2. A high-resolution, high-precision model. *Geophys. J. Int.*, **115**, 960–990.

Lambeck, K., P. Johnston, C. Smither & M. Nakada, 1996. Glacial Rebound of the British Isles .3. Constraints on Mantle Viscosity. *Geophys. J. Int.*, **125**(2), 340–354.

Le Meur, E., 1996. Isostatic postglacial rebound over Fennoscandia with a self-gravitating spherical visco-elastic Earth model. *Ann. Glaciol.*, **23**, 318–327.

Le Meur, E. & P. Huybrechts, 1996. A comparison of different ways of dealing with isostasy: examples from modelling the Antarctic ice sheet during the last glacial cycle. *Ann. Glaciol.*, **23**, 309–317.

Letreguilly, A., N. Reeh & P. Huybrechts, 1991. The Greenland ice sheet through the last glacial- interglacial cycle. *Palaeogeog., Palaeoclim., Palaeoecol.*, **90**, 385–394.

Letreguilly, A. & C. Ritz, 1993. Modelling of the Fennoscandian Ice Sheet. In *Ice in the Climate System* (edited by W. R. Peltier), volume 12, pp. 21–46. Springer-Verlag Berlin, NATO ASI Series.

Lingle, C. S. & J. A. Clark, 1985. A Numerical Model of Interactions Between a Marine Ice Sheet and the Solid Earth: Application to a West Antarctic Ice Stream. *J. Geophys. Res.*, **90**(C1), 1100–1114.

Livermann, D. G. E., 1994. Relative sea-level history and isostatic rebound in Newfoundland, Canada. *Boreas*, **23**, 217–230.

Marshall, S. J., G. K. C. Clarke, A. S. Dyke & D. A. Fisher, 1996. Geologic and topographic controls on fast flow in the Laurentide and Cordillerian Ice Sheets. *J. Geophys. Res.*, **101**(B8), 17827–17839.

Marsiat, I., 1994. Simulation of the Northern Hemisphere Continental Ice Sheets over the last Glacial-Interglacial Cycle: Experiments with a latitude-longitude vertically integrated Ice Sheet Model coupled to a zonally averaged Climate Model. *Paleoclimates*, **1**, 59–98.

Martinson, D. G., N. G. Pisias, J. D. Hays, J. Imbrie, T. C. Moore & N. J. Shackleton, 1987. Age dating and the orbital theory of the ice ages: development of a high-resolution 0 to 300,000-year chronostratigraphy. *Quat. Res*, **27**, 1–29.

McConnell, R. K., Jr., 1965. Isostatic adjustment in a layered Earth. *J. Geophys. Res.*, **70**, 5171–5188.

McKenzie, D. P., 1967. The viscosity of the mantle. *Geophys. J. R. astr. Soc.*, **14**, 297–305.

Mitrovica, J. X., 1996. Haskell [1935] revisited. *J. Geophys. Res.*, **101**(B1), 555–569.

Mitrovica, J. X., J. L. Davis & I. I. Shapiro, 1994. A spectral formalism for computing three-dimensional deformations due to surface loads 2. Present-day glacial isostatic adjustment. *J. Geophys. Res.*, **99**(B4), 7075–7101.

Mitrovica, J. X. & W. R. Peltier, 1989. Pleistocene Deglaciation and the Global Gravity Field. *J. Geophys. Res.*, **94**(B10), 13651–13671.

Mitrovica, J. X. & W. R. Peltier, 1992. A comparison of methods for the inversion of viscoelastic relaxation spectra. *Geophys. J. Int.*, **108**, 410–414.

Nakada, M. & K. Lambeck, 1987. Glacial rebound and relative sea-level variations: a new appraisal. *Geophys. J. R. astr. Soc.*, **90**, 171–224.

Nakiboglu, S. M. & K. Lambeck, 1991. Secular Sea-Level Change. In *Glacial Isostasy, Sea-Level and Mantle Rheology* (edited by R. Sabadini, K. Lambeck & E. Boschi), volume 1, pp. 237–258. Kluwer Academic Publishers, Netherlands.

Oerlemans, J., 1980. Model experiments on the 100 000-yr glacial cycle. *Nature*, **287**, 430–430.

Oerlemans, J. & C. J. Van der Veen, 1984. *Ice Sheets and Climate*. Dordrecht, Reidel.

Officer, C. B., W. S. Newman, J. M. Sullivan & D. R. Lynch, 1988. Glacial Isostatic Adjustment and Mantle Viscosity. *J. Geophys. Res.*, **93**(B6), 6397–6409.

Paterson, W. S. B., 1971. *The Physics of Glaciers*. Pergamon Press, Oxford.

Payne, A. J., D. E. Sugden & C. M. Clapperton, 1989. Modelling the Growth and Decay of the Antarctic Peninsula Ice Sheet. *Quat. Res*, **31**, 119–134.

Peltier, W. R., 1974. The impulse response of a Maxwell Earth. *Rev. Geophys. Space Phys.*, **12**, 649–669.

Peltier, W. R., 1980. Models of Glacial Isostasy and Relative Sea Level. In *Dynamics of plate interiors* (edited by A. W. Bally), volume 1, pp. 111–128. American Geophysical Union, Washington D.C.

Peltier, W. R., 1982. Dynamics of the Ice Age Earth. *Adv. Geophys.*, **24**, 1–146.

Peltier, W. R., 1988. Lithospheric Thickness, Antarctic Deglaciation History, and Ocean Basin Discretization Effects in a Global Model of Postglacial Sea Level Change: A Summary of Some sources of Non-uniqueness. *Quat. Res*, **29**, 93–112.

Peltier, W. R., 1994. Ice Age Paleotopography. *Science*, **265**, 195–201.

Peltier, W. R., 1996a. Global sea level rise and glacial isostatic adjustment: An analysis of data from the east coast of North America. *Geophys. Res. Lett.*, **23**(7), 717–720.

Peltier, W. R., 1996b. Mantle Viscosity and Ice-Age Ice Sheet Topography. *Science*, **273**, 1359–1364.

Peltier, W. R. & J. T. Andrews, 1976. Glacial-Isostatic Adjustment-1. The Forward Problem. *Geophys. J. R. astr. Soc.*, **46**, 605–646.

Peltier, W. R. & J. T. Andrews, 1983. Glacial geology and glacial isostasy of the Hudson Bay region. In *Shorelines and isostasy* (edited by D. E. Smith & A. G. Dawson), volume 16, pp. 285–319. Academic Press, London.

Pollard, D., 1978. An investigation of the astronomical theory of the ice ages using a simple climate-ice sheet model. *Nature*, **272**, 233–235.

Pollard, D., 1982. A simple ice sheet model yields realistic 100 kyr glacial cycles. *Nature*, **296**, 334–338.

Reeh, N., 1982. A plasticity theory approach to the steady-state shape of a three-dimensional ice sheet. *J. Glac.*, **28**(100), 431–455.

Rizos, C., 1979. An efficient computer technique for the evaluation of geopotential from spherical harmonic models. *Aust. J. Geod. Photo. Surv.*, **31**, 161–169.

Shea, D. J., 1986. Climatological atlas: 1950-1979. Surface air temperature, precipitation, sea-level pressure, and sea-surface temperature (45 S-90 N). Technical Note NCAR/TN-269+STR, NCAR, Boulder, CO. 35 pp plus 158 figures and 10 microfiche.

Shepard, F. P., 1963. *Thirty-five thousand years of sea level.* University of Southern California Press.

Siegert, M. J. & J. A. Dowdeswell, 1995. Numerical Modelling of the Late

Weichselian Svalbard-Barents Sea Ice Sheet. *Quat. Res*, **43**, 1–13.

Sigmundsson, F., 1991. Post-glacial rebound and asthenosphere viscosity in Iceland. *Geophys. Res. Lett.*, **18**(6), 1131–1134.

Sneddon, I. N., 1951. *Fourier transforms*. McGraw-Hill, New York.

Spencer, N. E. & P. L. Woodworth, 1993. Data holdings of the Permanent Service for Mean Sea Level. Technical report, Permanent Service for Mean Sea Level, Bidston, Birkenhead.

Stern, T. A. & U. S. Ten Brink, 1989. Flexural Uplift of the Transantarctic Mountains. *J. Geophys. Res.*, **94**(B8), 10315–10330.

Takeuchi, H., 1963. Time Scales of Isostatic Compensations. *J. Geophys. Res.*, **68**(8), 2357.

Tushingham, A. M. & W. R. Peltier, 1991. ICE-3G: A New Model Of Late Pleistocene Deglaciation Based Upon Geophysical Predictions Of Post-Glacial Relative Sea Level Change. *J. Geophys. Res.*, **96**(B3), 4497–4523.

Van Bremmelen, R. W. & H. P. Berlage, 1935. Versuch einer mathematischen behandlung geotektonisher bewegung unter besonderer berücksichtegung der undationstheorie. *Gerlands Beitr. Geophys.*, **43**, 19–55.

Vernekar, A. D., 1972. *Long-period global variations of incoming solar radiation*. Meteorological Monographs, Vol 12.

Walcott, R. I., 1970. Isostatic response to loading of the crust in Canada. *Can. J. Earth Sci.*; **7**, 716–731.

Walcott, R. I., 1973. Structure of the Earth from Glacio-Isostatic Rebound. *Ann. Rev. Earth Planet. Sci.*, **1**, 15–37.

Wolf, D., 1984. The relaxation of spherical and flat Maxwell Earth models and effects due to the presence of the lithosphere. *J. Geophys.*, **56**, 24–33.

Wu, P., 1993. Postglacial rebound in a power-law medium with axial symmetry and the existence of the transition zone in relative sea-level data. *Geophys. J. Int.*, **114**, 417–432.

Wu, P., 1995. Can observations of postglacial rebound tell whether the mantle is linear or nonlinear? *Geophys. Res. Lett.*, **22**(13), 1645–1648.

Wu, P. & W. R. Peltier, 1983. Glacial isostatic adjustment and the free air gravity anomaly as a constraint on deep mantle viscosity. *Geophys. J. R.*

astr. Soc., **74**, 377–449.

Zonneveld, J. I. S., 1973. Some notes on the last deglaciation in Northern Europe compared with Canadian Conditions, in Symposium Discussion. *Arc. Alp. Res.*, **5**, 223–228.

10. APPENDIX A

This section presents a site by site comparison of the relative sea level prediction made by the isostatic model with both the parabolic profile and time dependent ice sheet model used for the ice sheet reconstruction. The data in the figures in this Appendix is used to produce the geographic distribution of error figures in Chapter 5 (Figures 5.14 and 5.25). For the plots in this appendix the x axes only present the period between 7 kyr BP and the present day. This is because this is the period of time over which the relative sea level data is used in the calculation. For clarity the x axes are not labelled. The relative sea level amplitudes are shown on the y axes. The dotted line represents the model prediction using the time dependent ice sheet model and the solid line represents the model prediction using the parabolic profile ice sheet thickness assumption. The locations of the relative sea level sites are listed in alphabetical order on the next page.

Site Name	Latitude	Longitude	Site Name	Latitude	Longitude
ADDISON ME	44°18′	−67°42′	J BRONLUND FJORD GR	82°0′	−31°0′
ALERT ELL	82°18′	−63°0′	JAMES BAY QUE	53°0′	−79°0′
ARCHER FIORD ELL	81°12′	−69°0′	JAMES R VA	37°0′	−77°0′
BAIRD PEN BAF	69°0′	−74°0′	JUNEAU AK	58°12′	−134°0′
BARNSTABLE MA	41°42′	−70°18′	K FREDERICK VIII LA	80°06′	−20°42′
BARROW AK	71°18′	−156°36′	KAPISIGDLIT GRL	64°18′	−50°18′
BATHURST INLET NWT	67°18′	−107°0′	KEEWATIN NWT	4°18′	−95°0′
BATHURST IS	76°0′	−100°0′	KETCHIKAN AK	55°36′	−131°36′
BAY FIORD ELL	78°18′	−86°0′	LA JOLLA CA	32°54′	−117°18′
BAY OF FUNDY NS	45°0′	−65°0′	LUNENBURG BAY NS	44°18′	−64°18′
BERMUDA	32°0′	−65°0′	MAKTAK FIORD BAF	67°24′	−65°0′
BOAT PT DEV	76°0′	−90°0′	MESTERS VIG GRL	72°0′	−24°0′
BOOTHIA PEN NWT	69°0′	−92°0′	MONTREAL QUE	45°18′	−74°0′
BOSTON MA	42°48′	−70°48′	MYRTLE BEACH SC.	33°42′	−78°42′
BOWERS DE	39°0′	−75°18′	N GULF OF CALIF ME	31°18′	−114°54′
BRIGANTINE NJ	39°18′	−74°18′	N MELVILLE PEN	69°18′	−82°0′
BRODEUR PEN BAF	71°0′	−85°0′	N SOMERSET IS	74°0′	−93°42′
BROUGHTON IS BAF	67°18′	−64°0′	NARPAING FIORD BAF	67°42′	−65°24′
BURTON BAY BAF	63°42′	−68°36′	NEOLUKSEAK FIORD BA	67°18′	−66°0′
C CHARLES VA	37°0′	−76°0′	NEW HAVEN CT	41°12′	−73°0′
C HENRIETTA MARIA	55°0′	−82°18′	NEW YORK NY	41°0′	−74°0′
C MAY NJ	39°12′	−74°42′	NW NEWFOUNDLAND	51°18′	−56°18′
C ROYAL SC	33°18′	−79°18′	OKOA FIORD BAF	68°0′	−66°0′
C STORM ELL	76°18′	−88°0′	OTTAWA IS NWT	59°48′	−80°18′
C TANFIELD BAF	63°0′	−70°0′	PHILLIPS INLET ELL	82°0′	−85°0′
CAPE BRETON IS NS	46°0′	−60°0′	PLUM IS MA	41°18′	−70°0′
CAREY IS GRL	76°48′	−73°0′	PRINCE RUPERT BC	54°18′	−130°12′
CHARLESTON SC	33°0′	−80°0′	QUEEN CHARLOTTE	51°0′	−128°0′
RAMBOW HILL ELL	83°0′	−75°42′	RAMBOW HILL ELL	83°0′	−75°42′
CHARLOTTETOWN PEI	46°18′	−63°18′	RIMOUSKI QUE	48°18′	−68°18′
CHEESEQUAKE NJ	40°24′	−74°18′	RIVIERE DU LOUP QUE	48°0′	−69°0′
CHESTER R MD	39°0′	−76°0′	S CAPE FIORD ELL	76°18′	−84°0′
CHEZZETCOOK NS	45°0′	−63°0′	S MELVILLE IS	75°0′	−109°0′
CHURCHILL MAN	58°0′	−94°0′	S SOMERSET IS.	72°48′	−93°36′
CLEM MARKHAM INLET	82°36′	−68°0′	SAM FORD FIORD BAF	70°0′	−71°18′
CLINTON CT	41°12′	−72°18′	SAN FRANCISCO BAY CA	37°36′	−122°24′
COLUMBIA R WA	46°12′	−124°0′	SAVANNAH GA	32°0′	−81°0′
COPPER R AK	60°24′	−145°0′	SKELDAL GRL	72°0′	−26°0′
CORNWALLIS IS	75°0′	−95°0′	SONDRE STOMFJORD GR	67°0′	−50°12′
DARIEN GA	31°12′	−81°18′	SOUTHAMPTON IS NWT	64°18′	−84°0′
DISCOVERY HARBOUR	81°42′	−66°0′	SOUTHPORT NC	34°0′	−78°0′
DISRAELI FIORD ELL	82°48′	−73°48′	ST GEORGE'S BAY NFL	48°0′	−59°0′
E AXEL HEIBERG IS	80°0′	−88°0′	ST JOHN NB	45°18′	−66°0′
E LONG ISLAND NY	41°0′	−72°18′	STADARHOLSKIRKJA ICE	65°18′	−21°48′
E VANCOUVER IS BC	49°0′	−124°0′	TANQUARY FIORD ELL	81°0′	−78°0′
FRENCH R PEI	46°18′	−63°18′	TAY SOUND BAF	72°18′	−79°0′
GASPE QUE	49°0′	−66°0′	TAY SOUND BAF	72°18′	−79°0′
GOOSE BAY LAB	53°0′	−60°0′	THORES R ELL	82°36′	−72°48′
HALIFAX NS	44°42′	−63°42′	TIGNISH PEI	47°0′	−64°0′
HALL LAND GRL	81°36′	−60°12′	TRUELOVE INLET DEV	75°36′	−84°36′
HAMILTON INLET LAB	54°12′	−58°0′	TUKTOYAKTUK PEN NWT	70°0′	−133°0′
HOME BAY BAF	69°0′	−68°42′	UNGAVA PEN QUE	62°0′	−75°0′
HUDSON R NY	41°18′	−74°0′	VICTORIA BC	48°18′	−123°18′
IGLOOLIK IS NWT	69°0′	−82°0′	WARD HUNT IS ELL	83°06′	−74°0′
INUGSUIN FIORD BAF	70°0′	−68°0′	WARWICK SOUND BAF	62°48′	−65°18′
IPIK BAY BAF	69°0′	−75°18′	YAKUTAT AK	58°42′	−137°42′
ISLES OF SHOALS NH	43°06′	−70°42′	YARMOUTH NS	43°54′	−66°0′

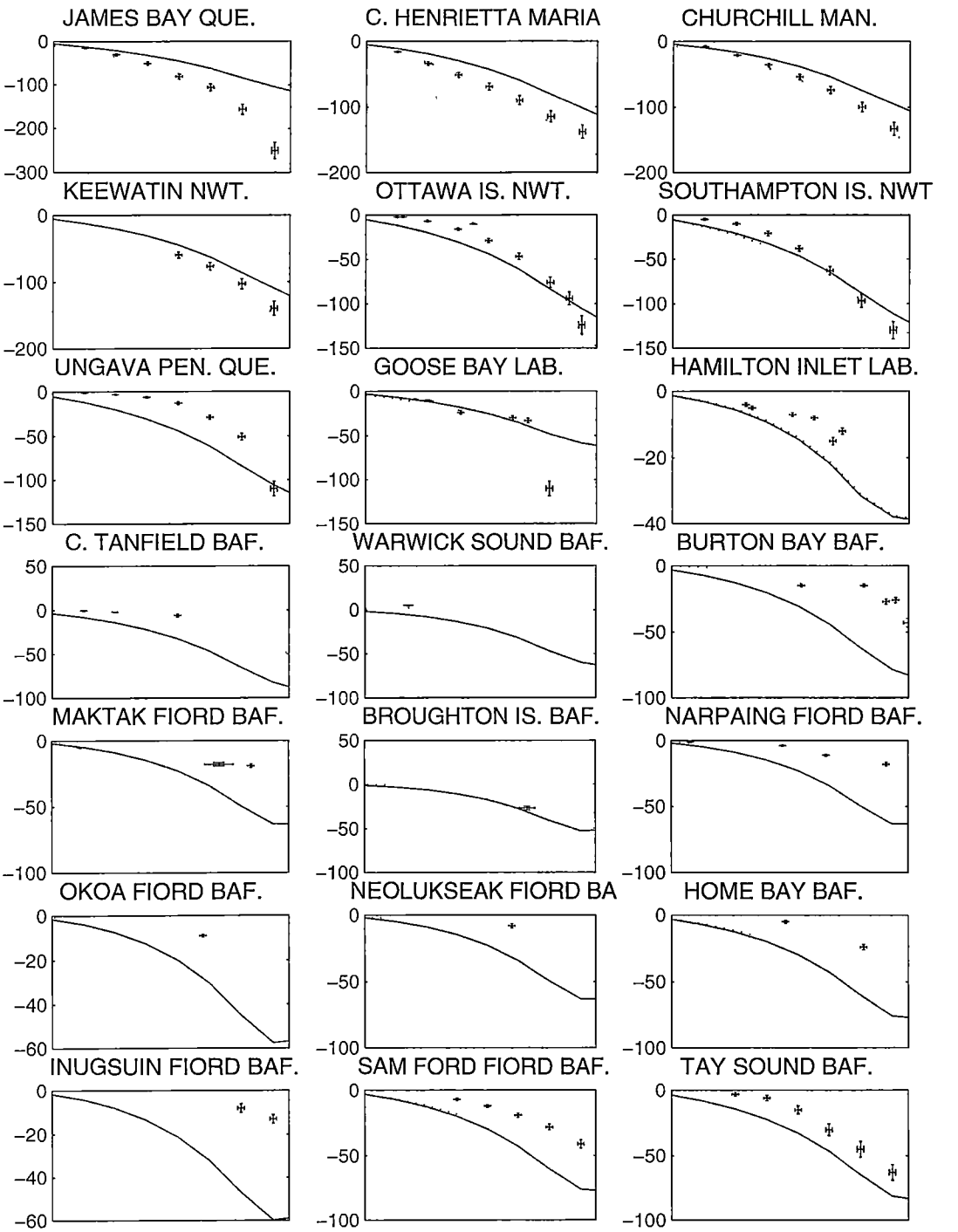
JAMES BAY QUE.
C. HENRIETTA MARIA
CHURCHILL MAN.
KEEWATIN NWT.
OTTAWA IS. NWT.
SOUTHAMPTON IS. NWT
UNGAVA PEN. QUE.
GOOSE BAY LAB.
HAMILTON INLET LAB.
C. TANFIELD BAF.
WARWICK SOUND BAF.
BURTON BAY BAF.
MAKTAK FIORD BAF.
BROUGHTON IS. BAF.
NARPAING FIORD BAF.
OKOA FIORD BAF.
NEOLUKSEAK FIORD BA
HOME BAY BAF.
INUGSUIN FIORD BAF.
SAM FORD FIORD BAF.
TAY SOUND BAF.

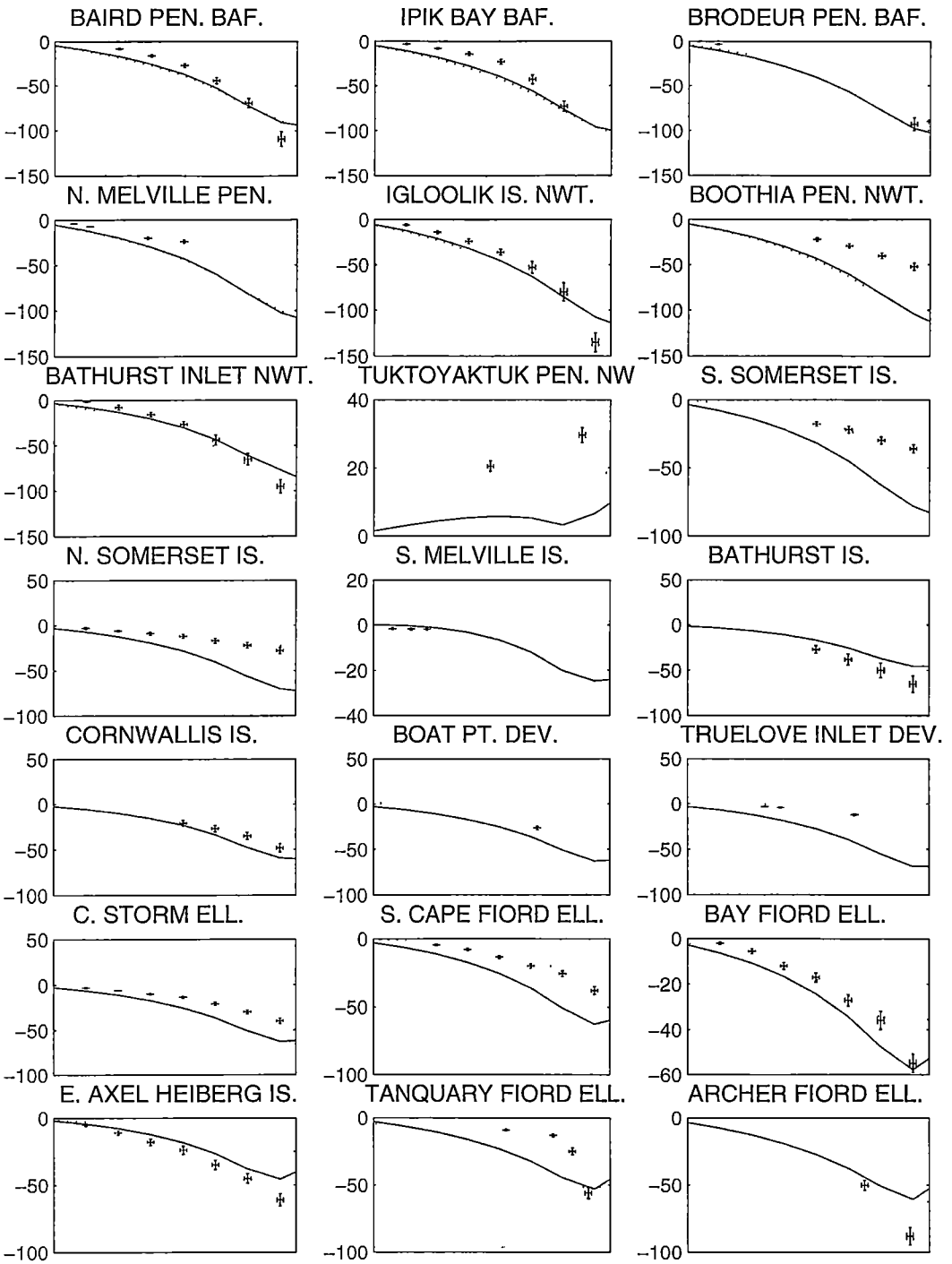
BAIRD PEN. BAF.
IPIK BAY BAF.
BRODEUR PEN. BAF.
N. MELVILLE PEN.
IGLOOLIK IS. NWT.
BOOTHIA PEN. NWT.
BATHURST INLET NWT.
TUKTOYAKTUK PEN. NW
S. SOMERSET IS.
N. SOMERSET IS.
S. MELVILLE IS.
BATHURST IS.
CORNWALLIS IS.
BOAT PT. DEV.
TRUELOVE INLET DEV.
C. STORM ELL.
S. CAPE FIORD ELL.
BAY FIORD ELL.
E. AXEL HEIBERG IS.
TANQUARY FIORD ELL.
ARCHER FIORD ELL.

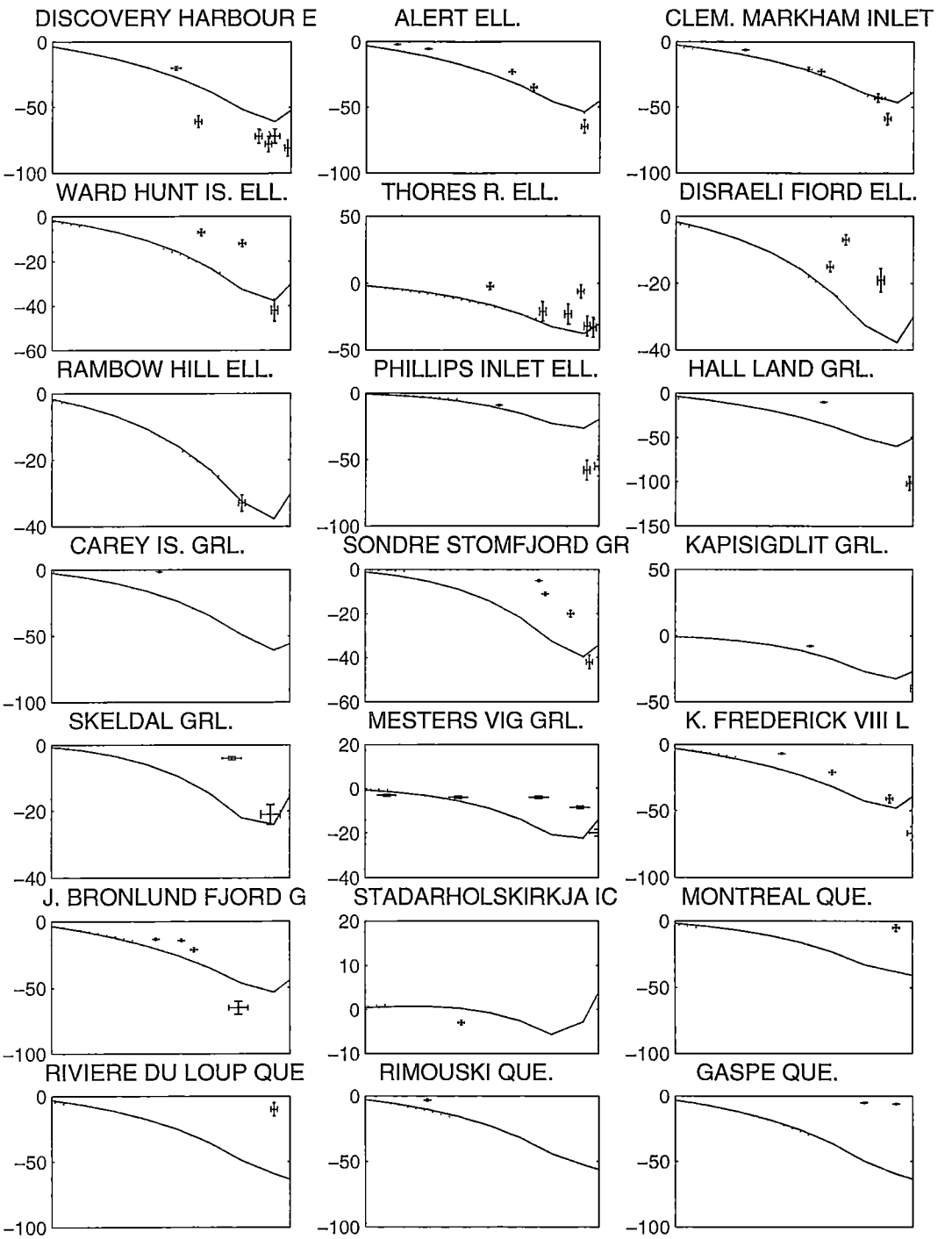
DISCOVERY HARBOUR E
ALERT ELL.
CLEM. MARKHAM INLET
WARD HUNT IS. ELL.
THORES R. ELL.
DISRAELI FIORD ELL.
RAMBOW HILL ELL.
PHILLIPS INLET ELL.
HALL LAND GRL.
CAREY IS. GRL.
SONDRE STOMFJORD GR
KAPISIGDLIT GRL.
SKELDAL GRL.
MESTERS VIG GRL.
K. FREDERICK VIII L
J. BRONLUND FJORD G
STADARHOLSKIRKJA IC
MONTREAL QUE.
RIVIERE DU LOUP QUE
RIMOUSKI QUE.
GASPE QUE.

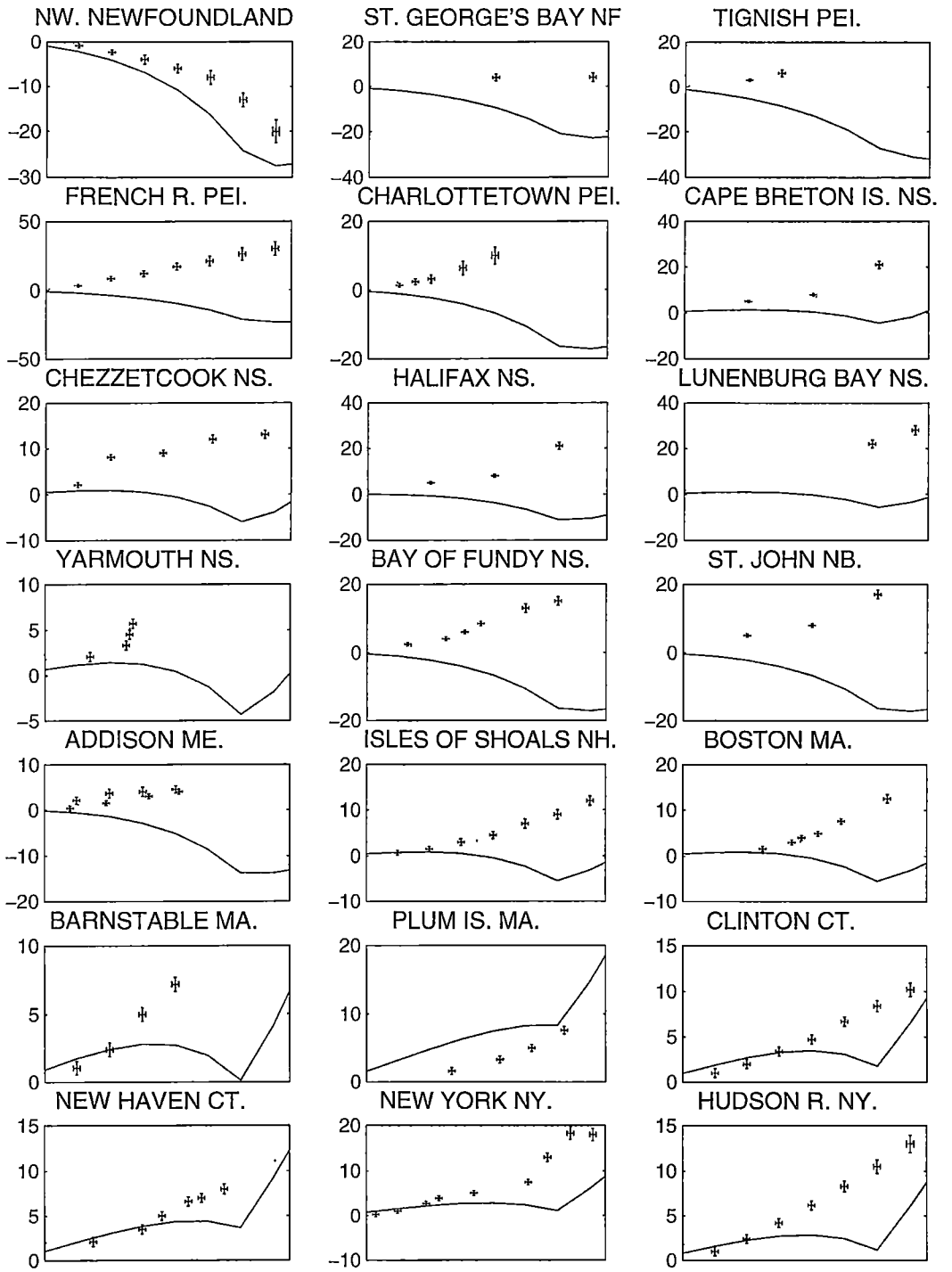
NW. NEWFOUNDLAND
ST. GEORGE'S BAY NF
TIGNISH PEI.
FRENCH R. PEI.
CHARLOTTETOWN PEI.
CAPE BRETON IS. NS.
CHEZZETCOOK NS.
HALIFAX NS.
LUNENBURG BAY NS.
YARMOUTH NS.
BAY OF FUNDY NS.
ST. JOHN NB.
ADDISON ME.
ISLES OF SHOALS NH.
BOSTON MA.
BARNSTABLE MA.
PLUM IS. MA.
CLINTON CT.
NEW HAVEN CT.
NEW YORK NY.
HUDSON R. NY.

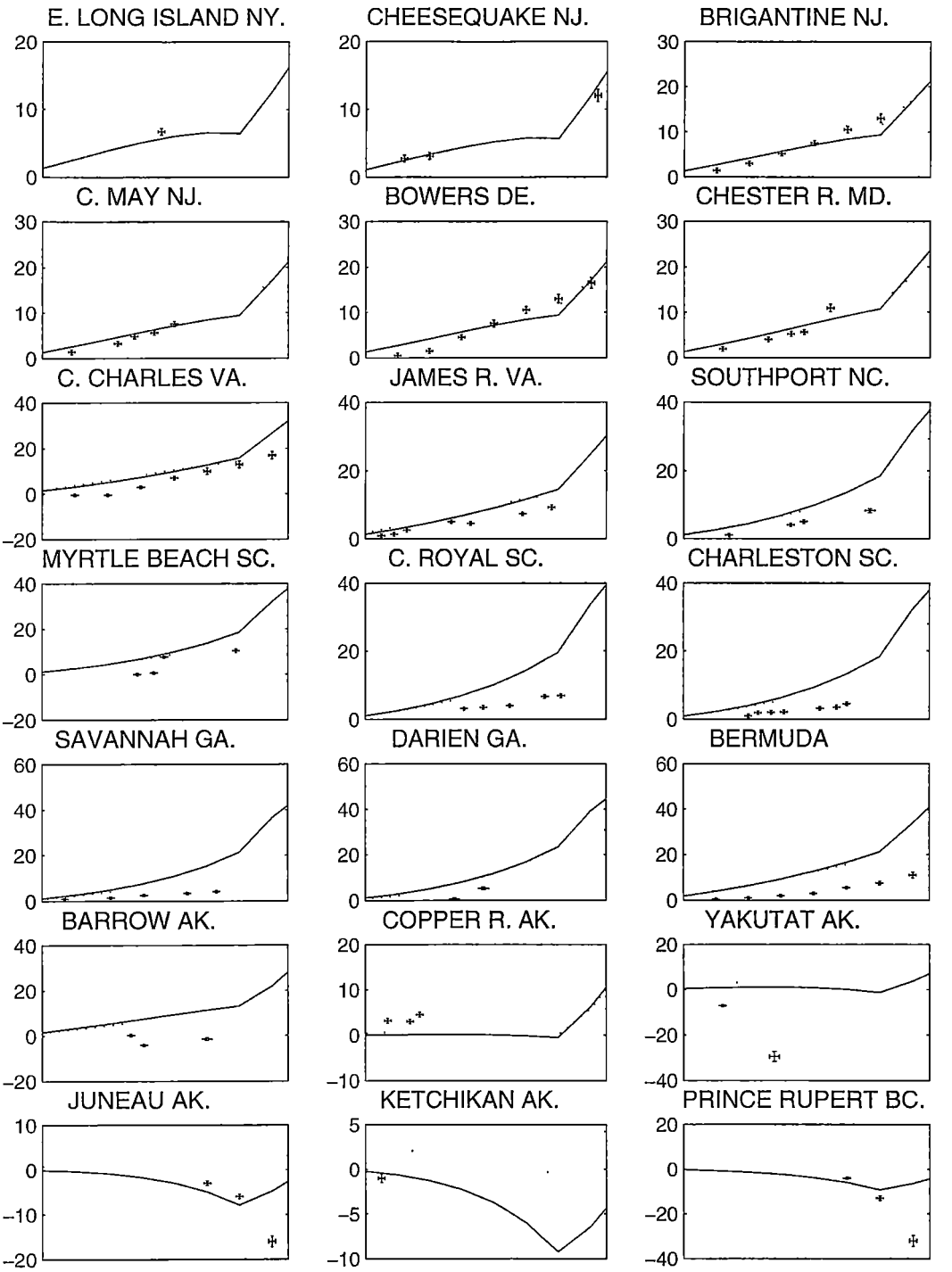
E. LONG ISLAND NY.
CHEESEQUAKE NJ.
BRIGANTINE NJ.
C. MAY NJ.
BOWERS DE.
CHESTER R. MD.
C. CHARLES VA.
JAMES R. VA.
SOUTHPORT NC.
MYRTLE BEACH SC.
C. ROYAL SC.
CHARLESTON SC.
SAVANNAH GA.
DARIEN GA.
BERMUDA
BARROW AK.
COPPER R. AK.
YAKUTAT AK.
JUNEAU AK.
KETCHIKAN AK.
PRINCE RUPERT BC.

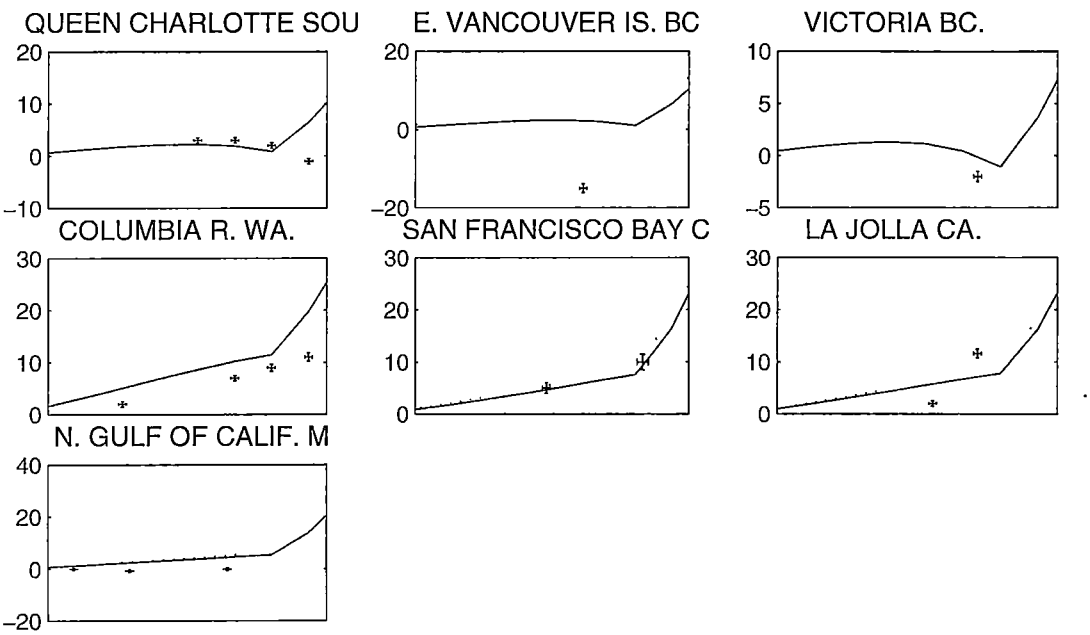
QUEEN CHARLOTTE SOU
E. VANCOUVER IS. BC
VICTORIA BC.
COLUMBIA R. WA.
SAN FRANCISCO BAY C
LA JOLLA CA.
N. GULF OF CALIF. M

11. APPENDIX B

This appendix shows the same calculation as for Appendix A but for the Northern European adjustment. The relative sea level data site names and locations are listed in alphabetical order below.

Site Name	Latitude	Longitude	Site Name	Latitude	Longitude
AND FJORD NOR	69°06′	16°0′	MERSEYSIDE ENG	53°30′	−3°12′
ANGERMANLAND SWE	63°0′	18°0′	MONT-SAINT MICHEL FR	48°42′	−1°30′
BELFAST N IRE	54°18′	−5°48′	MOUTH OF THE SHANNON	52°36′	−9°42′
BJUGN NOR	63°42′	9°36′	N UIST SCOT	57°24′	−7°18′
BORGUNDVAG NOR	62°0′	5°18′	NARVA ESTONIA	59°0′	27°42′
BREDSTEDT WG	54°36′	8°54′	NEW QUAY WALES	52°12′	−4°18′
BREMERHAVEN WG	53°48′	8°30′	NEWPORT WALES	51°24′	−3°0′
BREST FRA	48°42′	−4°24′	NORFOLK ENG	53°0′	0°18′
CUMBERLAND ENG	54°12′	−3°12′	ONSALA SWE	57°18′	12°0′
DUBLIN IRE	53°24′	−6°12′	OOSTENDE BEL	51°06′	2°48′
E BLEKINGE SWE	56°12′	16°0′	ORONSAY SCOT	56°0′	−6°12′
FIRTH OF FORTH SCOT	56°06′	−3°48′	OSLO NOR	60°0′	10°54′
FJALLBACKA SWE	58°36′	11°12′	PRAESTO DEN	55°0′	12°0′
FONNES NOR	60°48′	5°0′	RHINE DELTA NETH	51°48′	4°0′
FREDERIKSHAVN DEN	57°30′	10°30′	RODBYHAVN DEN.	54°18′	11°06′
FROSTA NOR	63°36′	10°36′	S OSTFOLD NOR	59°30′	11°0′
FROYA NOR	63°36′	8°30′	SAN SEBASTIAN SP	43°18′	−2°0′
GOTEBORG SWE	57°42′	11°42′	SAREMA ESTONIA	58°0′	22°30′
GRONINGEN NETH	53°12′	7°0′	SARTHE R FRA	47°12′	−2°0′
HELSINKI FIN	60°12′	24°54′	SHETLAND IS SCOT	60°30′	−1°0′
HITRA NOR	63°24′	8°48′	SKJAEAFASSEN NOR	70°0′	21°0′
HUMBER R ENG	53°36′	−0°24′	SOBORG SWE	56°30′	13°0′
INGOY NOR	71°0′	24°0′	SOMERSET LEVELS ENG	51°12′	−3°06′
JAEREN NOR	59°0′	5°30′	SOUTHAMPTON ENG	50°48′	−1°18′
K FREDERICK VIII LA	80°06′	−20°42′	STOCKHOLM SWE	59°18′	18°12′
KEIL BAY WG	54°36′	10°12′	SULA NOR	62°18′	6°12′
KRISTIINANKAUPUNKI F	62°18′	21°24′	TALLINN ESTONIA	59°0′	24°30′
KVALVIKA NOR	69°30′	18°0′	TEES R ENG	54°42′	−1°12′
LE HAVRE FRA	49°30′	0°06′	THAMES R. ENG	51°30′	0°36′
LEEUWARDEN NETH	53°06′	5°18′	THE MACHARS SCOT	54°54′	−4°24′
LISTA NOR	58°0′	6°42′	TORQUAY ENG	50°30′	−3°30′
LOCH FYNE SCOT	56°06′	−5°18′	VARANGER FJORD NOR	70°0′	29°0′
LOUGH FOYLE N IRE	55°18′	−7°0′	VERDALSOYA NOR	63°48′	11°0′
LOUGHHROS MORE BAY I	54°42′	−8°30′	VILAINE R FRA	47°30′	−2°30′
LUBECK WG	54°0′	10°36′	WEYMOUTH ENG	50°36′	−2°30′
MANDAL NOR	58°0′	7°42′			

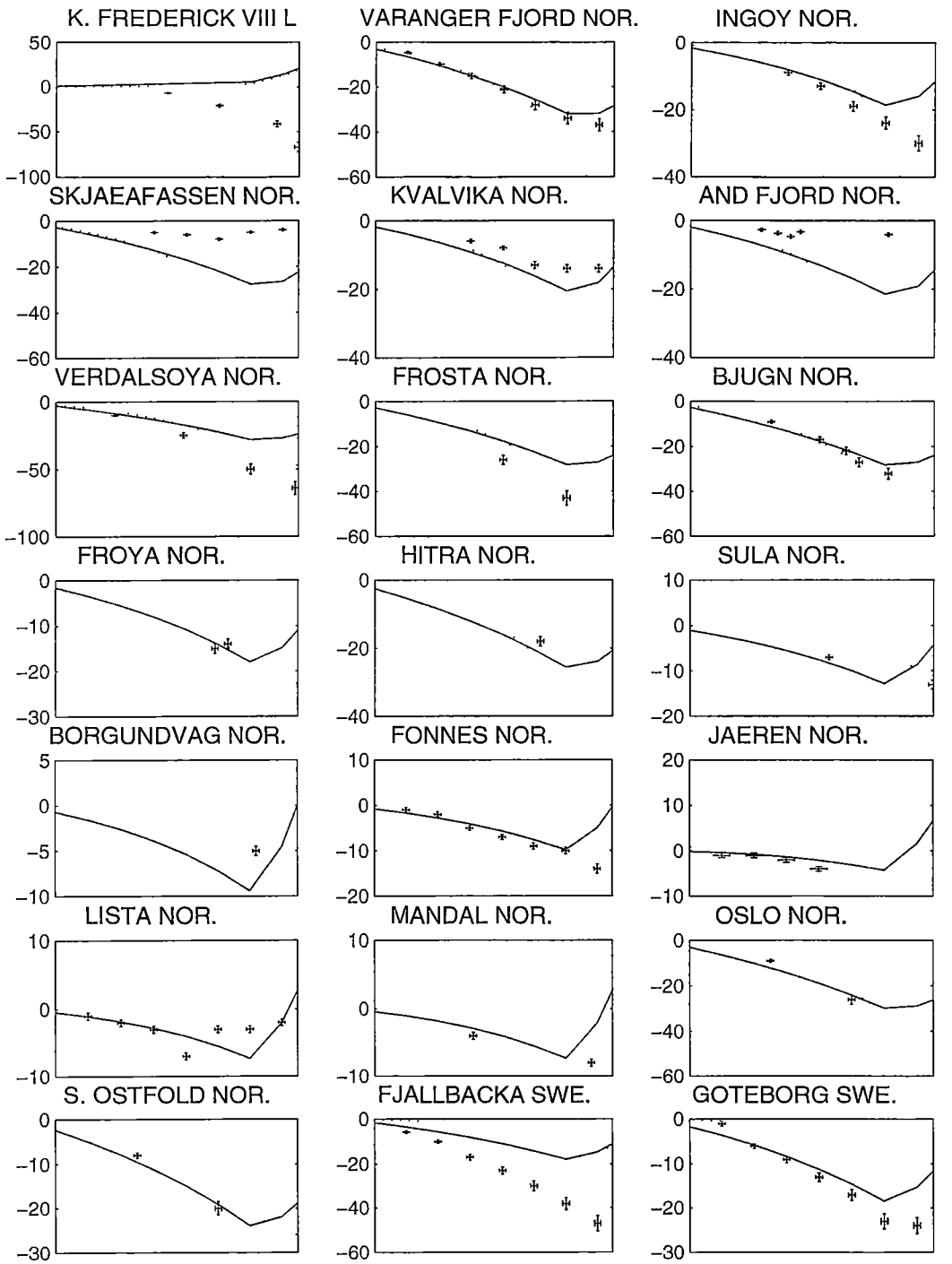
K. FREDERICK VIII L
VARANGER FJORD NOR.
INGOY NOR.
SKJAEAFASSEN NOR.
KVALVIKA NOR.
AND FJORD NOR.
VERDALSOYA NOR.
FROSTA NOR.
BJUGN NOR.
FROYA NOR.
HITRA NOR.
SULA NOR.
BORGUNDVAG NOR.
FONNES NOR.
JAEREN NOR.
LISTA NOR.
MANDAL NOR.
OSLO NOR.
S. OSTFOLD NOR.
FJALLBACKA SWE.
GOTEBORG SWE.

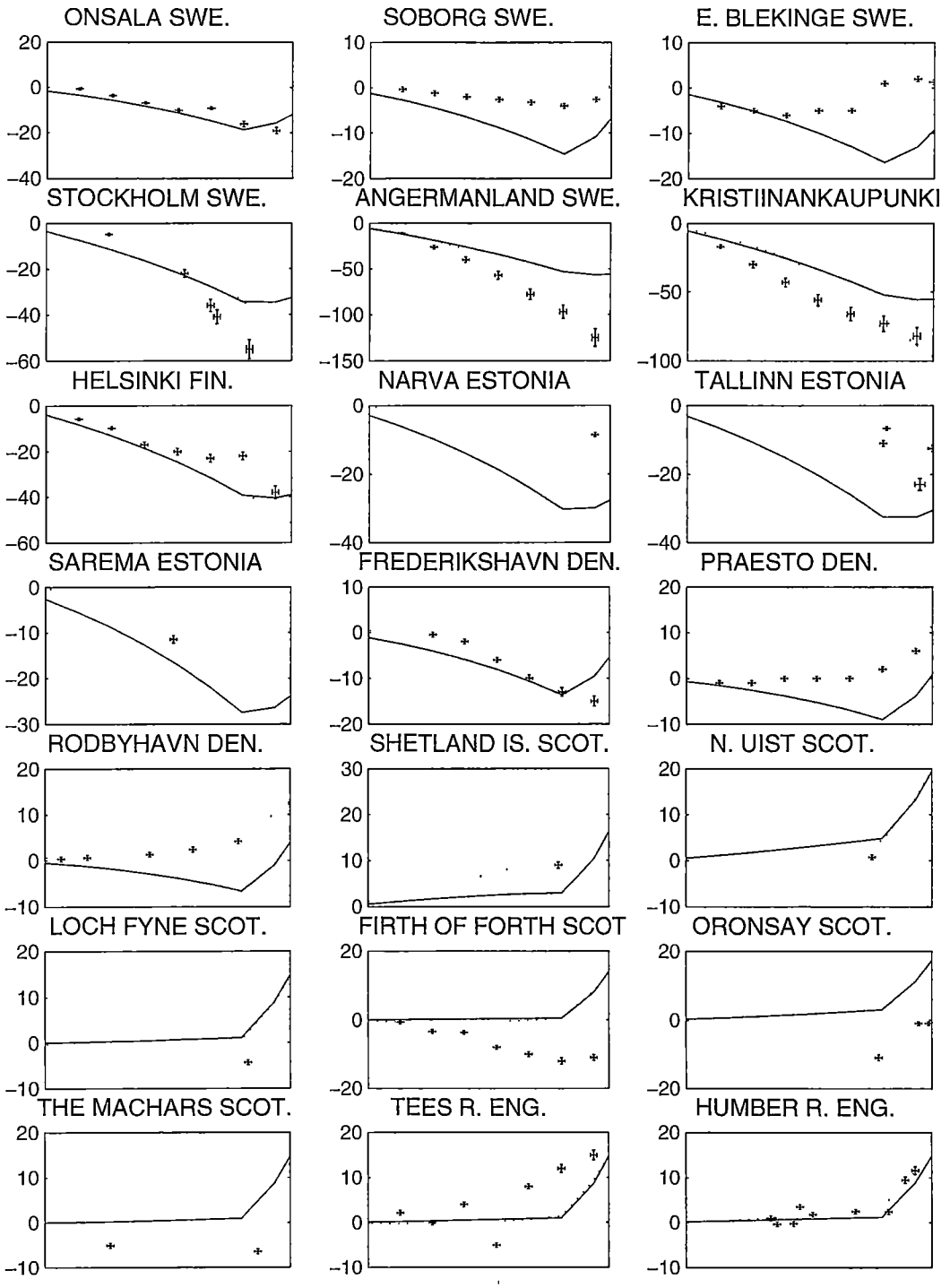
ONSALA SWE.
SOBORG SWE.
E. BLEKINGE SWE.
STOCKHOLM SWE.
ANGERMANLAND SWE.
KRISTIINANKAUPUNKI
HELSINKI FIN.
NARVA ESTONIA
TALLINN ESTONIA
SAREMA ESTONIA
FREDERIKSHAVN DEN.
PRAESTO DEN.
RODBYHAVN DEN.
SHETLAND IS. SCOT.
N. UIST SCOT.
LOCH FYNE SCOT.
FIRTH OF FORTH SCOT
ORONSAY SCOT.
THE MACHARS SCOT.
TEES R. ENG.
HUMBER R. ENG.

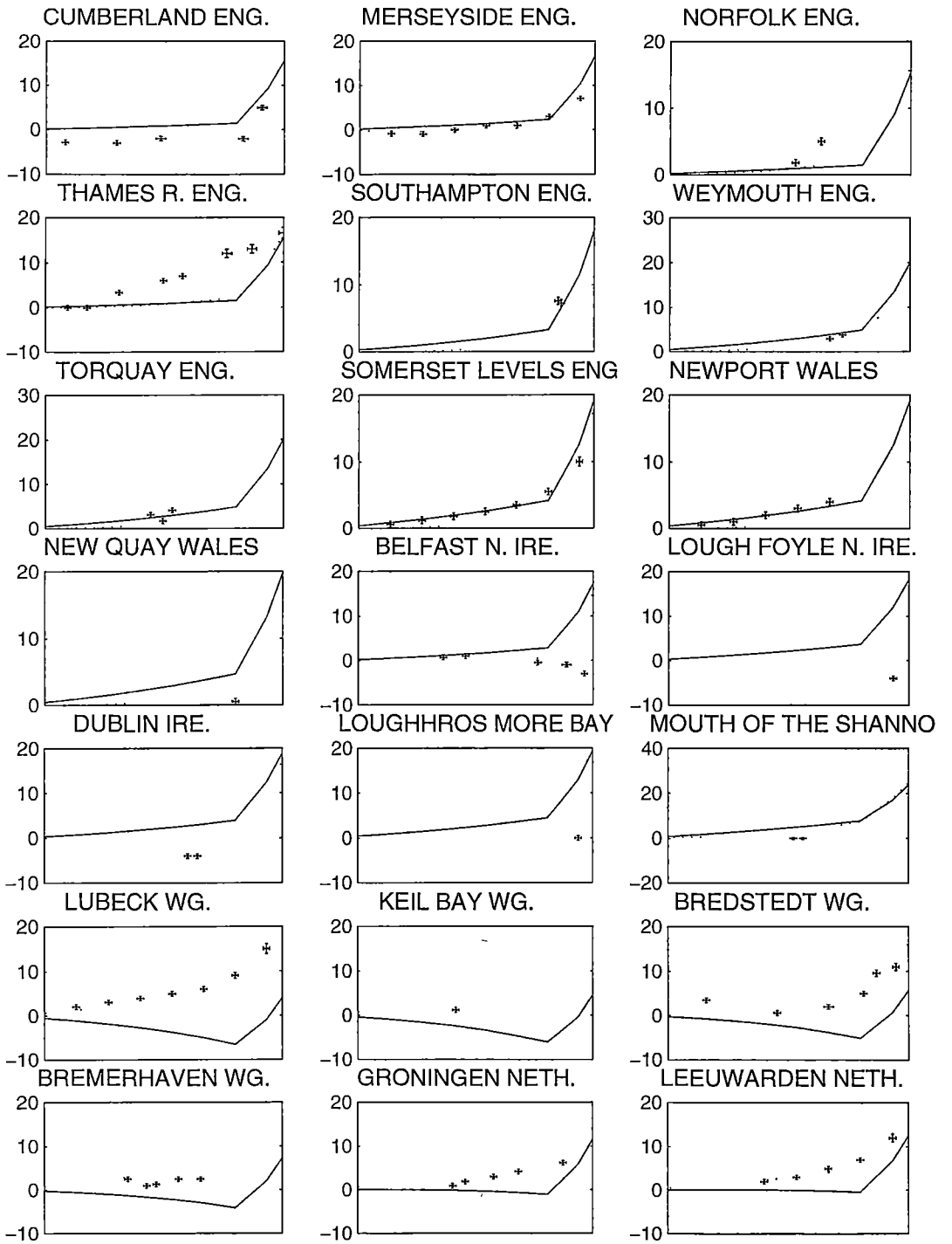
CUMBERLAND ENG.
MERSEYSIDE ENG.
NORFOLK ENG.
THAMES R. ENG.
SOUTHAMPTON ENG.
WEYMOUTH ENG.
TORQUAY ENG.
SOMERSET LEVELS ENG
NEWPORT WALES
NEW QUAY WALES
BELFAST N. IRE.
LOUGH FOYLE N. IRE.
DUBLIN IRE.
LOUGHHROS MORE BAY
MOUTH OF THE SHANNO
LUBECK WG.
KEIL BAY WG.
BREDSTEDT WG.
BREMERHAVEN WG.
GRONINGEN NETH.
LEEUWARDEN NETH.

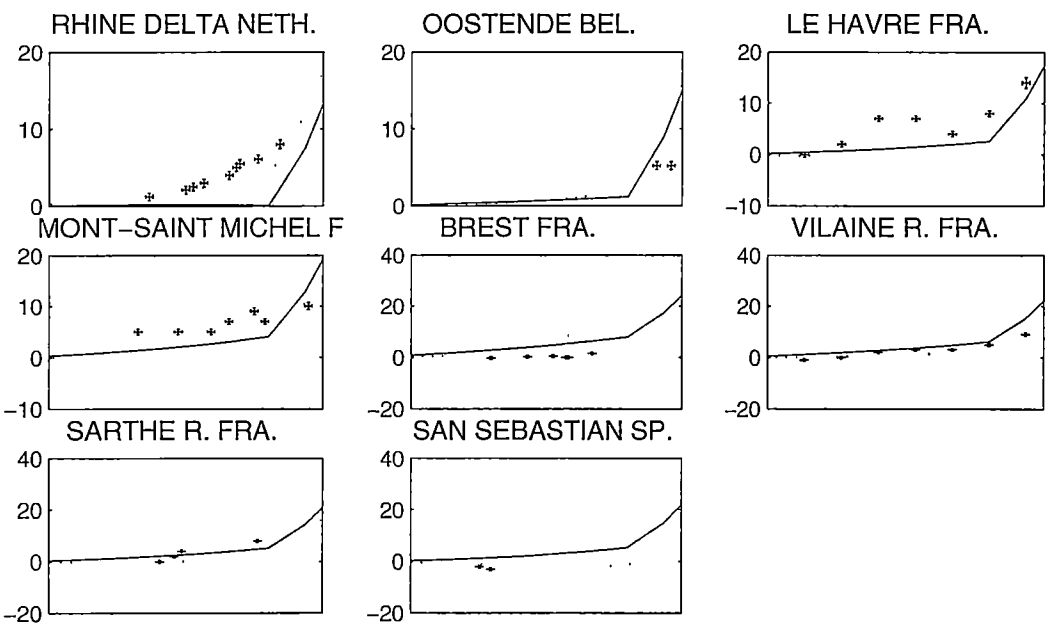
RHINE DELTA NETH.
OOSTENDE BEL.
LE HAVRE FRA.
MONT-SAINT MICHEL F
BREST FRA.
VILAINE R. FRA.
SARTHE R. FRA.
SAN SEBASTIAN SP.